Design and Characterisation of Solid Electrolytes for All-Solid-State Lithium Batteries

Sveinbjörnsson, Dadi Þorsteinn

Publication date:
2014

Document Version
Publisher's PDF, also known as Version of record

Daði Þ. Sveinbjörnsson

Design and Characterisation of Solid Electrolytes for All-Solid-State Lithium Batteries

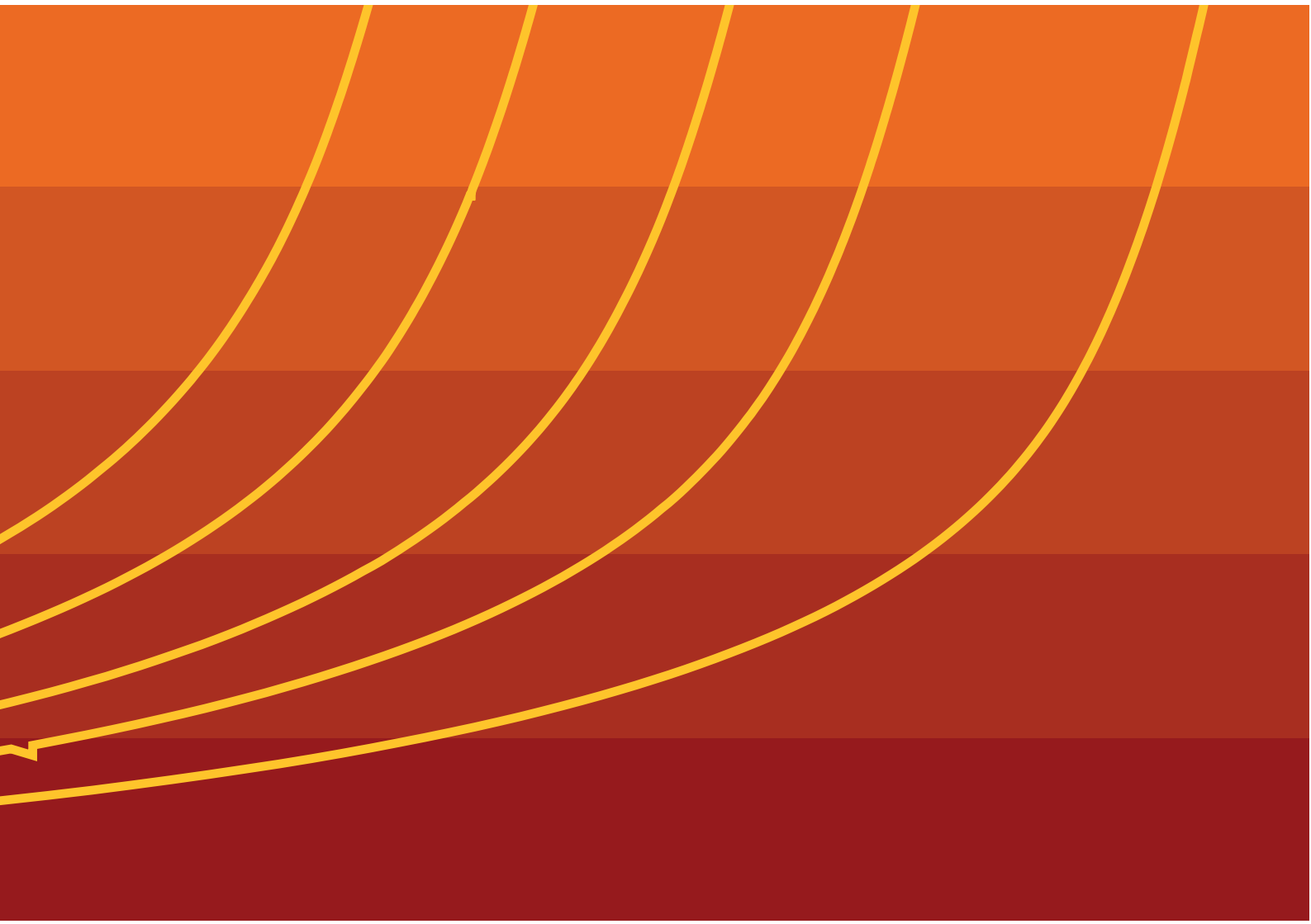

DTU Energy Conversion
Department of Energy Conversion and Storage

DTU

Daði Þ. Sveinbjörnsson

Design and Characterisation of Solid Electrolytes for All-Solid-State Lithium Batteries

Submitted in candidacy for the degree Doctor of Philosophy

Supervisors
Prof. Tejs Vegge
Assoc. Prof. Poul Norby
Prof. Mogens Bjerg Mogensen

Design and Characterisation of Solid Electrolytes for All-Solid-State Lithium Batteries

Author
Daði Þorsteinn Sveinbjörnsson
E-mail: dasv@dtu.dk

Supervisors
Prof. Tejs Vegge
Section for Atomic Scale Modeling and Materials
Department of Energy Conversion and Storage
Technical University of Denmark
E-mail: teve@dtu.dk

Assoc. Prof. Poul Norby
Section for Atomic Scale Modeling and Materials
Department of Energy Conversion and Storage
Technical University of Denmark
E-mail: pnor@dtu.dk

Prof. Mogens Bjerg Mogensen
Research Professor
Department of Energy Conversion and Storage
Technical University of Denmark
E-mail: momo@dtu.dk

Technical University of Denmark
Section for Atomic Scale Modeling and Materials
Department of Energy Conversion and Storage
Technical University of Denmark
Frederiksborgvej 399
DK-4000 Roskilde
Denmark
www.ecs.dtu.dk
Tel: +45 46 77 58 00
E-mail: info@ecs.dtu.dk

Release date:	December 20th, 2013
Comments:	This report is part of the requirements to achieve the degree of Doctor of Philosophy (PhD) at the Department of Energy Conversion and Storage, Technical University of Denmark.

Abstract

The development of all-solid-state lithium batteries, in which the currently used liquid electrolytes are substituted for solid electrolyte materials, could lead to safer batteries offering higher energy densities and longer cycle lifetimes. Designing suitable solid electrolytes with sufficient chemical and electrochemical stability, high lithium ion conduction and negligible electronic conduction remains a challenge.

The highly lithium ion conducting $LiBH_4$-LiI solid solution is a promising solid electrolyte material. Solid solutions with a LiI content of 6.25%-50% were synthesised by planetary ball milling and annealed at 140 °C. Their crystal structure was investigated using powder x-ray diffraction and their ionic conductivity was measured using impedance spectroscopy. The ionic conductivity is found to exceed 0.1 mS/cm at 30 °C and 10 mS/cm at 140 °C. The formation of defect-rich microstructures during ball milling is found to significantly influence the conductivity of the samples. The long-range diffusion of lithium ions was measured using quasi-elastic neutron scattering. The solid solutions are found to exhibit two-dimensional conduction in the hexagonal plane of the crystal structure, with the formation of Frenkel pairs playing a large role.

The charge and discharge performance of all-solid-state batteries with $LiBH_4$-LiI as an electrolyte is reported for the first time. Lithium titanate ($Li_4Ti_5O_{12}$) was used for the positive electrode and lithium metal for the negative electrode. The electrochemical stability of $LiBH_4$-LiI is found to be limited to 3 V. The all-solid-state cells reach 81% of their theoretical discharge capacity at 60 °C and a discharge rate of 10 μA, but a capacity fade of 1.6% per charge-discharge cycle and a large overvoltage are observed. Impedance spectroscopy results show a strong correlation between changes in the discharge capacity of the cells and changes in the cell resistance over 200 cycles. This may be due to a possible formation of a passivating areas in the cell as well as contact issues between the electrode-electrolyte interfaces.

The crystal structure and ionic conductivity of the $LiBH_4$-$Ca(BH_4)_2$ composite were also studied. No formation of a solid solution is observed and the ionic conductivity is lower than that of pure, ball milled $LiBH_4$. Heat treatment of the samples leads to the formation of a small amount of defect-rich, electronically conducting CaH_2 with a cubic crystal structure. Its formation has an effect on the measured conductivity of the samples and increases the risk of an internal short-circuit. This reveals a more general issue that must receive attention in further research on solid electrolytes.

Resumé

Udviklingen af fuld-fast-fase litium batterier, hvori de nuværende elektrolytter i væske fase bliver udskiftet med elektrolytmaterialer på fast form, kan medføre sikrere batterier, som har højere energitætheder og tåler flere op- og afladningscyklusser. Det er dog stadig en udfordring at designe passende elektrolytter på fast form med nødvendig kemisk og elektrokemisk stabilitet, høj ledningsevne for litiumioner og ubetydelig eletrisk ledningsevne.

Den faste opløsning $LiBH_4$-LiI som udviser høj litiumion ledningsevne er et lovende materiale til en elektrolyt på fast form. Faste opløsninger med en LiI koncentration mellem 6.25% og 50% blev syntetiseret ved brug af en planetarisk kuglemølle og udglødet ved 140 °C. Krystalstrukturen blev undersøgt med pulver røntgendiffraktion og materialets ledningsevne af ioner blev målt med impedansspektroskopi. Den ioniske ledningsevne er målt til at overstige 0.1 mS/cm ved 30 °C og 10 mS/cm ved 140 °C. Når materialet bliver malet i kuglemøllen dannes mikrostrukterer rige på defekter, dette viser sig at influere stærkt på prøvernes ledningsevne. Den langtrækkende diffusion af litiumioner blev målt med kvasi-elastisk neutronspredning. De faste opløsninger bliver bestemt til at udvise todimensionel ledning i krystalstrukturens hexagonale plan, heri spiller dannelsen af Frenkelpar en stor rolle.

For første gang bliver virkningsgraden af op- og afladningen for fuld-fast-fase batterier med $LiBH_4$-LiI som elektrolyt rapporteret. Litiumtitanat ($Li_4Ti_5O_{12}$) er benyttet som positiv elektrode og litiummetal som den negative elektrode. Den elektrokemiske stabilitet af $LiBH_4$-LiI er bestemt til at være begrænset til 3 V. Fuld-fast-fase battericellerne når 81% af deres teoretiske afladningskapacitet ved 60 °C og en afladningsrate på 10 μA, men der observeres en stor overspænding samt at kapaciteten aftager med 1.6% per op- og afladninscyklus. Resultater fra impedansspektroskopi viser en stærk sammenhæng mellem ændringen i afladningskapacitet af cellerne og ændringen i cellemodstanden over 200 cyklusser. Dette kan skyldes den mulige dannelse af passiverende områder i cellen samt kontaktproblemer mellem elektrode-elektrolyt grænsefladerne.

Krystalstrukturen og den ioniske ledningsevne af $LiBH_4$-$Ca(BH_4)_2$ komposit materialet blev også undersøgt. Dannelse af en fast opløsning blev ikke observeret og den ioniske ledningsevne er lavere end i rent kuglemalet $LiBH_4$. Varmebehandling af prøverne fører til dannelsen af små mængder defektrigt, elektrisk ledende CaH_2 i en kubisk krystalstruktur. Denne dannelse har en effekt på den målte ledningsevne af prøverne og forøger risikoen for en intern kortslutning. Dette afslører et mere generelt problem som skal undersøges grundigere i fremtidige studier af elektrolytter på fast form.

Ágrip

Þróun fastefnisrafhlaðna, þar sem hinum fljótandi rafvökum sem notaðir eru í dag er skipt út fyrir fastefnisrafvaka, gæti leitt til öruggari rafhlaðna með meiri orkurýmd og lengri heildarlíftíma. Hentugir fastefnisrafvakar, sem hafa nægilegan efnafræðilegan og rafefnafræðilegan stöðugleika ásamt því að vera jónaleiðandi en ekki rafleiðandi, eru enn sem komið er vandfundnir.

Efnin $LiBH_4$ og LiI mynda lausn á föstu formi sem leiðir liþíum jónir vel og er frambærilegur fastefnisrafvaki. Slíkar lausnir með 6.25%-50% LiI magni voru myndaðar með kúlumölun (e. planetary ball milling) og bakaðar við 140 °C. Röntgenbeygjugreining (e. x-ray diffraction) var notuð til að rannaska kristallabyggingu efnanna og jónaleiðni þeirra var skoðuð með samviðnámsrófgreiningu (e. impedance spectroscopy). Jónaleiðni fastefnislausnanna mældist 0.1 mS/cm við 30 °C og 10 mS/cm við 140 °C. Gallar í kristallabyggingu efnanna, sem myndast við kúlumölun, hafa umtalsverð áhrif á jónaleiðni þeirra. Sveim liþíum jóna var mælt með hlutfjaðrandi nifteindadreifingu (e. quasi-elastic neutron scattering). Niðurstöðurnar gefa til kynna að liþíum jónirnar ferðist eftir tvívíðum plönum í hinum sexstrendu kristöllum efnisins. Þær sýna jafnframt að Frenkel pör gegna veigamiklu hlutverki við jónaleiðnina.

Niðurstöður fyrir hleðslu og afhleðslu fastefnisrafhlaðna með $LiBH_4$-LiI sem rafvaka eru kynntar í fyrsta sinn. Liþíum títanat ($Li_4Ti_5O_{12}$) var notað sem jákvætt rafskaut og liþíum málmur sem neikvætt rafskaut. Sýnt er fram á að rafefnafræðilegur stöðugleiki $LiBH_4$-LiI takmarkast við 3 V. Fastefnisrafhlöðurnar ná allt að 81% af fræðilegri afhleðslurýmd sinni við 60 °C og 10 μA straum. Hleðsla og afhleðsla eiga sér hins vegar stað við talsverða yfirspennu, og rafhlöðurnar missa að jafnaði 1.6% af rýmd sinni við hverja hleðslu- og afhleðslulotu. Niðurstöður samviðnámsgreiningar sýna að beint samhengi er á milli afhleðslurýmdar og viðnáms í rafhlöðunum fyrir 200 hleðslu- og afhleðslulotur. Þetta gæti mögulega verið vegna myndunar einangrandi svæða í rafhlöðunni eða vegna minnkunar á snertiflötum rafvakans og rafskautanna.

Kristallabygging og jónaleiðni $LiBH_4$-$Ca(BH_4)_2$ blöndunnar voru líka rannsökuð. Ekki fundust merki um að þessi efni myndi lausn á föstu formi, og jónaleiðni blöndunnar er nokkru lakari en jónaleiðni kúlumalaðs $LiBH_4$. Sýnt er fram á að rafleiðandi CaH_2 með teningslaga kristallabyggingu myndast í litlu magni þegar sýnin eru hituð. Myndun þess hefur áhrif á niðurstöður leiðnimælinga og getur aukið hættu á skammhlaupi inni í rafhlöðunum. Nauðsynlegt er að hafa augun opin fyrir hættunni á slíku við frekari þróun fastefnisrafvaka.

Preface

This thesis is submitted in candidacy for the degree Doctor of Philosopy (PhD) from the Technical University of Denmark (DTU). It is based on work carried out from January 2011 to December 2013 at the section for Atomic-Scale Modeling and Materials at the Department of Energy Conversion and Storage, DTU Risø campus. A part of the work was performed during an external research stay at the Institute for Materials Research at Tohoku University in Sendai, Japan. The work has also included numerous shorter research periods at international large-scale research facilities and presentations at international meetings and conferences in Europe and N-America. The work was funded by the Danish Ministry of Science Globalization Fund.

First of all, I would like to thank my supervisor Tejs Vegge for making this project possible and for his great guidance along the way. Tejs has an amazing ability of providing motivation by constantly coming up with new ideas and by always focussing on the positive aspects when things are uphill.

I would like to thank my co-supervisor Poul Norby for his excellent guidance and countless helpful discussions, especially related to x-ray diffraction. I would also like to thank my co-supervisor Mogens Bjerg Mogensen for his good guidance, especially regarding electrochemistry.

Thanks to Prof. Shin-Ichi Orimo at Tohoku Univeristy for making my research stay there possible and to the members of his research group for making the stay so enjoyable.

Special thanks to Didier Blanchard for both being my mentor and a great colleague throughout my MSc and PhD projects. Special thanks also to Jón Steinar for the friendship and help along the way. Thanks to Jakob, Steen, Ane and Nonni and everyone else in our research group for the enjoyable company and the good working atmosphere.

Thanks to Didier, Jón Steinar and Ane for proofreading this thesis and to Steen and Jakob for their help with translations to Danish. Thanks to Lene Danielsen for keeping things organised and solving every practical problem with a smile on her face. Thanks to Mike Wichmann, Lars Lorentzsen and the other technicians for their reliable and skillful help with the experimental equipment.

Thanks to my friends in Copenhagen for all the swingin' good times and for helping me to finish this project with a smile on my face.

Special thanks to my mother, father and grandmother for always believing in me. I would not have come this far without their constant support.

And finally, thank you Guðrún for your endless love and support. I could not have finished this without you.

Roskilde, December 19$^{\text{th}}$, 2013
Daði Þorsteinn Sveinbjörnsson

Contents

List of Figures

List of Tables

Chapter 1

Introduction

I would like to begin this thesis by putting its rather specialised research subjects in perspective with some of the great challenges we face regarding our energy consumption habits and how battery research is important for the transition towards a more sustainable usage of energy. At the end of this introductory chapter, I will summarise the aims of my PhD project, explain the structure of the thesis and list the publications that arose from this work.

1.1 Motivation

1.1.1 Energy Demand

The past three centuries have been a period of tremendous scientific and technological advance. This development has transformed the world and resulted in countless fascinating ideas and inventions, but it has also resulted in a society which requires access to an enormous amount of cheap and convenient energy. The easy access to fossil fuels (oil, coals and natural gas) has been an vital factor in the technological revolution during this time, making it possible to power e.g. the transportation sector, food production and heavy industry and to provide domestic electricity and heating.

The demand for cheap and convenient energy is still rising [1]. Looking at Figure 1.1a this is not surprising, as there is a correlation between primary energy consumption and wealth (measured in GDP per capita). People in the poorer and less developed parts of the world use much less energy per capita than people in the wealthier countries [1, 2]. As the developing economies strive towards economic growth, they must therefore be able to increase their energy consumption as well. This means that continued supply of cheap energy is not only an important issue for developed economies, but a vital one for developing economies. Here countries are categorised according to the methodology of the United Nations [3], where the countries of Europe as well as the USA, Canada, Japan, S-Korea, Hong Kong, Singapore, Australia and New Zealand are considered developed countries while the remaining areas are considered developing countries.

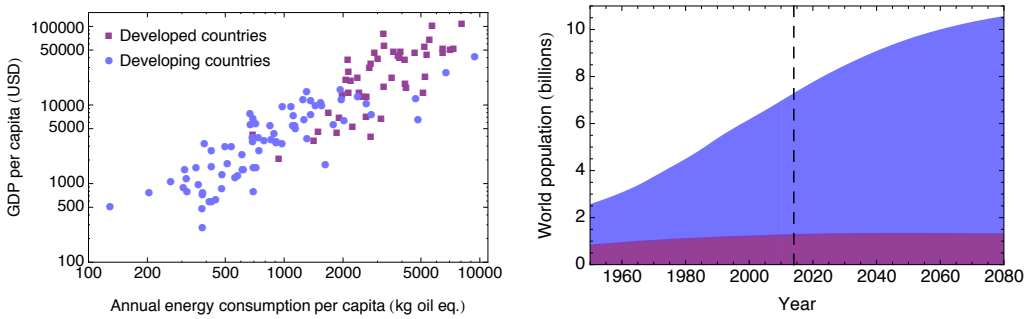

(a) (b)

Figure 1.1: a) A double logarithmic plot of the gross domestic product (GDP) per capita (in U.S. Dollars) as a function of the annual primary energy consumption per capita (in kg of oil equivalents). The data is from 2011 [1, 2]. Developed countries are shown with dark blue rectangles and developing countries are shown with light blue circles. There is a clear positive correlation between the energy consumption and the GDP per capita. **b)** The world population from 1950 until 2080. The black, dashed line shows the current status, and values from there on are based on the mean projection of the United Nations [3]. The world population is currently over 7 billion, and is expected to reach 10 billion within the lifetime of my generation. The population growth is projected to originate from the developing countries, while the population of the developed countries is expected to remain almost constant.

The global energy consumption is also increasing due to population growth [4]. Figure 1.1b shows the projected development of the world population until 2080. The world population has increased greatly in the past decades and will continue to do grow throughout this century [3]. The population growth is expected to mainly take place in the developing countries, while the population growth in the wealthier countries has almost stagnated. The growing population of the developing countries and the increased energy demand per capita along with the economic growth in these countries will thus lead to an increasing world energy demand throughout the 21st century.

1.1.2 Sustainable Energy

There is, however, a very serious problem with our energy consumption habits. As a result of our energy-intensive lifestyle, fossil fuels are being burned at an unsustainable rate, such that our activities have started altering the climate of the earth [5]. This development is projected to have serious consequences for our environment, which in turn would greatly affect our safety and quality of life by e.g. inducing warmer temperatures, rising sea-levels and more frequent extreme weather events [5, 6]. Fossil fuels are also being burned at an unsustainable rate in the sense that the stocks of oil, coal and natural gas that has accumulated in the earth's crust over hundreds of millions of years are now being depleted relatively quickly. This does not necessarily mean that we are likely to run out of fossil fuels any time soon. It does, however, mean that oil supply is bound to reach its peak at some point [7], and if oil demand just keeps rising, the world will eventually move into a period of a permanent oil crisis. The same is

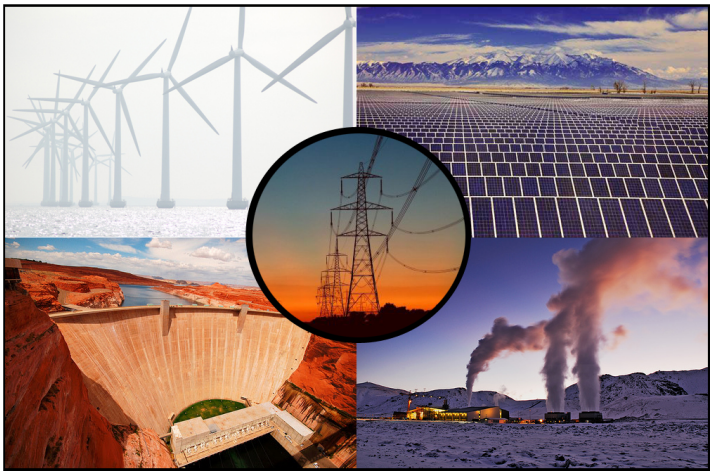

Figure 1.2: Examples of power plants that harness renewable energy sources; a wind farm off the shore of Copenhagen, a huge array of photovoltaics and a hydropower dam in the USA and a geothermal power plant near Reykjavík, Iceland. These power plants all generate electricity.

true for natural gas and coal. With our large and ever-increasing consumption, the time will therefore come when fossil fuels will no longer be as cheap and easily accessible as they have been for the last three centuries. Considering the importance of energy for the world's economy, it is better to prepare for this scenario too early than too late.

It is therefore clear that we must change our habits when it comes to energy consumption. We must make a transition to a more sustainable energy usage, and we must do so while still making it possible for developing economies to increase their energy consumption per capita. This is an enormous challenge, but it is necessary that the fossil fuel era comes to and end and that a new period of sustainable energy usage begins. A more efficient use of energy can surely be a part of the solution as well. Luckily, there are plenty of options for harnessing energy in a sustainable manner, and a few examples of renewable energy sources are shown in Figure 1.2. Other examples include biofuels and waste, as well as nuclear power, which remains a highly controversial source of energy due to its inherent risk.

The process of moving towards a more sustainable energy consumption policy has already started. The EU has established goals for greatly increasing the share of sustainable energy usage in the coming decades [8], and Denmark has set the ambitious goal of being independent of fossil fuels by 2050 [9]. Perhaps even more importantly, the price of renewable energy is falling rapidly and in some cases, electricity produced using renewable energy is reaching prices that are compatible with those of electricity produced using fossil fuels [10, 11].

1.1.3 Energy Storage

Fossil fuels are very convenient in the sense that they are energy sources and energy carriers at the same time. This means that the chemical energy they contain can be stored and easily transported before consuming the energy by

burning the fuel. This is not the case for most sources of renewable energy, as the sources in Figure 1.2 along with most other renewable energy sources are used for electricity generation. Many of those sources, such as solar and wind energy, are furthermore intermittent, meaning that their energy production cannot be controlled to match fluctuations in demand. To end our dependence on fossil fuels, new and efficient methods of energy storage are needed, both for balancing the difference between production and load in the electric grid and for applications in transportation.

There are many possible means for energy storage and the methods of choice will vary depending on the application. In land transportation, which is almost entirely dependent on oil, electric vehicles have in recent years begun to be viable alternatives to fossil fuelled vehicles, especially for travel over relatively short distances. The two most common forms of non-hybrid electric vehicles are battery electric vehicles (BEV) and hydrogen powered fuel cell electric vehicles (FCEV). They can be powered without consuming fossil fuels, provided that the electricity or the hydrogen are produced using other energy sources. BEVs are currently gaining popularity faster than HEVs, partly due to advances in battery technology and problems with finding an efficient hydrogen storage method. In the long run, both of these types of electric vehicles are likely to play a big role in ending the dependence of land transportation on fossil fuels [12, 13].

1.2 Batteries and Solid Electrolytes

1.2.1 Lithium Battery Technology

The most commonly used batteries in BEVs today are lithium ion batteries (Li-ion). Li-ion batteries play an important role in the modern society. They are dominant in the portable electronics sector, and most of us use Li-ion batteries every day to power our laptop computers and mobile phones. There are, however, various challenges that must be solved before lithium based batteries can be as successful in the automotive industry as they have been in the electronics industry for the past two decades [12, 14].

The current Li-ion technology offers batteries with specific energies of around 150 Wh/kg, volumetric densities of around 650 Wh/l and a specific power of around 500 W/kg [15, 16]. It can be estimated that a typical BEV battery needs to store approximately 50 kWh for a driving range of around 200 km [17], which means that the battery must weigh around 300 kg and take up at least 75 liters of space. These numbers should be reduced by increasing the energy density of the batteries. The current batteries cannot be expected to retain their capacity for much more than 1000 charge and discharge cycles, which can be a problem for the resale value of the vehicle as the battery can account for around half the price of a BEV. The cycle life must therefore be improved and price must go down [17]. Last but not least, safety is an issue for Li-ion batteries [18], and numerous fire incidents have been reported in electric vehicles and in airplanes as a result of thermal runaway or short-circuit [19, 20]. Such incidents pose a serious risk in transportation applications due to the large size of the batteries and must be prevented.

These aspects are all related to the chemistry of the batteries, and improvements must be made by developing new materials for the electrodes as well as the electrolyte [14, 18]. The current Li-ion batteries have organic liquid or gel electrolytes, their main advantage being the high lithium ion conductivity (e.g. 12 mS/cm for 1 M $LiPF_6$ in EC-DMC at 27 °C) [21]. They do, however, have the disadvantage of being flammable, which can result in fire incidents as mentioned above. Furthermore, lithium dendrites can grow from the interfaces of the electrolyte with the electrodes, which can decrease the battery capacity over time and increase the risk of an internal short-circuit in the cell [14]. One way of improving the cycle lifetime and the safety of the batteries would therefore be to replace the currently used organic liquid and gel electrolytes with solid-state electrolytes, in which such dendrite formation would be avoided [14,18,22]. Using solid electrolytes would also increase the energy density of the batteries by allowing for thinner electrolytes and more compact packaging, as well as by enabling the use of metallic lithium as the negative electrode. This could double the energy density of the cells [17].

1.2.2 Solid Electrolytes

A potential solid electrolyte material must meet several requirements. It must have high ionic conductivity (more than 0.1 mS/cm over the operating temperature range [18], preferentially 1 mS/cm [23, 24]) and a negligible electronic conductivity. It must have good chemical stability with the electrodes over the working temperature range of the battery, and good electrochemical stability within the operating potentials of the cell. It should furthermore retain good contact at the interfaces with the electrodes. Ideally it should also have low toxicity, be non-flammable and be inexpensive. Designing suitable solid electrolyte materials for lithium batteries that meet these requirements is a great challenge [18].

Various types of crystalline solid-state lithium ion conducting materials are known [22]. Among these are Li_3N [25], perovskite type oxides such as lithium lanthanum titanate (LLTO) [26–29], garnet type structures such as $Li_6BaLa_2Ta_2O_{12}$ [30], NASICON type structures [31, 32], LISICON type structures [33] and $Li_{10}GeP_2S_{12}$ [34]. There are, however, some problems with the usage of most of these materials as solid electrolytes in lithium batteries. The decomposition voltage of Li_3N is too low for practical use. LLTO and NASICON are not stable in contact with elemental lithium and reducible Ti_4^+ ions make the electronic conductivity of LLTO too high [35]. The lithium ion conductivity of LISICON is low and in some cases decreases with time [36]. These materials all have a lithium ion conductivity lower than 1 mS/cm at room temperature, with the exception of $Li_{10}GeP_2S_{12}$, which is the most promising of these materials and is currently being investigated by Toyota for BEV battery applications [37]. Further search for crystalline electrolyte materials with lithium ion conductivities above 1 mS/cm is of great fundamental interest and of practical importance for Li-ion battery research. It is also important for research on other, emerging battery technologies, such as lithium-air batteries, which could benefit from the advantages of solid electrolytes over liquid electrolytes.

1.3 About This Work

1.3.1 The Aims of the Project

The main aim of this work has been to develop and characterise promising solid electrolyte materials for use in all-solid-state lithium batteries.

- The focus of the project has been on lithium borohydride, which is an excellent lithium ion conductor in its high temperature structure. Mixtures of lithium borohydride and other materials have been investigated with the aim of understanding and optimising their ionic conductivity.
- The lithium ion conduction mechanism of lithium borohydride mixtures has been investigated with the aim of gaining a fundamental understanding of their high ionic conductivity. A better understanding of the underlying principles can hopefully be beneficial for optimising their conductivity and/or identify fast ionic conduction in similar materials.
- Working battery cells containing lithium borohydride mixtures have been assembled and tested, with the aim of characterizing the performance of these mixtures as a solid electrolyte material and to gain a fundamental understanding of their strengths and weaknesses in that setting. This can hopefully also provide an insight into some of the more general challenges facing all-solid-state batteries.

1.3.2 Outline of Thesis

The contents of the thesis are divided into seven chapters. The research results of the project are reported in chapters 4, 5 and 6, and the work presented in those chapters was carried out by me unless otherwise stated. This work resulted in four peer-reviewed publications, which are attached as an appendix to the thesis. The thesis may well be read prior to reading the papers, with the exception of section 4.5 on the lithium ion conduction mechanism of $LiBH_4$-LiI, for which the reader would benefit from additional knowledge from Paper B. The chapter outline is as follows:

2 Theory
The main principles of batteries and the theory behind the main experimental methods employed in this work are explained in this chapter. These methods are powder x-ray diffraction, impedance spectroscopy and quasi-elastic neutron scattering.

3 Experimental Procedures
In this chapter I describe the practical aspects of the measurements performed in this work. The sample preparation and is described as well as the the experimental setup for the x-ray diffraction, impedance spectroscopy and quasi-elastic neutron scattering measurements. The assembly and measurements of all-solid-state battery cells are also described in this chapter.

4 The $LiBH_4$-LiI Solid Solution
This chapter begins with an overview of lithium borohydride, its main properties and how its high temperature phase may be stabilised at room temperature. Results on the lithium ion conduction of $LiBH_4$-LiI solid solutions are presented, and the effect of microstructure and heat treatment on the conductivity is discussed. These results are the same as presented in Paper A. Results on the lithium ion conduction mechanism in $LiBH_4$-LiI solid solutions are summarised in the last section of this chapter. These results are an excerpt of the results presented in Paper B, which should be read for further details.

5 The $LiBH_4$-$Ca(BH_4)_2$ Composite
This chapter begins with an overview of the crystal structures of calcium borohydride. Results on the crystal structure and ionic conductivity of $LiBH_4$-$Ca(BH_4)_2$ composites are presented. The formation of cubic and orthorhombic CaH_2 during heat treatment of the composites is reported and its effect on the conductivity of the samples are discussed. The results in this chapter are the same as presented in Paper C.

6 $Li_4Ti_5O_{12}$ Batteries with a $LiBH_4$-LiI Electrolyte
In the last result chapter, the findings on the conductivity of the $LiBH_4$-LiI solid solutions are utilised to assemble working all-solid-battery cells with this material as the electrolyte. The electrochemical stability of the solid solution is reported and results of charge and discharge measurements are presented. Results on the impedance of the cells are presented and the observed changes in the cell capacity and the cell impedance with cycle number are discussed. The results in this chapter are the same as presented in Paper D.

7 Summary and Outlook
A partial summary is given at the end of each respective result chapter, but in this chapter a final summary of the main findings is given and the outlook for this work is discussed.

1.3.3 List of Included Publications

A *Effect of Heat Treatment on the Lithium Ion Conduction of the $LiBH_4$-LiI Solid Solution.*
Dadi Sveinbjörnsson, Jon Steinar Gardarsson Myrdal, Didier Blanchard, Janet Jonna Bentzen, Takumi Hirata, Mogens Bjerg Mogensen, Poul Norby, Shin-Ichi Orimo, Tejs Vegge.
Journal of Physical Chemistry C **117**, 20760-20765 (2013).

B *Li-ion Conduction in the $LiBH_4$:LiI System from Density Functional Theory Calculations and Quasi-Elastic Neutron Scattering*
Jon Steinar Gardarsson Myrdal, Didier Blanchard, Dadi Sveinbjörnsson, Tejs Vegge.
Journal of Physical Chemistry C, **117**, 9084-9091 (2013).

C *Ionic Conductivity and the Formation of Cubic CaH_2 in the $LiBH_4$-$Ca(BH_4)_2$ Composite.*
Dadi Sveinbjörnsson, Didier Blanchard, Jon Steinar Gardarsson Myrdal, Reza Younesi, Rasmus Viskinde, Marit Dalseth Riktor, Poul Norby, Tejs Vegge.
Journal of Solid State Physics, accepted (2013).
(`http://dx.doi.org/10.1016/j.jssc.2013.12.006`)

D *The $LiBH_4$-LiI Solid Solution as an Electrolyte in an All-Solid-State Battery.*
Dadi Sveinbjörnsson, Ane Sælland Christiansen, Rasmus Viskinde, Poul Norby, Tejs Vegge.
Submitted to the Journal of Power Sources (2013).

List of Publications not Included

E *Ammonia dynamics in magnesium ammine from DFT and neutron scattering.*
Adem Tekin, Jens Strabo Hummelshøj, Hjalte Sylvest Jacobsen, Dadi Sveinbjörnsson, Didier Blanchard, Jens Kehlet Nørskov, Tejs Vegge.
Energy & Environmental Science, **3**, 448-456 (2010).

F *Hydrogen Rotational and Translational Diffusion in Calcium Borohydride from Quasielastic Neutron Scattering and DFT Calculations.*
Didier Blanchard, Marit Dalseth Riktor, Jon Bergmann Maronsson, Hjalte Sylvest Jacobsen, Jan Kehres, Elisa Gil Bardají, A. Léon, Fanny Juranyi, Joakim Wuttke, Bjørn C. Hauback, Maximilian Fichtner, Tejs Vegge.
The Journal of Physical Chemistry C, **114**, 20249-20257 (2010).

G *Hindered Rotational Energy Barriers of BH_4-Tetrahedra in β-$Mg(BH_4)_2$ from Quasielastic Neutron Scattering and DFT Calculations.*
Didier Blanchard, Jon Bergmann Maronsson, Marit Dalseth Riktor, Jan Kehres, Dadi Sveinbjörnsson, Elisa Gil Bardají, A. Léon, Fanny Juranyi, Joakim Wuttke, Kim Lefmann, Bjørn C. Hauback, Maximilian Fichtner, Tejs Vegge.
The Journal of Physical Chemistry C, **116**, 2013-2023 (2012).

Chapter 2

Theory

This chapter begins with a very brief discussion of the principles of lithium batteries, their behaviour during charge and discharge and some properties of solid electrolytes. In the remaining sections of this chapter I will provide an overview of the theory behind the three most important measurement techniques employed in this work; powder x-ray diffraction, impedance spectroscopy and quasi-elastic neutron scattering.

2.1 Lithium Batteries

2.1.1 The Working Principle of Lithium Batteries

Rechargeable batteries act both as transducers and as energy storage devices. They convert electrical energy into chemical energy and store it until it is needed again in the form of electrical energy. A main advantage of electrochemical transduction methods over thermal conversion methods is that they are not subject to the Carnot limit [38]. This means that energy conversion using batteries and fuel cells can take place with a much higher efficiency than e.g. in internal combustion engines.

Batteries exist in a variety of different chemistries, but the discussion here will be limited to lithium batteries. A thorough discussion of batteries from a materials science aspect can be found in [38]. As pictured in Figure 2.1, lithium batteries are generally composed of three main components; a positive electrode (cathode), an electrolyte and a negative electrode (anode). The electrolyte acts as a separator between the two electrodes and only allows the flow of ions, while electrons flow from one electrode to the other through an external electric circuit. During discharge, the electrical work performed by the current flow can be used to power auxiliary devices. To charge the battery, electrical work must be performed by an external power source in order to reverse the flow of electrons in the circuit, and thereby the flow of ions within the cell.

A highly simplified schematic of the chemical reactions that take place within a lithium battery upon charge and discharge is shown in Figure 2.2. Let us assume that the two electrodes are composed of the species A and B, respectively,

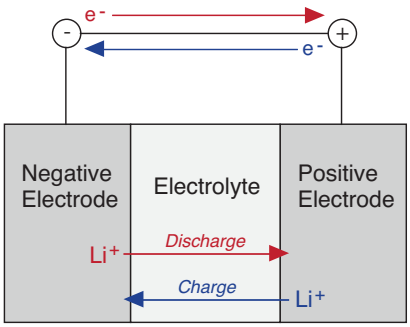

Figure 2.1: A simple schematic of the operating principle of lithium batteries. A potential difference between the two electrodes causes the flow of charged species in the cell. During discharge (shown in red), lithium ions move from the negative electrode, through the electrolyte and to the positive electrode. At the same time, a current of electrons flows from the negative to the positive electrode through an external circuit. During charge (shown in blue), the process is reversed as electrons are forced to flow in the other direction. This leads to the flow of lithium ions from the positive electrode to the negative electrode. In this work the positive electrode will be referred to as the anode and the negative electrode will be referred to as the cathode, regardless of the direction of the current.

and that the electrolyte is a conductor of A ions. This could, for example, correspond to a cell with lithium as the negative electrode, a lithium intercalation material (e.g. $Li_4Ti_5O_{12}$ or $LiCoO_2$) as the positive electrode and a Li^+ conducting electrolyte. The two electrodes have different chemical potentials, which gives rise to a chemical driving force across the cell. Assuming that the reaction $A + B \rightarrow AB$ takes place during discharge, the chemical driving force can be expressed in terms of the standard Gibbs free energy change of the reaction, i.e. the difference between the standard Gibbs free energies of formation of the products and reactants

$$\Delta G_r^\circ = \Delta G_f^\circ(AB) - (\Delta G_f^\circ(A) + \Delta G_f^\circ(B)). \tag{2.1}$$

Furthermore, the mobile ionic species A have an electrostatic energy per mol of $-zFU_{th}$. Here z is the charge number of the ionic species, U_{th} is the theoretical voltage between the electrodes and F is the Faraday constant. Under open circuit conditions, i.e. when no current is flowing, the chemical and electrical forces upon the A ions must be in balance, and the following equation must therefore hold:

$$\Delta G_r^\circ = -zFU_{th} \tag{2.2}$$

Note that it is assumed that the chemical reaction $A + B \rightarrow AB$ takes place between electrically neutral species, but that only ions (and no electrons) are transferred through the electrolyte. For the reaction to proceed, it is therefore necessary that electrons are transferred from the negative to the positive electrode through an external circuit. This means that if the flow of electrons is interrupted, i.e. if the electrical circuit is opened, the ions will also not be transferred through the electrolyte and the whole reaction stalls.

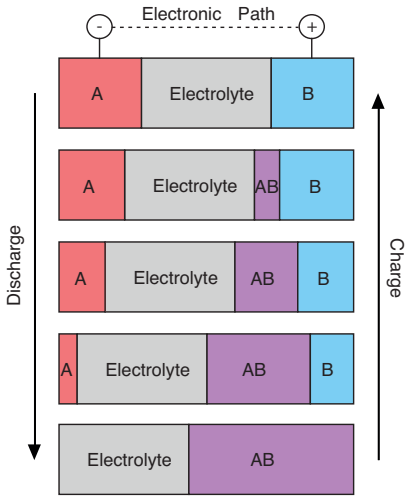

Figure 2.2: A very simple model of a chemical reaction within a battery. Here it is assumed that A^+ are transferred through the electrolyte, and that a new phase AB is formed upon discharge. For the reaction to take place, electrons must be transferred from A to B through an external circuit. The reaction can proceed until the anode species A have been depleted. During charge, the whole process can be reversed by applying a voltage to the cell in order to overcome the driving force caused by the potential difference of the electrodes. Adapted from [38].

2.1.2 Charge and Discharge

The processes of battery charge and discharge are usually presented in the form of charge and discharge curves showing the output voltage of the battery as a function of its state of charge. The state of charge can be measured in a number of different units, such as time (in seconds or hours), capacity (in mAh or mAh/g) or relative to the theoretial capacity of the cell (in percentage). Three schematic examples of discharge curves are shown in Figure 2.3. The output voltage of most batteries varies with the state of charge. This variation depends on a number of factors, including the chemistry of the battery, the operating current and the internal resistance of the cell.

Assuming that no electrons are transferred through the electrolyte, i.e. that the ionic transference number equals unity (which is not always strictly true in reality), the open circuit voltage U_{OCV} of the cell is approximately equal to its theoretical voltage U_{th}. When current flows through the cell during discharge, a voltage drop related to the total internal resistance to ionic conduction in the cell will be observed. Thus, the output voltage will be

$$U_{\mathrm{out}} = U_{\mathrm{OCV}} - I_{\mathrm{out}} R. \tag{2.3}$$

This decrease in voltage follows Ohm's law, and is consequently called an ohmic loss. Note that during charge, the current flows in the opposite direction and the ohmic loss will cause the voltage to increase. Because of this, a higher voltage than U_{OCV} is required to charge the battery. The difference between the open circuit voltage and the observed voltage during charge and discharge is called an overvoltage:

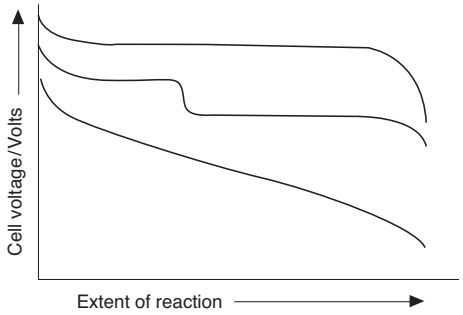

Figure 2.3: Schematic representations of discharge curves with different characteristics. The shape of the discharge curves depends on the chemistry of the batteries (i.e. which phases are present and which chemical reactions take place), on the internal cell resistance and on the operating current. Figure from [38].

$$U_{\mathrm{OV}} = |U_{\mathrm{out}} - U_{\mathrm{OCV}}| \tag{2.4}$$

Repeated charging and discharging of a battery is referred to as cycling. It is highly desirable that batteries retain their overall charge and discharge behaviour over a large number of cycles (at least a few hundred in most practical applications). However, some irreversible chemical reactions may take place in the cell during cycling that do not contribute to charging or discharging the battery. Such reactions may consume some of the cell capacity that was available after charging, and consequently less than 100% of the charge that was transferred during charging will be available during the next discharge. This fraction is called the Coulombic efficiency, which is

$$\eta_C = \frac{Q_{\mathrm{discharge}}(i)}{Q_{\mathrm{charge}}(i)} \tag{2.5}$$

for the i-th charge and subsequent discharge of the cell. Such capacity decrease due to irreversibility in the cell usually takes place during each cycle. Therefore the capacity of the cell as a function of cycle number is subject to an exponential decay, and even small losses in Coulombic efficiency can result in a significantly decreased cell capacity after a large number of cycles as shown in Figure 2.4. It is worth noting that if irreversible reactions that involve charge transfer take place in the cell, those may be included in the measured cell capacity. In such a case, the actual reversible charge and discharge capacity of the cell would be overestimated, introducing the possibility of observing a Coulombic effiency greater than 100%. Care must therefore be taken in the interpretation of the Coulombic efficiency.

Another way of quantifying the performance of a battery over a number of charge and discharge cycles is to measure its discharge capacity retention. In contrast to the Coulombic efficiency, this is not a measure of the relationship between charge and discharge capacity (i.e. of irreversible losses within the cell), but rather a direct measure of the change in discharge capacity between cycles. This can be written as

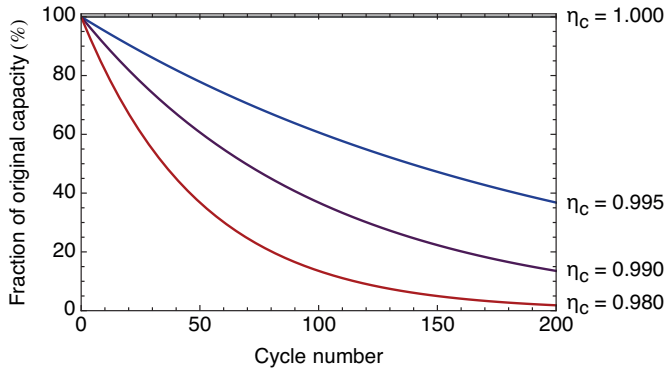

Figure 2.4: An illustration of the effect of Coulombic efficiency on the battery capacity as a function of cycle number. The development of the cell capacity is shown for a few values of η_C. Note that an efficiency loss of merely 1% per cycle causes a battery to lose half of its capacity in only 70 cycles.

$$\Delta Q_{\text{discharge}}(i) = \frac{Q_{\text{discharge}}(i)}{Q_{\text{discharge}}(i-1)} \tag{2.6}$$

where $Q_{\text{discharge}}(i)$ denotes the discharge capacity of the i-th cycle. Similar to the Coulombic efficiency, the discharge capacity retention is subject to an exponential decay as shown in Figure 2.4. It is a useful measure of the health of a battery after many cycles, especially when charge and discharge are set to take place within fixed voltage windows as done in this work.

2.1.3 All-Solid-State Lithium Batteries

As discussed in section 1.2, the battery cells in this work are all-solid-state cells with solid electrolytes. The advantages of using solid electrolytes rather than liquid electrolytes were also discussed in section 1.2. The assembly of good batteries with solid electrolytes is, however, challenging. In conventional batteries, the electrodes are soaked in a liquid electrolyte, assuring a good contact between the electrolyte and the electrodes. In all-solid-state batteries, the electrodes and electrolyte have relatively well defined interfaces, and their contact is of utmost importance for the performance of the cell. This can affect the shape of the charge and discharge curves and cause further drops in the output voltage than simply the expected ohmic loss in the cell accounted for in equation 2.3. To avoid strain and loss of contact at these interfaces it is also important to choose electrode materials that do not change their volume significantly upon lithium ion insertion and extraction.

The ionic conduction properties of solids are closely related to their crystal structures. Other microstructural effects such as the presence of grain boundaries are also important for ionic conduction. Heat treatment can therefore cause sintering effects that may affect the conductivity of solid electrolytes. Because of this, combining powder x-ray diffraction measurements and impedance spectroscopy measurements is a powerful method of characterising solid electrolyte materials and for optimising their lithium conductivity. The conduction mechanism of such materials can be investigated by using quasi-elastic neutron

scattering to observe lithium diffusion while applying an electrical signal to the material. In this work, these experimental techniques have formed the basis for my solid electrolyte research and will be introduced in the following sections.

2.2 Powder X-ray Diffraction

2.2.1 X-ray Diffraction and Bragg's Law

In this work, I used powder X-ray diffraction (XRD) for structural characterisation of the powder samples. X-rays are electromagnetic waves (or photons) with the energy $E = hc/\lambda$, for which the wavelength λ is on the order of an Ångström, or 10^{-10} m (h denotes Planck's constant and c is the speed of light). The fact that atom sizes and interplanar distances between the atoms are also on the order of an Ångström provides an explanation for why x-ray scattering off crystalline materials is useful for crystal structure determination.

In a powder diffraction measurement, an incident (nearly) monochromatic

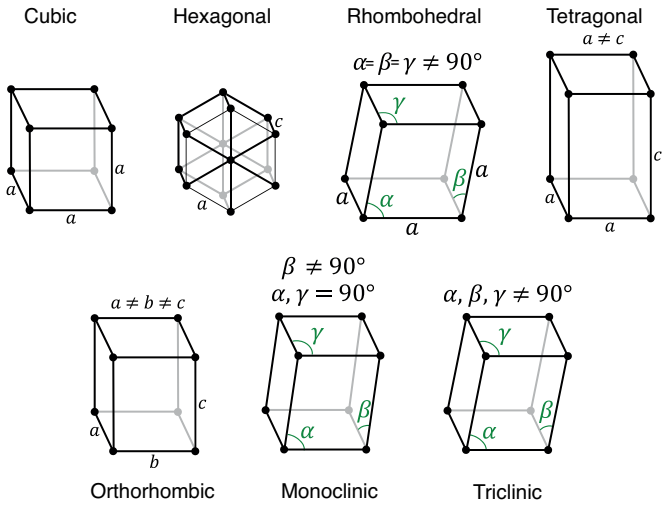

Figure 2.5: The seven 3-dimensional crystal lattice systems. The number of symmetry axes varies between the lattice systems; the cubic system has the most symmetry axes and the triclinic lattice system has no symmetry axis. Only primitive lattices are shown here (systems with lattice points on the cell corners only), but all 14 possible Bravais lattices can be obtained from these seven crystal lattice systems by introducing body-centred, face-centred and base-centred lattice points.

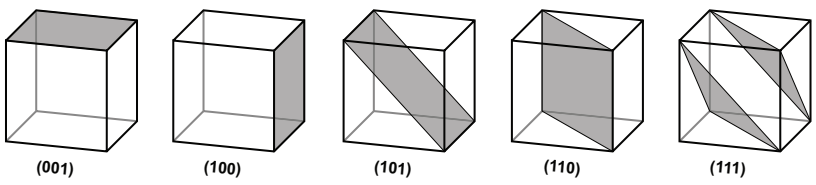

Figure 2.6: Examples of planes with different Miller indices in a cubic crystal. Parallel planes have identical Miller indices. Scattering off parallel planes will interfere constructively at a certain angle according to Eq. 2.7 and consequently yield a peak in the diffraction pattern.

x-ray beam is scattered off a polycrystalline material and onto a detector, which measures the intensity of the scattered wave. The resulting powder diffraction pattern can be used to solve the three-dimensional crystal structures of the phases in the powder. The details of powder diffraction patterns are discussed in section 2.2.2 and the Rietveld method for crystal structure characterisation is presented in section 2.2.4.

The powder samples to be investigated in the diffraction measurement are composed of one or more crystalline phases. Each phase takes on one of the seven possible crystal lattice structures shown in Figure 2.5, which describe the symmetry of the crystal. The seven lattice systems can be divided into 14 categories called Bravais lattices, which can be further divided into 230 different space groups depending on the placement of atoms in the lattice. Exactly one such space group can be assigned to the crystal structure of every crystalline material (with the exception of quasi-crystals).

As the crystals are composed of repetitive structures with a certain degree of symmetry, it is possible to draw different sets of planes containing the atoms in the lattice. One method of describing such lattice planes is by using the Miller indices (hkl), as shown in Figure 2.6. The planes described by the different combination of indices form all possible directions of scattering planes in a crystal. Furthermore, this works in a periodic manner, as all planes with identical Miller indices (hkl) are parallel to each other and equally spaced with an interplanar spacing d_{hkl}. Each plane in such a set of (hkl) planes can be thought of as a separate scattering object.

Let us now consider scattering off infinite parallel lattice planes (hkl) separated by a distance d_{hkl}, as pictured in Figure 2.7. At a certain scattering angle θ, the difference in the path lengths of beams that scatter off atoms in separate parallel planes will equal an integer multiple of the wavelength and Bragg's law [39],

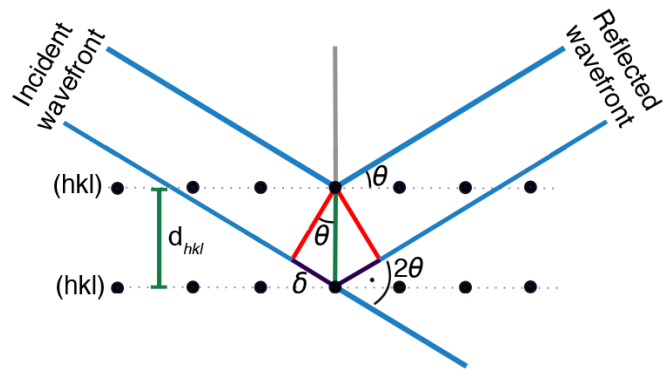

Figure 2.7: An illustration of Bragg's law. Consider two incident x-ray beams that hit atoms situated in separate parallel scattering planes of a crystal. The path lengths of the two beams, from the x-ray source to the detector, differ by twice the length denoted by δ in the figure. By simple triangular geometry it can be found that $2\delta = 2d_{hkl} \cdot \sin(\theta_{hkl})$. It is assumed that the two incident beams are in phase before hitting the lattice. If the outgoing beams shall also be in phase, the difference in their path lengths must equal an integer multiple of the wavelength λ, i.e. 2δ must equal $m\lambda$, $m \in \mathbb{Z}$. Thus, for the beams to interfere constructively, the condition of Equation 2.7 must be fulfilled.

$$2d_{hkl} \cdot \sin(\theta_{hkl}) = m\lambda, \tag{2.7}$$

holds. Here λ is the wavelength of the incident x-ray beam, θ_{hkl} is the angle between the incident beam and the scattering plane (hkl), and $m \in \mathbb{Z}$. Constructive wave interference occurs exactly when the condition of Bragg's law is met. At all other angles destructive wave interference cancels out the scattered wave. As a consequence, the number of counts registered by the detector increases greatly exactly at the scattering angles θ for which Bragg's law holds. This results in a peak in the diffraction pattern corresponding to the scattering off the plane (hkl). As this occurs for every set of parallel planes, i.e. for each combination of the Miller indices (hkl), a complete diffraction pattern with a peak corresponding to each set of parallel planes emerges from the XRD measurement.

2.2.2 The Powder Diffraction Pattern

The powder diffraction pattern is a plot of the detected intensity as a function of the scattering angle 2θ in either one or two dimensions, depending on the geometry of the experiment and the detector type. Examples of both types of diffraction patterns, from a measurement of a $LiBH_4$-LiI solid solution, are shown in Figure 2.8. A further discussion of the experimental setup of these XRD measurements can be found in section 3.2.

As a result of Bragg's law, the positions of the peaks in a diffraction pattern

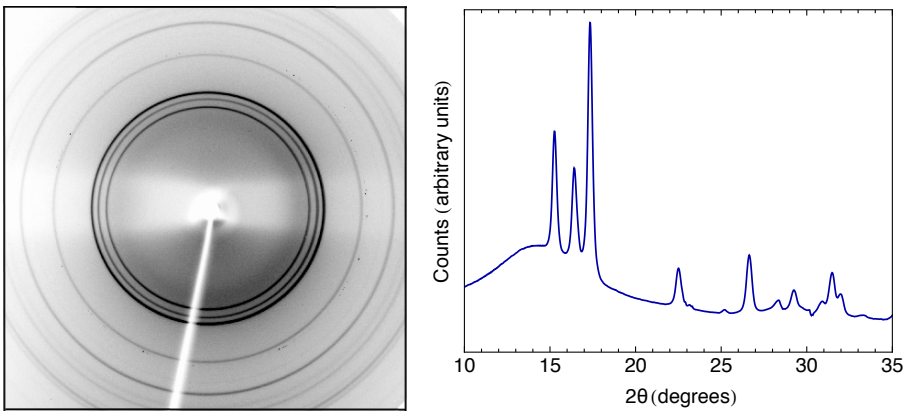

(a) **(b)**

Figure 2.8: Diffraction patterns from a measurement of a $LiBH_4$-LiI solid solution performed at the MAX II synchrotron at MAX-lab in Lund, Sweden. **a)** A diffraction pattern recorded using a two-dimensional detector in a transmission geometry. The pattern appears rotationally symmetrical around the direction of the incident beam due to the random orientations of the crystallites in the powder. As a result, the pattern forms so-called Debye-Scherrer rings. The needle-shaped white line is a beam-stop to prevent the incident beam from hitting the detector. **b)** Here the two-dimensional pattern in Figure a) has been integrated over the axis of rotational symmetry, resulting in a one-dimensional diffraction pattern. This method yields much better counting statistics than by simply plotting a single cross section of the Debye-Scherrer rings.

depend on the atom locations, i.e. on the unit cell size of the crystal lattice and on the positions of the atoms in the cell. The intensities of the peaks mainly depend on the scattering cross-section of the atoms in the crystal. X-rays scatter off electrons and therefore the scattering cross-section of each atom is directly related to its electron density. This is a rather unfortunate fact in this work, considering that most of the powder investigated here includes H, Li and B ions. These atoms have very low electron densities and are therefore poor x-ray scatterers.

The knowledge of the unit cell size and the atom types and locations in the crystal lattice is sufficient to distinguish one crystalline phase of a material from another. Since these are exactly the parameters that govern the position and the intensities of the diffraction peaks, it is clear that each crystalline phase has a unique diffraction pattern. This clarifies how XRD measurements can serve as a method to identify which crystalline phases are present in a sample.

Powder samples are composed of a large number of small crystallites. Each crystallite is assumed to have a random orientation, which means that, on average, scattering off each plane is as likely in any direction. If, however, the crystallites in the sample have some preferred orientations, the scattering off some planes will be more intense than expected. This will affect the intensities of the diffraction peaks and must be taken into account when modelling the diffraction patterns.

The peaks in a diffraction pattern are not ideal delta-shaped peaks, but instead have a finite width. This broadening is due to several effects and arises because in practise, Bragg's law is never fulfilled at a single, discrete value of θ but rather within a statistical distribution of θ values. The broadening can be described by a peak shape function P, which is a convolution of the contributions to the peak broadening:

$$P(\theta) = \Omega(\theta) \otimes \Lambda(\theta) \otimes \Psi(\theta) + \beta_0(\theta) \tag{2.8}$$

Here Ω denotes the instrumental resolution function, Λ is the wavelength dispersion function, Ψ is the sample broadening function and $\beta_0(\theta)$ is the measurement background function.

The instrumental resolution is limited due to a number of physical and geometrical factors. It can, however, be determined by measuring a well-known standard sample and analysing the resulting diffraction pattern. The wavelength dispersion function accounts for the fact that the incident wave is not truly monochromatic, which causes Bragg's law to be fulfilled for a distribution of λ values. The background contribution arises because of noise registered by the detector and because of possible amorphous phases present in the sample. The sample function describes broadening due to the physical properties of the sample, and is therefore the most scientifically interesting contribution to the peak broadening. The sample broadening mainly arises for two reasons; the broadening due to the size of the crystallites in the powder (size broadening) and the broadening due to strain on the crystal lattice (strain broadening).

2.2.3 Size and Strain Broadening

When describing Bragg's law in the previous section, the assumption was made that the material was composed of a practically infinite number of lattice planes. If this is true, diffraction peaks will appear only at the true Bragg angle, while negative interference will cancel out the waves at all other angles. This approximation holds for relatively large crystals, but starts breaking down if the crystal size is on the order of 100 nm or smaller. Then there are only a few tens or hundreds of parallel scattering planes, which may not be sufficient to cancel out all reflections at angles slightly off the true Bragg angle. Bragg's law will thus be fulfilled within a distribution of angles for scattering off small crystals, resulting in a peak broadening. A decrease in crystallite size will thus lead to broader diffraction peaks. The relationship between the crystallite size and size broadening can be described by the Scherrer equation [40]

$$\mu = \frac{k\lambda}{\beta \cos\theta}, \tag{2.9}$$

where μ is the average crystallite size, λ is the wavelength of the incoming beam, θ is the diffraction angle and β is the full width at half-maximum (FWHM) of the diffraction peak located at the angle θ. Note that the broadening due to the instrumental resolution should be subtracted from the value of β. The Scherrer constant k is a shape factor and is usually taken to equal 0.9. The Scherrer equation assumes that all crystallites in the powder have the same shape.

Strain broadening arises if the lattice structure of the crystal is not perfectly relaxed, i.e. if the atom positions are shifted as a result of deformation forces that bend the lattice out of its expected shape. Such forces can e.g. be present if the crystal lattice contains point defects or if the sample is composed of an inhomogeneous solid solution. In this case, the atoms in the crystal will not all be strictly positioned at their expected lattice sites, but rather be slightly distributed around those sites. This will cause Bragg's law to be fulfilled for a distribution of angles θ. The strain broadening can be described by the Stokes-Wilson equation [41]

$$\eta = \frac{\beta}{4 \tan\theta} \tag{2.10}$$

where η quantifies the lattice strain. Similar to the case of size broadening, the broadening due to the instrumental resolution should be subtracted from the value of β.

Note that the size and the strain broadening effects have different angular dependencies. When modelling the peak shapes in a diffraction pattern, it is therefore often possible to distinguish the contributions from the crystallite size and from the lattice strain, even if both effects cause a non-negligible peak broadening at the same time. This is performed by modelling numerous diffraction peaks corresponding to a single crystalline phase and observing the development in the FWHM of the peaks with θ.

A combined expression of the contributions to the peak broadening can be derived from eq. 2.9 and 2.10. Assuming that the instrumental broadening is known and that other possible broadening effects are negligible, the FWHM of a diffraction peak at the angle θ is

$$\beta(\theta) = \sqrt{\left(\frac{k\lambda}{\mu \cos\theta}\right)^2 + (4\eta \tan\theta)^2 + \beta_0^2} \tag{2.11}$$

where β_0 denotes the contribution of the background signal. This expression can be used for modelling the shapes of individual peaks, e.g. if the quality of the data at hand does not allow for a complete modelling of the diffraction pattern.

2.2.4 Rietveld Refinement

Rietveld Refinement is a least-squares method for modelling a full diffraction pattern using the structural parameters of the crystalline sample [42]. A more detailed description of the contents of this subsection can e.g. be found in [43]. The observed intensity at each step of the diffraction pattern can be written as

$$Y_c = Y_b + \sum Y_r \tag{2.12}$$

where Y_b is the background contribution at that step and the second term is the summed contribution from all Bragg peaks located near that step of the diffraction pattern. The Bragg contributions are assumed to have a certain peak shape, e.g. a Gaussian or a Lorentzian shape, while the background is assumed to be a smooth function that is often modelled by a polynomial. In order to find the best least-squares fit to the observed data, the expression

$$\sum w(Y_o - Y_c)^2 \tag{2.13}$$

must be minimised. Here Y_c is the calculated fit to the observed data-point Y_o and w is a weight factor depending on the variance in Y_o. The solution to this minimisation problem is usually found using software specifically designed for Rietveld refinement. The refinements presented in this work were carried out using the GSAS software [44].

It is important to be able to assess the quality of the least-squares refinement in order to have an indication of the accuracy of the physical parameters that are extracted from the model. The so-called 'goodness of fit' is defined as

$$\chi^2 = \frac{\sum w(Y_o - Y_c)^2}{N_{obs} - N_{var}} \tag{2.14}$$

where N_{obs} is the number of observations (data points) and N_{var} is the number of variables in the model. χ^2 equals approximately unity for an optimal refinement. The expected weighted residuals are indicated by

$$R_{wp} = \sqrt{\frac{\sum w(Y_o - Y_c)^2}{\sum w Y_o^2}}. \tag{2.15}$$

The residuals approach zero with increased refinement quality.

A number of physical parameters can be estimated using the Rietveld method. These include, but are not limited to: The unit cell parameters, the average crystallite size (Eq. 2.9), the lattice strain (Eq. 2.10), the relative phase abundances, preferred orientations in the sample, atom occupancies and atom displacement. It must, however, be kept in mind that the quality of a refinement can never

exceed the quality of the measured data. And due to the large number of fitting parameters, especially in samples containing multiple crystalline phases, I believe the following words should be kept in mind when modelling x-ray diffraction data:

"A Rietveld refinement is never perfected, merely abandoned"

-Peter Stephens

2.3 Impedance Spectroscopy

2.3.1 Impedance

The conductivity of the solid electrolyte materials was measured using impedance spectroscopy. This is a well-suited technique for solid electrolyte research as the interfaces in a solid state cell will polarise in a certain way when an electric signal is applied. Examples of such interfaces are those of two different components of the cell (e.g. electrolyte and electrode) or interfaces between grains in a polycrystalline cell component. If the direction of the electric signal is reversed, the polarity at the interfaces will change with a time constant that is characteristic for each particular type of interface. In an impedance spectroscopy measurement, this phenomenon is utilised by applying an alternating current (AC) electric signal to the cell and measuring its response. By repeating this for a large array of AC frequency values, information can be obtained about the response of the various types of interfaces in the cell. A comprehensive discussion of impedance spectroscopy can be found in [45].

In an impedance spectroscopy measurement, the response to an electric signal is measured in terms of the impedance. Similar to how the resistance R is the ratio of the voltage to current in a direct current (DC) circuit, the impedance Z is the ratio of the voltage to current in an alternating current (AC) circuit. While the resistance is a measure of the opposition to DC flow, the more general concept of impedance is a measure of the opposition to AC flow and describes both the resistance and the phase shift of the resulting signal.

As visualised in figure 2.9, the impedance can be written as a complex number

$$Z = R + iX = |Z|e^{i\theta} \tag{2.16}$$

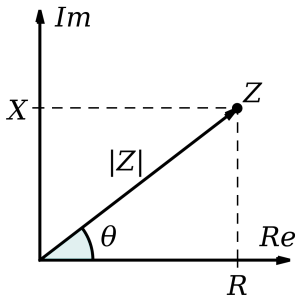

Figure 2.9: An Argand diagram of the impedance Z. The plot shows both the rectangular coordinate representation of Z in terms of R and X, as well as the polar coordinate representation in terms of $|Z|$ and θ.

where the real part corresponds to the resistance and the imaginary part (called 'reactance') accounts for the phase difference;

$$\begin{aligned} \mathrm{Re}(Z) = R = Z' = |Z|\cos(\theta) \\ \mathrm{Im}(Z) = X = Z'' = |Z|\sin(\theta) \end{aligned} \tag{2.17}$$

where the modulus and the phase angle are given by

$$|Z| = \sqrt{(Z')^2 + (Z'')^2} \qquad \text{and} \qquad \theta = \arctan(Z''/Z') \tag{2.18}$$

respectively.

Impedance spectroscopy measurements can be performed either by applying a single-frequency voltage U to the sample and measuring the amplitude and the phase shift of the resulting current I (potentiostatic) or by driving the current I through the sample and measuring the resulting voltage U (galvanostatic). The two methods are equivalent if the electric signals are small (i.e. $U < RT/F$ where R is the gas constant, T is the temperature and F is Faraday's constant), because then the sample response will be linear [45].

In this work, the potentiostatic method was mainly used. In that case an AC single-frequency voltage

$$u(t) = U\sin(\omega t) \tag{2.19}$$

is applied to the sample. Here U is the magnitude of the voltage and $\omega = 2\pi f$ is the angular frequency of the AC signal. The resulting current will be

$$i(t) = I\sin(\omega t + \phi). \tag{2.20}$$

where ϕ denotes the phase shift between the input and the output signal. The impedance is the ratio of the voltage to the current, i.e.

$$Z = \frac{u(t)}{i(t)} = \frac{U\sin(\omega t)}{I\sin(\omega t + \phi)}. \tag{2.21}$$

If such a measurement is repeated for a large range of frequencies ω, the outcome will be an impedance spectrum. The spectrum is usually plotted in a Nyquist plot, which is a plot of $Z'' = \mathrm{Im}(Z)$ as a function of $Z' = \mathrm{Re}(Z)$. Examples of Nyquist plots are shown in figure 2.10. As already mentioned, the impedance spectrum often contains contributions from multiple interface processes in the cell. If changes in polarity at these interfaces occur with different time constants, their contributions will appear in different frequency ranges in the Nyquist plot. One way of separating and identifying the different contributions in an impedance spectrum is therefore to fit a model to the Nyquist plot.

2.3.2 Equivalent Circuit Elements

Impedance is defined in a manner that is analogous to the definition of resistance. It is a measure of the response of a system to an electric signal, and therefore it is somewhat natural to describe the outcome of an impedance measurement in terms of electrical circuit components. The most common method of modelling

an impedance spectrum is to find an electrical circuit that has a frequency response equivalent to that of the measured cell. In such an equivalent circuit model, the impedance of resistors, capacitors and other circuit elements can be combined in a circuit that yields a Nyquist plot corresponding to the measured plot.

In this work, four different equivalent circuit elements have been utilised to describe the measured impedance spectra. Two of these elements, the resistance and the capacitance, correspond directly to ideal well-known electrical circuit elements that are expected to be point-shaped (i.e. have no expansion in space). The other two are the constant-phase element (CPE) and the Warburg element, which do not correspond directly to commonly used electrical components. These are distributed circuit elements that arise partly due to the fact that the measured sample is not point-shaped but of finite size and therefore distributed in space. Let us now turn to the contribution of each of these elements to the impedance.

Resistance

In the case of a purely resistive behaviour, the impedance is identical with the resistance R, i.e. the phase shift ϕ equals zero and Z is a purely real quantity. Then the ratio between the voltage and the current is described by Ohm's law

$$Z_R = \frac{u(t)}{i(t)} = \frac{U\sin(\omega t)}{I\sin(\omega t)} = R. \tag{2.22}$$

Capacitance

In the case of a purely capacitive behaviour, the response to the voltage $u(t)$ is described by $C = q/u(t)$, where C is the capacitance and q is the electric charge. Then the resulting current is

$$i(t) = \frac{dq}{dt} = C\frac{du(t)}{dt}. \tag{2.23}$$

For a combination of many capacitive elements, the problem of solving such differential equations may prove extremely difficult. It is therefore more convenient to Fourier transform Eq. 2.23 into an algebraic equation in the frequency domain. This results in

$$I(\omega) = i\omega C \cdot V(\omega). \tag{2.24}$$

where i is the imaginary unit, not to be confused with the current $i(t)$ in the time domain. An example of how this may be derived can be found in Appendix A of my MSc thesis [46]. The ratio between the voltage and the current for a purely capacitive behaviour is

$$Z_C(\omega) = \frac{V(\omega)}{I(\omega)} = \frac{1}{i\omega C}. \tag{2.25}$$

as expressed in the frequency domain. This expression is purely imaginary and corresponds to a phase shift only.

Constant-Phase Element

The constant-phase element (CPE) is a distributed equivalent circuit element which models the behaviour of a double-layer, which can be viewed as an imperfect capacitor. The finite distribution of the sample in space makes it a non-ideal element, but other imperfections such as the roughness of the electrodes may also contribute here [45]. In this case, the Nyquist plot forms a depressed circular arc, i.e. a semi-circle that has its origin below the Z' axis. The CPE has an impedance of

$$Z_Q(\omega) = \frac{1}{Q_0(i\omega)^n} \tag{2.26}$$

where $Q_0 = 1/|Z|$ at $\omega = 1$ rad/s, and $n \in [0, 1]$. The fit parameters in this equation are Q_0 and n. Note that for $n \to 1$, $Q_0 \to C$ and $Z_{\mathrm{CPE}} \to Z_C$, as can be seen by comparison with eq. 2.25. In such a case, the Nyquist plot forms a perfect, non-depressed semi-circle. In this work the exponent n usually takes on values of $0.9 < n < 1$ and thus Q_0 can be referred to as a 'pseudo-capacitance' [47].

Warburg Element

The Warburg element is a distributed equivalent circuit element which models semi-infinite diffusion. When charge passes in a cell for a prolonged time, diffusion of the active ions to the surface of the electrodes interface must take place to maintain the concentration of these ions. A process that is limited by the diffusion rate will appear as an additional time-dependent contribution to the impedance spectrum. This contribution can be modelled by the Warburg element, which has a constant phase of 45°. The impedance of this element is

$$Z_W(\omega) = \frac{A_W}{\sqrt{\omega}} + \frac{A_W}{i\sqrt{\omega}} \tag{2.27}$$

The fit parameter A_W is the Warburg coefficient, a diffusion coefficient of ions in a solid solution.

2.3.3 Nyquist Plots and Equivalent Circuit Models

In order to fit the circuit elements to a Nyquist plot, they must be combined into an equivalent circuit that adequately describes the shape of the plot. Once a circuit has been chosen, the parameters of the equivalent circuit can be fitted to the measured data using least-squares methods. In this work, this has been performed using the software ZSimpWin. It should be noted that the equivalent circuit model will not be unique, as an arbitrary number of circuit elements may be combined to fit the impedance spectrum. However, using more circuit elements than necessary is usually avoided, because for a good interpretation of the model one should be able to assign a physical process in the cell to each element of the equivalent circuit.

To illustrate how equivalent circuits can be employed to model impedance spectra in a Nyquist plot, two of the equivalent circuits that have been used for fitting the impedance spectra measured during this work are shown in Figure

2.10. Note that this figure shows the calculated impedance of these circuits, i.e. it is not based on any measured data. The impedance of the circuits is calculated by combining the impedances of the individual circuit elements. This is performed in the same manner as when combining resistors; elements connected in series are directly summed while the reciprocals of elements connected in parallel are summed.

In this work, I used the circuit in Figure 2.10a for fitting the impedance spectra of symmetrical cells with a solid electrolyte and lithium metal electrodes. It can be denoted as an $(RQ)(RQ)$ circuit (the parenthesis denote the knot

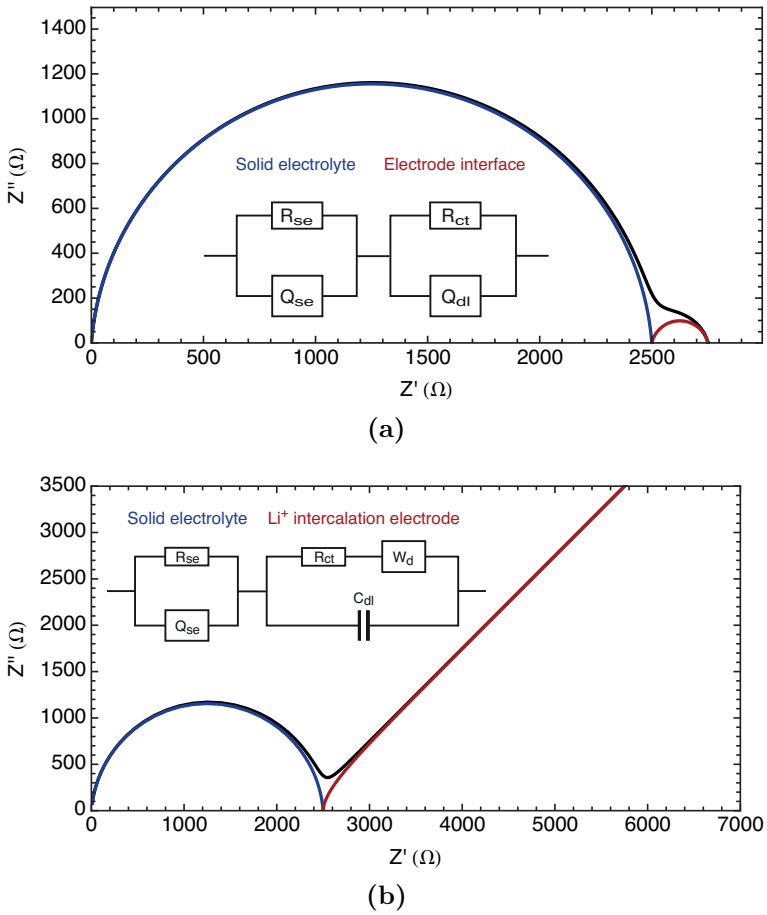

Figure 2.10: Nyquist plots of two equivalent circuit models made from calculated values using Eq. 2.28 and 2.29 respectively. The frequency ω ranges from 1 MHz to 1 Hz and decreases from left to right in the plots. The resistor sizes are chosen as $R_{\text{se}} = 2500\ \Omega$ and $R_{\text{ct}} = 250\ \Omega$ in both plots. **a)** Two (RQ) circuits (i.e. circuits containing a resistor and a CPE in parallel) connected in series. The Nyquist plot of the total circuit is shown in black while the plots of the two sub-circuits are shown in blue and red, respectively. The two arcs are slightly depressed semi-circles with $n_1 = 0.95$ and $n_2 = 0.85$. **b)** A series connection of an (RQ) circuit and an $([RW]C)$ (Randles) circuit. The Nyquist plot of the total circuit is shown in black, while the plots of the individual sub-circuits are shown in blue and red, respectively. The Warburg element describes the tail at the low-frequency end of the plot. The tail has a slope of 45° and can usually be attributed to a diffusion process.

points of parallel connections) where each of the two arcs in the Nyquist plot in Figure 2.10a corresponds to a (RQ) sub-circuit. The larger, high-frequency arc is expected to arise due to the impedance of the bulk and the grain boundaries of the solid electrolyte, and can be modelled in terms of a resistance R_{se} and a pseudo-capacitance (CPE) Q_{se}. The smaller, low-frequency arc is expected to correspond to the impedance of the interface between the solid electrolyte and the lithium metal electrodes and can be modelled as a charge transfer resistance R_{ct} and a double layer pseudo-capacitance (CPE) Q_{dl} [48]. The $(RQ)(RQ)$ circuit has a total impedance of

$$Z(\omega) = Z_{R_{\mathrm{se}}Q_{\mathrm{se}}} + Z_{R_{\mathrm{ct}}Q_{\mathrm{dl}}} = \left(\frac{1}{Z_{R_{\mathrm{se}}}} + \frac{1}{Z_{Q_{\mathrm{se}}}}\right)^{-1} + \left(\frac{1}{Z_{R_{\mathrm{ct}}}} + \frac{1}{Z_{Q_{\mathrm{dl}}}}\right)^{-1}. \quad (2.28)$$

I used the circuit in figure 2.10b for fitting the impedance spectra of battery cells with a solid electrolyte, lithium metal as the negative electrode and a Li^+ intercalation material as the positive electrode. It can be denoted as an $(RQ)([RW]C)$ circuit (where the rectangular parenthesis denote a series connection within the parallel sub-circuit). As before, the high-frequency arc corresponds to the impedance of the bulk and the grain boundaries of the solid electrolyte. The $([RW]C)$ sub-circuit is called the Randles circuit and describes the impedance spectrum of a lithium intercalation electrode in terms of a charge transfer resistance R_{ct}, a double layer capacitance C_{dl} and a Warburg diffusion element W_{d} [48,49]. In this case, the Warburg element describes the diffusion of lithium ions to and from the surface within the particles of the the intercalation material, and is thus connected in series with the charge transfer resistance. The $(RQ)([RW]C)$ circuit has a total impedance of

$$Z(\omega) = Z_{R_{\mathrm{se}}Q_{\mathrm{se}}} + Z_{[R_{\mathrm{ct}}W_{\mathrm{d}}]C_{\mathrm{dl}}} = \left(\frac{1}{Z_{R_{\mathrm{se}}}} + \frac{1}{Z_{Q_{\mathrm{se}}}}\right)^{-1} + \left(\frac{1}{Z_{R_{\mathrm{ct}}} + Z_{W_{\mathrm{d}}}} + \frac{1}{Z_{C_{\mathrm{dl}}}}\right)^{-1}. \quad (2.29)$$

The total impedance of each circuit can be obtained using the expressions for the impedance of the individual circuit elements shown in section 2.3.2. The equivalent circuit fits yield the values of the defining parameters for each circuit element, such as R for a resistor and C for a capacitor. The equivalent circuit model thus gives quantitative information about the physical parameters of those individual processes that can be separated in an impedance spectrum.

2.3.4 The Brick Layer Model

As discussed in section 2.3.1, it is possible to separate contributions from processes that change their polarity with different time constants, as these will appear in different frequency ranges in the impedance spectra. Some processes do, however, change their polarity with similar time constants, and may therefore not be possible to resolve separately in an impedance spectroscopy measurement. A general model for interpreting impedance spectra of polycrystalline materials,

termed the Brick Layer Model [50,51], addresses this issue. An excellent discussion of the model was given by Haile *et al.* [47] and a shorter summary of the model can be found in my MSc thesis [46].

The Brick Layer Model is described in Figure 2.11. The idea behind the model is that the conductivity paths can be divided into four regions; the bulk (grain interior), the grain boundaries parallel to the current flow, the grain boundaries perpendicular to the current flow and the electrodes. The model also assumes that the sample has a typical microstructure, i.e. that the volume of the bulk is far greater than the volume of the grain boundaries. Each of the regions is assumed to change its polarity with a certain time constant when an AC signal is applied. It is, however, not clear if the impedance contributions from the different regions can be separated in all cases. The answer to this mainly depends on the relative conductivities of the regions and on the characteristic frequencies of their response to the AC signal. The characteristic freqency $\omega_0 = 1/(RC)$ in an impedance spectrum is defined as the frequency at which the maximum of an arc in a Nyquist plot is located.

An equivalent circuit for the Brick Layer Model is shown in Figure 2.12a. It is, however, highly unlikely in practise that the impedance contributions from the grain interiors and the parallel grain boundaries can be resolved in an impedance spectrum. The equivalent circuit can therefore be simplified by merging the two parallel (RQ) sub-circuits of these contributions into one, as shown in Figure 2.12b.

The two (RQ) sub-circuits can be thought of as two competing conduction pathways within the material. In order to investigate how the two conduction pathways relate to the observed arcs in a Nyquist plot, the ratio of their corresponding conductivities $\sigma_{\mathrm{b+gb}\parallel}$ and $\sigma_{\mathrm{gb}\perp}$ can be investigated. The conductivity of a material is an extensive quantity and depends on its dimensions and its electrical resistance by

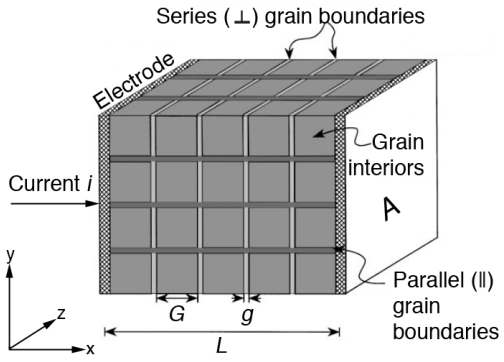

Figure 2.11: A schematic of the Brick Layer Model. It is assumed that the grains in the polycrystalline material are cube-shaped with grain boundaries between each cube. The boundaries are divided in two categories: Grain boundaries that lie parallel to direction of the expected main current flow between the electrodes (the x-direction) are termed 'parallel' grain boundaries, while the boundaries perpendicular to these are termed 'perpendicular' (or 'series') grain boundaries. The model assumes that the sample has a typical microstructure, i.e. that $g \ll G$. Figure reprinted from [47].

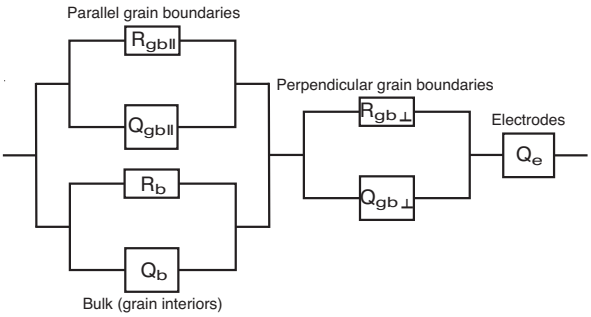

(a)

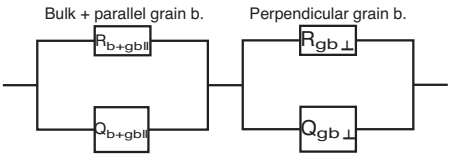

(b)

Figure 2.12: a) An equivalent circuit for the brick layer model presented in figure 2.11. The bulk conduction and the parallel grain boundary conduction are assumed to flow in parallel, while the perpendicular grain boundaries are assumed to be connected in series with those. The electrodes are assumed to have a double layer capacitance in series with the rest. **b)** A simplified equivalent circuit where the two parallel (RQ) circuits have been merged together and the capacitance of the electrodes has been taken to be negligible.

$$\sigma = \frac{L}{AR}, \tag{2.30}$$

where L is the thickness of the material and A its area. The effective conductivity of the circuit elements is found by directly summing elements that are connected in parallel and summing the inverse of those connected in series.

According to Figure 2.11, each building block of the Brick Layer Model consists of a bulk cube, a perpendicular grain boundary and two parallel grain boundaries. It is assumed that the parallel and perpendicular grain boundaries are composed of the same material and therefore both types of boundaries have the same conductivity, i.e. $\sigma_{\mathrm{gb}\parallel} = \sigma_{\mathrm{gb}\perp} = \sigma_{gb}$. Using geometric considerations in Figure 2.12b, the effective conductivity of the two conduction paths is found to be

$$\frac{1}{\sigma_{\mathrm{eff}}} = \frac{1}{\sigma_{\mathrm{b+gb}\parallel}} + \frac{1}{\sigma_{\mathrm{gb}\perp}} = \frac{1}{\sigma_{\mathrm{bulk}} + 2\frac{g}{G}\sigma_{\mathrm{gb}}} + \frac{1}{\frac{G}{g}\sigma_{\mathrm{gb}}}. \tag{2.31}$$

To better understand how much each of the two conduction pathways contributes to the impedance spectrum, the ratio of the two conductivity values σ_{bulk} and σ_{gb} can be investigated:

$$\frac{\sigma_{\mathrm{b+gb}\parallel}}{\sigma_{\mathrm{gb}\perp}} = \frac{R_{\mathrm{gb}\perp}}{R_{\mathrm{b+gb}\parallel}} = \frac{g}{G}\frac{\sigma_{\mathrm{bulk}}}{\sigma_{\mathrm{gb}}} + \frac{2g^2}{G^2} \tag{2.32}$$

For a Nyquist plot to display two distinguishable arcs (one for each (RQ) subcircuit in figure 2.12b), both of the following criteria must be met:

1. $R_{\mathrm{b+gb}\parallel}$ and $R_{\mathrm{gb}\perp}$ must have comparable magnitude, i.e. approximately $0.01 \leq R_{\mathrm{b+gb}\parallel}/R_{\mathrm{gb}\perp} \leq 100$. Otherwise the smaller arc might be overshadowed by the larger one.

2. The characteristic frequencies ω_0 of the two conduction mechanisms must differ significantly. Similar characteristic frequencies will lead to a superposition of the two arcs which may make them indistinguishable.

The two criteria can be considered for three different cases:

Case 1: $\sigma_{\mathrm{bulk}} > \sigma_{\mathrm{gb}}$

As already mentioned, the Brick Layer Model assumes that $g \ll G$. As a result, the first term will dominate Eq. 2.32 and the approximation can be made that the second term is negligible, i.e.

$$\frac{\sigma_{\mathrm{b+gb}\parallel}}{\sigma_{\mathrm{gb}\perp}} = \frac{R_{\mathrm{gb}\perp}}{R_{\mathrm{b+gb}\parallel}} \approx \frac{g}{G}\frac{\sigma_{\mathrm{bulk}}}{\sigma_{\mathrm{gb}}} \tag{2.33}$$

Because $g/G < 1$ and $\sigma_{\mathrm{bulk}}/ > \sigma_{\mathrm{gb}}$ in this case, it is reasonable to assume that the first criterion is met for many combinations of these parameters.

The characteristic frequency can be written as $\omega_0 = 1/(RC) = \sigma/(\varepsilon_r\varepsilon_0)$, where ε_r and ε_0 are the dielectric constants of the material and of vacuum, respectively. It can be assumed that the dielectric constants of the bulk material and of the grain boundaries are rather similar. Because $\sigma_{\mathrm{bulk}} > \sigma_{\mathrm{gb}}$, it is clear that $\omega_{0,\mathrm{bulk}} > \omega_{0,\mathrm{gb}}$ and criterion 2 also holds. In this case, two distinguishable arcs will thus be observed in the impedance spectrum. The arc at the higher frequency will correspond to the conduction pathway through the bulk material and the parallel grain boundaries, whereas the arc at the lower frequency will correspond to the conduction pathway through the perpendicular grain boundaries.

Case 2: $\sigma_{\mathrm{gb}} > \sigma_{\mathrm{bulk}}$

If $\sigma_{\mathrm{gb}}/\sigma_{\mathrm{bulk}} \geq G/(2g)$, the conduction path through the parallel grain boundaries is more feasible than through the bulk. Eq. 2.32 can therefore be approximated as

$$\frac{\sigma_{\mathrm{b+gb}\parallel}}{\sigma_{\mathrm{gb}\perp}} = \frac{R_{\mathrm{gb}\perp}}{R_{\mathrm{b+gb}\parallel}} \approx \frac{2g^2}{G^2}. \tag{2.34}$$

But since $g \ll G$ holds, it is clear that $R_{\mathrm{b+gb}\parallel} \ll R_{\mathrm{gb}\perp}$ and the two arcs will have very different magnitudes.

If $\sigma_{\mathrm{gb}}/\sigma_{\mathrm{bulk}} < G/(2g)$, the approximation in Eq. 2.34 does not hold, but the approximation in Eq. 2.33 becomes valid again. But because $g \ll G$ and $\sigma_{\mathrm{bulk}} < \sigma_{\mathrm{gb}}$, it becomes clear that $R_{\mathrm{b+gb}\parallel} \ll R_{\mathrm{gb}\perp}$ and the two arcs will again have very different magnitudes. The first criterion is therefore not met, and the smaller arc will most likely be overshadowed by the larger one.

Case 3: $\sigma_{\text{bulk}} \approx \sigma_{\text{gb}}$

In this case the ratio between σ_{bulk} and σ_{gb} approaches 1. Because $g \ll G$, the approximation can be made that the second term in 2.32 can be neglected, and the approximation in Eq. 2.33 holds. This means that $R_{\text{b+gb}\parallel} \ll R_{\text{gb}\perp}$, i.e. the arcs have very different magnitudes. The same argumenation as in Case 1 can again be employed to show that this time, $\omega_{0,\text{bulk}} \approx \omega_{0,\text{gb}}$ holds. Therefore the two arcs will not only have different magnitudes, but they will also fall in a very similar region of the impedance spectrum and will thus not be distinguishable from each other. Note that here the smaller arc, that will be overshadowed by the larger arc, corresponds to the perpendicular grain boundaries. The single arc observed in this case can therefore, in practise, be attributed to the combined response of the parallel grain boundaries and the grain interiors.

Summary

The relationship between the conduction pathways and the shape of the Nyquist plot according to the Brick Layer Model can be summarised as follows:

- In all cases we assume a polycrystalline material with a typical microstructure and expect the Nyquist plot to exhibit either one or two arcs.
- The *only* case where two arcs are observed is if $\sigma_{\text{bulk}} > \sigma_{\text{gb}}$. I.e. in the case of two arcs being observed, it can immediately be concluded that the bulk conductivity is larger than that of the grain boundaries.
- In *all other* cases, i.e. for $\sigma_{\text{bulk}} \approx \sigma_{\text{gb}}$ or $\sigma_{\text{bulk}} < \sigma_{\text{gb}}$, only a single arc will be displayed. It is a combination of both parallel grain boundary conduction and grain interior conduction. Without additional knowledge of the sample microstructure, the relative magnitudes and conductivity of the two mechanisms cannot be resolved using impedance spectroscopy only.

2.3.5 Relating Impedance to Conductivity

The impedance spectroscopy measurements in this work were all performed on symmetrical cells containing solid electrolytes, or on whole all-solid-state battery cells. Because of the criterion that solid electrolytes must have good ionic conductivity, the most important parameter of the equivalent circuit fits in this context is the resistance R of the samples.

The impedance spectra of the symmetrical cells were fitted using one or two (RQ) circuits in series (as shown in Figure 2.10a), depending on the shape of the Nyquist plot. Here the larger (RQ) arc was attributed to the combined bulk and parallel grain boundary impedance while the smaller arc (if present) was attributed to the impedance of the perpendicular grain boundaries. If the smaller arc was not present, its contribution was assumed to be drowned out by the larger arc.

The impedance spectra of the whole battery cells were fitted using an $(RQ)(RC)W$ circuit (as shown in Figure 2.10b). Here the (RQ) arc was attributed to the combined bulk and parallel grain boundary impedance, while the (RQ) arc was

attributed to the interface between the electrolyte and the cathode. The arc corresponding to the perpendicular grain boundaries was assumed to be overshadowed by the others in the whole battery cells.

The conductivity of the samples was found using Eq. 2.30. For the symmetrical cells the resistance of the electrolyte was assumed to be $R = R_1 + R_2$, i.e. the combined resistance of both (RQ) sub-circuits (if they could be resolved separately). For the whole battery cells, the electrolyte resistance was assumed to be $R = R_1$, i.e. the resistance of the (RQ) sub-circuit only.

For the symmetrical cells, the impedance spectroscopy measurements were carried out for a range of temperatures. The conductivity σ as a function of temperature T is expected to follow an Arrhenius behaviour, i.e.

$$\sigma(T) = Ae^{-E_a/(k_B T)} \qquad \Longleftrightarrow \qquad \ln(\sigma) = \ln(A) - \frac{E_a}{k_B T} \tag{2.35}$$

where E_a is the activation energy of the process, k_B is the Boltzmann constant and A is a pre-factor in the same units as σ. When plotted against $1/T$ in a semi-logarithmic plot, the Arrhenius equation forms a straight line. The slope of the line, which can be found by performing a linear least-squares fit of the Arrhenius plot, corresponds to the activation energy of the conduction process.

2.4 Quasi-Elastic Neutron Scattering

2.4.1 Neutron scattering

I used quasi-elastic neutron scattering (QENS) to study the mechanism for lithium ion conduction in the $LiBH_4$-LiI solid solution. The technique employs so-called 'cold neutrons', which makes it very well suited for detecting atomic motion, such as rotations and diffusion. The reason for this is that the energy of cold neutrons is on the same order of magnitude as the energy levels of atomic motion in crystals, and their wavelength is on the order of interatomic distances [52].

Neutrons are uncharged particles and thus have no Coulomb interaction with the nuclei of the sample. They can therefore easily penetrate deep into the sample. Free neutrons are not stable and have a mean lifetime of about 15 minutes. They can be produced by the fission of heavy nuclei, e.g. in a nuclear reactor. Because of this, QENS measurements are only available at large-scale research facilities. In this section, only a short discussion of the principles behind QENS is provided. An excellent overview of QENS can be found in [53], and a more comprehensive discussion of the method is given in [52].

A free neutron has a mass of $m_N = 1.675 \cdot 10^{-27}$ kg, an energy of $E = \frac{1}{2}m\vec{v}^2$ and a momentum of $\vec{p} = m\vec{v}$, where $\vec{v}$ is its velocity. Using the De Broglie relation, neutrons can also be regarded as plane waves with a wavelength of $\lambda = h/|\vec{p}|$ where h is Planck's constant. When free neutrons are produced, e.g. at a fission reactor, their energy can be lowered by equilibration at a low temperature, resulting in what is called cold neutrons. Their average thermal energy is given by Maxwell's law, $E = \frac{3}{2}k_B T$, where T is the equilibration

temperature and k_B is the Boltzmann constant. Neutrons are considered 'cold' if their average energy is in the range of 0.8 meV $< E <$ 5 meV.

The kinematics of the scattering process are shown in Figure 2.13. Consider an incident neutron with the energy

$$E_0 = \frac{p_0^2}{2m_N}. \tag{2.36}$$

When the neutron enters the sample it will either pass undisturbed through it, be absorbed by a nucleus in the sample, or be scattered by a nucleus in the sample. In the following, the last case is assumed, i.e. that a scattering event takes place. If the neutron has the energy E_1 and the momentum $\vec{p_1}$ after scattering off a nucleus, the energy transfer of the scattering event is

$$\Delta E = E_1 - E_0 \tag{2.37}$$

and the momentum transfer is

$$\Delta\vec{p} = \vec{p_1} - \vec{p_0} = \hbar\vec{Q}. \tag{2.38}$$

Here $\vec{Q}$ is defined as the scattering vector and $\hbar$ is the reduced Planck constant. Note that it is assumed that the total energy and momentum of the system are conserved during the scattering process. If $\Delta E = 0$, i.e. if the energy of the neutron does not change during the scattering event, the scattering is said to be elastic; otherwise it is said to be inelastic. In a QENS measurement, only near-elastic scattering is monitored, which is ensured by only allowing neutrons with specific energies to be detected by the instrument. A QENS measurement results in a histogram over a narrow energy window (on the order of μeV) centred around $\Delta E = 0$ and ranging from $-\Delta E$ to ΔE, which is called a QENS spectrum.

2.4.2 Quasi-Elastic, Incoherent Scattering

Here it has been assumed that the nuclei in the sample are not in motion prior to the scattering event. At finite temperatures this is, however, not true as processes such as thermal vibration, rotational motion and translational diffusion take place in the sample. Because of this, the observed ΔE in an elastic scattering measurement does not result in a Dirac delta peak at zero, but rather in

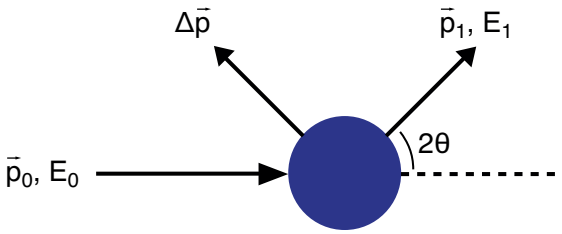

Figure 2.13: A schematic of the kinematics of neutron scattering. When an incident neutron with the energy E_0 and momentum $\vec{p_0}$ scatters off a nucleus, its changes its direction by 2θ and subsequently has the energy E_1 and momentum $\vec{p_1}$. It is assumed that the total energy and momentum of the system are conserved in the scattering process.

a finite probability distribution around zero. This phenomenon is called quasi-elastic scattering and forms the basis of QENS. With sufficient knowledge about the neutron energies and the scattering geometry, the shape of the probability distribution (the quasi-elastic signal) can be used to gain knowledge about the rates of the atomic motions in the sample.

In a QENS experiment, the measured quantity is the double differential cross-section

$$\frac{\partial^2\sigma}{\partial\Omega\partial E_1} = \left(\frac{\partial^2\sigma}{\partial\Omega\partial E_1}\right)_{\text{coh}} + \left(\frac{\partial^2\sigma}{\partial\Omega\partial E_1}\right)_{\text{inc}}, \tag{2.39}$$

which gives the probability that incident neutrons with energy E_0 are scattered into a solid angle element $\mathrm{d}\Omega$ around the direction Ω and subsequently possess an energy in the range of E_1 and $E_1 + \mathrm{d}E_1$. The scattering cross section can be separated in two parts, called coherent scattering and incoherent scattering. Neutrons that are scattered coherently off nuclei of different kinds in the sample interfere with each other and have a scattering potential that is randomly distributed around an average. Coherent scattering does therefore not lead to interference effects, and is only observed as a background signal in a QENS measurement [52]. Incoherent scattering of neutrons do, on the other hand, have a uniform scattering potential that gives rise to interference effects and thus a scattering signal with a certain probability distribution (and not a random distribution). Because of this, it is the incoherent scattering that is of importance here, as it gives information about the atomic motion in a QENS measurement.

Neutron scattering off a nucleus depends heavily on the type of nucleus in question. This is quantified in terms of the scattering cross-section σ, which varies greatly between different elements and isotopes. The scattering cross-section can be separated into coherent and incoherent cross-sections, such that $\sigma = \sigma_{\text{coh}} + \sigma_{\text{inc}}$. The values of σ are empyrical and the values for the isotopes used in QENS measurements in this work can be found in Table 3.3. The results of QENS measurements are usually modelled in terms of the scattering function $S(\vec{Q},\omega)$, which is related to the experimentally observed double differential cross-section and the isotope-dependent scattering cross-sections by

$$\left(\frac{\partial^2\sigma}{\partial\Omega\partial E_1}\right)_{\text{inc}} = \frac{\sigma_{\text{inc}}}{4\pi\hbar}\frac{\vec{p_1}}{\vec{p_0}} N S_{\text{inc}}(\vec{Q},\omega) \tag{2.40}$$

where σ_{inc} is the average incoherent scattering cross-section of the nuclei in the sample and N is the number of nuclei.

2.4.3 The Scattering Function

The scattering function $S(\vec{Q},\omega)$ describes the scattering in the frequency space, but by Fourier transforming it into the time space the so-called intermediate scattering function $I(\vec{Q},t)$ is obtained:

$$I_{\text{inc}}(\vec{Q},t) = \int S_{\text{inc}}(\vec{Q},t)e^{i\omega t}\mathrm{d}t \tag{2.41}$$

The incoherent intermediate scattering function can be separated into a time-independent and a time-dependent part

$$I_{\text{inc}}(\vec{Q},t) = I_{\text{inc}}(\vec{Q},\infty) + I_{\text{inc}}^{\text{td}}(\vec{Q},t). \tag{2.42}$$

By Fourier transforming this expression back into frequency space, this can be expressed in terms of the scattering function

$$S_{\text{inc}}(\vec{Q},\omega) = I_{\text{inc}}(\vec{Q},\infty)\delta(\omega) + S_{\text{inc}}^{\text{inel}}(\vec{Q},\omega), \tag{2.43}$$

where $\delta(\omega)$ is the Dirac delta function. Here the first term in the sum denotes the purely elastic scattering component, which yields a zero-width peak at $\Delta E = 0$ in the QENS spectrum. The second term is the quasi-elastic component, which contains information about the atomic motion in the sample. This term results in a probability distribution around $\Delta E = 0$ that is usually modelled with a Lorentz distribution

$$L(\Gamma,\omega) = \frac{\Gamma}{\pi(\omega^2+\Gamma^2)}, \tag{2.44}$$

where Γ denotes the half-width at half-maximum (HWHM) of the distribution.

The atomic motion can be split into three different kinds: Reorientational motion, intramolecular vibrations and lattice vibrations. The first kind describes e.g. rotations and diffusion of atoms in the sample and thus contains the information of interest in a QENS measurement. The last two kinds arise due to thermal vibrations, i.e. due to the kinetic energy of the atoms at finite temperatures. The thermal vibrations are typically much faster than the reorientational motion, and will therefore not be observable on the time scale that the instrument can measure. When modeling the QENS spectra, it is therefore reasonable to include the contribution of the thermal vibrations as a background function $B(\vec{Q})$. Furthermore, the measurement instrument has a finite resolution, which is accounted for by convoluting the scattering function with an instrumental resolution function $R(\vec{Q},\omega)$. This function is found by performing a QENS measurement at $T \to 0$ K, as the sample will show negligible atomic motion at close to the absolute zero. After these considerations, the scattering function used for modelling the impedance spectra becomes

$$S_{\text{inc}}^{\text{tot}}(\vec{Q},\omega) = R(\vec{Q},\omega) \otimes (A_0(\vec{Q})\delta(\omega) + A(\vec{Q})L(\Gamma,\omega)) + B(\vec{Q}). \tag{2.45}$$

The factors $A(\vec{Q})$ and $A_0(\vec{Q})$ are the integrated intensities that correspond to the inelastic and elastic contribution to the spectra, respectively. The fraction of the total quasielastic intensity that corresponds to the purely elastic peak can be quantified using the elastic incoherent structure factor (EISF), which is defined as

$$A_{\text{EISF}}(\vec{Q}) = \frac{A_0(\vec{Q})}{A(\vec{Q}) + A_0(\vec{Q})}. \tag{2.46}$$

The EISF describes the ratio between the elastic and the inelastic signal observed in a QENS measurement.

2.4.4 Rotational motion

There are mainly two types of reorientational atomic motion that are of interest for this work. The $LiBH_4$-LiI solid solutions exhibit rotation of the BH_4 tetrahedra. Such motion is well known in borohydrides and has been observed for the $LiBH_4$-LiI solid solution (as discussed in Paper B). [54, 55]. A long-range diffusion of lithium ions is also expected when an electric signal is applied to the solid solution, due to its good Li^+ conduction properties.

To describe the rotation motion of the BH_4 tetrahedra, a three-site jump model was used. The model describes rotations in 120° steps around an axis perpendicular to one face of the tetrahedron. This axis is called a C3 axis and is pictured in Figure 2.14. Note that one hydrogen atom remains immobile during the rotation (neglecting thermal vibration motions). The basis for the model, which arises from the probabilities of atoms jumping from one site to another, will not be discussed here, but a detailed description can be found in chapter 6 in [52].

The scattering function for the model of the C3 rotation motion can be modelled as

$$S_{C3}(\vec{Q},\omega) = A_{C3}(\vec{Q})\delta(\omega) + (1 - A_{C3}(\vec{Q}))L(\Gamma,\omega) \tag{2.47}$$

i.e. as a Dirac delta peak corresponding to the elastic signal and a Lorentzian distribution corresponding to the quasi-elastic signal. Here $A_{C3}(\vec{Q})$ is the elastic incoherent structure factor (EISF) for the C3 rotation

$$A_{C3}(\vec{Q}) = \frac{1}{4} + \frac{3}{4}A_3(\vec{Q}). \tag{2.48}$$

The two terms in this expression indicate that only three out of every four hydrogen atoms are moving. The EISF for the three hydrogen atoms that are in motion is based on the probabilities for jumps among three equivalent, equidistant sites on a circle (i.e. 120° jumps). It can be written as

$$A_3(\vec{Q}) = \frac{1}{3}(1 + 2j_0(\vec{Q}r_3\sqrt{3})) \tag{2.49}$$

where $j_0(x) = \sin x/x$ is the spherical Bessel function of zeroth order. The parameter r_3 is the radius of the rotation and $r_3\sqrt{3}$ is thus the jump distance

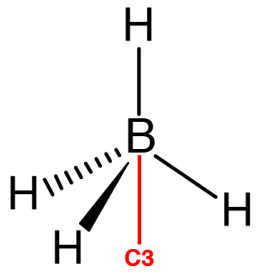

Figure 2.14: An illustration of the rotation of a BH_4 tetrahedron around a C3 axis. The rotation axis runs through the H atom at the top of the tetrahedron, which remains immobile during the rotation. The remaining three H atoms rotate in steps of 120°.

in the 120° rotations. In the C3 model, the HWHM (denoted by Γ) of the Lorentzian $L(\Gamma, \omega)$ is related to the jump rate τ_{C3}^{-1} of the motion by

$$\Gamma_{C3} = \frac{3}{2}\tau_{C3}^{-1}. \tag{2.50}$$

Note that the HWHM for the C3 model does not depend on the scattering vector $\vec{Q}$, and does therefore not change with scattering angle.

To see if the model fits the measured data from a QENS experiment, the experimental EISF $A_{\mathrm{EISF}}(\vec{Q})$ can be compared to the theoretical EISF $A_{C3}(\vec{Q})$. Furthermore, the jump length $r_3\sqrt{3}$ and the jump rate τ_{C3}^{-1} can be directly compared to calculated values from density functional theory (DFT) atomic-scale calculations. In this way, QENS and DFT can be applied as complimentary methods of modelling motion on the atomic level.

2.4.5 Diffusion

The conduction of lithium ions in the solid solution is expected to be observed in QENS as a long-range diffusion. This can be modelled by the Chudley-Elliott model, which describes jump-diffusion between nearest-neighbor sites on a Bravais lattice [56]. The model assumes that the time it takes an atom to perform a jump is negligible compared to the average residence time of an atom at a given site. The basis for the scattering function corresponding to this model, which arises from the probability of locating an atom at a certain point in space at a given time, will not be covered here, but is discussed in chapter 5 in [52].

The intermediate incoherent scattering function for such a jump-diffusion motion is

$$I_{\mathrm{inc}}(\vec{Q}, t) = I_{\mathrm{inc}}(\vec{Q}, 0)\exp(-\Gamma t) \tag{2.51}$$

where $I_{\mathrm{inc}}(\vec{Q}, 0)$ is the time-independent part of the function. The Fourier transform of $I_{\mathrm{inc}}(\vec{Q}, t)$ into freqency space gives the scattering function

$$S_{\mathrm{inc}}(\vec{Q}, t) = \frac{1}{\pi}\frac{\Gamma(\vec{Q})}{(\Gamma(\vec{Q}))^2 + \omega^2}, \tag{2.52}$$

which is a Lorentz distribution with a HWHM of Γ, as seen by comparison with Equation 2.44. In the Chudley-Elliott model, the relationship of the HWHM of the Lorentzian to the scattering angle $\vec{Q}$, the diffusion jump rate τ_D^{-1} and the effective jump length L is given by

$$\Gamma_{\mathrm{D}}(\vec{Q}) = \hbar\tau_D^{-1}(1 - j_0(\vec{Q}L)). \tag{2.53}$$

Here $j_0(x) = \sin x/x$ is again the spherical Bessel function of zeroth order. In the jump-diffusion model, the HWHM is a function of the scattering vector $\vec{Q}$, i.e. it changes with the scattering angle. A fit of the HWHM as a function of $\vec{Q}$ gives the values of the diffusion jump rate τ_D^{-1} and the effective jump length L.

Furthermore, A Taylor expansion of $\Gamma_D(\vec{Q})$ for low values of $\vec{Q}$ up to the third order gives

$$\Gamma_D(\vec{Q}) = \frac{l^2}{2n\tau}Q^2, \tag{2.54}$$

where n is the dimensionality of the motion (for one-, two- or three-dimensional motion). From this expression it can be seen that HWHM varies as DQ^2, where

$$D = \frac{l^2}{2n\tau} \tag{2.55}$$

is the diffusion constant of the jump motion. The values for the jump rate τ_D^{-1}, the effective jump length L and the diffusion coefficient D obtained from the Chudley-Elliott model can be directly compared to the results of DFT calculations. QENS and DFT have been used as complimentary methods for describing long-range diffusion in $LiBH_4$-LiI solid solution in Paper B, as well as in the PhD thesis of Jón Steinar Garðarsson Mýrdal [57].

Chapter 3

Experimental Procedures

This chapter describes the practical aspects of the measurement equipment and the experimental methods used in this work. First, I discuss the synthesis and preparation methods of the solid electrolyte materials. The next sections cover the experimental procedures of the powder x-ray diffraction measurements, the conductivity measurements and the battery cell measurements. I conclude the chapter by a short description of the quasi-elastic neutron scattering samples and of the experimental setup for those measurements.

3.1 Synthesis and Preparation of Samples

3.1.1 Planetary Ball Milling

I performed all synthesis and preparation of the solid electrolyte materials using the planetary ball milling method. A Fritsch Pulverisette P6 ball mill was used to rotate a stainless steel vial with an inner volume of 250 ml at 650 rpm for two hours for all samples. A total of 2 g of precursor powder was inserted into the vial for each milling together with 25 tungsten carbide balls, resulting in a sample-to-ball mass ratio of 1/100. During my research stay at Tohoku University in Sendai, Japan, I used a Fritsch Pulverisette P7 ball mill to rotate a stainless steel vial with an inner volume of 45 ml containing 0.5 g of precursor powder. There, the sample-to-ball mass ratio was 1/180. The milling vials were always filled and sealed inside a glove box under argon atmosphere. The solid electrolyte powders and their precursors are all sensitive to oxygen and moisture, and therefore all sample handling during this work was carried out in argon atmosphere.

During planetary ball milling, the tungsten carbide balls constantly bombard the particles of the sample, as shown in Figure 3.1. In this process, the crystallites are broken into smaller pieces, increasing the reaction surface of the powder. The rather violent milling process mechanically provides an activation energy that can allow chemical reactions to take place at those surfaces. The milling process can also affect the microstructure of the grains by inducing crystal defects such as vacancies and dislocations. In this way, the milling process can change the physical and chemical properties of the powder even without any

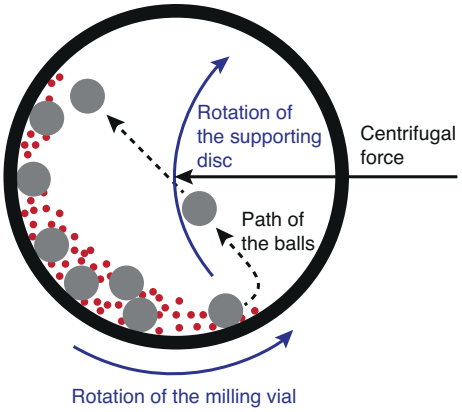

Figure 3.1: The kinetics of planetary ball milling. The milling vial is rotated around itself, and the supporting disk, on which the vial is sitting, also rotates, exerting a centrifugal force on the vial and its contents. As a result, the tungsten carbide balls (shown as gray circles in the figure) follow approximately the path shown with the dashed lines before hitting the walls of the vial and bombarding the powder (shown as red dots in the figure).

chemical reactions taking place, as discussed in section 4.1.3 and Paper A.

3.1.2 Sample Preparation

The $LiBH_4$ - LiI Solid Solution

Solid solutions of lithium borohydride ($LiBH_4$) and lithium iodide (LiI) were synthesised by planetary ball milling as described in section 3.1.1. $LiBH_4$ powder of >95% purity and LiI beads of >99% purity were used, both from Alfa Aesar Co. The solid solutions were syntesised in the mixing ratios shown in Table 3.1. The pure $LiBH_4$ powder was also ball milled, to allow direct comparison with the properties of the ball milled solid solutions. Powder x-ray diffraction measurements and impedance spectroscopy measurements were performed on the as-milled powder. To investigate the effect of heat treatment on the microstructure and the lithium ion conductivity of the powder, a fraction of the powder from each milling was annealed under Ar atmosphere at 140 °C for 70 hours.

The $LiBH_4$ - $Ca(BH_4)_2$ Composite

$LiBH_4$-$Ca(BH_4)_2$ composites were prepared by planetary ball milling as described in section 3.1.1. $LiBH_4$ powder of >95% purity from Alfa Aesar Co. and $Ca(BH_4)_2$ powder (of unknown purity) from Sigma Aldrich Co. were used. The composites were mixed in the ratios shown in Table 3.2. Pure $LiBH_4$ and pure $Ca(BH_4)_2$ were also milled for comparison with the composite powder. Powder x-ray diffraction measurements were performed after each milling to determine the phase composition of the powder, and impedance spectroscopy measurements were performed to investigate the ionic conduction of the composites.

Table 3.1: The mixing ratios of the ball milled $LiBH_4$-LiI samples. Pure $LiBH_4$ was also ball milled for comparison. The molar ratios x are shown as percentages and as fractions, as both terminologies are used in this work. The mixing ratios were, in some cases, chosen in accordance with those used for density functional theory (DFT) calculations, as the limited number of unit cells that are practical in a calculation poses limits to the mixing ratios that are accessible using DFT. Such calculations are presented in [57]

.

x (%)	x (*fraction*)	$(1-x)LiBH_4 + xLiI$
0	0	$LiBH_4$
6.25	1/16	$15/16LiBH_4 + 1/16LiI$
12.5	1/8	$7/8LiBH_4 + 1/8LiI$
18.75	3/16	$13/16LiBH_4 + 3/16LiI$
25	1/4	$3/4LiBH_4 + 1/4LiI$
31.25	5/16	$11/16LiBH_4 + 5/16LiI$
40.625	3/32	$19/32LiBH_4 + 13/32LiI$
50	1/2	$1/2LiBH_4 + 1/2LiI$

Table 3.2: The mixing ratios of the ball milled $LiBH_4$-$Ca(BH_4)_2$ samples. Composites covering a wide range of $Ca(BH_4)_2$ content were prepared. The precursor powders were also ball milled in their pure form for comparison.

x (%)	x (*fraction*)	$(1-x)LiBH_4 + xCa(BH_4)_2$
0	0	$LiBH_4$
12.5	1/8	$7/8LiBH_4 + 1/8Ca(BH_4)_2$
18.75	3/16	$13/16LiBH_4 + 3/16Ca(BH_4)_2$
25	1/4	$3/4LiBH_4 + 1/4Ca(BH_4)_2$
33.33	1/3	$2/3LiBH_4 + 1/3Ca(BH_4)_2$
50	1/2	$1/2LiBH_4 + 1/2Ca(BH_4)_2$
66.67	2/3	$1/3LiBH_4 + 2/2Ca(BH_4)_2$
75	3/4	$1/4LiBH_4 + 3/4Ca(BH_4)_2$
100	1	$Ca(BH_4)_2$

3.2 Powder X-ray Diffraction

3.2.1 Laboratory Measurements

All ball milled samples, as well as the precursor materials, were characterised using powder x-ray diffraction. I performed these measurements using a Cu Kα Bruker D8 laboratory diffractometer with a LynxEye detector, operating at 40 kV and 40 mA. The instrument has a Bragg-Brentano geometry as shown in Figure 3.2. All measurements were performed at room temperature. The samples were prepared under argon atmosphere and sealed inside an airtight polyethylene sample holder from Bruker Co. The instrument was typically set to an exposure time of 3 seconds per step (sometimes more) and a step size of 0.02°. All measurements were performed using a variable slit size. After each

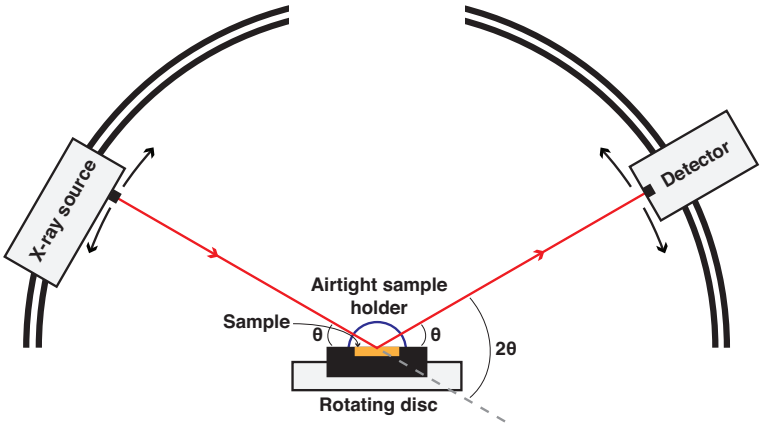

Figure 3.2: The Bragg-Brentano geometry of the Bruker D8 diffractometer. Both the Cu Kα x-ray source and the detector move on a circular path, but their movement is coupled so that both are always positioned at the same angle θ with respect to the sample surface. In this way, only photons that are specularly reflected (i.e. have the same incoming and outgoing reflection angle) are registered by the detector. With this setup, the x-ray diffraction of the sample can be measured over a wide range of diffraction angles in Bragg's law (Eq. 2.7). The sample holder is situated on a rotating disc in order to minimise scattering from preferred orientations in the sample. The airtight sample holder has a dome-shaped polyethylene cap (blue in the figure) which results in a considerable background signal in many of the diffraction patterns.

measurement, the data intensity was corrected for the variable slit size and the Kα_2 signal was subtracted.

The ball milled samples have rather small crystallite sizes, on the order of a few hundred nanometers. This leads to a broadening of the diffraction peaks, as seen in the Scherrer equation (Eq. 2.9). Furthermore, Li, B and H are poor x-ray scatterers, as discussed in section 2.2.2, and therefore the intensity of the diffraction peaks is rather low for most of the samples in this work. This limits the quality of the data, and in many cases it was not possible to successfully perform a full Rietveld refinement of the diffraction patterns that were measured using the laboratory diffractometer.

I performed Rietveld refinements of the data using the GSAS software [44]. When a full refinement was not possible, e.g. for the $LiBH_4$-LiI solid solutions (see chapter 4 and Paper A), I used the GSAS software to find the diffraction peak positions with the Le Bail method [58]. This method is a 'structureless refinement', which models the positions of the peaks using their integrated intensities, without any modelling of the peak shapes. In some cases, when the full refinement was not possible, I found the full width at half-maximum (FWHM) of selected diffraction peaks using the peak fitting software FITYK [59]. The contributions to the FWHM from the crystallite size and from crystallographic defects (strain) were separated using the combined expression for the size and strain broadening in Equation 2.11.

3.2.2 Synchrotron Measurements

Synchrotron x-ray sources deliver x-rays with an intensity that is many orders of magnitude greater than that of a laboratory diffractometer. Synchrotron measurements can therefore be valuable to obtain diffraction patterns of a higher quality, i.e. with more intensity and better counting statistics than laboratory equipment can offer. During this work, I participated in synchrotron x-ray diffraction measurements at the ID11 beamline at the ESRF in Grenoble, France; at the P07 beamline at the Petra III synchrotron at DESY in Hamburg, Germany and at the I711 beamline at the MAX II synchrotron in MAX-lab in Lund, Sweden. Although the main focus of these measurement periods was on other materials (not directly related to this work), I had the chance to measure diffraction patterns of the $LiBH_4$-LiI solid solution in a few mixing ratios and of all-solid-state battery cells containing the solid solution at these facilities. An example of a two-dimensional diffraction pattern from such a measurement in shown in figure 2.8. These measurements were, however, not performed in a systematic manner for many different mixing ratios of annealed and non-annealed solid solutions. As it is difficult to compare microstructural XRD information obtained using different instruments, the synchrotron measurements are not included in chapter 4 nor Paper A.

X-ray diffraction patterns from synchrotrons are, on the other hand, included in chapter 5 and Paper C. These measurements were performed at the beamline BM01A of the Swiss-Norwegian Beamlines (SNBL) at ESRF in Grenoble, France by Marit Dalseth Riktor, and at the I11 beamline at the Diamond Light Source in Oxfordshire, England by my co-supervisor Poul Norby. I handled the sample preparation and the analysis of the resulting data. The samples were mounted in glass capillaries that were sealed under argon atmosphere using an epoxy adhesive. The diffraction patterns of $(1-x)LiBH_4+xCa(BH_4)_2$ with $x = \{0.125, 1.0\}$ were measured at ESRF. A Pilates 2M detector was used, and the radiation had a wavelength of 0.69386 Å. The data were calibrated using a NIST LaB_6 standard sample and data processing was carried out using the SNBL tool box [60]. The diffraction patterns of $(1-x)LiBH_4+xCa(BH_4)_2$ with $x = \{0.25, 0.5\}$ were measured at the Diamond Light Source, a Mythen II PSD detector was used at 2θ angles ranging from 1° to 91° and a wavelength of 0.82712 Å. The data were calibrated using Si as an external standard. All synchrotron measurements were performed at room temperature. The two-dimensional diffraction patterns were integrated using the Fit2D software [61] and Rietveld refined using the GSAS software.

3.3 Conductivity Measurements

The electrical conductivity of the solid electrolyte samples was measured using impedance spectroscopy. I implemented and tested the experimental setup used for the measurements as part of my MSc project, and a more detailed description of it can be found there [46]. Photos and schematics of the setup are shown in Figure 3.3. The setup was further improved at the beginning of this work by positioning the measurement rig inside a glove box, thereby ensuring that as little oxygen and moisture as possible would reach the samples. All sample

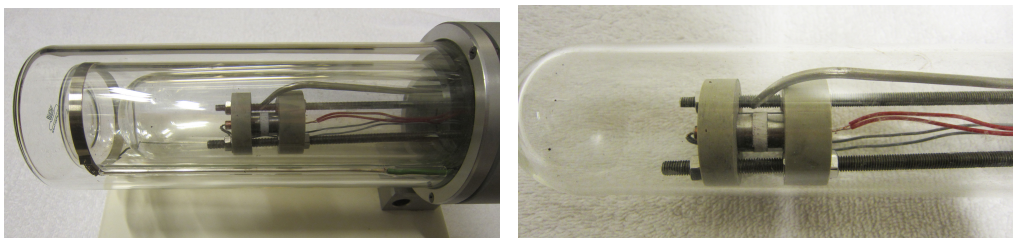

(a) (b)

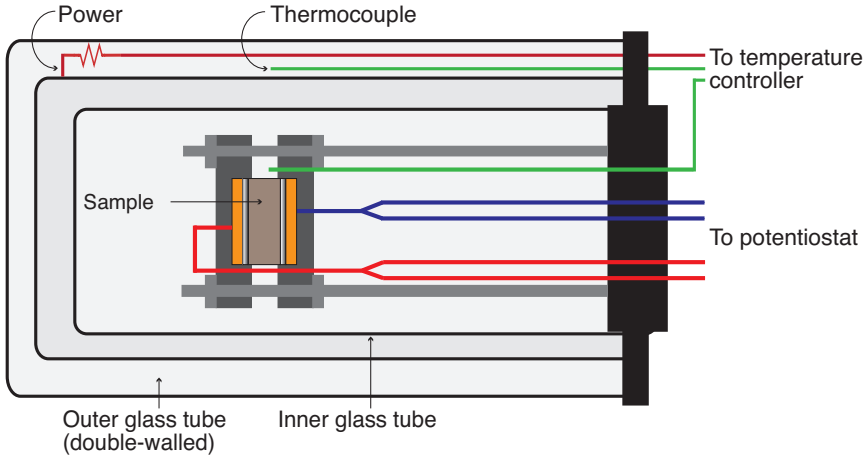

(c)

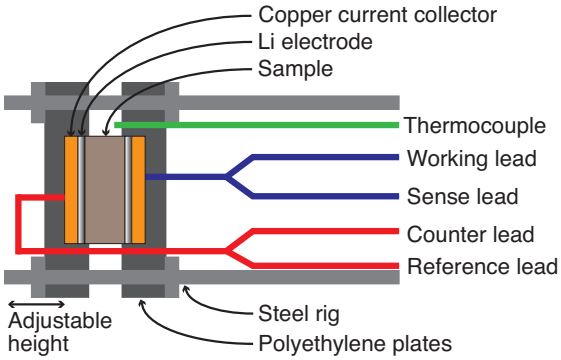

(d)

Figure 3.3: The impedance spectroscopy experimental setup, which is situated inside an argon-filled glove box. **a)** A photo of glass furnace, containing the sample rig. **b)** A close-up of the sample rig. **c)** The sample rig is enclosed within two cylindrical glass tubes. The outer tube is double-walled, and is a furnace with a heating element (red in the figure) and a thermocouple (green). The inner tube contains the sample rig as well as a second thermocouple (green) that measures the temperature at the sample. The heater and the two thermocouples are connected to a Eurotherm temperature controller **d)** A close-up of a cross-section of the sample rig. The rig is made of steel rods (light gray) and polyetheretherketone (PEEK) plates (dark gray), which hold the sample (brown) in place. The height of the plates can be adjusted to ensure that the sample sits tightly in the rig regardless of its thickness. The sample is situated between two copper discs (orange), which serve as current collectors and are connected to the potentiostat via electric wires (red and blue).

preparation and measurements thus took place under argon atmosphere. As shown in Figure 3.3a, the sample rig is positioned inside glass vials. These vials serve as a furnace, and have a heating element that is connected to a Eurotherm temperature controller. During the measurements, the samples were heated from 30°C and to 100°C or 140°C (depending on the sample type) in steps of either 5°C or 10°C, and subsequently cooled back down to 30°C using the same step size. The samples were equilibrated at a constant temperature for at least 40 minutes prior to each measurement.

For the impedance spectroscopy measurements, the powder samples were pressed in a stainless steel die into cylindrically shaped pellets with a diameter of 13 mm and a thickness of 1.5 - 3.0 mm. Lithium foil of 0.38 mm in thickness (from Sigma Aldrich Co.) was placed onto both faces of the pellets as electrodes. The powder and the lithium were pressed simultaneously at 1 ton/cm^2. By comparing the density of the pressed pellets to the theoretical density of the material, the porosity of the pellets was estimated to be 0.4 - 0.5. For the measurements, a Princeton PARSTAT 2273 potentiostat was used to apply a constant voltage of 1 V and measure the resulting current. The frequency range of the AC signal was typically set to 100 mHz to 1 MHz. Impedance spectroscopy measurements were also performed during my research stay at Tohoku University in Sendai, Japan. There, all parameters were the same except that a Hioki 3532-80 potentiostat was used, and the pellets were 8 mm in diameter and 0.9 mm in thickness.

3.4 Battery Cells

3.4.1 The Battery Components and Cell Assembly

I tested the $(1-x)$LiBH$_4$+xLiI solid solutions in all-solid-state working battery cells. Lithium titanate ($Li_4Ti_5O_{12}$, also denoted LTO), a lithium ion intercalation material with a capacity of 175 mAh/g, was used as the positive electrode in the battery cells. Lithium metal was used as the negative electrode. The open circuit voltage of LTO against lithium is approximately $U_{\mathrm{OCV}} = 1.56$ V. The all-solid-state battery measurements were all carried out at 60°C. The solid electrolytes were synthesised by planetary ball milling as described in section 3.1.1. Solid solutions with $x = 3/16$ were used in the battery cells, as the impedance spectroscopy measurements show that at 60°C, this mixture has the best lithium ion conduction properties out of the mixing ratios tried in this work (see section 4.4 and Paper A).

The positive electrodes were prepared by Ane Sælland Christiansen, a fellow PhD student at DTU Energy Conversion. They were made by coating a mixture of 80 wt% $Li_4Ti_5O_{12}$ from Sigma Aldrich Co., 10 wt% Super C65 from Timcal and 10 wt% polyvinylidene fluoride in N-Methyl-2-pyrrolidone (NMP) on aluminium foil. The electrodes were dried at 80°C in air, followed by compression in a roll press. They were subsequently punched into discs of 10 mm in diameter. Afterwards the cathodes were transferred to an argon filled glove box and dried overnight in a vacuum oven at 80°C. The electrodes had a layer thickness of 3 μm and an active particle load of 0.5 mg/cm^2. The mass of LTO in each of the positive electrodes was estimated to be 0.37 mg. The negative electrodes were

made of lithium foil of 0.38 mm in thickness from Sigma Aldrich Co. that was punched into discs of 8 mm in diameter. The mass of each negative electrode was approximately 10 mg.

The all-solid-state cells were assembled inside a cylindrical polyetheretherketone (PEEK) die, described in figure 3.4. The battery cells were assembled by pressing them between two steel pistons, which also serve as current collectors. Note that the PEEK die is electrically insulating, and pieces of hard rubber were used as padding between the steel pistons and the press on both sides to prevent short-circuiting the cell while pressing. The cell assembly and pressing was performed in an argon-filled glove box, but after pressing the cells were sealed tightly enough in the die to allow for measurements under atmospheric conditions. The porosity of the solid electrolyte was estimated to be similar to that of the pellets described in section 3.3, or around 0.5, and the thickness of the electrolyte was approximately 1.2 mm. These cells will be referred to as LTO | $LiBH_4$-LiI | Li cells.

Cells containing a steel electrode instead of the positive electrodes were assembled for electrochemical testing of the electrolyte. In these cells, one lithium metal electrode, 50 mg of $(1-x)LiBH_4$-xLiI powder and a stainless steel disc of 10 mm in diameter were pressed in the same manner as described above. These cells were used for investigating lithium transfer through the electrolyte, and for estimating the electrochemical stability of the electrolyte. These cells will be referred to as Steel | $LiBH_4$-LiI | Li cells.

Cells containing a liquid electrolyte were assembled by Ane Sælland Christiansen for comparison with the all-solid-state cells. In these cells, the positive and negative electrodes were the same as in the cells described above. However, instead of the LiBH4-LiI solid solution, a porous glass fibre membrane filled with 1 M $LiPF_6$ in EC:DMC (1:1, vol., Merck & Co) was used as the electrolyte.

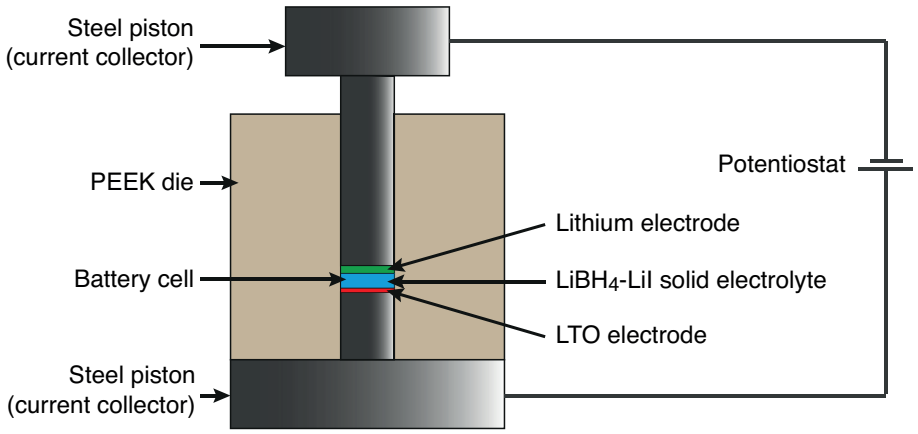

Figure 3.4: A cross-sectional view of the die used for the battery measurements. The PEEK die contains a cylindrical hole with a diameter of 10 mm. The battery cell is assembled by stacking the three components of the battery (the LTO electrode, the solid electrolyte and the lithium electrode) on top of a steel piston inside the hole and subsequently inserting a second steel piston on top of the cell. The two steel pistons are then pressed together at around 1 ton/cm^2. The steel pistons also serve as current collectors and are connected to the potentiostat.

These cells were assembled under Ar atmosphere, and strips of copper and aluminium foil were placed on opposite sides of the cell as current collectors. The cells were sealed in polymer-coated aluminium laminate cells (pouch bag cells), using a vacuum sealer. These cells will be referred to as LTO | $LiPF_6$ | Li cells.

3.4.2 Battery Measurements

Charge and discharge measurements on the LTO | $LiBH_4$-LiI | Li cells and the LTO | $LiPF_6$ | Li cells were performed using a Biologic VMP3 multichannel potentiostat. The charge and discharge measurements of the LTO | $LiBH_4$-LiI | Li cells were performed at a temperature of 60 °C, but the measurements of the LTO | $LiPF_6$ | Li were carried out at room temperature. The all-solid-state cells were under a mechanical load of 1.2 MPa during the measurements. The cells were charged and discharged with a constant current I (galvanostatic). An array of current values was tried, with $I \in \{2\mu A, 5\mu A, 10\mu A, 15\mu A, 20\mu A\}$. The cells were charged and discharged until reaching a voltage limit, which was set at 2.6 V or 3.0 V for charge and 1.0 V for discharge. The cells are assembled in the charged state, and upon discharge the following reaction occurs from left to right at the LTO electrode:

$$Li_4Ti_5O_{12} + 3Li^+ + 3e^- \longleftrightarrow Li_7Ti_5O_{12} \tag{3.1}$$

Upon charge, this reaction takes place from right to left.

Impedance spectroscopy measurements were performed after each charge and discharge of the LTO | $LiBH_4$-LiI | Li cells using the Biologic VMP3 potentiostat. The frequency range of the impedance measurements was set from 1 Hz to 300 kHz. In order to decrease noise in the resulting data, each data point is an average value of five consecutive measurements. The temperature during the impedance spectroscopy measurements was the same as during the charge-discharge measurements, i.e. 60°C. The resistance R of lithium ion conduction in the solid electrolyte can be estimated from the results of the impedance spectroscopy measurements using Eq. 2.30.

Cyclic voltammetry measurements were performed on a Steel | $LiBH_4$-LiI | Li cell in order to evaluate the electrochemical stability of the solid solution. These measurements were carried out by Rasmus Viskinde, a MSc student at DTU Energy Conversion [62]. The measurements were done using a Princeton PARSTAT 2773 potentiostat. A scan rate of 1 mV/s was used. The voltage was cycled three times from 0 V to 2V, then three times from 0 V to 3 V, another three times from 0 V to 4 V and a final three times from 0 V to 5 V.

A galvanostatic electric signal was applied to a Steel | $LiBH_4$-LiI | Li cell. The aim was to estimate the amount of lithium ions that could be deposited on the surface of the steel electrode (lithium plating), in order to get an idea of which process limits the discharge capacity of the all-solid-state batteries. A Princeton PARSTAT 2773 potentiostat was used for running a constant current of -10 μA through the cell.

3.5 Quasi-Elastic Neutron Scattering

3.5.1 Samples and Isotopes

During this work, I performed QENS measurements using the instruments IN10 and IN16 at the Institut Laue-Langevin in Grenoble, France; the instrument SPHERES at the Forschungs-Neutronenquelle Heinz Maier-Leibnitz (FRM II) in Garching-bei-München, Germany and the instrument HFBS at the NIST Center for Neutron Research in Gaithersburg, Maryland, USA. These research facilities all operate their own nuclear reactor for the production of neutrons. The measurements were performed in a collaboration with Didier Blanchard, a senior researcher at DTU Energy Conversion.

As already mentioned, the QENS measurements were performed on the $LiBH_4$-LiI solid solution in order to study the mechanism for lithium ion conduction. Due to the great variation in neutron scattering cross-sections and absorption coefficients with different elements and isotopes, it is important to select the correct isotopes of Li, B, H and I for the purpose of the measurement. The cross-section and absorption coefficient for each isotope are shown in Table 3.3. As discussed in Section 2.4.2, only incoherent scattering contributes to the quasi-elastic signal, and therefore the coherent scattering-cross section σ_{coh} is not of importance here.

Table 3.3: The neutron scattering cross-sections and absorption coefficients for hydrogen, lithium, boron and iodine. The fraction of the isotopes in the naturally occurring elements, called relative abundance, is also shown. Data from [63].

Isotope	*Relative abundance (%)*	σ_{coh} *(barn)*	σ_{inc} *(barn)*	σ_{abs} *(barn)*
H	99.985	1.7599	79.91	0.3326
D	0.015	5.597	2.04	0.00051
^{6}Li	7.5	0.51	0.41	940
^{7}Li	92.5	0.619	0.78	0.0454
^{10}B	20	0.14	3.0	3837
^{11}B	80	5.56	0.22	0.0055
^{53}I	100	3.50	0.0	6.2

As shown in Table 3.3, hydrogen has by far the largest incoherent scattering cross-section of these isotopes. In order for the scattering signal from lithium to be better visible in the resulting QENS spectrum, hydrogen must be substituted by deuterium. The use of ^{6}Li and ^{10}B should also be avoided, as they have very large absorption coefficients and would therefore attenuate the intensity of the scattered signal. ^{53}I is the only isotope of iodine, and has no incoherent contribution to the scattering. Due to these considerations, the samples used in the QENS measurements were composed of $0.75{}^{7}Li^{11}BD_4 + 0.25{}^{7}LiI$.

The mixing ratio of the two compounds was chosen based on the conductivity of the $(1\text{-}x)LiBH_4 + xLiI$ as measured by impedance spectroscopy (see chapter 4 and Paper A). Samples composed of $0.75{}^{7}Li^{11}BH + 0.25{}^{7}LiI$ were also synthesised and measured for comparison with the deuterated samples. For the

sample preparation, $^{7}Li^{11}BD_4$ (purity >94%) ,$^{7}Li^{11}BD_4$ (purity >94%) and ^{7}LiI (purity >98%) were purchased from Katchem. The solid solution was synthesised by planetary ball-milling, as described for the $LiBH_4$-LiI solid solutions in section 3.1.1. Powder XRD was performed on the resulting powder to confirm that a solid solution with the hexagonal HT crystal structure of $LiBH_4$ had been formed.

3.5.2 The Sample Cell and the Application of an Electric Signal

We used a flat sample cell made of aluminium, shown in Figure 3.5. Aluminium has a very low incoherent scattering cross-section compared to the isotopes in the sample (0.0085 barns) and a rather low neutron absorption coefficient (0.231 barns). For the measurements, 0.5 to 1.0 g of sample were inserted into the cell and subsequently pressed at approximately 1 ton/cm^2. The dimensions of the sample after pressing were 4.0 cm by 3.0 cm with a thickness of around 0.5 mm.

The sample holder in Figure 3.5 is made of two aluminium plates that are held together by aluminium screws. Thin Teflon flanges (white in the figure) were inserted to isolate the two plates electrically from each other. Note that in this way, the screws are only in direct electrical contact with one of the aluminium plates. The Teflon flange situated in between the two aluminium plates also serves the purpose of atmospherically sealing the cell, which is important as the sample is sensitive to oxygen and moisture.

In order to enhance the motion of lithium ions in the sample, an alternating current (AC) electric signal was applied to the sample *in-situ*, i.e. during the neutron measurements. For this, electrical wires were connected to each side of the sample cell, as shown in Figure 3.5a. A Parstat 2273 potentiostat was used to apply a 1000 Hz AC signal with a constant voltage of 2 V or 3 V. Impedance

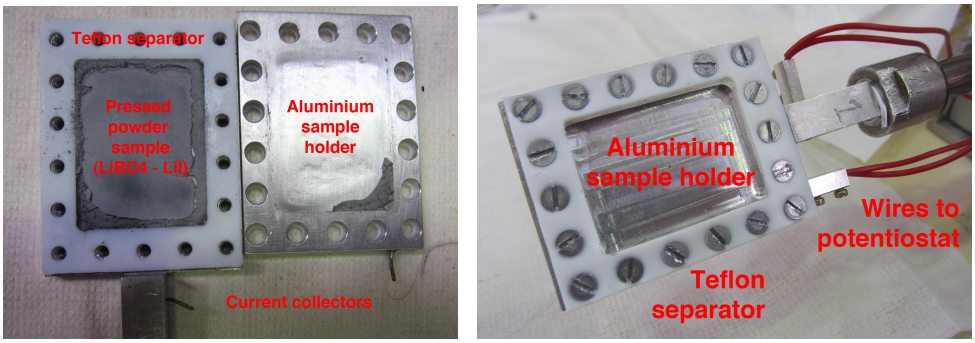

(a) **(b)**

Figure 3.5: The flat aluminium sample cell used for the QENS measurements. **a)** An open sample holder containing a pressed sample. The white Teflon flange ensures atmospheric sealing of the cell when it has been closed and pressed, but also serves as an electrical insulator. Both aluminium plates have a small current collector for connecting the cell to the potentiostat. **b)** A sealed sample holder mounted on the sample stick of the QENS instrument. The red wires that are connected to the two current collectors of the cell are connected to the potentiostat for the application of electrical signal *in-situ*. A thin layer of Teflon tape electrically isolates the sample cell from the rest of the stick.

spectroscopy measurements were also performed prior to each *in-situ* neutron measurement. In this way the contribution of the sample to the impedance could be observed, thereby confirming that the setup was correct and that the electric signal was indeed running through the sample and not through some other channel.

QENS spectra were measured at temperatures ranging from 4 K to 420 K (147°C). The instrument resolution function $R(\vec{Q},\omega)$ was taken to be a QENS spectrum measured at 4 - 10 K, as atomic motion at such low temperatures is too slow to appear in the QENS spectra. Based on results from DFT calculations, the C3 rotation of the BH_4 was expected to be primarily observed at temperatures below 300 K. At higher temperatures, the signal from the C3 rotation was expected to be very broad and mainly appear as an almost flat background in the measurements. The diffusion of lithium ions was expected to be observed at temperatures from approximately 300 K to 420 K, and measurements were thus performed at various temperatures in this range. The C3 rotations and the diffusion motion have different jump rates, and is therefore be possible to separate their contributions to the broadening in the QENS spectra.

At each of these temperatures, QENS spectra were measured both with and without applying an electric signal with the aim of observing possible differences in the quasi-elastic signal between the two cases. When a potential is applied, the lithium ions gain electrical energy in addition to their thermal energy. As a result, the average lithium ion can overcome a larger potential barrier than before and the mean number of Li^+ jump events is thus increased. By comparing QENS spectra obtained with and without an applied potential, it is possible to separate the signal due to the increased motion of lithium ions from other atomic motion in the sample. This can be achieved by fitting the resulting QENS spectra using the Chudley-Elliott model (see Section 2.4.5) and comparing the resulting jump lengths and jump rates for both cases. This has been done in Paper B.

3.5.3 Backscattering Spectrometers

The four different instruments used for the QENS measurements during this work are all backscattering spectrometers. A schematic of the working principle of such spectrometers is shown in Figure 3.6. This schematic is based on the layout of the SPHERES backscattering spectrometer, but the same principles hold for the other QENS instruments used in this work although e.g. the number of analyzer crystals and detectors varies between instruments.

The backscattering method may not be the simplest scattering setup, but it allows for an energy resolution on the order of μeV, making the detection of the quasi-elastic signal possible. A backscattering spectrometer works as follows: An incoming beam of neutrons is directed towards the instrument via a neutron guide. It passes through a monochromator (a velocity selector), which only lets through neutrons with the energy E. Those neutrons are then focussed at a mirror, which deflects them into the so-called Doppler drive. The Doppler drive is a mechanical oscillator that receives monochromatic neutrons with the energy E but reflects them with a known energy distribution across an energy spectrum $[E-\mathrm{d}E, E+\mathrm{d}E]$. These neutrons form the incident beam that hits the sample. The incident neutrons are scattered spherically (i.e. in all directions)

by the sample with some neutrons gaining energy and others losing energy in the scattering process. Some of the neutrons are scattered onto silicon crystals (analysers), which cover a segment of the spatial scattering angle. Note that the position of each analyser crystal corresponds to a certain scattering vector $\vec{Q}$. Due to Bragg's law (Eq. 2.7), each analyser crystal only reflects neutrons of a single energy. These neutrons are 'backscattered' into detectors situated opposite to the analyser crystals. Because the energy distribution of the incident neutron beam was known, it is possible to deduce how much energy change ΔE the detected neutrons underwent in the scattering process. This reconstruction of ΔE yields a histogram, which is called the QENS spectrum. Furthermore, due to the presence of multiple analyser crystals and detectors, the scattered signal can also be resolved in terms of the scattering vector $\vec{Q}$.

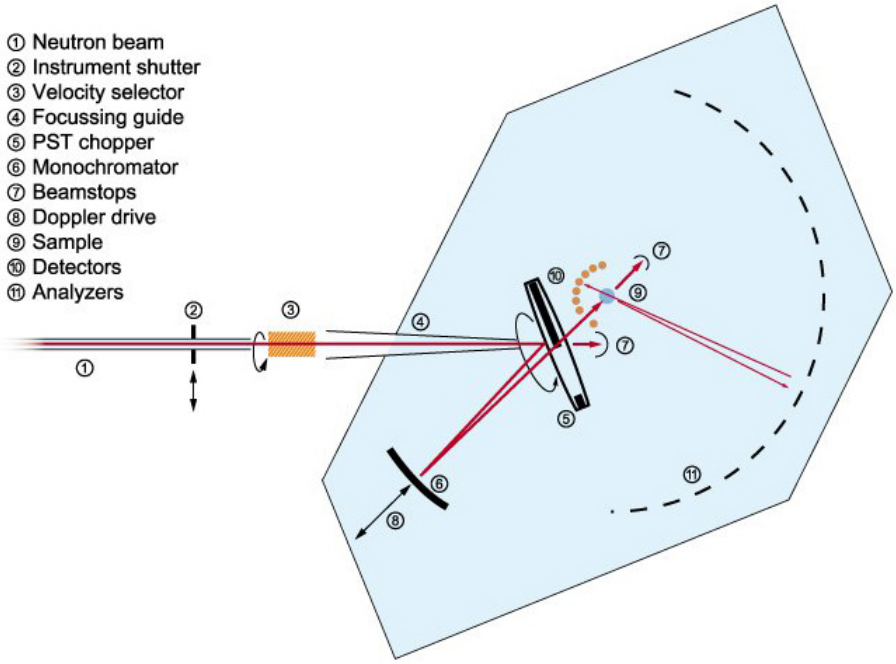

Figure 3.6: The operating principle of a neutron backscattering spectrometer. The red arrows in the figure denote the path of the neutron beam as it enters the instrument, is reflected, scattered off the sample and backscattered by the analyser crystals. The most important components of the instrument are labelled in the figure. A backscattering instrument is typically rather large, or a few meters in both diameter and height. This figure is a schematic of the SPHERES backscattering spectrometer at FRM-II, and is obtained from the NMI3 information portal (http://nmi2.eu)

Chapter 4

The $LiBH_4$-LiI Solid Solution

The $LiBH_4$-LiI solid solution is the topic of Papers A and B. This chapter begins with a short overview of lithium borohydride, the versatile material which forms the centrepiece of this PhD project. Its crystal structure and general properties are briefly surveyed, followed by a discussion of its fast ionic conduction properties and how ball milling and heat treatment affect its conductivity.

In the next two sections of this chapter I present the findings of Paper A, along with some additional information. Section 4.2 discusses how the highly conducting high temperature phase of $LiBH_4$ can be stabilized at room temperature by adding lithium halides, in particular how LiI addition affects the phase transition temperature. Section 4.3 focusses on the crystalline structure, conduction properties, relative phase stabilities and phase transition temperatures of the $(1-x)LiBH_4$-xLiI solid solution for a wide range of LiI content x. It provides a discussion of how these properties are correlated, with the aim of both providing a fundamental understanding of the microstructural properties of the solid solution and addressing the more practical question of how its lithium ion conductivity can be optimized.

In section 4.5 I briefly present the experimental findings of Paper B, which reports on the results of density functional theory calculations and quasi-elastic neutron scattering measurements of the $LiBH_4$-LiI solid solution, with the aim of revealing the lithium ion conduction mechanism in the high temperature crystal structure. As the section only contains a summary of the results from Paper B, reading Paper B prior to reading section 4.5 is recommended. In the last section of this chapter I summarise of the results on the $LiBH_4$-LiI solid solution.

4.1 Lithium Borohydride

4.1.1 Crystal Structure and General Properties of $LiBH_4$

Lithium borohydride, $LiBH_4$, is a white, crystalline solid material. At room temperature it has an orthorhombic ($Pnma$) crystal structure, but around 110°C it undergoes a reversible structural transition to a hexagonal structure ($P6_3mc$) [64]. In the following, the two polymorphs will be referred to as the LT phase

(low temperature, orthorhombic) and HT phase (high temperature, hexagonal), respectively. The layout of the crystal structures is shown in Figure 4.1.

$LiBH_4$ is lightweight, with a density of 0.666 g/cm^3. Hydrogen accounts for 18.5% of its mass, and it has been extensively investigated as a possible hydrogen storage material [65–69]. It releases hydrogen in a few steps at temperatures from 200 °C to 600 °C [70], but this temperature can be lowered by doping with e.g. aluminium, titanium or SiO_2 [65, 68]. Rehydrogenation after hydrogen release is, however, difficult because diborane (B_2H_6) is usually formed during hydrogen release [70].

$LiBH_4$ is an electrical insulator in both crystal structures, with calculations

Table 4.1: The crystal structure parameters of the LT and HT structures of $LiBH_4$. The melting point of $LiBH_4$ is 275 °C. Z denotes the number of formula units per unit cell. Values obtained from [64].

	$T < 110$°C	110°C$< T <$ 275°C
Symmetry	Orthorhombic	Hexagonal
Space group	*Pnma*	$P6_3mc$
a (Å)	7.178	4.276
b (Å)	4.437	4.276
c (Å)	6.83	6.948
Volume (Å^3)	216.7	110.0
Z	4	2

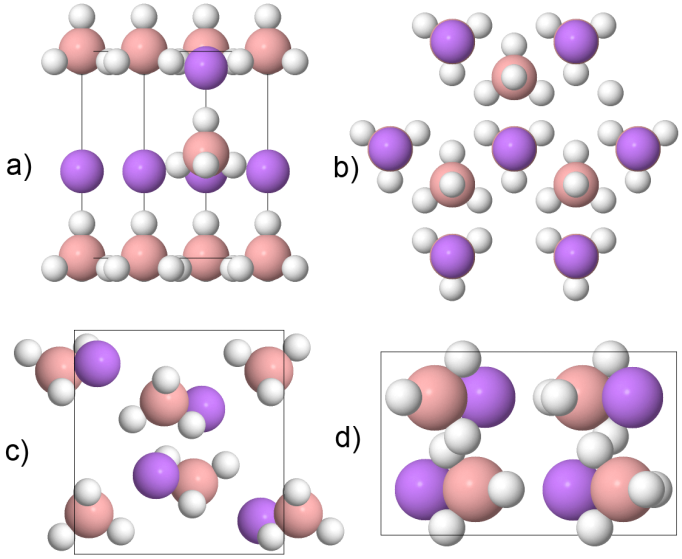

Figure 4.1: The HT (hexagonal) and LT (orthorhombic) crystal structures of $LiBH_4$. Lithium atoms are purple in the figure, boron atoms are pink and hydrogen atoms are white. **a)** One unit cell and neighboring atoms of the HT structure shown from the side. **b)** The hexagonal HT structure shown from the top. **c)** One unit cell and neighboring atoms of the LT structure shown from the side. **d)** One unit cell and neighboring atoms of the LT structure shown from the top. Figure reprinted from [57].

showing a large band gap of approximately 6.7 eV [71, 72]. Furthermore, $LiBH_4$ is a strong reducing agent and is used for that purpose in organic synthesis, in particular for the reduction of esters and amides. It is highly reactive with oxygen and water, and must therefore be handled in an inert atmosphere, e.g. in a glove box.

The exact crystal structure of the high temperature phase of $LiBH_4$ has not yet been fully agreed upon and has been the subject of quite a few studies in recent years. Early accounts from the 1970's discuss it as a tetragonal structure, but after a more recent x-ray diffraction study, Soulié *et al.* concluded that it is a hexagonal structure with the space group $P6_3mc$ [64]. The results of a density functional theory (DFT) study showed, however, that the $P6_3mc$ structure was unstable with regard to lattice vibrations and suggested a Cc structure [73, 74]. Findings from more recent DFT calculations and molecular dynamics simulations suggest that the $P6_3mc$ structure has two possible lithium sites along the c-axis, and this double splitting is likely to be the origin of the previously calculated instability [75, 76]. Aeberhard *et al.* also report on a double splitting of the lithium sites in very recent molecular dynamics simulation, but suggest the space group $P6_3/mmc$ [77, 78]. The results of the most recent neutron and x-ray diffraction studies of the structure support a $P6_3mc$ structure [79–81], but report an orientational disorder of the borohydride groups [82, 83]. In this work, the $P6_3mc$ structure as published by Soulié *et al.* [64] has been used for the Rietveld refinement of x-ray diffraction data.

4.1.2 Fast Ionic Conduction in $LiBH_4$

The orthorhombic, low temperature structure of $LiBH_4$ shows very low ionic conduction. However, when $LiBH_4$ undergoes the structural transformation from

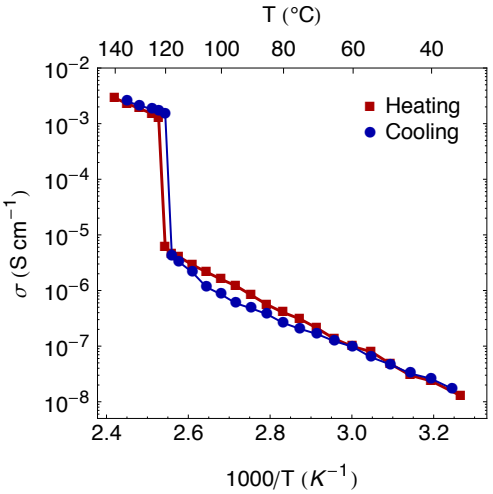

Figure 4.2: The ionic conductivity of as-received $LiBH_4$, as measured by impedance spectroscopy. The red symbols denote measurements during heating and the blue symbols are measured during cooling. A very small hysteresis in the phase transition temperature is observed. The conductivity increases by almost three orders of magnitude as the crystal structure changes from the LT phase to the HT phase. These results are in good agreement with the original results of Matsuo *et al.* [84].

the LT structure to the HT structure, its conductivity increases by almost three orders of magnitude. The superionic conductivity of the HT structure (i.e. $\sigma > 1$ mS/cm) was first reported by Matsuo *et al.* [84]. This behaviour is shown in Figure 4.2. The results of nuclear magnetic resonance (NMR) measurements have shown that the increase in conductivity is caused by an increase in lithium ion motion [84–86]. Being an electrical insulator, as already mentioned, the observed high electric conductivity can thus be attributed to fast conduction of lithium ions. $LiBH_4$ has furthermore been shown to be electrochemically stable up to 5 V [87]. This makes $LiBH_4$ a promising electrolyte for high temperature all-solid-state batteries [76, 84, 85].

4.1.3 The Effect of Ball Milling and Heat Treatment

Ball milling and heat treatment were found to have a considerable impact on the conductivity of $LiBH_4$. XRD patterns of $LiBH_4$ at different states of treatment are shown in Figure 4.3. The diffraction peaks of the ball-milled sample (blue) are broader than those of the as-received sample (gray), showing that ball milling reduces the crystallite size and/or induces strain on the crystal lattice. The diffraction peaks of the annealed sample (red) are slightly narrower than those of the ball-milled sample (blue), indicating that some sintering took place during the heat treatment.

These changes in the microstructure of the sample also affect its conductivity. The conductivity of as-received (non-milled) and ball-milled $LiBH_4$, as measured using impedance spectroscopy, is shown in Figure 4.4. The as-received (non-milled) $LiBH_4$ is in its poorly conducting LT phase. At around 120 °C, the sample changes to the HT phase and the conductivity increases by almost three

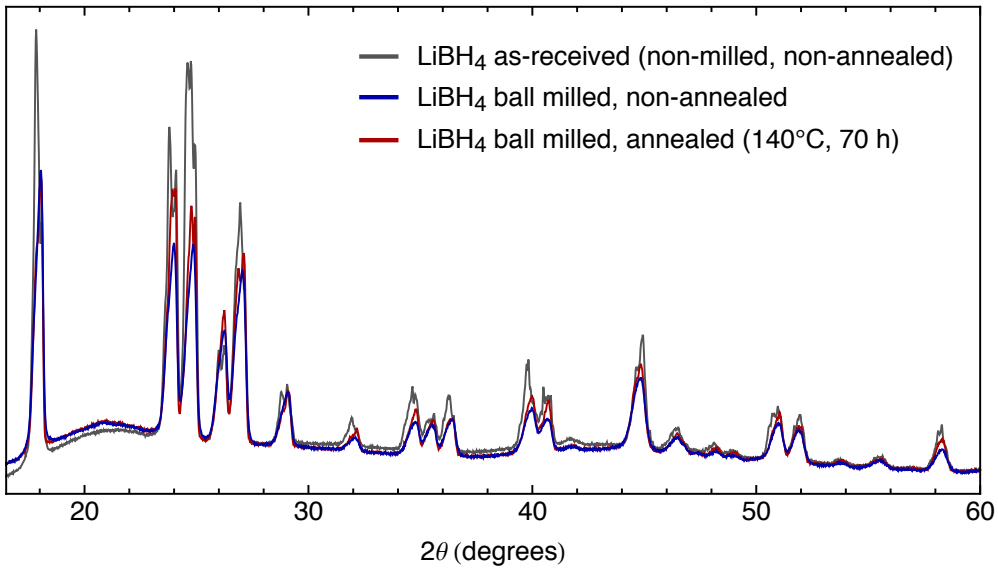

Figure 4.3: X-ray diffraction patterns of as-received $LiBH_4$ (not ball-milled, non-annealed), ball-milled $LiBH_4$ (non-annealed) and $LiBH_4$ that has been ball-milled and annealed at 140 °C for 70 hours. The broadening of the diffraction peaks varies depending on which treatment the samples had prior to the XRD measurement.

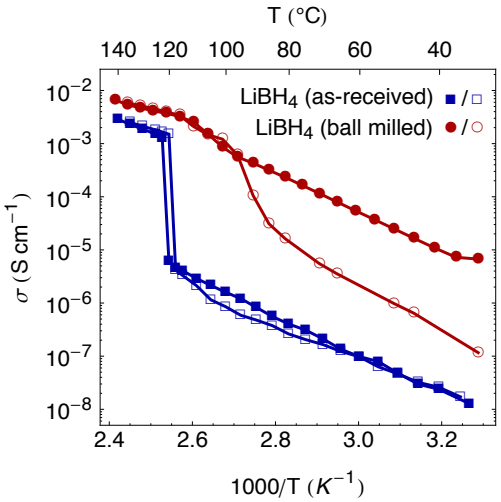

Figure 4.4: The ionic conductivity of lithium borohydride before and after ball milling. The filled symbols are measured during heating and the empty symbols are measured during cooling. This notation will be followed throughout this work to distinguish between heating and cooling runs. The sample is still in the LT phase after the milling. Ball milling induces defects in the crystal structure of $LiBH_4$, which greatly increases the conductivity of the sample. The defects are, however, partially mended during the heating and cooling cycle of the impedance spectroscopy measurement, again lowering the conductivity of the sample.

orders of magnitude, as discussed in section 4.1.2. The ball-milled $LiBH_4$ is also in the poorly conducting LT phase (see Figure 4.3). However, defects arising during the milling may open up new lithium ion conduction pathways. This causes an increase in conductivity by almost three orders of magnitude close to room temperature, compared to the non-milled $LiBH_4$. When the ball-milled $LiBH_4$ is heated up above the phase transition temperature it takes on the HT structure, presumably mending some of the defects caused by the ball milling. The return to the LT phase when cooling the sample down most probably mends the defects even further. As a result, some of the conduction pathways that were present during the heating run are closed during the cooling run. Because of this, the conductivity of the LT phase is substantially lower during the cooling run than during the heating run. After the thermal treatment, the sample is not, however, defect-free and the conductivity of the ball-milled sample is still higher than that of the as-received $LiBH_4$. This analysis is supported by the changes that are observed in the broadening of the diffraction peaks in Figure 4.3.

4.2 Stabilisation of the HT Phase of $LiBH_4$ at Room Temperature

4.2.1 Lithium Iodide Addition

Practical operating temperatures for most batteries are considerably lower than 120 °C, and high ionic conductivity at lower temperatures is therefore desirable

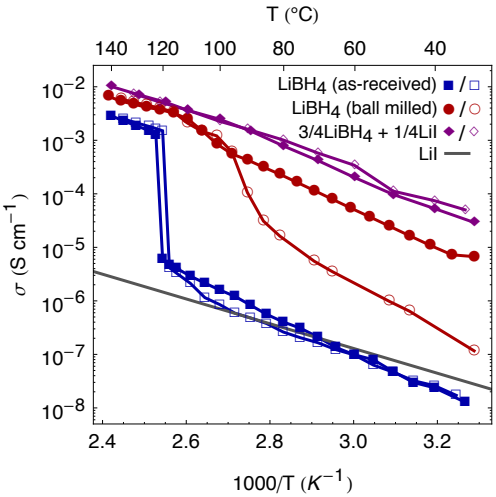

Figure 4.5: The ionic conductivity of $LiBH_4$ with LiI addition. A mixture with 25% LiI molar content is shown here as an example. The conductivities of LiI as well as as-received and ball milled $LiBH_4$ are shown for comparison. The filled symbols are measured during heating and the empty symbols are measured during cooling. LiI forms a solid solution with $LiBH_4$, which lowers the phase transition temperature of $LiBH_4$ and stabilises the high conductivity trend of the HT phase at room temperature. The results are in good agreement with the original results of Maekawa *et al.* [88]. The data for LiI is from [89].

for applications in working battery cells. Maekawa *et al.* showed that it is indeed possible to lower the transition temperature between the HT and the LT phases of $LiBH_4$, thereby stabilising the highly conducting hexagonal crystal structure at room temperature [88]. This is achieved by the addition of lithium halides (LiI, LiBr and LiCl), with lithium iodide addition giving the best lithium ion conduction results.

Lithium iodide has a low temperature modification below 0 °C known as β-LiI, which has a $P6_3mc$ structure and is thus isostructural with the HT phase of $LiBH_4$. LiI itself is a very poor ionic conductor ($\sigma \approx 10^{-8}$ S/cm at room temperature) [89, 90], but forms a solid solution with $LiBH_4$ [91] in the crystal structure of $LiBH_4$. The formation of the solid solution results in a lowering of the structural transition temperature of $LiBH_4$ by more than a 100 °C for 20% LiI addition [92]. The $LiBH_4$-LiI solid solution has been investigated as a hydrogen storage material [93] and as a lithium ion conductor [57, 92]. Furthermore, the reorientational motion of the borohydride groups in the solid solution have been investigated by quasi-elastic neutron scattering [54, 55].

4.2.2 Phase Transition Temperature

The phase transition temperatures of $(1-x)LiBH_4+xLiI$ solid solutions with different LiI contents x were measured using differential scanning calorimetry (DSC). The measurements were handled by Didier Blanchard, a senior scientist at DTU Energy Conversion, but I performed the analysis of the resulting data. Figure 4.6 shows the results of the measurements for five different mixing ratios x. Some of the DSC spectra show two maxima of different intensity, most prob-

ably due to microstructural inhomogeneity in the samples. In these cases, the phase transition temperature is taken to be that at which the greater maximum is located.

In Figure 4.7a, the phase transition temperature between the HT and the LT phase of the $LiBH_4$-LiI system is shown as a function of LiI content. For

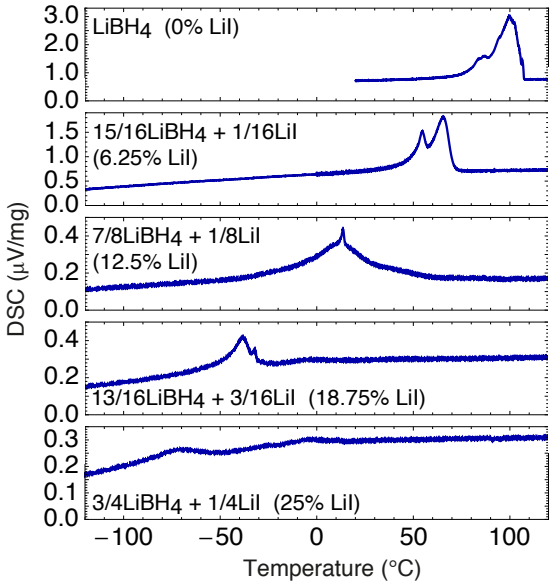

Figure 4.6: Differential scanning calorimetry results for different mixing ratios of the $LiBH_4$-LiI solid solution. The measurements were performed during cooling runs.

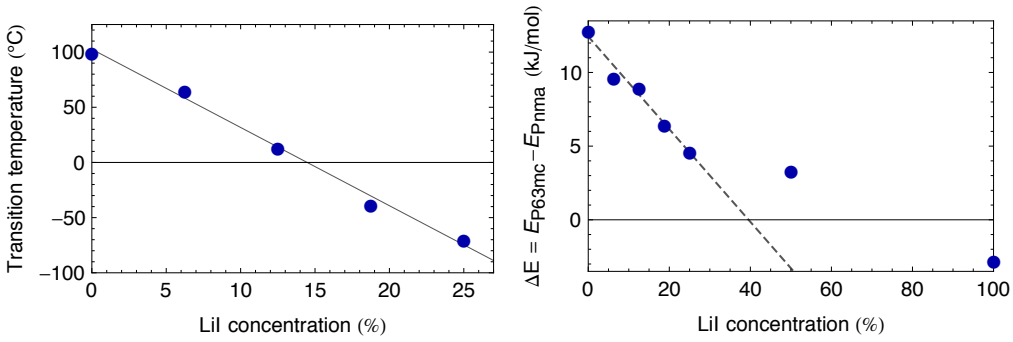

Figure 4.7: a) The phase transition temperature between the HT and the LT phases of the $LiBH_4$-LiI solid solution, as measured using DSC. A LiI addition of $\geqslant$ 12.5% suffices to decrease the transition temperature below room temperature. The measured transition temperatures are somewhat lower than those published by Miyazaki *et al.* [92]. **b)** The ground state energy difference between the HT and the LT structures of $LiBH_4$ as a function of LiI content, as calculated using DFT. The stabilisation of the HT structure relative to the LT structure is approximately linear up to a LiI content of 25%. The dotted line shows a linear fit of the data points for LiI contents from 0% to 25% to emphasise this. The calculations were performed by Jón Steinar Garðarsson Mýrdal.

the measured LiI content there is a clear linear dependency, with the transition temperature decreasing by approximately 70 °C for every 10% of LiI addition. For all measured mixtures with a LiI content equal to or above 12.5%, the transition temperature lies below room temperature.

The relative ground state energy difference between the HT and LT phases, $\Delta E = E_{P6_3mc} - E_{Pnma}$, was calculated using density functional theory (DFT) by Jón Steinar Garðarsson Mýrdal, a fellow PhD student at DTU Energy Conversion. The results, which are shown in Figure 4.7b, indicate that there is a linear stabilisation with increasing LiI content up to a content of 25%. There seems to be little gain in stability by increasing the LiI content to 50%, but for pure LiI the HT structure comes out more stable than the LT structure. The results of the calculations might not be very reliable for high LiI content, because the LT structure of $LiBH_4$ is not the ground state structure of LiI. The calculations are, however, expected to give fairly good estimates for small LiI content, and fit very well with the observed DSC data.

4.3 Crystal Structure of $LiBH_4$-LiI and the Effect of Heat Treatment

4.3.1 Crystal Structure

I performed x-ray diffraction measurements on the $(1-x)LiBH_4{+}xLiI$ solid solution for various mixing ratios x. The diffraction patterns of both non-annealed and annealed (140 °C for 70 hours) samples are shown in Figure 4.8. A diffraction pattern of non-annealed, ball-milled $LiBH_4$ is also shown for comparison. All measurements are performed at room temperature. The pure $LiBH_4$ sample has the LT structure, while the sample with 6.25% LiI is a blend of the LT and HT structures. For all samples with LiI content equal to or greater than 12.5%, only the HT phase is detected.

The positions of the reflections from the crystallographic planes $(hk0)$, parallel to the hexagonal plane, are only slightly shifted to higher values when the LiI content is increased, reflecting a small expansion of the a axis with increased LiI content. The c axis, perpendicular to the hexagonal plan, is found to shrink with increasing LiI content up to 30% and then to expand with increasing LiI content between 30% and 50% (see figure 4.8, in which a line is drawn to emphasise the shift of the (002) reflection).

The evolution of the lattice parameter c is plotted as a function of the LiI content in Figure 4.9a. The non-monotonic evolution of the c-axis is unexpected and the contraction of c with increasing LiI content below a LiI content of 30% differs from what has previously been reported by Miyazaki *et al.* [92]. For a LiI content above 30%, the c-axis expands as expected when compared with the unit cell parameters of the hexagonal phases of pure $LiBH_4$ and pure LiI respectively and is in agreement with the values reported by Miyazaki *et al.* [92]. and Rude *et al.* [93].

One possible explanation for this behaviour is the presence of solid solutions containing different amounts of iodine and different lattice constants that merge into one upon heating, as reported by Rude *et al.* [93]. Another possibility is the

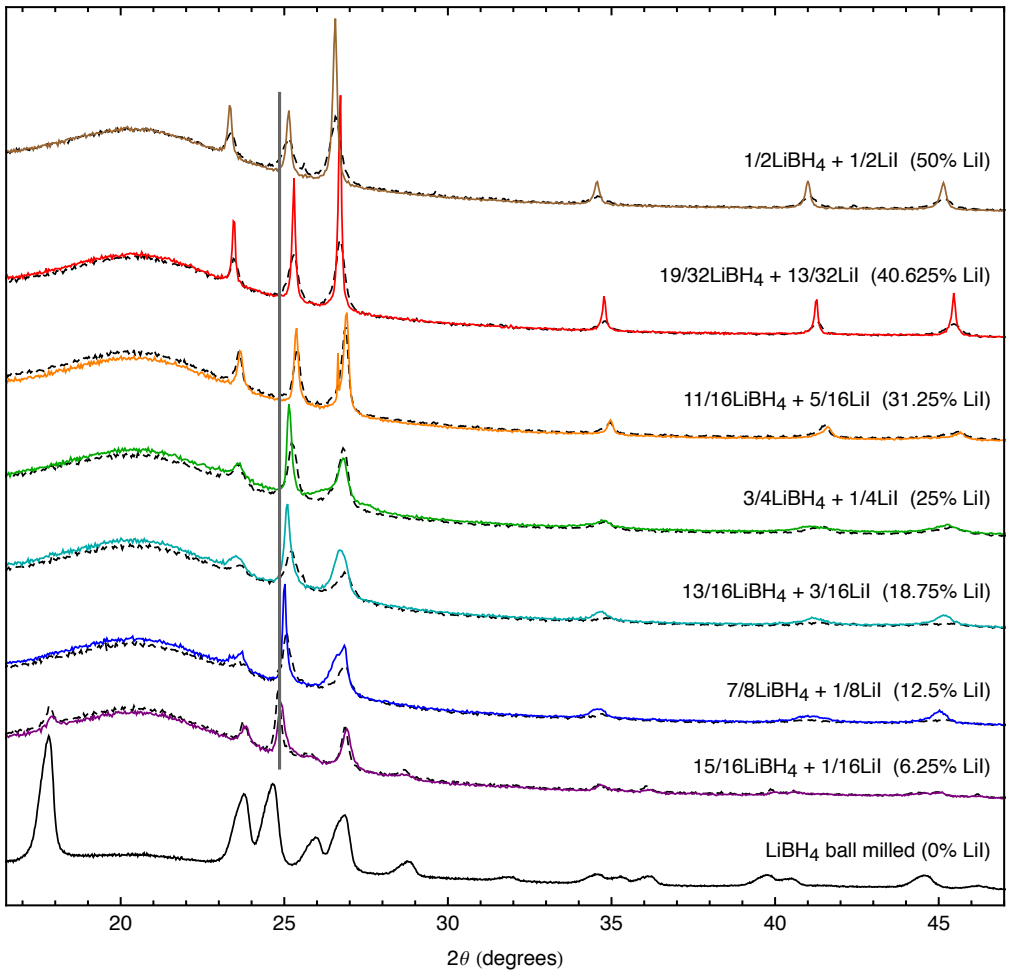

Figure 4.8: Powder x-ray diffraction patterns of the $LiBH_4$-LiI solid solutions in various mixing ratios before and after heat treatment. The black, dashed lines show diffraction patterns of non-annealed samples. The colored, solid lines show diffraction patterns of samples which have been annealed at 140 °C for 70 hours. The black, solid line shows the diffraction pattern of ball milled, non-annealed $LiBH_4$ for comparison. The vertical line at around 25 °is drawn to emphasise the shift of the (002) reflection with LiI content. All measurements were performed at room temperature. The broad bump at the lowest angles is due to the polyethylene sample holder. The intensity of the diffraction pattern of the pure $LiBH_4$ has been scaled down by 1/3 in order to better fit the intensities of the remaining patterns in the figure.

existence of some intermediate phases as described by Oguchi *et al.* [91]. These effects could be the origin of the very asymmetric peak shapes and large peak broadening visible in Figure 4.8 for low LiI content. Such broadening at low LiI content is also visible in the diffraction patterns presented in [67, 68].

4.3.2 The Effect of Heat Treatment on the Microstructure

Sintering effects are observed for the annealed $LiBH_4$-LiI solid solutions in the form of narrower peaks for the annealed samples than for the non-annealed ones. However, the peculiar behavior of the c axis is still present in the annealed

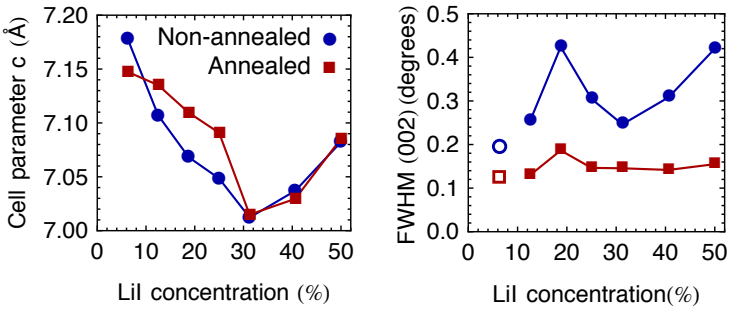

Figure 4.9: a) The evolution of the unit cell parameter c in $(1-x)LiBH_4+xLiI$ with LiI content. **b)** The FWHM of the (002) reflection of the $(1-x)LiBH_4+xLiI$ diffraction patterns as a function of LiI content. The FWHM of the samples with 6.25% LiI content are shown with empty dots; their values are not reliable because of overlapping diffraction peaks from the LT and HT structures of $LiBH_4$.

samples. As an example of the peak sharpening, the evolution of the full-width at half-maximum (FWHM) of the (002) reflection with LiI content is shown in figure 4.9b. The FWHM of the non-annealed powder varies with the LiI content and has a minimum at around 30% LiI content. This is also the LiI content for which the cell parameter c (see Figure 4.9a) is closest to the value reported for the cell parameters of pure $LiBH_4$ [64]. After the annealing, the FWHM values are almost independent of the LiI content.

The broadening contribution from the strain and the crystallite sizes was analyzed using Equation 2.11. This analysis was performed on the FWHM of four to six peaks depending on the diffraction patterns. Due to the limited quality of the data, no absolute values for D and η are reported here. Their relative contribution and evolution will, however, be discussed in connection with the LiI content and the effect of the annealing.

It was found that before the annealing, the broadening due to the strain is dominant over the size effect up to a LiI content of 25%. Knowing that the FWHM values are larger for the sample with 18.25% LiI content than for samples with a higher content of LiI, the density of defects is greater for the former than for the latter. After annealing, the strain values are smaller and almost independent of the LiI content. Furthermore, the crystallite sizes of the annealed powders are found to be around three times greater than those of the non-annealed powders for samples with LiI contents larger than 25%. Overall, the FWHM are found to be lowered by the heat treatment.

It should be noted that the difference in strain before and after the annealing is found to be smallest for the sample with 30% LiI content, which is the LiI content at which the minima in the cell parameter c and the FWHM before annealing are observed (see Figure 4.9. It should also be noted that the sample with 6.25% LiI content contains two coexisting structures with overlapping diffraction peaks at the position of the (002) reflection of the HT phase. Therefore the measured FWHM values are probably not accurate for this sample and have been left out for this analysis.

4.4 Lithium Ion Conductivity of $LiBH_4$-LiI

4.4.1 Conductivity Results

The conductivity of the $(1-x)LiBH_4+xLiI$ solid solution was measured using impedance spectroscopy for various mixing ratios x. The measurements resulted in a Nyquist plot showing a single arc. The explanation for this can either be that only one contribution to the conduction is present, or that two or more arcs, each corresponding to concurrent bulk and/or grain boundary contributions, overlap completely in the Nyquist plots. In such a case, however, it is not possible to separate the contributions from the bulk and the grain boundary conductivities using only impedance spectroscopy, as discussed in section 2.3.4 on the Brick Layer Model. Therefore, the conductivity values presented in the following are to be taken as the total conductivity of the sample. No contribution to the Nyquist plots from the Li electrodes was observed. The Nyquist plots were all fitted using an (RQ) equivalent circuit model, i.e. a resistor and a constant phase element (CPE) in parallel. Examples of Nyquist plots from these measurements are shown in Figure 4.10. The conductivity of the samples is given by Equation 2.30.

Figure 4.11 shows Arrhenius plot of the lithium ion conductivities measured for the $LiBH_4$-LiI samples in six different mixing ratios x, during heating and cooling. The pellets consisted of the as-milled powders and the measurements were performed while first heating the pellets from room temperature to 140 °C and then cooling them back down to room temperature. The $(1-x)$LiBH4+xLiI solid solutions show very high ionic conductivity, with the sample with 40% LiI content exceeding 0.1 mS/cm at 30 °C and the 18.75% LiI containing sample exceeding 10 mS/cm at 140 °C.

The slope of each Arrhenius plot denotes the activation energy E_a of the conduction process (see Equation 2.35. Figure 4.12 shows the activation energies of the lithium ion conduction in the $LiBH_4$-LiI solid solution is shown as a function of LiI content. The values are obtained by performing a linear least-

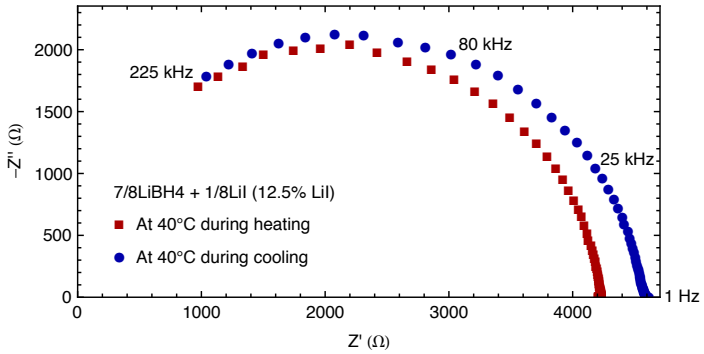

Figure 4.10: Typical examples of Nyquist plots obtained from the impedance spectroscopy measurements on the $LiBH_4$+LiI samples. The impedance measurements were performed during heating/cooling cycles from 30 °C to 140 °C and back to 30 °C. The red squares were measured at 40 °C at the beginning of such a heating/cooling cycle and the blue circles were measured at 40 °C at the end of the cycle. The Nyquist plots all show a single arc and were fitted using an (RQ) equivalent circuit model.

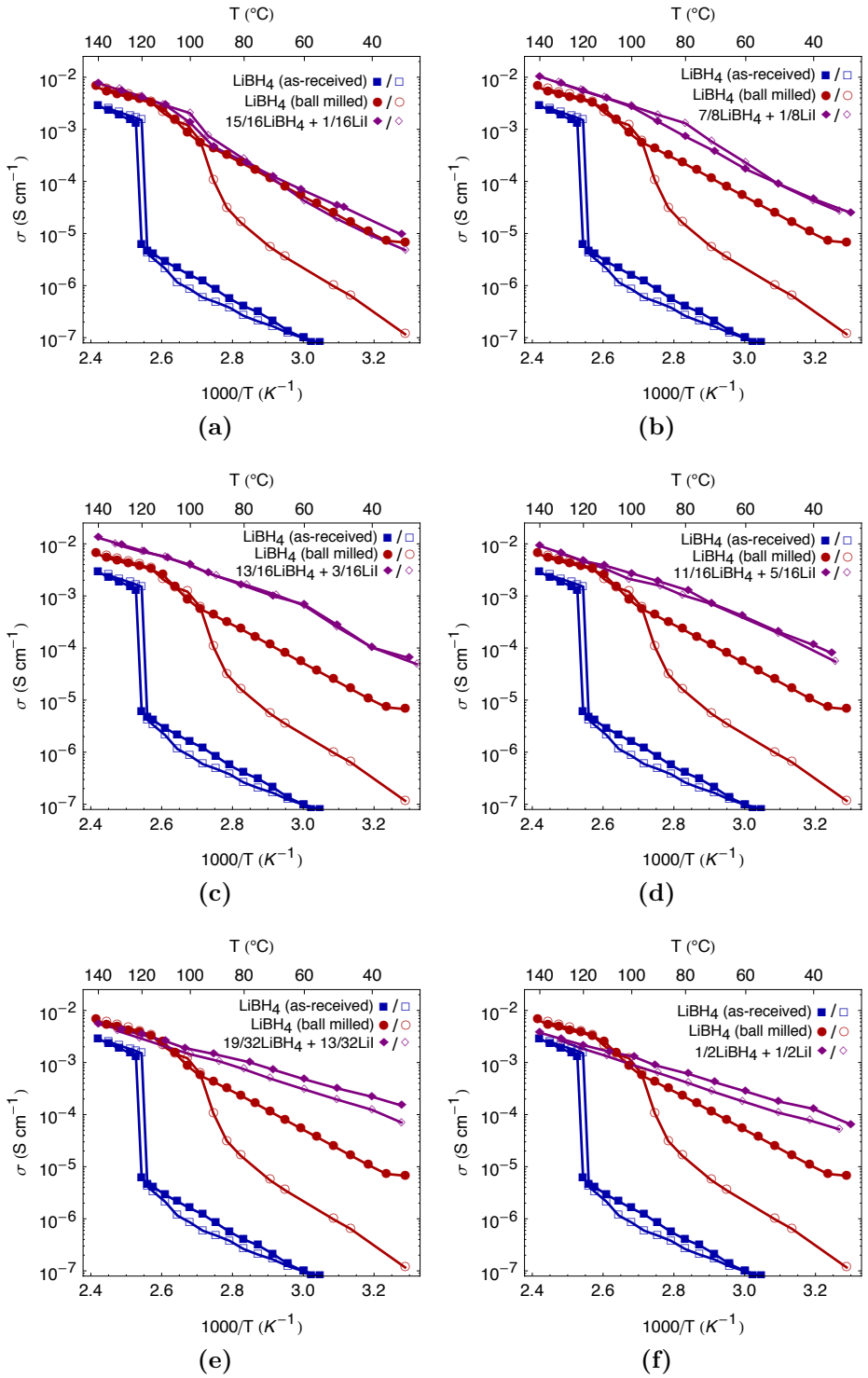

Figure 4.11: Lithium ion conductivities of six different mixing ratios of the $(1-x)LiBH_4$-$xLiI$ solid solution. The filled symbols are measured during heating, the empty symbols are measured during cooling. The mixture with $x = 3/16$ (Figure **c)**) has the highest conductivity at high temperature while the mixture with $x = 13/32$ (Figure **e)**) has the highest conductivity close to room temperature. The conductivities of as-received and ball-milled $LiBH_4$ are shown in each plot for comparison. Note that a plot of the conductivity of the mixture with $x = 25$ can be found in Figure 4.5.

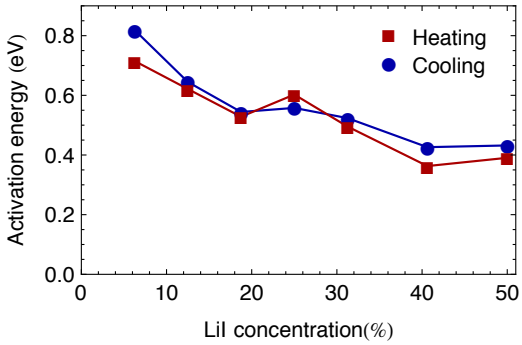

Figure 4.12: The activation energy of the lithium ion conduction in the $LiBH_4$-LiI solid solutions, as measured by impedance spectroscopy. The activation energy is found to generally decrease with increased LiI content. The activation energies during heating and cooling are similar for most mixing ratios of the solid solution.

squares fit of the Arrhenius plots in Figure 4.11. There is a general trend that the activation energy of the lithium ion conduction decreases with increasing LiI content. Furthermore, as a result of the decreasing slopes with increasing LiI content, the samples with a low LiI content generally have a higher lithium ion conductivity at the highest measured temperatures than the samples with high LiI content. Note that these values for the activation energies should not be compared directly to values calculated by DFT, which are usually considerably lower (see Paper B and [57]. Such calculations generally yield a value of the energy barrier for a single conduction process, whereas the measured values presented here represent a combined value arising from multiple processes in an imperfect sample.

4.4.2 The Effect of Heat Treatment on the Conductivity

The conductivity values at 50 °C are shown as a function of the LiI content in Figure 4.13. This temperature is chosen because it represents an approximate temperature at which a lithium battery could be operated. At 50 °C, the conductivity is 0.3 mS/cm for LiI contents of 18% and 40%. Although this temperature is at the upper limit of consumer battery usage, the $LiBH_4$-LiI solid solution is still around a factor of three away from the 1 mS/cm target.

The heat treatment that the samples undergo during the impedance spectroscopy measurements can be important for their conductivity, similar as described for pure $LiBH_4$ in section 4.1.3. The conductivity values at 50 °C are equal or higher during the heating runs than during the subsequent cooling runs. The difference in the conductivity between the heating and the cooling measurements is smallest for samples with LiI content between 18% and 30%. This result is in good harmony with the result shown in Figure 4.9b, namely that the particle size and/or density of defects in the non-annealed samples is closest to those in the annealed samples for solid solutions with moderate LiI content.

Together, the XRD and conductivity results indicate that the microstructure of the samples is important for their conductivity, and that freshly ball-milled samples with defect-rich microstructure yield higher conductivity values than

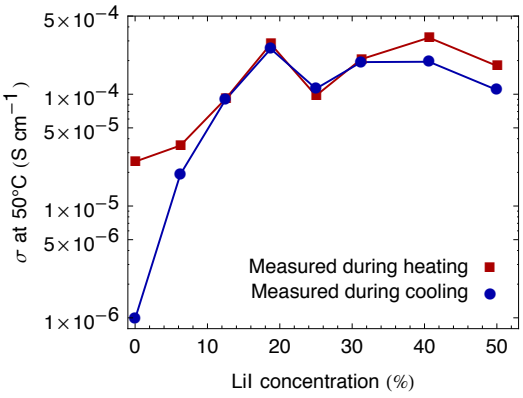

Figure 4.13: The lithium ion conductivity of the $LiBH_4$-LiI samples at 50 °C as a function of the LiI content for non-annealed (red) and annealed (blue) samples. The data points for pure $LiBH_4$ in this figure are from a measurement on ball-milled powder.

those in which the defects have been mended by annealing. This is also emphasised by the fact that the measured conductivity does not follow the evolution of the lattice parameter c (see Figure 4.9a), which has a minimum at a LiI content of 30%. If the left part of Figure 4.9a is omitted (as it most probably does not reflect the trend of a single phase) one would expect an increase in conductivity in connection with the lattice expansion in the c direction. This is, however, not found to be the case here and strongly suggests that a part of the lithium ion conduction might occur along the defects, e.g. grain boundaries or dislocations. The lithium conduction mechanism in the $(1-x)LiBH_4{+}xLiI$ solid solution is discussed further in section 4.5.

4.4.3 Conductivity During Multiple Heating and Cooling Runs

Figure 4.14 shows the conductivity of a sample with 50% LiI content measured during five consecutive heating and cooling cycles. As shown for the sample with 50% LiI content in Figure 4.13, the conductivity during cooling is lower than that during heating. However, during the next four temperature cycles, the conductivity performance is very stable and reproducible, confirming the good thermal stability of the HT phase of the solid solution. This sample was synthesised and measured during my research stay at Tohoku University, Sendai, Japan, i.e. under slightly different experimental conditions than the other samples in this chapter (see sections 3.1.1 and 3.3). Because the density of defects and particle size are important parameters for the conductivity of the samples, it was to be expected that the conductivity values from this measurement could differ from those presented in Figures 4.11 and 4.13. This explains why the conductivity of the sample in figure 4.14 is higher at 50 °C than shown for the sample with 50% LiI content in Figure 4.13. This also gives an indication of how reproducible the conductivity results are between different laboratory equipment.

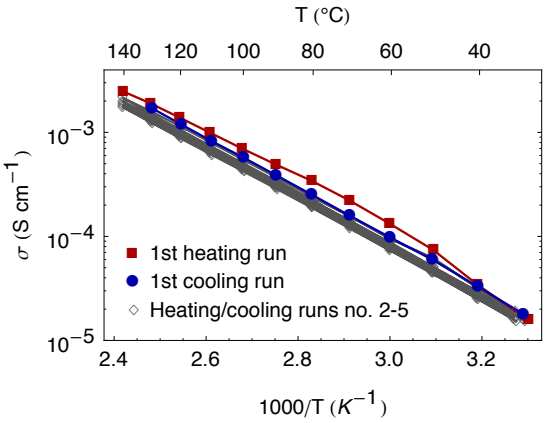

Figure 4.14: Lithium ion conductivity of a sample with 50% LiI content as measured by impedance spectroscopy during five heating and cooling cycles. The red and the blue symbols show the results of the first heating and cooling runs, respectively. The gray symbols show the results of the four subsequent heating and cooling runs.

4.5 Conduction Mechanism

4.5.1 Studies on the Lithium Ion Conduction Mechanism

The mechanism of fast lithium ion conduction in the HT structure of $LiBH_4$ has previously been studied using molecular dynamics. The results of Ikeshoji *et al.* show the formation of Frenkel pairs [76], which are defects where a lithium ion is displaced from its lattice site, creating a vacancy V^- and an interstitial Li^+. In these results, which were calculated at a simulated temperature of 560 K, the interstitial was displaced by around 2.5 Å, and the formation energy of the defect pair was estimated as 0.29 eV. It was suggested that the diffusion of lithium ions takes place when Frenkel pairs are formed and neighboring lithium ions subsequently move into the vacancy site. It was furthermore discussed that double splitting of lithium lattice sites along the *c*-axis plays an important role in the high ionic conductivity. The results of Aeberhard *et al.* also show a double splitting, and that the BH_4 have no favourable orientation in the HT phase [77, 94]. The results show some density of lithium ions in the interstitial region, and a similar lithium ion diffusion mechanism is presented as in the work of Ikeshoji *et al.*. The reorientational motion of the BH_4 tetrahedra in $LiBH_4$-LiI have previously been investigated using QENS [54, 55], but Paper B reports for the first time on combined results from QENS measurements and DFT calculations on the lithium ion motion in the solid solution.

QENS measurements were performed on $0.75^7Li^{11}BD + 0.25^7LiI$ samples in order to investigate the lithium ion conduction mechanism in the $LiBH_4$-LiI solid solution. The measurements were performed with and without an applied potential of 3 V. The measurements presented here were performed at temperatures of 300 K and 380 K. The results presented in this section (and in Paper B) were obtained using the IN10 backscattering spectrometer at the Institut Laue-Langevin in Grenoble, France. We have recently performed additional measurements at temperatures from 360 K to 420 K, but the results of those measurements were not fully analysed when this was written.

In these measurements, I collaborated with Didier Blanchard, a researcher at DTU Energy Conversion, who also performed the analysis of the resulting data. Later in this section (and in Paper B) The QENS results are compared to DFT calculations performed by Jón Steinar Garðarsson Mýrdal, a fellow PhD student at DTU Energy Conversion. Since my contribution to this work mainly consisted of preparing the samples and performing the measurements, only a short summary of the results of the QENS measurements will be presented in this section. For further details on the analysis of the QENS results and on the DFT calculations please refer to Paper B.

4.5.2 The Quasi-Elastic Neutron Scattering Results

The normalised elastic neutron scattering intensity of $0.75^7Li^{11}BD + 0.25^7LiI$ and $0.75^7Li^{11}BH + 0.25^7LiI$ samples is shown as a function of temperature in Figure 4.15. The evolution of the mean-square displacement $< u^2 >$ with temperature for the hydrogenated sample is also shown. The mean-square displacement is related to the thermal vibrations in the sample and is obtained by performing a least-squares fit of

$$I(T) = I(0)e^{-Q^2<u(T)^2>}, \tag{4.1}$$

where the exponent is the so-called Debye-Waller factor and Q is taken to be the average momentum transfer across all detectors.

The plots in Figure 4.15 can be split into three different regions. The LT structure of $LiBH_4$ is present from 3 K to 180 K, from approximately 180 K 220 K there is a transition region where the LT and the HT structures coexist, and from 220 K to 430 K the sample is in the HT structure. This is in good agreement with the transition temperature as measured by DSC, shown in Figure 4.6. The elastic intensity decreases with temperature because the atomic motion

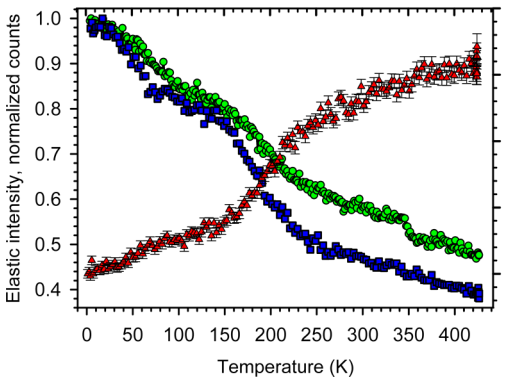

Figure 4.15: The normalised elastic intensity for $LiBH_4$-LiI (green circles) and $LiBD_4$ (blue squares) samples as a function of temperature. The mean-square displacement $< u^2 >$ of the hydrogenated sample is also shown (red triangles). The heating ramp during the measurement was 2.0 K/min. The graph helps to identify the temperature regions in which the two polymorphs are present, and thus in estimating in which temperature range the fast diffusion motion of lithium ions should be expected. The HT phase is present in the right-most region of the graph, from roughly 220 K to 430 K.

in the sample increases and more and more neutrons are scattered ineleastically. With increasing temperature, more and more neutrons are also scatterd with an exchange energy outside of the energy window that is detectable by the instrument ($\pm 15\mu$eV). As hydrogen has a much larger scattering cross section than deuterium (as discussed in section 3.5.1), the drop in the normalised elastic intensity is more pronounced for the hydrogenated sample.

The instrument used for these measurements has seven detectors. QENS spectra recorded by each individual detector, with and without an applied potential, are shown in Figure 4.16. The spectra recorded at different scattering vectors Q exhibit different broadening. As discussed in section 2.4.5, a Q-dependent broadening represents a non-localised, diffusive motion. It is also very apparent that the intensity of the elastic component changes with the application of a potential.

Examples of fitted QENS spectra for a deuterated sample measured at 300 K are shown in Figure 4.17. The fits were performed using Equation 2.45 with two Lorentzian terms, one describing the rotation of the BH_4 tetrahedra and the other describing the motion of lithium ions. As seen in the figure, the Lorentzian corresponding to the spectrum where a potential was applied during the measurement (orange circles) is broader than the Lorentzian related to the spectrum measured without an applied potential (green triangles). This is as expected, indicating that the application of the potential increases the quasi-elastic contribution from the lithium ion motion.

Fits to the measured data were carried out for the spectra from each of the seven detectors, both for measurements with and without an applied potential The resulting Lorentz distributions describing the lithium ion motion have Q-dependent HWHM. The Chudley-Elliott model (Equation 2.53), which describes long-range diffusion motion, was used to fit the HWHM as a function of Q. The results are shown in Figure 4.18. For the measurements at 300 K, it was not possible to fit the data measured with an applied potential satisfactorily with the Chudley-Elliott model. The data from the measurements at 300 K without

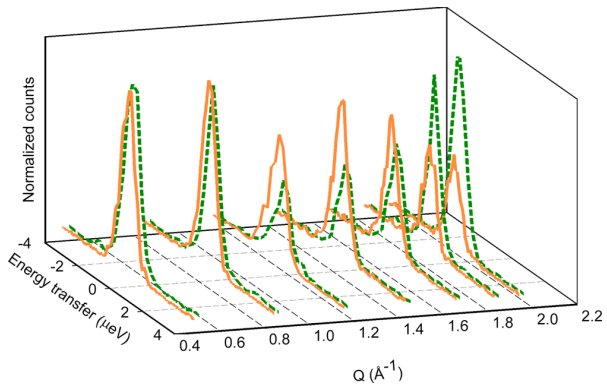

Figure 4.16: QENS spectra recorded by the individual detectors without (orange solid lines) and with (green dashed lines) an applied potential of 3 V. The measurements were performed at 300 K on a $0.75\,^{7}Li^{11}BD + 0.25\,^{7}LiI$ sample. The broadening of the spectra clearly depends on the scattering vector Q, and the Q-dependence changes with the application of a potential.

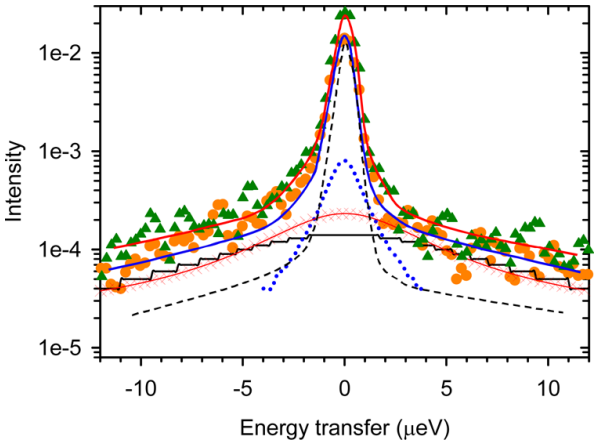

Figure 4.17: Examples of QENS spectra, measured with (orange circles) and without (green triangles) an applied potential of 3 V. These spectra are measured at 300 K on a $0.75{}^{7}Li^{11}BD + 0.25{}^{7}LiI$ sample. The solid blue and red lines are fits to the measured data. The individual components of the fit are also shown; the crossed red line is the Lorentzian function that models the lithium motion with an applied potential, the dotted blue line is the Lorentzian of the lithium motion without an applied potential, the dashed black line is the instrumental resolution function and the solid black line is the Lorentzian used to model the rotation of the BH_4 tetrahedra.

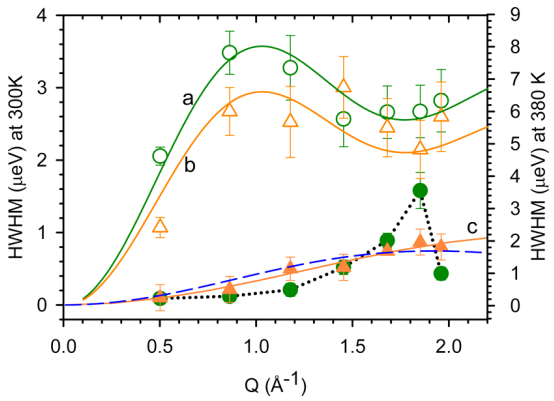

Figure 4.18: Fits of the Q-dependent broadening of the lorentzians describing the lithium ion motion, performed using the Chudley-Elliott model. The open symbols at the top of the graph were measured at 380 K without (orange triangles) and with (green circles) an applied potential. The filled symbols were measured at 300 K, also with (orange triangles) and without (green circles) a potential. The solid lines labelled a - c are fits to the measured data using the Chudley-Elliott model. The dashed blue line is the result of such a fit where the jump length was fixed to $L = 2.3$ Å. The dotted black line only serves as a guide to the eye.

an applied potential and the data from the measurements at 380 K with and without potential were fitted successfully. The resulting values for the jump length L, the jump rate τ_D^{-1} and the diffusion coefficient D (calculated using Equation 2.54) at 380 K are shown in Table 4.2.

Table 4.2: The jump lengths and jump rates obtained from the Chudley-Elliott fit of the QENS data on the $0.75^{7}Li^{11}BD + 0.25^{7}LiI$ sample at 380 K, with and without an applied potential. The diffusion coefficient of the motion has been calculated from Equation 2.54 assuming a motion in two dimensions, i.e. in the hexagonal crystal plane.

QENS, 380 K	0 V	3 V
L (Å)	3.6 ± 0.3	4.3 ± 0.2
$\tau_D^{-1} \cdot 10^9$ (s^{-1})	8.3 ± 0.3	10 ± 0.16
$D \cdot 10^{-6}$ (cm^2/s) for $n = 2$	2.7 ± 3	4.6 ± 3

4.5.3 Combined Analysis of QENS and DFT Results

Density functional theory calculations of various types of lithium ion motion and vacancy formation were performed, and are presented in Paper B as well as in [57]. Some of the calculated values are in good agreement with the experimentally determined values shown in Table 4.2. By combining the results of the QENS measurements and the DFT calculations, it is possible to gain an understanding of which type of lithium diffusion mechanism takes place in the solid solution. The DFT results that fit best to the results of the QENS data analysis are shown in Table 4.3, but a much more detailed account of this can be found in Paper B.

The formation energy of Frenkel pairs, i.e. a Li^+ interstitial and a V_{Li}^- vacancy, is found to be rather low, or 0.46 eV. The jump lengths of diffusional motion are on the order of one unit cell length, both for the QENS results and in the DFT results. The jump rates of the Li^+ interstitials and the V_{Li}^- vacancies correspond well with the observed value without an applied potential, and the observed jump rate in the QENS sample increases when a potential is applied, as expected. The application of a potential should also increase the lifetime of Frenkel pairs, as it drives the Li^+ and the V_{Li}^- apart from each other. The results thus suggest that the lithium diffusion takes place in the hexagonal plane (i.e. that it is two-dimensional), and that interstitials and vacancies (i.e. Frenkel pairs) play a key role in the conduction mechanism. Such pairs are expected to be created at electrode-electrolyte interface in a battery cell, where lithium ions leave and enter the electrolyte.

Table 4.3: Transition barriers, jump lengths and jump rates calculated using DFT. The results for three different processes are shown here; for a Li^+ interstitial moving between two equivalent lattice sites (called 1/3 sites in Paper B), for a Li^+ vacancy moving from an I^- to a BH_4^- site and for the formation of a Frenkel pair. Different transition barriers depend on the direction of the jumps.

DFT, 380 K	Li^+ interstitial	V_{Li}^+ vacancy	Frenkel pair
Barrier (eV)	0.26	0.33/0.28	0.46/0.02
L (Å)	4.32	4.27	3.32
τ_D^{-1} (s^{-1})	$8.3 \cdot 10^9$	$9.8 \cdot 10^8$	$2.9 \cdot 10^6$

4.6 Summary of the Results on the $LiBH_4$-LiI Solid Solution

The LiI content and the phase transition temperature between the HT and the LT phase are linearly dependent up to at least 25% LiI content as measured using DSC. A decrease in the transition temperature by 70 °C for every 10% of LiI addition is found. DFT calculations show that there is a close to linear stabilisation of the HT structure with LiI addition up to a LiI content of 25%. For all samples with a LiI content equal to or greater than 12.5%, the phase transition temperature lies below room temperature and after ball milling the samples only contain the HT phase as observed using XRD.

The $(1-x)LiBH_4+xLiI$ solid solutions show a high lithium ion conductivity. At 30 °C the conductivity exceeds 0.1 mS/cm (for the sample with 40% LiI content) and at 140 °C it exceeds 10 mS/cm (for the sample with 18.75% LiI content) as measured using impedance spectroscopy. Which mixing ratio of $(1-x)LiBH_4+xLiI$ yields optimal conductivity depends greatly on which temperature range is in question. The conductivity is equal or higher during heating than during cooling, with the least difference between heating and cooling results for a LiI content between 18% and 30%. Impedance spectroscopy measurements during five temperature cycles show that the conductivity of the material is stable and reproducible.

Non-annealed samples with a low LiI content have apparent densities of defects greater than those with a high LiI content, as revealed by analysing the FWHM of the reflections in the XRD data. This could be an artefact due to the presence of inhomogeneities and/or intermediate phases with similar but different cell parameters. After annealing, the density of defects appears to be almost the same for all samples, but the crystallite sizes grow with increasing LiI content. This could explain why samples with low LiI content tend to have a higher conductivity at high temperature than the samples with low LiI content, emphasising the importance of grain boundaries for the conduction.

The least change between the non-annealed and annealed samples is observed for a LiI content of around 30%. It is found that samples with defect-rich microstructure, most probably dislocations and/or grain boundary defects, yield higher conductivity values than those in which the defects have been mended by heat treatment and where only intrinsic point defects might exist. This shows that microstructure and heat treatment are important for the conductivity of the samples. Finally, it is found that the expansion of the lattice parameter c is not a predominant parameter for increased conductivity.

The combined results of the QENS measurements and the DFT calculations suggest that the lithium ion diffusion in the $LiBH_4$-LiI solid solution is mostly two-dimensional and takes place in the hexagonal plane of the crystal lattice. The QENS and DFT results show jump lengths on the order of one unit cell length for diffusion in this plane, as well as comparable jump rates. The formation of Frenkel pairs, which are found to have a rather low energy of formation, most likely plays a major role for the conduction. Further QENS measurements have already been performed, and hopefully their results will shed better light on the lithium ion conduction mechanism in hexagonal $LiBH_4$-LiI.

Chapter 5

The $LiBH_4$-$Ca(BH_4)_2$ Composite

The $LiBH_4$-$Ca(BH_4)_2$ composite is the subject of Paper C. This chapter begins with a short introduction of calcium borohydride and its crystal structures. In the next sections I present the findings of Paper C. Results on the crystal structure, phase compositions and the ionic conductivity of the composite are presented and discussed in sections 5.2 and 5.3, respectively. The surprising formation of orthorhombic and cubic CaH_2 during the heat treatment of the composites is reported in section 5.4, and the implications of this for the conductivity of the samples are discussed. The chapter ends with a brief summary of the findings on the $LiBH_4$-$Ca(BH_4)_2$ composite.

5.1 Calcium Borohydride

5.1.1 The Polymorphs of $Ca(BH_4)_2$

Calcium borohydride, $Ca(BH_4)_2$, is a white, crystalline solid material, which has been found to take on three polymorphs at room temperature and atmospheric pressure. It has been investigated extensively as a hydrogen storage material [95–102]. The crystal structures of $Ca(BH_4)_2$ were only resolved relatively recently, and four polymorphs of calcium borohydride have been characterised. α-$Ca(BH_4)_2$ has an orthorhombic structure ($Fddd$ [95, 103] or $F2dd$ [104]). β-$Ca(BH_4)_2$ has a tetragonal crystal structure (P-4 [104] or $P4_2/m$ [103, 105]). β-$Ca(BH_4)_2$ is sometimes referred to as a high-temperature polymorph, as it has been observed to become the dominant phase above 130 °C [105]. γ-$Ca(BH_4)_2$ has an orthorhombic crystal structure ($Pbca$) [103, 106]. The fourth polymorph, α'-$Ca(BH_4)_2$, is a high-temperature modification of the α structure that appears by a second order phase transition at around 220 °C. This polymorph has a tetragonal crystal structure (I-42d, a supergroup of $F2dd$) [104] and was not observed in this work. High-pressure polymorphs of $Ca(BH_4)_2$ have furthermore been proposed based on density functional theory calculations [107]. The layout of the α, β and γ crystal structures is shown in Figure 5.1.

As the enthalpy differences between the α, β and γ polymorphs are rather small (35-135 meV) [106, 108], these usually coexist. The relative quantity of

Table 5.1: The crystal structure parameters of the α, β and γ structures used for the Rietveld refinement of the diffraction patterns in this chapter. Z denotes the number of formula units per unit cell. Values for α-$Ca(BH_4)_2$ and β-$Ca(BH_4)_2$ from [104], values for γ-$Ca(BH_4)_2$ from [103].

	α	β	γ
Symmetry	Orthorhombic	Tetragonal	Orthorhombic
Space group	*F*2*dd*	*P*-4	*Pbca*
a (Å)	8.7759	6.91894	7.525
b (Å)	13.0234	6.91894	13.109
c (Å)	7.4132	4.34711	8.403
Volume (Å^3)	847.27	208.1	828.92
Z	8	2	8

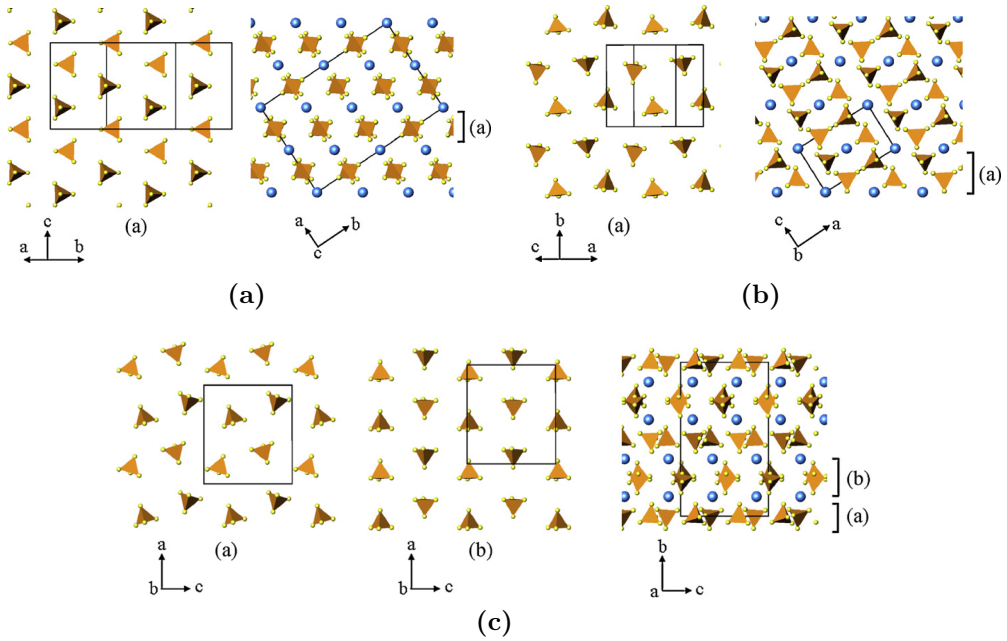

Figure 5.1: The three polymorphs of $Ca(BH_4)_2$ observed in this work. The blue spheres denote calcium atoms, the yellow spheres denote hydrogen atoms and boron atoms are located at the center of each tetrahedron. **a)** The α structure. The arrangement of BH_4 tetrahedra in the plane parallel to (100) is shown on the left, and the stacking of planes is shown on the right. **b)** The β structure. The arrangement of BH_4 tetrahedra in the plane parallel to (101) is shown on the left, and the stacking of planes is shown on the right. **c)** The γ structure. The two different arrangements of BH_4 tetrahedra in the plane parallel to (010) is shown on the left and in the middle, and the stacking of planes is shown on the right. Figure from [103].

the phases can even differ significantly between batches [102]. As shown in this work, the addition of $LiBH_4$ possibly has a large effect on the relative quantities of the $Ca(BH_4)_2$ polymorphs, which depend heavily on the mixing ratio of the two compounds. Furthermore, the possibility of Ca^{+2} substitution in $LiBH_4$ is

discussed in this work, as such introduction of relatively large cations in $LiBH_4$ could lead to compensating vacancies, which would likely enhance the lithium ion conduction. As an example, divalent doping of chlorides has been found to increase their ionic conductivity [109].

5.1.2 Mixtures of $LiBH_4$ and $Ca(BH_4)_2$

The main idea behind mixing lithium borohydride and calcium borohydride in this work was that the mixture might have better ionic conductivity than the precursor materials and possibly exhibit dual ionic conduction, i.e joint conduction of both lithium and calcium ions. Reports on the structure and hydrogen storage properties of the $LiBH_4$-$Ca(BH_4)_2$ composite have previously been published [110,111]. Accounts of the nature of the $LiBH_4$-$Ca(BH_4)_2$ mixtures differ, however, as Z. Fang *et al.* reported on the formation of a dual-cation borohydride $LiCa(BH_4)_3$, while J. Y. Lee *et al.* concluded that $LiBH_4$ and $Ca(BH_4)_2$ coexist as a physical mixture but not as a compound or a solid solution. This chapter seeks to resolve this controversy by reporting on the structural properties of the $LiBH_4$-$Ca(BH_4)_2$ mixtures using synchrotron x-ray diffraction. Furthermore, this chapter reports on the crystal structures and the phase composition of $(1-x)LiBH_4+xCa(BH_4)_2$ mixtures in various ratios. The main focus of the chapter is on the ionic conductivity of the composites and on the formation of CaH_2 in both orthorhombic and cubic structures that was observed upon heat treatment of the $LiBH_4$-$Ca(BH_4)_2$ composites. The chapter will also discuss how the low chemical stability of $LiBH_4$-$Ca(BH_4)_2$, illustrated by the formation of CaH_2, affects the suitability of the mixtures for usage as solid electrolytes, and how this can increase the risk of a short-circuit in the cell.

5.2 Crystal Structure and Phase Composition

The diffraction patterns of pure $LiBH_4$, pure $Ca(BH_4)_2$ and four composites of the two compounds are shown in Figure 5.2, along with a Rietveld refinement of each diffraction pattern. The phase factors, the unit cell parameters as well as the strain and the size broadening parameters were refined for all phases. Pseudo-Voigt profiles were used for modelling the shapes of the diffraction peaks. The background signal was modelled using a polynomial expression, and the zero point was refined. The isotropic thermal motion parameters were refined for all atoms except hydrogen and preferred diffraction orientations in the powder were modelled if needed. The occupancy of Ca^2 was refined in α-$Ca(BH_4)_2$ and the γ-$Ca(BH_4)_2$ phases. The resulting values for γ-$Ca(BH_4)_2$ are shown in Table 5.2. For γ-$Ca(BH_4)_2$ the refinement of the Ca^{+2} positions showed full occupancies in all cases. The peak to parameter ratio was greater than two for all refinements and greater than five for most refinements. The weighted profile agreement factor R_{wp} (see Equation 2.15) at the end of the refinements ranged from 2.2% to 4.25% and the data were refined for convergence, i.e until the squared sum of all parameter shifts divided by the estimated standard deviation (i.e $\sum(\text{shift}/\sigma)^2$) reached < 0.1.

The diffraction pattern presented for $LiBH_4$ is from a ball-milled sample. For $Ca(BH_4)_2$, diffraction patterns were acquired for as-received and ball milled

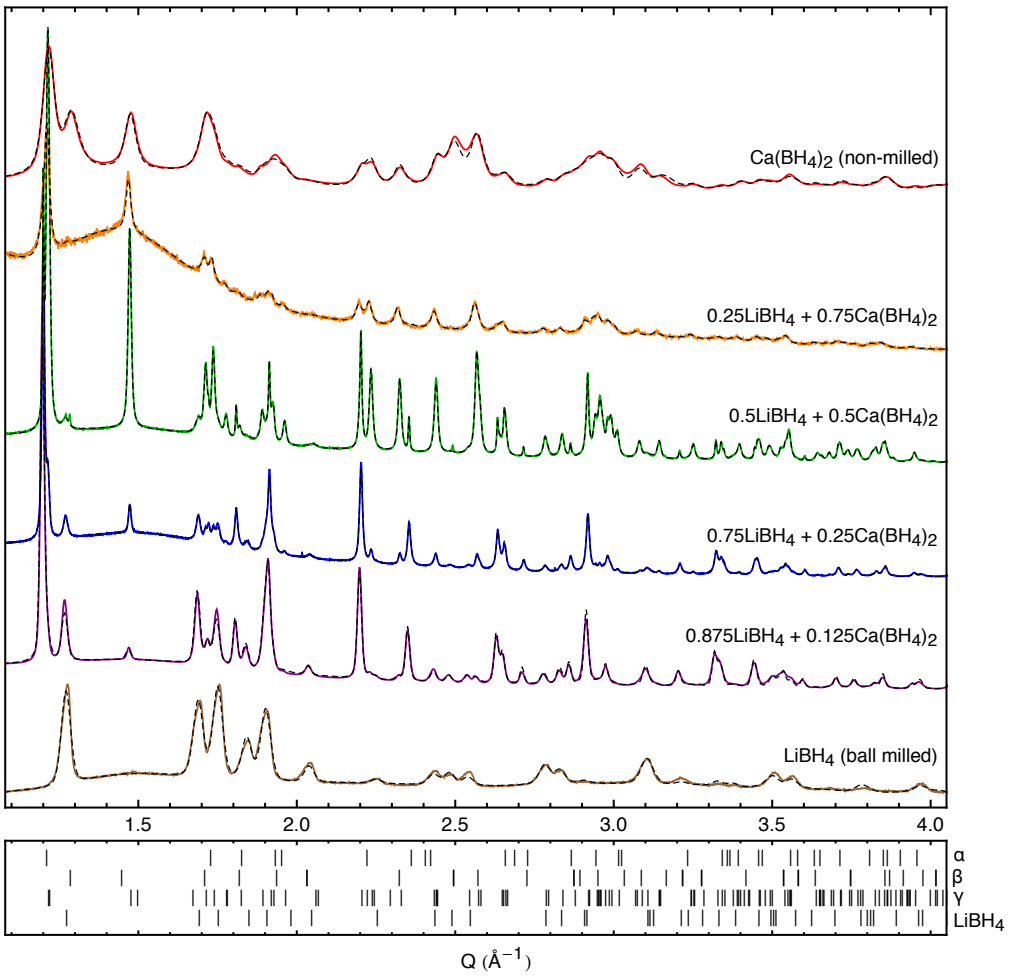

Figure 5.2: Powder x-ray diffraction patterns for different ratios of $(1-x)LiBH_4+xCa(BH_4)_2$. The solid, coloured lines show the measured data, the dashed, black lines show the Rietveld refinement of each measurement. The tick marks below the diffraction patterns show the locations of the Bragg reflections of α-$Ca(BH_4)_2$, β-$Ca(BH_4)_2$ γ-$Ca(BH_4)_2$ and orthorhombic $LiBH_4$. No other phases were detected in the samples. The diffraction pattern of pure $LiBH_4$ only contains orthorhombic $LiBH_4$. In the diffraction pattern of pure $Ca(BH_4)_2$, β-$Ca(BH_4)_2$ and γ-$Ca(BH_4)_2$ coexist, but no α-$Ca(BH_4)_2$ is detected. In the $(1-x)LiBH_4+xCa(BH_4)_2$ mixtures, α-$Ca(BH_4)_2$, γ-$Ca(BH_4)_2$ and orthorhombic $LiBH_4$ coexist, but no β-$Ca(BH_4)_2$ is detected. All data in the figure comes from synchrotron measurements except for the sample with x = 0.75 (see section 3.2).

powders. Only the diffraction pattern of the as-received compound is shown here since the milling alters the crystallinity of the powder, reducing the quality of the diffraction pattern and the Bragg peak intensities of the already poorly scattering $Ca(BH_4)_2$ powder. It was thus not possible to perform a trustworthy Rietveld refinement of the milled $Ca(BH_4)_2$ or to identify its phase composition in any reliable manner from its diffraction pattern.

The relative phase quantities of the mixtures in weight percentage, as obtained by Rietveld refinement, are shown in Table 5.2 and graphically in Figure 5.3. The milled $LiBH_4$ sample only contains the orthorhombic phase, as

Table 5.2: The relative phase quantities (in weight percentage) in the $(1-x)LiBH_4 + xCa(BH_4)_2$ samples, obtained from the Rietveld refinement of the XRD data. There are large variations in the phase quantities of the α and γ phases of $Ca(BH_4)_2$ with $LiBH_4$ content, but the β phase is only present in pure $Ca(BH_4)_2$. The rightmost column of the table shows the refined Ca^{+2} occupancies in the α-$Ca(BH_4)_2$ phase, but only for those mixtures for which synchrotron data were available. The Ca^{+2} occupancies in the β-$Ca(BH_4)_2$ and γ-$Ca(BH_4)_2$ phases were found to equal unity in all cases.

Sample (x in mol)	α-$Ca(BH_4)_2$ (wt%)	β-$Ca(BH_4)_2$ (wt%)	γ-$Ca(BH_4)_2$ (wt%)	$LiBH_4$ LT (wt%)	Ca^{+2} occ. in α-$Ca(BH_4)_2$
0	0.0	0.0	0.0	100.0	N/A
0.125	24.1	0.0	3.2	72.7	0.972
0.1875	22.1	0.0	13.2	64.7	N/A
0.25	39.0	0.0	10.6	50.4	0.931
0.33	6.2	0.0	46.5	47.3	N/A
0.50	8.7	0.0	62.4	28.9	0.975
0.67	18.0	0.0	65.0	17.0	N/A
0.75	15.8	0.0	62.7	21.5	N/A
1.00	0.0	36.9	63.1	0.0	N/A

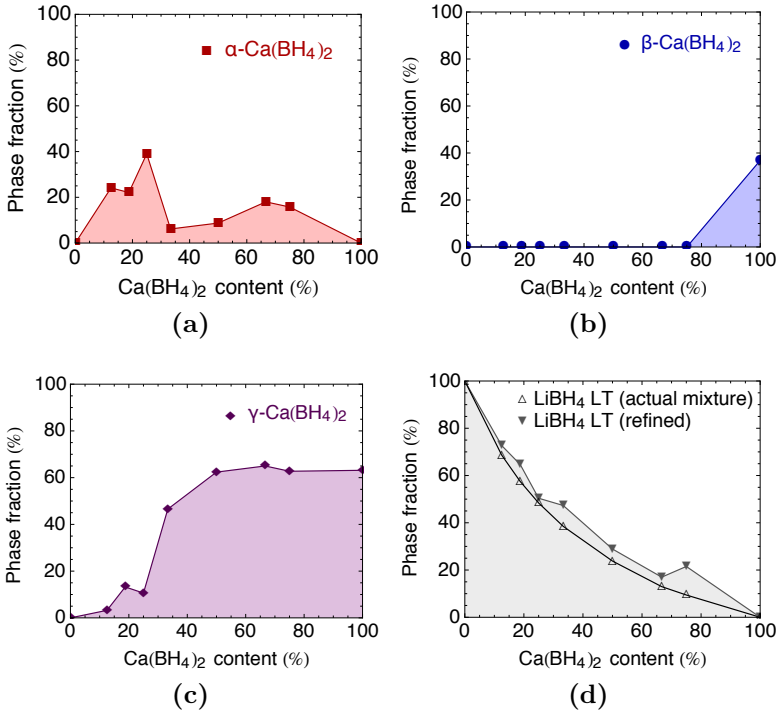

Figure 5.3: The relative phase quantities in the $LiBH_4$-$Ca(BH_4)_2$ samples a function of $Ca(BH_4)_2$ content. The data is obtained from the Rietveld refinement of the diffraction patterns, and is the same as in Table 5.2. The refined phase quantity of LT $LiBH_4$ is expected to equal the actual $LiBH_4$ weight percentage in each mixture. This means that, for an optimal refinement, the two curves in Figure **d)** should be identical. The Rietveld refinements are, however, somewhat imperfect with regard to this, most probably due to the low scattering power of $LiBH_4$ relative to $Ca(BH_4)_2$.

expected. The pure, as-received $Ca(BH_4)_2$ sample contains β-$Ca(BH_4)_2$ and γ-$Ca(BH_4)_2$, but no α-$Ca(BH_4)_2$ is present. All composites are composed of orthorhombic $LiBH_4$, α-$Ca(BH_4)_2$ and γ-$Ca(BH_4)_2$ only; no other phases or new compounds are formed during the ball milling. Note that the amount of $LiBH_4$ in the composite samples is generally overestimated, as compared to the actual mixing ratios of the samples. This indicates the accuracy of the Rietveld refinements performed on $LiBH_4$, which is composed of elements with low electron densities and is thus a poor x-ray scatterer relative to $Ca(BH_4)_2$. Small sample inhomogeneities may also contribute to this discrepancy in the $LiBH_4$ phase quantities.

As mentioned in the introduction, the enthalpy differences between the different $Ca(BH_4)_2$ phases are small, and therefore the relative phase quantities of the $Ca(BH_4)_2$ polymorphs are very sensitive to modifications of the mixture. Interestingly, no β-$Ca(BH_4)_2$ is detected in the composites although it is present in pure $Ca(BH_4)_2$, which is consistent with the findings of Lee et al. [48]. The relative quantities of the two remaining $Ca(BH_4)_2$ phases are very sensitive to any modifications of the mixture. α-$Ca(BH_4)_2$ is found to have the largest relative phase quantity for $x = 0.25$. For samples with large amounts of $LiBH_4$, only small amounts of γ-$Ca(BH_4)_2$ are found, but for composites with $x \geq 0.5$ it becomes the dominant phase with a similar relative phase quantity as in the pure $Ca(BH_4)_2$ sample.

The formation of α-$Ca(BH_4)_2$, which is not present in the as-received $Ca(BH_4)_2$, is either facilitated by the introduction of $LiBH_4$ (even in small amounts), or simply by the ball milling process. As already mentioned, the crystallinity of the pure, ball-milled $Ca(BH_4)_2$ samples was very poor, and it was unfortunately not possible to deduce the relative quantities of the $Ca(BH_4)_2$ polymorphs from its diffraction pattern. It can thus not be inferred with certainty whether the polymorph changes in $Ca(BH_4)_2$ take place due to $LiBH_4$ addition or due to the milling itself. It is, however, clear that the introduction of $LiBH_4$ increases the crystallinity of the $Ca(BH_4)_2$ polymorphs, as compared to the as-received and ball-milled $Ca(BH_4)_2$ samples.

The lattice parameters in all samples were found to deviate by less than 1% from the previously published values presented in Tables 5.1 and 4.1. The lattice parameters of the composite samples are in all cases very similar to those of the phases in the precursor compounds and do not change much with the mixing ratio x. It is therefore concluded that the $(1-x)LiBH_4$+x$Ca(BH_4)_2$ composites are physical mixtures rather than solid solutions. This finding is in good agreement with those previously reported by Lee et al [48].

After ball milling, a fraction of each sample was annealed in a glass container at 100 °C for 60 hours under Ar atmosphere. XRD measurements of the annealed powders show that such heat treatment does not change the phase compositions, which remain very close to those presented in 5.2. It was therefore not expected that the heat treatment during the impedance spectroscopy measurements would alter the phase composition of the samples.

5.3 Conductivity of the $LiBH_4$ - $Ca(BH_4)_2$ Composites

The conductivity of $(1-x)LiBH_4+xCa(BH_4)_2$ was measured for three mixing ratios, i.e $x \in \{1/4, 1/2, 3/4\}$. Figure 5.4 shows examples of Nyquist plots obtained by impedance spectroscopy. All Nyquist plots showed one arc (a slightly depressed semi-circle). The explanation for this can be either that only one contribution to the conduction is present, or that two or more arcs of concurrent bulk and/or grain boundary contributions overlap completely in the Nyquist plots. Unfortunately, it is not possible to separate different contributions to the conductivity in such a case using only impedance spectroscopy, as discussed in section 2.3.4. At the highest temperatures, some of the Nyquist plots also showed a small tail at the low-frequency end, which is attributed to the lithium electrodes.

As the Nyquist plots only show one arc, they were fitted using an (RQ) equivalent circuit model, i.e a resistor and a constant phase element (CPE) in parallel (see section 2.3.3). The Nyquist plots containing a low-frequency tail were fitted using two such circuits in series. The sample resistance R was taken to be the point of intersection between the Z' axis and the low-frequency end of the large arc. The conductivity of the samples is given by Equation 2.30.

The ionic conductivities of the $(1-x)LiBH_4+xCa(BH_4)_2$ samples are shown in Figure 5.5. The conductivity of pure $LiBH_4$, both as-received (non-milled) and ball-milled, is shown for comparison. Attempts were made at measuring the conductivity of pure $Ca(BH_4)_2$. This did, however, not succeed, most probably due to the ionic conduction of $Ca(BH_4)_2$ being too poor for measurements with this experimental setup (i.e $< 10^{-9}$ S/cm).

The ionic conductivity of the samples is very sensitive to defects in the crystal structure of the powders, as discussed in sections 4.1.3 and 4.4. The ball-milled $LiBH_4$ has a much higher conductivity ($4.6 \cdot 10^{-5}$ S/cm at 40 °C) than the non-milled (as-received) sample ($2.4 \cdot 10^{-8}$ S/cm at 40 °C), although both samples are in the orthorhombic, poorly conducting phase. This can be explained by

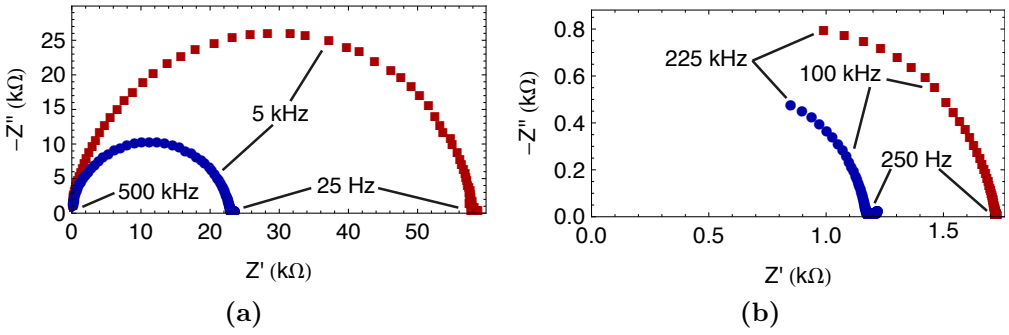

Figure 5.4: Examples of Nyquist plots obtained from impedance spectroscopy on $1/2LiBH_4+1/2Ca(BH_4)_2$. The red squares are measured during heating, the blue circles are measured during cooling. **a)** Measurements performed at 40 °C. **b)** Measurements performed at 80 °C. The Nyquist plots mostly show only one arc, but at the higher temperatures a small contribution from the electrodes is sometimes observed at the low-frequency end of the plots.

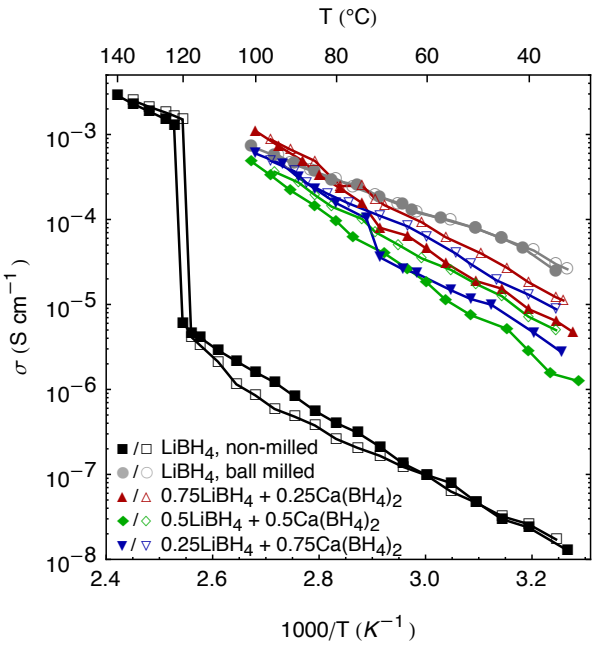

Figure 5.5: An Arrhenius plot of the ionic conductivity of the $LiBH_4$-$Ca(BH_4)_2$ mixtures. The ionic conductivity of non-milled and ball-milled pure $LiBH_4$ is shown for comparison. The filled symbols denote measurements during heating runs, the empty symbols denote measurements during cooling runs. The conductivity of the composites is in all cases lower than that of the ball-milled $LiBH_4$. Note that the conductivity of the composite samples is in all cases higher during cooling than during heating.

the formation of defects during the milling which may open new lithium ion conduction pathways, as explained in 4.1.3 and in Paper A. Note that the data presented in this section is not from the same measurement as the conductivity data for ball-milled $LiBH_4$ presented in section 4.1.3. As this sample was only heated up to 100 °C, and not above the $LiBH_4$ phase transition temperature of approximately 110 °C, the defects formed during the milling are not mended by the heat treatment and the conductivity of the ball-milled $LiBH_4$ remains similar during cooling.

The $(1-x)LiBH_4$+$xCa(BH_4)_2$ pellets consisted of as-milled powders. The $3/4LiBH_4$+$1/4Ca(BH_4)_2$ sample has the highest conductivity of the measured composites, or $8.8 \cdot 10^{-6}$ S/cm at 40 °C. A comparison of the phase compositions shown in Figure 5.3 with the conductivities of the composite samples shown in Figure 5.5 indicates that the presence of α-$Ca(BH_4)_2$ grain boundaries might be slightly more favourable for the conductivity than the presence of γ-$Ca(BH_4)_2$ grain boundaries. The ionic conductivity of all the composite samples is, however, in the range of 0.001 - 0.01 mS/cm, and thus considerably lower than the conductivity target of 1 mS/cm discussed in section 1.2.2. This is probably too low for application as a bulk electrolyte in working battery cells. However, at 100 °C the $3/4LiBH_4$+$1/4Ca(BH_4)_2$ sample reaches a conductivity of 1 mS/cm, which might be of interest in battery applications at elevated temperatures.

The fact that the Nyquist plots only show one arc that can be related to bulk and/or grain boundary conduction strongly suggests that Li^+ is the only charge

carrier in the composite, i.e that the contribution of Ca^{+2} to the conduction is negligible, This hypothesis is further strengthened by the observation that the conductivities of the $(1-x)LiBH_4+xCa(BH_4)_2$ samples are only slightly lower than that of ball-milled pure $LiBH_4$ in Figure 5.5, while the ionic conduction of pure $Ca(BH_4)_2$ is very poor.

The presence of a small number of Ca^{+2} vacancies in α-$Ca(BH_4)_2$ (which is indicated by the Rietveld refinement of the synchrotron data, see Table 1) could indicate that some Ca^{+2} substitute into $LiBH_4$, or that they form a grain boundary interface of Ca^{+2}. The formation of such an interface could enhance the ionic conduction in the $LiBH_4$-$Ca(BH_4)_2$ composite. The difference in the activation energies, which are derived from the slope of the Arrhenius plots, could also be an indication that the conduction mechanisms differ slightly between the pure $LiBH_4$ and the composites. The activation energy of the ball-milled $LiBH_4$ is found to be around 0.55 eV while the activation energies of the composites are found to be approximately 0.8 eV in all cases. Further work using other experimental techniques would be needed to determine which conductive species contribute to the ionic conductivity of the $(1-x)LiBH_4+xCa(BH_4)_2$ composite.

5.4 Formation of CaH_2

5.4.1 Orthorhombic and Cubic CaH_2

When the samples were heated up to 100 °C during the impedance spectroscopy measurements (under Ar atmosphere), a new phase formed over the course of a few hours. This phase consisted of a black layer, growing at the interfaces between the Li electrodes and the electrolyte. This surprising finding was observed even if no potential was applied to the sample.

In order to identify this phase, synchrotron XRD was performed on a black coloured part of a sample. The resulting diffraction pattern is shown in Figure 5.6, along with a Rietveld refinement of the data. The majority of the powder consists of α-$Ca(BH_4)_2$ and orthorhombic $LiBH_4$. However, the refinement reveals two additional phases that were not detected in the diffraction patterns of the as-milled samples shown in Figure 5.2. One of the phases was identified as calcium hydride, CaH_2 in its regular orthorhombic ($Pnma$) crystal structure (3.6 wt%). The second phase was indexed as a cubic structure with the space group $Fm\text{-}3m$, isostructural with CaF_2. Its lattice parameter is 5.490 Å, compared to 5.464 Å for CaF_2 [112]. After further investigations, this cubic phase was identified as CaH_2 (4.2 wt%). The crystal structures and the lattice parameters of the detected phases in the diffraction pattern in Figure 5.6 are shown in Table 5.3. No other phases or unexplained Bragg peaks were detected in the diffraction pattern. That does, however, not fully exclude the presence of small amounts of poorly scattering phases such as elemental boron or lithium.

5.4.2 The Stability of Cubic CaH_2

Solid solutions of $CaH_{2-x}F_x$ in the cubic CaF_2 crystal structure with various concentrations of hydrogen have previously been reported, first by Brice et al. [113] and more recently in connection with research on $Ca(BH_4)_2$ thermal decom-

Table 5.3: The crystal structures and the lattice parameters of the refined structures shown in Figure 5.6.

Phase	*Crystal structure*	*a* (Å)	*b* (Å)	*b* (Å)
$LiBH_4$ LT	*Pnma*	7.201	4.452	6.857
α-$Ca(BH_4)_2$	*F*2*dd*	8.815	13.184	7.543
CaH_2 orthorh.	*Pnma*	5.974	3.617	6.849
CaH_2 cubic	*Fm*-3*m*	5.488	5.488	5.488

position [98, 114]. Smithson et al. [115] have performed ab-initio calculations that show that at zero pressure, the formation energies for orthorhombic CaH_2 and cubic CaH_2 are very similar. Pinatel et al. [116] have recently calculated the phase diagram of the $CaH_{2-x}F_x$ solid solution and found that the cubic and orthorhombic phases can coexist near room temperature with very a low concentration of fluoride. Furthermore, Li et al. have detected a high-pressure phase of CaH_2 using in-situ Raman scattering, which reportedly starts forming at about 15.5 GPa and is thought to possess a higher symmetry than orthorhombic CaH_2 [117].

To investigate the possibility of the formation of cubic CaH_2 without any

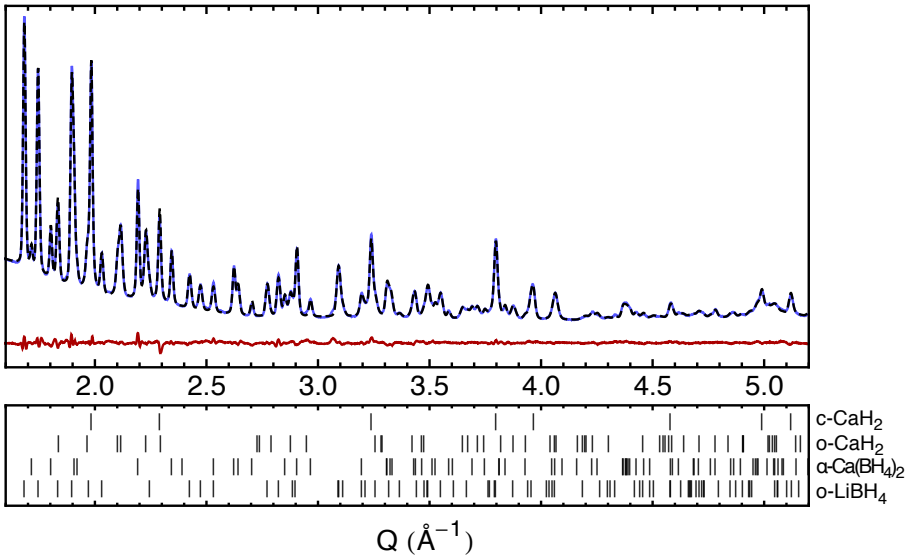

Figure 5.6: Synchrotron XRD data (from SNBL) and a Rietveld refinement of a black-coloured part of a $7/8LiBH_4$+$1/8Ca(BH_4)_2$ sample after it had been heat treated up to a temperature of 100 °C during the impedance spectroscopy measurements. The blue, solid line shows the measured data, the black, dashed line shows the Rietveld refinement of the data and the red, solid line on the bottom shows the difference between the measured data and the refinement. The Rietveld refinement reveals that the diffraction pattern consists of α-$Ca(BH_4)_2$, and the LT phase of $LiBH_4$, along with 3.6 wt% of orthorhombic CaH_2 and 4.2 wt% of cubic CaH_2 (in a CaF_2 crystal structure). No other phases were detected. The tick marks below the diffraction patterns show the locations of the diffraction peaks for the four phases according to the Rietveld refinement.

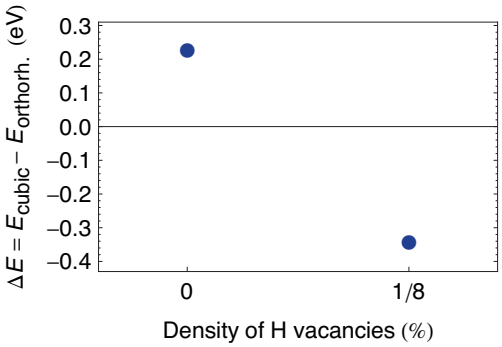

Figure 5.7: The calculated stability of cubic CaH_2 relative to orthorhombic CaH_2 for structures with no defects and for structures with a 1/8 density of charged hydrogen vacancies. The cubic structure is found to be more stable than the orthorhombic structure with the introduction of the H vacancies. The calculations were performed by Jón Steinar Garðarsson Mýrdal.

fluoride content, the relative stability of the orthorhombic and the cubic CaH_2 phases was calculated by Jón Steinar Garðarsson Mýrdal. The calculations were performed for structures with and without a 1/8 density of hydrogen vacancies. Calculations were carried out both for neutral vacancies and charged vacancies. In the case of neutral vacancies, a proton and an electron were removed from the cell. In the case of charged vacancies, only ap proton was removed from the cell, but a compensating positive background charge was smeared uniformly over the cell to prevent an infinite charge build-up over the periodic images of the cell. The results of the calculations without vacancies and with charged vacancies are shown in Figure 5.7. For the structures with no vacancies, orthorhombic CaH_2 is found to be more stable than cubic CaH_2 by 0.23 eV. However, when the hydrogen vacancies are introduced, cubic CaH_2 is found to be more stable than orthorhombic CaH_2 by 0.02 eV for neutral vacancies and 0.34 eV for charged vacancies. This indicates that for structures with crystal defects, cubic CaH_2 could form and probably coexist with orthorhombic CaH_2.

Note that the particular density of vacancies used for the calculations was simply chosen as a representative number for the possible density of defects in the structure, and is not based on experimental findings. The main goal of the calculations was to see if the presence of vacancies would increase the stability of the orthorhombic phase relative to the cubic phase. The actual density of defects in the structure, if any, cannot be determined using the experimental techniques presented here, but could be measured using neutron diffraction as a part of further studies on this subject.

5.4.3 XPS and SEM Measurements

To gain more information on the surface composition, chemical bonds and morphology of the black-coloured powder, X-ray photoelectron spectroscopy (XPS) measurements and Energy-Dispersive X-ray Spectroscopy (EDS) measurements were performed. The XPS measurements were performed at Uppsala University in Sweden by Reza Younesi, a post-doctoral fellow at DTU Energy Conversion. He also handled the analysis of the results. The EDS measurements were per-

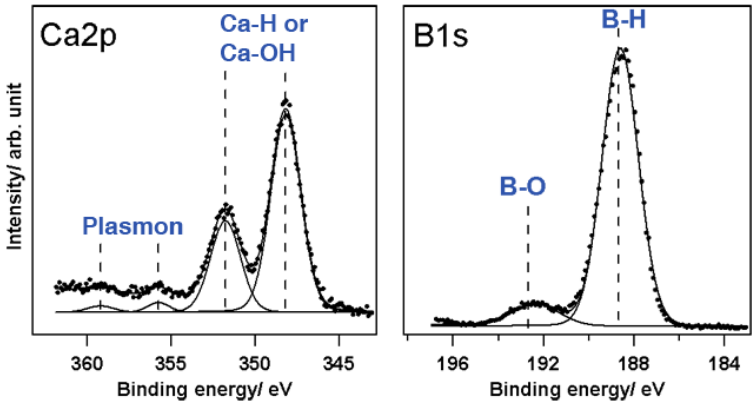

Figure 5.8: The XPS results for calcium and boron. The chemical bonds corresponding to the measured peaks are marked in the figure. **Left:** The binding energy of calcium bonds at the surface of the sample. Due to spin-orbital coupling, two peaks are observed for each bond type in calcium. The only observed chemical bonds of calcium are either Ca-H or Ca-OH bonds, and since the sample is not expected to contain oxygen (except possibly in very small amounts due to air contamination), we conclude that this binding energy corresponds to hydrogen bonds. The low peaks correspond to plasmon interactions, and no other chemical bonds of calcium are found. **Right:** Boron is almost exclusively found to have hydrogen bonds, although a small amount of oxygen bonds (related to impurities in the sample) is observed. The binding energy of B-B bonds is very similar to that of B-H bonds, and the possible presence of B-B bonds may thus be drowned out by the strong signal from the B-H bonds. The presence of elemental boron in the sample can therefore not be excluded based on these results.

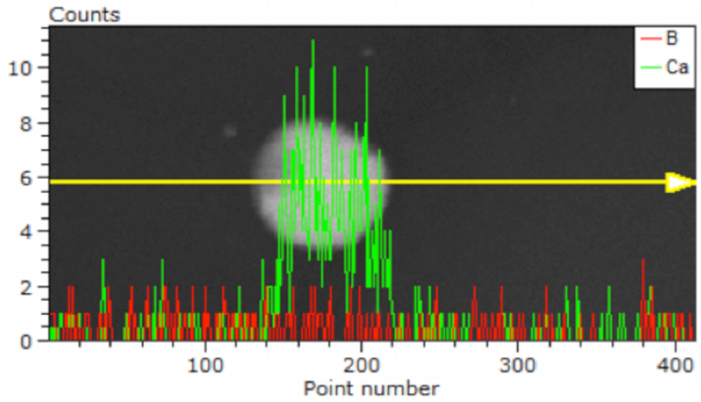

Figure 5.9: A SEM image of a black-coloured part of a $7/8LiBH_4+1/8Ca(BH_4)_2$ sample after heat treating it up to a temperature of 100 °C during the impedance spectroscopy measurements. Elemental mapping using EDS revealed that the bulk of the powder is a physical mixture of $LiBH_4$ and $Ca(BH_4)_2$, possibly along with some elemental boron, while areas that appear light gray in the were found to be calcium-rich. The light gray particle in the middle of the image is approximately 10 μm in diameter. The result of an elemental mapping line scan is shown. A clear increase in calcium concentration is detected at the position of the light gray area, but no increase in the concentration of boron (or any other element) is detected. Note that the EDS equipment cannot detect hydrogen or lithium. Also note that the colours of the SEM image do not represent the actual colours of the sample, and that the light gray area in the figure may thus well be black in reality.

formed using a scanning electron microscope (SEM) with the assistance of Marc Overgaard, a MSc student at DTU Energy Conversion. Further information about the XPS and the EDS measurements can be found in Paper C.

XPS measures the binding energy of atoms at or near the surface of the sample and thus yields information about which chemical bonds are present. Due to the low concentration of calcium atoms on the surface of the sample, it is difficult to analyze the results for Ca. The calcium is detected by looking at the p orbital, and due to spin-orbital coupling two peaks are observed for each type of bonds for calcium atoms. The two low intensity peaks between 355 eV and 360 eV do not denote chemical bonds, but originate from plasmon interactions. The two larger peaks between 345 eV and 355 eV represent one type of bond; Ca-H or Ca-OH bonds. Since the powder is expected to contain Ca-H bonds but no Ca-OH bonds, and since the XRD and EDS results do not suggest that Ca-OH bonds are present, we conclude that these two peaks correspond to Ca-H bonds. No other chemical bonds involving calcium are detected. This strongly suggests that the two CaH_2 phases are the only new calcium phases that have been formed in the sample during the heat treatment, and that no CaF_2 or amorphous phases are present.

The only chemical bonds of boron detected in the XPS measurements were B-H bonds and B-O bonds. A very small signal of the latter bond type was detected, most likely originating from slight impurities in the sample. It should, however, be noted that B-B bonds have a binding energy very similar to B-H bonds, and a possible signal from boron bonds may therefore be drowned out by the signal from hydrogen bonds. It can thus not be stated with certainty based on the XPS results that no elemental boron is present in the sample.

Figure 5.9 shows a SEM image of a black coloured part of $7/8LiBH_4{+}1/8Ca(BH_4)_2$ powder after the heat treatment during the impedance spectroscopy measurement. Elemental mapping of the microscope image was performed using the EDS technique. The bulk of the powder appears dark gray on the image and is found to have a rather constant concentration of both calcium and boron. This area is expected to be a physical mixture of $LiBH_4$ and $Ca(BH_4)_2$. The powder also contains small areas that appear light gray and were found to be calcium-rich. These areas are, however, not boron-rich, excluding the possibility that they consist of $Ca(BH_4)_2$. The EDS instrument is unfortunately not capable of detecting hydrogen, which is limiting for the conclusions that can be drawn from the SEM/EDS measurements in this study. But since the XPS results only indicate the presence of Ca-H bonds and no other bonds involving calcium, it is reasonable to assume that the calcium-rich areas in the SEM image are in fact CaH_2. It is of course also possible that these areas consist of pure calcium, but after the heat treatment this is not considered very likely. Although the EDS results are not strictly conclusive on their own, they are in good agreement with the XRD and XPS data, and strengthen the hypothesis that CaH_2 is formed.

5.4.4 The Part of Boron in the CaH_2 Formation Reaction

In the light of the combined results from XRD, calculations, XPS and EDS, we consider it very likely that the local environment in the powder, the heat treatment up to 100 °C and the direct contact of the $(1-x)LiBH_4{+}xCa(BH_4)_2$

sample with the lithium electrodes facilitates the formation of both orthorhombic and cubic CaH_2 with hydrogen defects. Further research would be needed to clarify the exact mechanism for such a formation. Note that it cannot be fully excluded that trace amounts of fluoride are present in this phase, and that it is in fact a $CaH_{2-x}Fx$ solid solution with a very small fluoride concentration. However, since the only source of fluoride would in this case be a TEFLON rig in the impedance spectroscopy experimental setup, with which the sample was never in direct contact, this is considered very unlikely. It can also not be excluded that some of the detected CaH_2 is indeed $Ca_{1-x}Lix H_{2-x}$, since the formation of the new phase takes place in close proximity with the Li electrodes. No indications of this could, however, be found in the Rietveld refinement of the diffraction pattern in Figure 5.6, and the formation of such a phase is not expected as LiH_2 and CaH_2 do not easily form a new compound, but rather form a eutectic mixture [118].

The two CaH_2 phases detected in the diffraction pattern in Figure 5.6 are expected to be a product of a reaction between some combination of $Ca(BH_4)_2$, $LiBH_4$ and/or Li. It must therefore be assumed that one or more phases containing the corresponding amount of boron are formed as well. No such phase is observed in the XRD data, and the formation of CaB_6 or some other phase containing the relatively highly scattering calcium atom is therefore not expected. As already mentioned, elementary boron would not necessarily be detectable in the diffraction pattern, and could be present although no diffraction peaks are assigned to it. Crystalline boron is black and could possibly be responsible for the black colour of the layers that form at the interface between the composites and the lithium electrodes. Its formation along with the formation of CaH_2 cannot be fully excluded. It must, however, be noted that elementary boron is considered very difficult to obtain, and is generally not observed as a reaction product of thermal decomposition of borohydrides below temperatures around 250 °C [119, 120]. Therefore, we do not consider it very likely that the majority of the boron atoms that become available during the reaction that forms CaH_2 go into the formation of elemental boron.

It is, on the other hand, considered very likely that diborane (B_2H_6) gas is released along with the formation of CaH_2. Diborane is typically released during thermal decomposition of borohydrides below 250 °C [68, 70, 121], but dissociates at that temperature [122]. It has proven difficult to avoid its formation in research on borohydrides for reversible hydrogen storage applications [120], and was very likely formed during this work as well. Its formation could not be observed with the experimental methods used in this work, but this could be addressed using mass spectroscopy in further studies on this topic. It should be noted that Fang *et al.* [111] state that no diborane is formed during thermal decomposition of the $LiBH_4$-$Ca(BH_4)_2$ composite, but because they do not report any release of hydrogen from the composite below 250 °C, such formation is not to be expected [65, 96]. Although the reaction responsible for the formation of CaH_2 in this work does not necessarily involve thermal decomposition of the borohydrides, we still consider it very likely that diborane is released during the formation of CaH_2, possibly along with the precipitation of some elemental boron.

5.4.5 A Possible Effect of CaH_2 Formation on the Conductivity

In the impedance spectroscopy measurements, the conductivity of the composites is in all cases found to be higher during cooling runs (see Figure 5.5), i.e after the samples have been heated to 100 °C in the impedance spectroscopy setup and the black powder discussed has formed. If one or both of the CaH_2 phases were electronically conducting, so that the resistivity of the layers in which they form were negligible compared to the resistivity of the $(1-x)LiBH_4+xCa(BH_4)_2$ composites, the contribution of the CaH_2 containing layers would not be visible in the impedance spectroscopy measurements. This also holds true if elemental boron is formed, as boron has an electronic conductivity of 0.1 mS/cm at room temperature, which is almost two orders of magnitude higher than the composite samples. Furthermore, since the thickness of the pelletised samples is used to estimate the conductivity of the composites (see Equation 2.30), the formation of such electronically conducting layers would result in a reduction of the effective thickness of the sample that can be related to the ionic conduction. Consequently, the measured pellet thickness d would no longer have the right value for Equation 2.30 and the ionic conductivity σ would be overestimated. With a continuing formation of such electronically conducting layers in the electrolyte, the pellet would eventually short circuit.

To investigate if this could be the case, and if the increased conductivity of the black layer could originate from the formation of CaH_2, the density of electron states for the two CaH_2 phases were calculated. The calculations were performed by Jón Steinar Garðarsson Mýrdal. Further details about the calculations can be found in Paper C. The band structure of cubic CaH_2 is shown in Figure 5.10. In the case of cubic CaH_2, the calculations were performed with no crystal defects and with a 1/8 density of hydrogen vacancies. The band gap of orthorhombic CaH_2 was calculated to be 5.84 eV and the band gap of defect-free, cubic CaH_2 was calculated to be 2.26 eV, which makes it a semi-conductor. These values are in good agreement with the results of Weaver et al. [123] who calculated the band structure of orthorhombic Ca_2 and a 'hypothetical' CaH_2

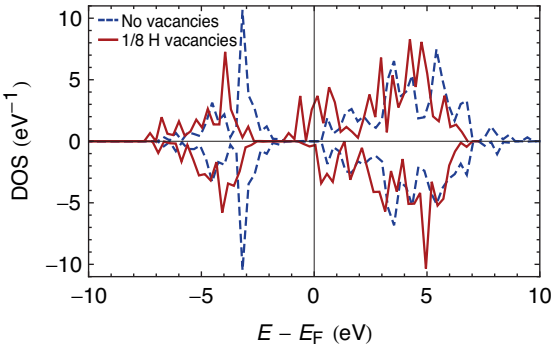

Figure 5.10: The calculated density of states of CaH_2 in the cubic CaF_2 crystal structure. E_F denotes the Fermi energy of the system. The results are shown for a structure without vacancies (blue, dashed lines), and for a structure with 1/8 density of negatively charged hydrogen vacancies (red, solid lines). In the structure containing vacancies, there are states that extend below the Fermi level, which suggests that the phase is electronically conducting.

phase with a cubic CaF_2 structure but a slightly smaller lattice parameter. Furthermore, as shown in Figure 5.10, cubic CaH_2 with 1/8 density of hydrogen vacancies has electronic states that reach below the Fermi level and is therefore electronically conducting, according to the calculations. This is the case both for charged (see Figure 5.10) and charge neutral vacancies. This could explain the increase in conduction of the samples that takes place upon the formation of CaH_2.

The total thickness of the two black layers in each pellet was, in most cases, estimated to be around 50% of the total thickness of the pellet. Assuming that Assuming that these layers are electronically conducting (with an electronic conduction that is much higher than the ionic conduction of the samples), one would expect the measured conductivity to double compared to the original pellet (according to Equation 2.30). A comparison of the conductivity values of the composite samples near room temperature before and after the heat treatment shows that this estimate is not far off. As an example, the conductivity of $3/4LiBH_4{+}1/4Ca(BH_4)_2$ at 35 °C is measured to be $6.4 \cdot 10^{-6}$ S/cm before the heat treatment and $1.21 \cdot 10^{-5}$ S/cm after the heat treatment, which is an increase by a factor of 1.9. If a thicker conducting layer were to be formed in the cell, or if the cells had a thinner layer of electrolyte to begin with, this effect would pose a serious risk of an internal short circuit in the cell.

The conclusion is therefore, that the measured conductivity after the heat treatment is always higher than prior to the heat treatment because of the unwanted formation of electronically conducting cubic CaH_2 with hydrogen defects near the lithium electrodes of the pelletised samples, and/or because of the possible formation of elemental boron. Further research will be needed to identify which of the two materials is responsible for the increased conduction, and to clarify if elemental boron is formed or not. This artifact, which arises due to a low chemical stability of the composites, poses a serious risk that the pelletised samples would eventually short-circuit with continued formation of the conducting layer. This observation is not encouraging for the idea of developing working battery cells containing the composite, but could nonetheless be of fundamental scientific interest. This finding furthermore highlights a serious general issue, namely that a slow formation of an electronically conducting layer in any solid electrolyte might eventually lead to a short-circuit. The chemical stability of any potential solid electrolyte material must therefore be investigated thoroughly before its introduction in commercial battery cells.

5.5 Summary of the Results on the $LiBH_4$-$Ca(BH_4)_2$ Composites

The $(1-x)LiBH_4{+}xCa(BH_4)_2$ composite forms a physical mixture of three phases, as measured with synchrotron x-ray diffraction; α-$Ca(BH_4)_2$, γ-$Ca(BH_4)_2$ and orthorhombic $LiBH_4$. The formation of a solid solution is not observed. Rietveld refinement of the diffraction patterns reveals that the relative fractions of the two $Ca(BH_4)_2$ phases changes considerably with $LiBH_4$ content, and γ-$Ca(BH_4)_2$ is found to be the dominant phase for $x \geq 0.5$. No β-$Ca(BH_4)_2$ is observed in the composite samples, although a third of the precursor $Ca(BH_4)_2$

powder had that crystal structure. Instead, a considerable fraction of the powder takes on the α-$Ca(BH_4)_2$ structure when small amounts $LiBH_4$ are added.

The formation of small amounts of two different phases of CaH_2 is observed upon heat treatment up to 100 °C during the impedance spectroscopy measurements. These are CaH_2 in its regular orthorhombic ($Pnma$) crystal structure and CaH_2 in a cubic (Fm-$3m$) CaF_2-type crystals structure. This result from the Rietveld refinement of synchrotron x-ray data is further supported by XPS and SEM/EDS data. The possibility of the formation of elemental boron is not excluded, and further research would be needed to clarify that. The relative stability of CaH_2 was calculated for both phases. The results indicate that cubic and orthorhombic CaH_2 with a 1/8 density of hydrogen defects are approximately equally stable, supporting the observed coexistence of the two phases.

As no hexagonal $LiBH_4$ was observed in the composites, the ionic conductivity of $(1-x)LiBH_4$+x$Ca(BH_4)_2$ is not as high as for example that of the $LiBH_4$+LiI solid solution (see section 4.4). Defects induced by ball milling do, however, increase the ionic conduction of orthorhombic $LiBH_4$ considerably ($4.6 \cdot 10^{-5}$ S/cm at 40 °C). The ionic conduction of $(1-x)LiBH_4$+x$Ca(BH_4)_2$ is, for all measured values of x, lower than that of the ball-milled $LiBH_4$. The $3/4LiBH_4$+$1/4Ca(BH_4)_2$ mixture has the best conductivity of the composites; $8.8 \cdot 10^{-6}$ S/cm at 40 °C and 1 mS/cm at 100 °C. Near room temperature, this is considerably lower than the conductivity target of 1 mS/cm, which is often mentioned as the minimum conductivity required for an electrolyte in a consumer battery. The composite, might, however, be of potential interest for battery applications at elevated temperatures.

It is not clear if lithium ions are the only charge carrier in the composites, or if calcium ions also participate in the conduction. The single-arc Nyquist plots and the slightly lower conductivity than ball-milled $LiBH_4$ suggest that Li^+ is the only charge carrier. However, the difference in the activation energy of the conduction between $LiBH_4$ and the composites indicates that the systems do not share the exact same conduction mechanism. Further work would be needed to clarify this.

The results of electronic band structure calculations for orthorhombic and cubic CaH_2, with and without hydrogen defects, indicate that the cubic structure with defects is electronically conducting. Elemental boron, if present, is also electronically conducting. This most probably explains the high conductivity observed for the heat-treated composites. The formation of an electronically conducting layer within the electrolyte in the cells is an unwanted artifact in the conductivity measurements, which increases the risk of short-circuiting in the cells. This finding reveals a more general issue that could be detrimental to other solid electrolytes and is thus of interest for further studies.

Chapter 6

$Li_4Ti_5O_{12}$ Batteries with a $LiBH_4$-LiI Electrolyte

All-solid-state batteries with lithium titanate positive electrodes and the $LiBH_4$-LiI solid solution as the electrolyte are the topic of Paper D. This chapter starts with a very short discussion of $LiBH_4$-LiI and lithium titanate as battery materials. The next section presents results on the electrochemical stability of $LiBH_4$-LiI, which was an important part of the decision to use lithium titanate for the positive electrodes. Section 6.3 shows the charge and discharge results of a cell with a liquid electrolyte, which are used for comparison with the results of the all-solid-state cells.

Section 6.4 presents and discusses the charge and discharge performance of the all-solid-state cells, as well as the resistance of the cells. In the same section, the development of the cell capacity and resistance is observed over 200 charge and discharge cycles, and the relationship between these two parameters is investigated. Lithium transfer through the solid electrolyte is discussed in section 6.5, in order to investigate which factors are limiting for the capacity of the cells. The last section of this chapter gives a summary of the results on the battery cells.

6.1 Lithium Titanate and the $LiBH_4$-LiI Solid Electrolyte

In my MSc project [46] and a during a large part of this PhD project, I have thoroughly investigated the crystal structure and the lithium ion conductivity of the $LiBH_4$-LiI solid solution (see Chapter 4 and Papers A and B). Considering the interesting results of that work, it was an important step for me to take the development of this solid electrolyte material to the next level by testing it in all-solid-state working battery cells. By doing so, the PhD project not only covers fundamental research on the properties of the solid solution, but also addresses the more practical matter of how it performs as an actual solid electrolyte. This report is, to my best knowledge, the first account of the usage of $LiBH_4$-LiI as an electrolyte in a working battery cell. It is very clear to me that many questions

are left unanswered in this chapter, but the main aim here is to provide a basic understanding of some of the advantages, limitations and challenges of this solid electrolyte material.

Working all-solid-state battery cells using $LiBH_4$ (without the addition of LiI) in the HT phase as an electrolyte and $LiCoO_2$ as a positive electrode has recently been reported by Takahashi *et al.* [124, 125]. They report that $LiBH_4$ has excellent chemical stability towards lithium metal negative anodes, but that it has a risk of decomposing if in contact with highly oxidative positive electrodes. This is due to the fact that $LiBH_4$ is a strong reducing agent, as already mentioned in section 4.1.1. In their work, the best results are obtained by coating the positive electrode with a very thin layer of Li_3PO_4 in order to protect it from reacting with $LiBH_4$. The reported charge and discharge measurements of this battery cell were, however, all performed at 120 °C, in order to obtain the highly conducting HT phase of $LiBH_4$.

In this work, lithium titanate ($Li_4Ti_5O_{12}$, also denoted LTO) was used as the positive electrode. It has a spinel type crystal structure (Fd-$3m$) and exhibits no volume change during the insertion of up to three Li^+ per formula unit [126]. This property is particularly advantageous for all-solid-state cells, as a large volume change during intercalation could lead to a loss of contact at the interface of the electrode and the electrolyte. $Li_4Ti_5O_{12}$ has a theoretical lithium insertion capacity of 175 mAh/g, with the intercalation reaction taking place at around 1.56 V vs. Li^+/Li. The open circuit voltage of the cells in this work is close to this value, and this relatively low voltage allows for the operation of the battery within the electrochemical stability window of $LiBH_4$-LiI, as discussed in the next section. Further information on the different kinds of cells discussed in this chapter can be found in section 3.4.2 and in Paper D.

6.2 Electrochemical Stability of $LiBH_4$-LiI

As mentioned in section 4.1.2, $LiBH_4$ has been shown to be electrochemically stable up to voltages of 5 V [87]. In order to investigate the electrochemical stability of the $LiBH_4$-LiI solid solution, cyclic voltammetry measurements were performed on a Steel | $LiBH_4$-LiI | Li cell containing 3/4$LiBH_4$ + 1/4 LiI. These measurements were performed by Rasmus Viskinde, a MSc student at DTU Energy Conversion [62]. The results of the measurements are shown in Figure 6.1. Almost no current is drawn in the voltage range of 0 - 2 V, indicating that the electrolyte is stable in this range. No increase in current flow was observed in the range of 0 - 3 V until towards the end of the third (and last) cycle in that range, during which a small increase in the current flow was observed. This indicates that the electrolyte may be unstable under prolonged exposure to voltages close to 3 V. In the voltage ranges of 0 - 4 V and 0 - 5 V, a considerable current flows. In the measurement from 0 ? 5 V, the observed current decreases with each cycle, indicating that a passivating process takes place.

During the measurement from 0 - 5 V, a total charge of $9.1 \cdot 10^{-3}$ C is found to accumulate in the system. A charge accumulation of this magnitude cannot be explained simply by capacitative effects in the cell [62]. It is therefore most likely that the charge accumulation during the measurements up to 4 V and 5

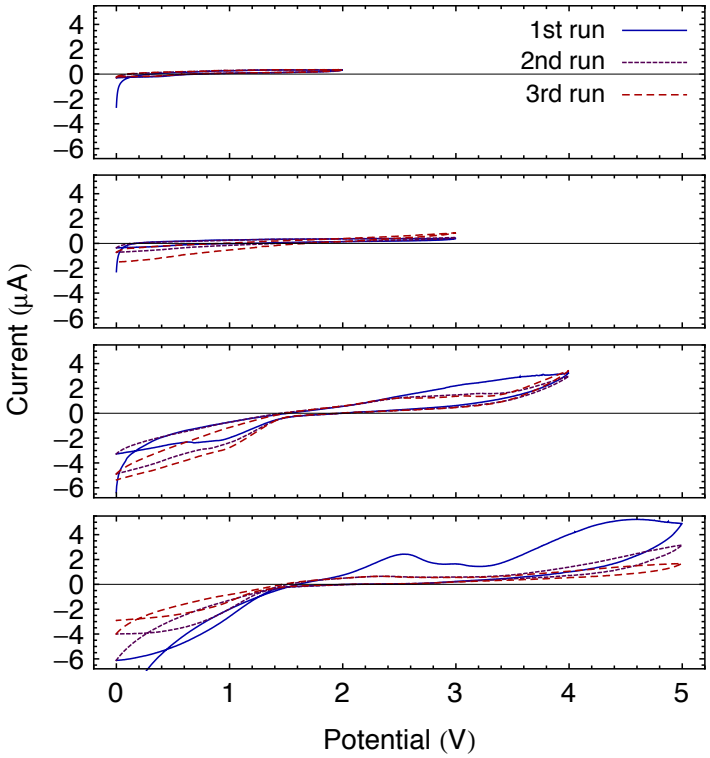

Figure 6.1: The results of a cyclic voltammetry measurement on a $3/4LiBH_4 + 1/4LiI$ solid solution. A scan rate of 1 mV/s was used. The open circuit voltage of the cell at the start of the measurement was 1.12 V. Each graph shows three consecutive measurement cycles. The first cycle is shown with a solid, blue line, the second cycle is shown with a purple, dashed line and the third cycle is shown with a dashed, red line. Very low current values are observed when potentials up to 3 V are applied. However, when potentials up to 4 V and 5 V are applied, a larger current flows, indicating electrolysis of the solid solution. It is considered most likely that this corresponds to an extraction of iodine from the electrolyte.

V occurs because of a decomposition of the electrolyte. Since pure $LiBH_4$ is electrochemically stable across a wider voltage range, it is most likely that it is iodine that begins to be drawn out of the solid solution already at a voltage of 3 V. It therefore seems that the operating voltage of batteries with $LiBH_4$-LiI as an electrolyte must be constrained to voltages smaller than 3 V.

In addition to the present work, the authors have also assembled all-solid-state batteries with $LiFePO_4$ as a positive electrode instead of LTO. Such cells have an open circuit voltage (OCV) of approximately 3.3 V. These cells did not accept charging, and after trying to charge, the OCV dropped to around 2 V. However, a short plateau at around 3.5 V was observed during the attempts to charge the cells. Interestingly, the standard hydrogen electrode potential for $I_{2\ (s)} + 2e^- \longleftrightarrow 2I^-$ is 0.54 V, and for $Li^+ + e^- \longleftrightarrow Li_{\ (s)}$ the standard potential is -3.04 V. This suggests that extraction of iodine from the electrolyte takes place close to a voltage of 3.5 V, which has also been reported to occur in similar systems [127, 128]. These observations on the $LiFePO_4$ cells strengthen our conclusion that operating voltages above 3 V should be avoided in cells

containing $LiBH_4$-LiI.

6.3 A LTO Battery with a Liquid Electrolyte

Cells containing a liquid electrolyte were measured for comparison with the all-solid-state cells. The assembly and measurements of this cell were carried out by Ane Sælland Christiansen, a fellow PhD student at DTU Energy Conversion. Figure 6.2 shows the results of the first seven discharge and charge cycles of a battery cell containing a liquid electrolyte. The LTO | $LiPF_6$ | Li cells have a discharge capacity corresponding to approximately 82% of the theoretical capacity and retain this capacity over the first seven cycles, at least. The cells have an open circuit voltage (OCV) of 1.56 V. Both the charge and the discharge curves are very flat. The overvoltage is very low, or on the order of 10 mV. This overvoltage can, at least partly, be explained by noting that $Li_7Ti_5O_{12}$ has a slightly lower conductivity that $Li_4Ti_5O_{12}$ [129]. The resistance of the cells is very low compared to the all-solid-state cells, or in the range of 10 - 100 Ω. The charge and discharge curves are highly reproducible, with only very small changes in capacity and overvoltage over the seven cycles. The excellent charge and discharge properties of this cell show that the experimental methods and the preparation of the LTO electrode work as expected, and provide a good reference point for the results on the all-solid-state cells presented in section 6.4.

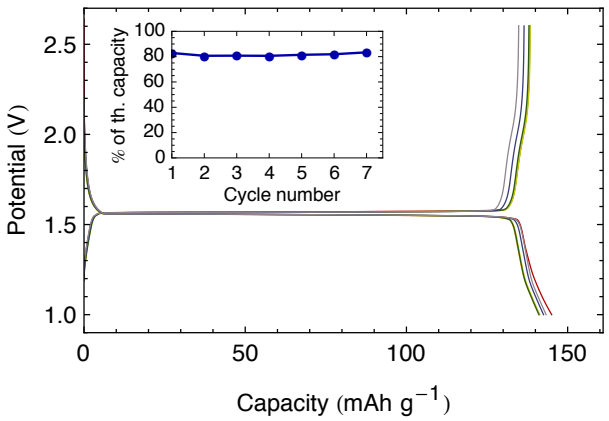

Figure 6.2: The first seven discharge/charge cycles of a LTO | $LiPF_6$ | Li battery. The measurement was performed at room temperature with a constant current of 10 μA. The inset shows the development of the discharge capacity with increasing discharge cycle number. The discharge capacity and the overvoltage do not change significantly during the first seven cycles.

6.4 Batteries with a $LiBH_4$-LiI Electrolyte

6.4.1 Charge and Discharge

The charge and discharge curves for the first ten cycles of a LTO | $LiBH_4$-LiI | Li cell are shown in Figure 6.3. During the second discharge, the cell has a discharge capacity of around 142 mAh/g, corresponding to 81% of its

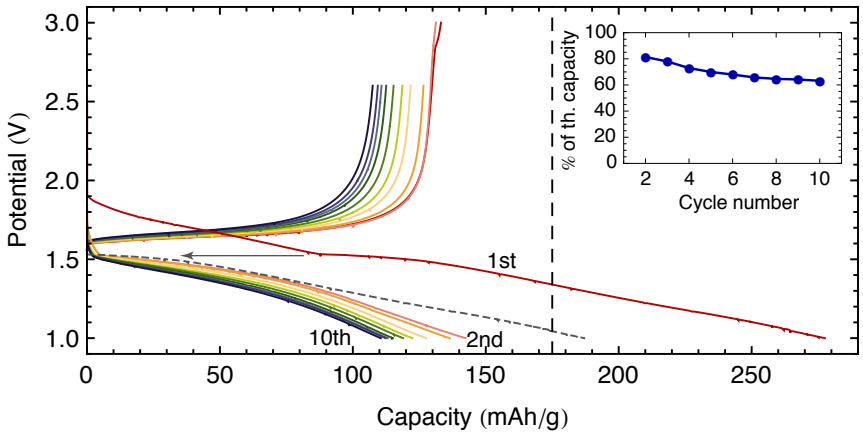

Figure 6.3: The first ten discharge and charge curves for a LTO | $LiBH_4$-LiI | Li battery cell. The measurements were performed at 60 °C with a constant current of 10 μA. During the first two charge runs, the upper voltage limit was set to 3.0 V, but was changed to 2.6 V for the remaining runs. The lower voltage limit was set to 1.0 V for all runs. A significant overvoltage and slope are observed, especially during discharge. The first discharge curve is much longer than the subsequent ones and continues until a capacity of 277 mAh/g is reached. The gray, dashed curve serves as a guide to the eye and shows how the first discharge curve would lie if it were translated to the left so that it starts from 1.54 V. The vertical, dashed line at 175 mAh/g indicates the full theoretical lithium ion intercalation capacity of the LTO positive electrode. The inset shows how the capacity, expressed as a percentage of the theoretical capacity, decreases with every discharge cycle, starting from the second discharge.

theoretical discharge capacity. This is similar to the discharge capacity of the LTO | $LiPF_6$ | Li cells. The performance of the all-solid-state cell does, however, differ considerably from the cell containing a liquid electrolyte (see Figure 6.2) in that it has a larger overvoltage, the curves have a steeper slope and a higher loss of capacity is observed with cycling. An average discharge capacity loss of 1.6% per cycle was observed for an all-solid-state cell that was charged and discharged 200 times (see section 6.4.5). One likely reason for the differences between the two cell types is that in the LTO | $LiPF_6$ | Li cell, the electrodes are soaked in the liquid electrolyte, but in an all-solid-state cell the electrodes have relatively well defined interfaces with the solid electrolyte. This is likely to cause contact issues that would increase the resistance to Li^+ transport in the all-solid-state cell, which in turn may reduce the charge and discharge performance of the cell.

6.4.2 The First Discharge Curve

As shown in Figure 6.3, the first discharge run is much longer than the successive discharge runs, and even greatly surpasses the theoretical discharge capacity of the cell. The presence of three distinct regions in the first discharge curve can be noted by observing the changes in its slope and shape. The first part of the curve lies above the expected open circuit voltage of the cell, and is therefore not expected to correspond to the intercalation of Li^+ in LTO, but rather to other electrochemical reactions or formation of interface layers in the cell. The curve has an almost constant slope until reaching 1.54 V, which is very close to the

expected open circuit voltage of the cell. Here the second region begins, as the slope of the curve changes and its shape becomes very similar to the shape of the subsequent discharge curves. This is indicated by the grey, dashed line in Figure 6.3, which is the first discharge curve shifted along the x-axis. This region is expected to correspond to the actual discharge of the cell, i.e. Li^+ intercalation in LTO. The third region of the first discharge curve begins at around 1.3 V, where the curve deviates from the shape of the subsequent discharge curves and again takes on a slope that is very similar to the slope of the first region.

The reason for this may be that the Li^+ intercalation reaction and the formation of the passivating layer possibly become concurring reactions at 1.3 V. In that case, the passivating layer formation may take over again during the last region of the curve. The total intercalation of Li^+ during the first discharge curve is thus expected to amount to approximately 140-150 mAh/g. The capacity exceeding this is expected to correspond to the electrochemical formation of new species close to the surface of the positive electrode, which may have a passivating effect.

This surprising finding was observed for the first discharge curves of all LTO | $LiBH_4$-LiI | Li cells measured during this work. This is, however, not observed for the LTO | $LiPF_6$ | Li cells, and is therefore expected to be related to the solid electrolyte. $LiBH_4$ is known to have a very good chemical stability towards lithium metal electrodes [124]. $LiBH_4$ is a strong reducing agent and is known to have a risk of reacting with oxidative positive electrodes, but we do not expect that $LiBH_4$ will reduce the LTO in the positive electrode at the potentials used in this work. The fact that more than 80% of the theoretical discharge capacity is available during the second discharge cycle supports the claim that $LiBH_4$ has not reacted with LTO during the first discharge run.

$LiBH_4$ does, however, react readily with water and oxygen. We do not consider it unlikely that trace amounts of atmospheric oxygen and/or moisture were present in the samples when the cells were assembled, although the assembly took place inside an argon-filled glove box. It is also possible that such impurities can enter the cell in trace amounts during its operation. When a potential is applied to the cells, those impurities would most likely oxidise $LiBH_4$ in an electrochemical redox reaction. In this reaction, charge would be transferred through the electrodes without any lithium intercalation in LTO taking place, which would explain how the first discharge can appear to have a capacity greatly exceeding the lithium intercalation capacity of the LTO electrode. The species formed in the reaction would form especially at the interface with the positive electrode. It should be noted that the mass of the electrolyte exceeds the mass of LTO in the cell by more than a factor of 100. The reaction of trace amounts of impurities with $LiBH_4$ can therefore easily have a large effect on the measured electron transport through the cell. Further research is needed in order to explain the behaviour during the first discharge with full certainty.

6.4.3 Coulombic Efficiency of the Cells

Each discharge curve in Figure 6.3 is slightly longer than the preceding charge curve. As a result, the Coulombic efficiency of the cell, defined in Equation 2.5, appears to be slightly higher than 100% for each cycle. A graph of the Coulombic

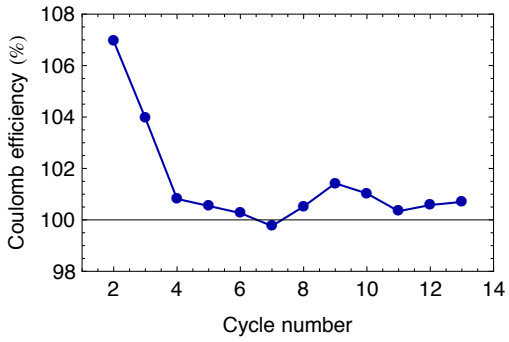

Figure 6.4: The Coulombic efficiency of a LTO | $LiBH_4$-LiI | Li cell. The Coulombic efficiency appears to be greater than 100% for each discharge, but this is most likely because a part of the charge that is transferred during discharge goes into the formation of an interface layer between the LTO electrode and the electrolyte. As a consequence, not all charge that is transferred takes part in the actual discharge of the cell by Li^+ intercalation into LTO.

efficiency as a function of cycle number is provided as supporting information. As discussed above, the measured charge transfer during the discharge run is a combination of the charge transfer due to the formation of a passivating areas and the charge transfer due to the intercalation of lithium ions in LTO. During charge, the current is reversed and less (if any) fraction of the charge contributes to the formation of the passivating areas. Because the formation of the passivating areas is a non-reversible process, the charge fraction that is used for the formation of those areas rather than for the lithium ion intercalation reaction appears as a Coulombic efficiency above 100% when calculated using Equation 2.5. The Coulombic efficiency thus gives an indication of the extent of the passivating layer formation during each cycle.

6.4.4 Cell Resistance

The impedance to lithium ion conduction in the cells was measured directly after assembling the cells as well as after each discharge. A Nyquist plot for a newly assembled cell is shown in Figure 6.5a. Nyquist plots measured after the ten first discharge cycles are shown in Figure 6.5b. Additional Nyquist plots, measured after each discharge of an all-solid-state cell that was charged and discharged 200 times, are provided as supporting information. The Nyquist plots were fitted using the equivalent circuit model discussed in section 2.3.3 and shown in Figure 2.10b, which is composed of an (RQ) circuit and a Randles circuit connected in series.

The large, high-frequency arc in each Nyquist plot was fitted with the (RQ) sub-circuit. The large arc of the newly assembled cell arises due to the impedance to lithium ion conduction through the bulk and the grain boundaries of the solid electrolyte, as discussed in section 4.4 and Paper A. The electrolyte is expected to have the largest impedance contribution of the cell components in the newly assembled cell, based on its thickness and lithium ion conductivity. The presence of smaller, additional arcs that completely overlap with the electrolyte contribution to the impedance can not be excluded, as it may not be possible to distin-

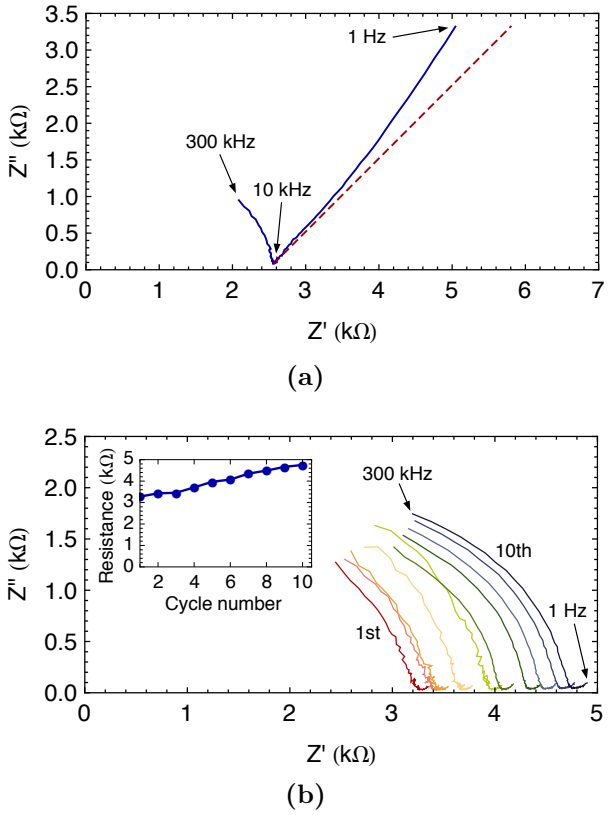

Figure 6.5: **a)** A Nyquist plot from an impedance spectroscopy measurement of a newly assembled LTO | $LiBH_4$-LiI | Li cell. The frequency ranges from 300 kHz to 1 Hz and decreases from left to right in the plot. Only the right side of the high-frequency impedance arc is visible in this frequency range, as higher frequencies than 300 kHz would be needed for the measurement to display the whole arc. The resistance of the cell is taken as the intercept of the arc with the Z' axis. The cell was measured in the charged state, i.e. before the first cell discharge. The impedance spectrum can be fitted using the equivalent circuit model in Figure 2.10b. The long tail arises due to diffusion and is described by the Warburg element. The diffusion is of a finite length and therefore the slope of tail increases towards its end. The red, dashed line has a slope of 45 °and is only drawn as a guide to the eye. **b)** Nyquist plots from impedance spectroscopy measurements of the LTO | $LiBH_4$-LiI | Li cell in Figure 6.3 after each of the first 10 discharge runs. The inset shows how the resistance increases with every discharge cycle.

guish them from the arc corresponding to the electrolyte in the Nyquist plots, as discussed in section 2.3.4. The long tail at the low frequency end in Figure 6.5a and the small tails at the low-frequency end of each Nyquist plot in Figure 6.5b are described by the Randles circuit. The Randles circuit describes an arc and a tail, and small arcs are most likely hidden within the tails in the Nyquist plots. As discussed in section 2.3.3, the circuit describes the impedance spectrum of a lithium intercalation electrode, i.e. the LTO electrode. The components in the circuit correspond to a lithium ion charge transfer resistance in the LTO electrode (R_{ct}), a double-layer capacitance at the LTO electrode interface (C_{dl}) and a finite-length diffusion of Li^+ to and from the reaction interface between

the LTO electrode and the electrolyte (W_d). No contribution to the impedance spectrum is observed from the lithium electrodes, as shown in section 4.4 and Paper A.

The impedance of the low-frequency tails in Figure 6.5b is smaller than that of the high-frequency arcs by approximately a factor of 100, and it proved difficult to obtain reliable values for the resistance R_{ct} in the equivalent circuit fits. Furthermore, the impedance of the large, high-frequency arcs in the Nyquist plots increases substantially with each charge and discharge cycle number, while the impedance of the low-frequency tails shows very small changes. Because of this, the small, constant contribution from the resistance R_{ct} is neglected in the following discussion and the cell resistance $R \approx R_{se}$ is taken to be the point of intersection between the Z' axis and the low-frequency end of the large arc. Using this approximation, the cell resistance after the first discharge is found to be around 3.2 kΩ. This is a very large resistance compared to the LTO | $LiPF_6$ | Li cell, but can be explained mostly by the fact that the conductivity of the $LiBH_4$-LiI solid solution at 60 °C is at least 12 times lower than that of 1 M $LiPF_6$ in EC:DMC [21].

Further evidence for the formation of passivating areas in the cell can be found by considering the Nyquist plots in Figure 6.5. Figure 6.5a shows that the cell has a considerably lower resistance (approximately 2.5 kΩ) in the newly assembled state than after it has been discharged once (approximately 3.2 kΩ). The plot also features a long tail with an initial slope of around 45 °and a slightly increasing slope with decreased frequency. As discussed earlier, the tail arises due to finite-length diffusion of lithium ions to the reaction surface of the LTO electrode and the electrolyte. This tail is not observed in any of the other impedance spectra, which suggests that the time dependence of this diffusion changes during the first discharge of the cell, so that it is not observed within the measured frequency range. This change in the diffusion time dependence, as well as the increase in resistance, could be explained by the formation of passivating areas in the cell during the first discharge. The impedance of those areas would not necessarily be identified in the impedance spectra of the discharged cell, because its contribution to the impedance could easily be overshadowed by the larger contribution from the electrolyte impedance.

The charge and discharge curves in Figure 6.3 do not exhibit flat plateaus, but all have a considerable slope. Towards the end of the curves, the discharge curves are observed to have a steeper slope than the charge curves. The slope can probably partially be explained by contact issues between the LTO electrode and the electrolyte. It is possible that during discharge, some channels across the electrode-electrolyte interface get blocked. This could for example happen if poorly conducting layers grow too thick and hinder the transport of lithium ions across the interface. This would make Li^+ intercalation in the LTO electrode increasingly difficult as the discharge proceeds. The increased slope towards the end of the discharge curves probably arises because it would be natural for Li^+ to first be intercalated into the areas of the LTO electrode that are in good contact with the electrolyte. As the discharge proceeds, the intercalation must take place in areas with ever less contact, resulting in an ever-greater overvoltage and consequently a steeper slope of the discharge curve. At the set potential limit of 1.0 V, this development is probably still taking place and some discharge

capacity remains in the cell. This may explain why there is not a sudden change in the slope of the discharge curves at the end of each discharge run, as there is for the charge runs.

6.4.5 The Relationship between Capacity and Resistance

The inset in Figure 6.3 shows how the discharge capacity of the LTO | $LiBH_4$-LiI | Li cell decreases with the number of charge and discharge cycles. Furthermore, the inset in Figure 6.5b shows how the cell resistance, as determined from the Nyquist plots, increases with the number of charge and discharge cycles. For a closer look at the correlation between the cell capacity and resistance, data from measurements of 200 charge and discharge cycles of a single LTO | $LiBH_4$-LiI | Li cell, shown in Figure 6.6 can be considered. Figure 6.6a shows the discharge capacity of the cell over 200 charge and discharge cycles. The capacity generally decreases with each cycle, with an average capacity degradation (see Equation 2.6) of 1.6% per cycle. The cell retains around 5% of its theoretical capacity after 200 cycles. Figure 6.6b shows the resistance of the cell after each discharge. The resistance generally increases with cycle number, and increases by more than a factor of 10 over 200 cycles. Figure 6.6c shows a plot of the discharge capacity of the cell as a function of its resistance. As seen the figure, the discharge capacity and the resistance values are highly correlated, with the plot of the two closely resembling a straight line. The Pearson product-moment correlation coefficient[1] of the two variables is $\rho_{c,R} = -0.975$, which indicates an almost linear negative correlation. The excellent correlation of the discharge capacity and the cell resistance strongly suggests that the development of both parameters with the number of charge and discharge cycles mostly has its roots in the same physical process in the cell.

The process that provides the most probable explanation for the correlation of the discharge capacity and resistance is a decrease in contact between the LTO electrode and the solid electrolyte with cycle number, and a possible formation of passivating areas in the cell that hinder lithium ion transport and intercalation. This can be explained as follows: The slope of each discharge curve, especially towards its end, governs how quickly the voltage limit of 1.0 V is reached upon discharge. The slope thus has a major influence on how large the discharge capacity of the cell will be. As discussed in sections 6.4.1 and 6.4.4, the slope is most likely a consequence of insufficient contact between the electrolyte and the LTO electrode or of the formation of passivating areas. The increase in slope with every discharge curve is probably due to further loss of contact areas on this interface or an increased growth of the poorly conductive areas. However, such loss of contact would also manifest as an increase in the measured resistance. If the effective contact area A between the electrolyte and one of the electrodes decreases, this leads to an increase in R (see Eq. 2.30), assuming that the thickness and the conductivity of the electrolyte material are constant. Thus,

[1] The Pearson product-moment correlation coefficient is a measure of the linear correlation of two variables x and y. It is defined as $\rho_{x,y} = \mathrm{cov}(x,y)/\sigma_x\sigma_y$, i.e. the covariance of the two variables divided by the product of their standard deviations. It takes on values ranging from -1 to 1, where 1 denotes full positive linear correlation, -1 denotes full negative linear correlation and 0 means no correlation.

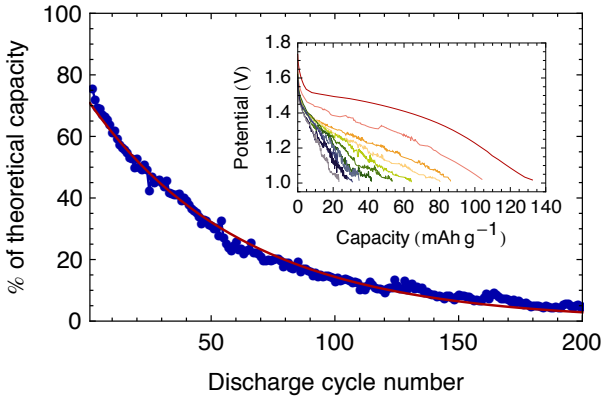

(a)

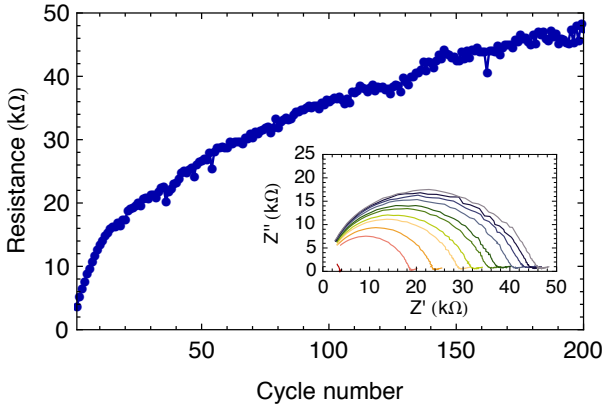

(b)

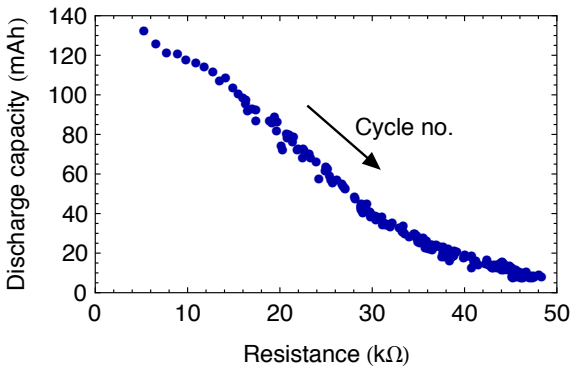

(c)

Figure 6.6: a) The development of the discharge capacity of a LTO | $LiBH_4$-LiI | Li cell over 200 discharge/charge cycles. The inset shows the discharge curves of every tenth measurement from cycles number 2 to 102. The red line is an exponential decay least-squares fit to the data. The average discharge capacity retention per cycle is 98.4%, which means a capacity degradation of 1.6% per charge-discharge cycle. **b)** The development of the cell resistance after discharge of the same cell as in a). The resistance increases by more than a factor of 10 over the course of 200 charge and discharge cycles. The inset shows the Nyquist plots of every 20th measurement from cycles number 1 to 191. **c)** The discharge capacity as a function of the cell resistance from a measurement of 200 charge and discharge cycles. The arrow indicates how the number of discharge cycles increases. The two variables follow a near-linear relationship, with a Pearson correlation coefficient of -0.975.

the loss of contact between the LTO electrode and the solid electrolyte most probably explains both the development of the cell resistance and of the discharge capacity with the number of cycles.

Using Equation 2.30, it can be estimated how much contact area would need to be lost (or rendered passive) on the electrode-electrolyte interface for such change to fully explain the increased cell resistance. In Figure 6.6b, the measured cell resistance is 3.65 kΩ after the first discharge, but has increased to 47.6 kΩ after the 200th discharge. This corresponds to a loss of 92% of the contact area between the LTO electrode and the electrolyte, assuming that all other contributions to the resistance remain constant. That assumption is, however, probably not strictly true, as other effects might contribute to an increase in the cell resistance. An example of this could be decreased grain boundary conduction within the electrolyte. The lithium ion conduction within the electrolyte is thought to take place at least partly along its internal grain boundaries, and a loss of such boundaries due to sintering (as the batteries operate at 60 °C for long periods of time) might somewhat decrease the lithium ion conductivity in the electrolyte (see section 4.4.2 and Paper A). Such contribution to an increased resistance would lower the estimated loss in contact area needed to account for the change in resistance. The contact issues and possible passivation issues do, however, probably mostly explain the excellent correlation observed between the increase in resistance and the decrease in discharge capacity. They are therefore thought to be the major factors in the development of the cell resistance with an increased number of charge and discharge cycles.

6.4.6 The Effect of Current Density on the Overvoltage

To see how the charge and discharge rate affects the performance of the all-solid-state cells, a LTO | $LiBH_4$-LiI | Li cell was charged and discharged using various current densities. As shown in Figure 6.7, the slope of the curves and

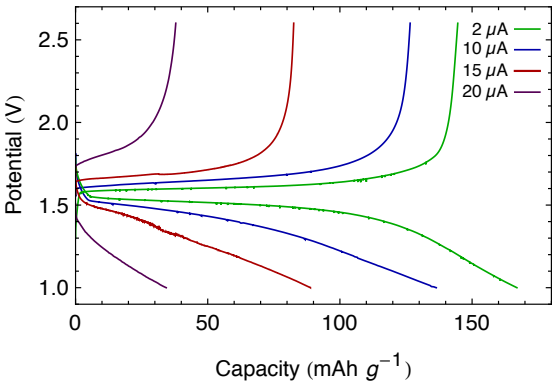

Figure 6.7: Charge and discharge curves of a LTO | $LiBH_4$-LiI | Li cell, measured for various charge rates. As expected, the overvoltage grows with increasing current, and correspondingly the capacity decreases. At a current of 2 μA, the charge and discharge curves are rather flat, but the curves quickly become steeper with increased current. This is most probably an indication that the conductivity in the cell, or the contact at the interface of the electrolyte and the LTO electrode, are not good enough to sustain higher currents than 10 μA without greatly compromising the performance of the cell.

the capacity of the cells are heavily dependent on the current density. This was somewhat expected, as battery overvoltage usually increases with increased operating current. It is, however, very interesting to see how flat the charge and discharge curves at 2 μA are, and that the cell reaches 96% of its theoretical discharge capacity at that rate. Such slow charge and discharge cycles were, however, considered unpractical for the measurements in this work, as one charge and discharge cycle at 2 μA takes up to 60 hours to complete. It is also interesting that increasing the operating current to 10 μA, which is the value used in all other measurements presented in this chapter, already has a substantial negative effect on the shape of the discharge curves and the capacity of the cell. At a current of 15 μA, the capacity of the cell is down to around 50% of the theoretical capacity. It should, however, be noted that these measurements were performed during subsequent charge and discharge cycles on a single cell, and the capacity of the cell is expected to decrease slightly with each cycle, as shown in Figure 6.3. This heavy dependence on the current density, even at the rather low current densities used in this work, is most probably a consequence of contact issues at the electrode-electrolyte interfaces and due to the large impedance of the cell compared to conventional battery cells.

6.5 Lithium Ion Transfer Through $LiBH_4$-LiI

To investigate which processes could be limiting for the capacity of the Li | $LiBH_4$-LiI | LTO cells, a galvanostatic signal was applied to a Steel | $LiBH_4$-LiI | Li cell. This cell can be viewed as a half-cell where the LTO electrode has been removed. Figure 6.8 shows the voltage over the cell as a function of capacity while a constant current of 10 μA was applied. Approximately 490 μAh of Li^+ are transferred, corresponding to a charge transfer of 1.76 C, before the voltage drops and the lithium ion transport stops. The lithium-steel interface was subsequently examined. It was clearly observed that a thin layer of lithium had been plated onto the steel electrode during the charge transfer. It is not clear why Li^+ transfer stopped at this point, but this could be due to contact issues between the electrodes and the solid electrolyte. Such issues could arise in the all-solid-state cell when a large number of Li have been removed from one side and deposited on the other, as the electrodes in such a cell are not soaked in a liquid electrolyte.

As already mentioned, the theoretical capacity of the LTO electrodes is 175 mAh/g. As discussed in section 6.4.1, it proved possible to reach 81% of this capacity by using LTO electrodes with a thickness of 3 μm and a mass of 0.37 mg. This capacity corresponds to a charge transfer of around 0.20 C. However, if the thickness of the electrode is increased, the percentage of the theoretical capacity that can be reached decreases. During this work, LTO | $LiBH_4$-LiI | Li cells with electrodes with a thickness of 140 μm and a mass of 17 mg were also assembled and measured. Interestingly, these cells only reached less than 5% of their theoretical capacity, corresponding to a charge transfer of around 0.4 C. Since the theoretical charge transfer capacity of these cells is around 9.5 C, one would expect them to transfer charge at least equal to that of the Steel | $LiBH_4$-LiI | LTO cells, or 1.76 C.

The observation that the charge transfer capacity in the all-solid-state cells is much greater without the LTO electrode than with it, leads to the conclusion that a capacity limiting process in the Li | $LiBH_4$-LiI | LTO batteries is on the LTO electrode side and most probably has to do with Li^+ intercalation in LTO. Such problems are not observed in the LTO | $LiPF_6$ | Li cell discussed in section 6.3, but in the all-solid-state cells, the LTO electrode is not soaked in the electrolyte. This could give rise to contact issues, which prevent the intercalation from taking place in LTO layers far away from the electrolyte-electrolyte interface. A formation of an inactive layer at the electrode-electrolyte interface could also lead to difficulties with lithium ion intercalation.

6.6 Summary of the All-Solid-State Battery Results

The $LiBH_4$-LiI solid solution has a conductivity close to 1 mS/cm at 60 °C and is a promising solid electrolyte material for all-solid-state lithium batteries. It is, however, not stable at potentials above 3 V, as observed using cyclic voltammetry measurements. Lithium titanate ($Li_4Ti_5O_{12}$) was used as a positive electrode in this work, both because it has an open circuit voltage against lithium of 1.56 V (i.e. well below 3 V), and because it shows virtually no volume expansion upon lithium intercalation.

The Li | $LiBH_4$-LiI | LTO battery cells measured for this work have an initial discharge capacity of around 142 mAh/g, which is around 81% of the theoretical capacity of LTO. This is very similar to a Li | $LiPF_6$ | LTO cell, which was measured for comparison and has a discharge capacity of around 82% of its theoretical capacity. The all-solid-state cells do, however, have a higher overvoltage and a steeper slope in the charge and discharge curves than the cell with the liquid electrolyte. Furthermore, their discharge capacity retention is worse than that of the liquid cell, and 1.6% of the capacity is lost on average during each charge/discharge cycle.

The resistance of the all-solid-state cells was measured after each discharge using impedance spectroscopy. The resistance is observed to be on the order of

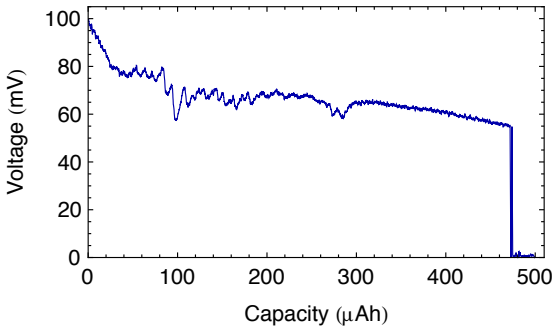

Figure 6.8: The voltage across a Steel | $LiBH_4$-LiI | Li cell during lithium ion transfer from the lithium electrode to the steel electrode (lithium plating on steel) at a constant current of 10 μA. Approximately 490 μAh of Li^+ are transferred, corresponding to a charge transfer of 1.76 C. This is almost nine times the amount of charge transfer observed in the LTO | $LiBH_4$-LiI | Li cells, which shows that lithium transfer through the electrolyte is not a limiting factor in the capacity of the all-solid-state battery cells.

a few kΩ, which is typically considered rather large in a battery cell. The electrolyte provides by far the largest resistance contribution of the cell components. Interestingly, there is an almost linear correlation between the development of the discharge capacity of the cells and the change in the measured resistance after discharge when the cells are charged and discharged numerous times. This indicates that the increased resistance is responsible for most of the loss in discharge capacity.

The most likely explanation for this is insufficient contact between the electrolyte and the LTO electrode, due to e.g. a rough interface with some empty space between the two components, and a possible formation of a passivating interface layer. This would hinder Li^+ intercalation into some areas of the interface and cause an increased overpotential at the LTO electrode. As each discharge proceeds, the most energetically favourable intercalation spots are filled up first and the intercalation process becomes increasingly difficult, causing an increased overvoltage. This leads to a steeper slope in the discharge curves, which in turn decreases the discharge capacity. Furthermore, such contact issues decrease the effective electrode area in the cell, causing an increase in the measured resistance. Due to the excellent linear correlation between the capacity and the resistance, it can be assumed that the contact issues between the electrolyte and the LTO electrode are mostly responsible for both the increase in cell resistance and the decrease in capacity as the cells are charged and discharged multiple times.

This work (and Paper D) is, to my best knowledge, the first report of a battery using the $LiBH_4$-LiI solid solution as an electrolyte. Further research is needed in order to better understand this battery cell, especially regarding the interface of the electrolyte and the positive electrode. The solid electrolyte is chemically well suited for use with the LTO electrodes, and it is chemically and electrochemically stable below 3 V. The cells show a very satisfactory initial discharge capacity and charging and discharging works rather well. Although there are many challenges related to the usage of this material in a battery, many of them could probably be solved by optimising the fabrication methods of the cells. More sophisticated techniques than mechanical pressing, such as deposition or cold rolling, could allow for a much thinner layer of electrolyte, thereby reducing the resistance of the cells substantially. Further research on the interface between the electrolyte and the LTO electrode will hopefully give better insight into the relevant processes and more knowledge about how to prevent contact issues from affecting the performance of the all-solid-state battery cells.

Chapter 7

Summary and Outlook

In this thesis I have presented the results of my research during the last three years. I have divided the results of into three chapters, and a summary of the findings has been given at the end of each chapter. It is not my intention to fully repeat those summaries here, but only to emphasise a few of the most important aspects of the work and briefly discuss the outlook of this research.

7.1 Summary of Main Results

During the PhD project I have, together with my co-workers, investigated solid lithium ion conducting materials with the aim of identifying and developing suitable solid electrolytes for all-solid-state lithium based batteries. This project has been focussed on metal borohydrides. I have intensively investigated the crystal structure, conductivity, conduction mechanism and battery performance of the $LiBH_4$-LiI solid solution, and have also searched for fast ionic conduction in other borohydrides. The main outcome of this work can be summarised as follows:

- The use of solid electrolytes could improve the safety, energy density and the cycle lifetime of lithium based batteries, and the highly Li^+ conducting $LiBH_4$-LiI solid solution is a promising material for that purpose.
- In this work the $LiBH_4$-LiI solid solution has been tested in working battery cells for the first time, showing that the solid solution is chemically stable towards lithium metal and $Li_4Ti_5O_{12}$ electrodes. Batteries containing the solid solution can be cycled up to 200 times, but with a significant overvoltage and capacity fade. The electrochemical stability of $LiBH_4$-LiI is found to be limited to potentials under 3 V.
- $LiBH_4$-LiI has a lithium ion conductivity close to 1 mS/cm at 60 °C, as measured using impedance spectroscopy. The conductivity of both pure $LiBH_4$ and the solid solutions is sensitive to LiI content and to changes in the microstructure of the powder due to ball milling and heat treatment.

Solid solutions with LiI content between 18% and 30% yield the highest conductivity near room temperature.

- The lithium ion conduction in $LiBH_4$-LiI mostly takes place in the hexagonal plane of the crystal structure and the formation of Frenkel pairs probably plays a major role for the conduction, as found by combining QENS and DFT. The conductivity of pure $LiBH_4$ and the solid solutions is found to increase with increased density of crystal defects, which implies that grain boundaries and dislocations are important for the conduction of lithium ions in the solid solution.

- No formation of a solid solution is observed in the $LiBH_4$-$Ca(BH_4)_2$ composite and its conductivity remains similar to that of pure $LiBH_4$. However, the formation of an electronically conducting cubic CaH_2 phase within the samples can occur during heat treatment, as observed using XRD, XPS, SEM/EDS and DFT. Continued formation of such a layer would eventually lead to a short circuit in the cell, revealing a more general issue that must receive attention in further development of solid electrolytes.

7.2 Outlook

All-solid-state battery technology has the potential of substantially improving the safety, energy density and cycle lifetime of lithium-ion batteries, but continued research efforts are needed to make this possible. It is especially important to gain a more detailed fundamental understanding of what governs the lithium ion conductivity of crystalline solids, and to use that knowledge for designing better solid-state lithium ion conductors. It is also important to find new methods for fabricating all-solid-state batteries so that contact problems at the electrode-electrolyte interfaces can be avoided.

Mixtures involving $LiBH_4$, the main subject of this thesis, currently meet some of the requirements for solid electrolyte materials listed in section 1.2.2, but not all. The $LiBH_4$-LiI solid solution has a negligible electronic conductivity, but its ionic conductivity is currently around one order of magnitude lower than the target of 1 mS/cm close to room temperature. It is chemically stable towards electrodes that are not highly oxidative, but an electrochemical stability limit of only 3 V limits the applications of $LiBH_4$-LiI as an electrolyte material. $LiBH_4$ is, however, a very interesting and versatile material, and I remain confident that further research on new material combinations involving $LiBH_4$ (but probably excluding iodine) can result in materials with adequate lithium ion conduction and excellent electrochemical stability. Continued research on its conduction mechanism could furthermore guide the way for discovering new and better lithium ion conductors. Last but not least, further test of battery cells containing $LiBH_4$ are needed to determine how its performance as an electrolyte may be optimised and to investigate its safety in a battery setting.

Solid electrolytes could e.g. be useful in lithium air batteries. A large, international research project on Li-air batteries is among the current battery research activities at DTU Energy Conversion. Li-air batteries could open up the possibility of batteries with energy densities up to ten times those of Li-ion

batteries, but the Li-air technology still faces a number of challenges [12, 130]. These include lithium dendride formation from the lithium metal electrode and the decomposition of liquid electrolytes at the interface of the positive electrode and the electrolyte. The usage of solid electrolytes in Li-air batteries could help to solve some of these challenges.

As mentioned in chapter 1, both Denmark and the EU have established ambitious aims of vastly increasing the share of sustainable energy in the next decades, and improved battery technology is needed to meet those targets. It is encouraging to see that battery research efforts are currently being increased in Denmark and elsewhere in Europe. Horizon 2020, the next EU framework program for research and innovation, started a few days before this was written and will hopefully provide opportunities for increased research on solid electrolytes and improved battery technology. Although the development of solid electrolytes will not resolve all challenges of lithium based batteries, and although batteries alone will probably not solve the whole challenge of finding new and efficient energy storage methods, it is my hope that all-solid-state batteries can form an important piece in the vast puzzle of moving towards a new era of sustainable energy usage.

Bibliography

[1] International Energy Outlook 2013. Technical report, U.S. Energy Information Administration, 2013.

[2] World Development Indicators 2013. Technical report, The World Bank, 2013.

[3] World Population Prospects: The 2012 Revision. Technical report, United Nations Department of Economic and Social Affairs, 2013.

[4] World Energy Outlook 2013. Technical report, International Energy Agency, 2013.

[5] Climate Change 2007: Synthesis Report. Contribution of Working Groups I, II and III to the Fourth Assessment Report of the Interngovernmental Panel on Climate Change. Technical report, International Panel on Climate Change, 2007.

[6] K. Richardson, W. Steffen, H. J. Schellnhuber, J. Alcamo, T. Barker, D. M. Kammen, R. Leemans, D. Liverman, M. Munasinghe, B. Osman-Elasha, N. Stern, and Ole Wæver. Synthesis Report: Climate Change: Global Risks, Challenges & Decisions. Technical report, University of Copenhagen, 2009.

[7] M. K. Hubbert. Nuclear Energy and the Fossil Fuels. Technical report, Shell Development Company, 1956.

[8] Towards a green economy in Europe: EU Environmental Policy Targets and Objectives 2010-2050. Technical report, European Environment Agency, 2013.

[9] Energy Strategy 2050 - From Oil and Gas to Green Energy. Technical report, The Danish Government, 2011.

[10] R. Schleicher-Tappeser. How renewables will change electricity markets in the next five years. *Energy Policy*, 48:64–75, 2012.

[11] M. Bazilian, I. Onyeji, M. Liebreich, I. MacGill, J. Chase, J. Shah, D. Gielen, D. Arent, D. Landfear, and S. Zhengrong. Re-considering the economics of photovoltaic power. *Renewable Energy*, 53:329–338, 2013.

[12] M. Armand and J.-M. Tarascon. Building better batteries. *Nature*, 451:652–7, 2008.

[13] W. I. F. David. Effective hydrogen storage: a strategic chemistry challenge. *Faraday Discussions*, 151:399–414, 2011.

[14] J.-M. Tarascon and M. Armand. Issues and Challenges Facing Rechargeable Lithium Batteries. *Nature*, 414:359–67, 2001.

[15] B. Scrosati, J. Hassoun, and Y.-K. Sun. Lithium-ion batteries. A look into the future. *Energy & Environmental Science*, 4:3287–3295, 2011.

[16] V. Etacheri, R. Marom, R. Elazari, G. Salitra, and D. Aurbach. Challenges in the development of advanced Li-ion batteries: a review. *Energy & Environmental Science*, 4:3243–3262, 2011.

[17] T. Vegge, P. Norby, and K. Edström. DTU International Energy Report 2013: Energy Storage Options for Future Sustainable Energy Systems. Technical report, Technical University of Denmark, 2013.

[18] John B. Goodenough and Y. Kim. Challenges for Rechargeable Li Batteries. *Chemistry of Materials*, 22:587–603, 2010.

[19] Plug-In Electric Vehicle Fire Incidents. *Wikipedia*. Viewed 17.12.2013. `http://en.wikipedia.org/wiki/Plug-in_electric_vehicle_fire_incidents`, 2013.

[20] Fact Sheet: Boeing 787 Battery Events Timeline. Technical report, Boeing, 2013.

[21] J. Y. Song, Y. Y. Wang, and C. C. Wan. Conductivity Study of Porous Plasticized Polymer Electrolytes Based on Poly(vinylidene fluoride) A Comparison with Polypropylene Separators. *Journal of the Electrochemical Society*, 147:3219–3225, 2000.

[22] P. Knauth. Inorganic Solid Li ion Conductors: An Overview. *Solid State Ionics*, 180:911–916, 2009.

[23] R. J. Brodd, W. Huang, and J. R. Akridge. Polymer Battery R&D in the U.S. *Macromolecular Symposia*, 159:229–245, 2000.

[24] M. Park, X. Zhang, M. Chung, G. B. Less, and A. M. Sastry. A Review of Conduction Phenomena in Li-Ion Batteries. *Journal of Power Sources*, 195:7904–7929, 2010.

[25] A. Rabenau. Lithium Nitride and Related Materials, Case Study of The Use of Modern Solid State Research Techniques. *Solid State Ionics*, 6:277–293, 1982.

[26] A. G. Belous, G. N. Novitskaya, S. V. Polyanetskaya, and Y. I. Gornikov. No Title. *Izvestiya Akademii Nauk SSSR*, 23:470–472, 1987.

[27] Y. Inaguma, C. Liquan, M. Itoh, T. Nakamura, T. Uchida, H. Ikuta, and M. Wakihara. High Ionic Conductivity in Lithium Lanthanum Titanate. *Solid State Commun.*, 86:689–693, 1993.

[28] K.-Y. Yang, K.-Z. Fung, and I.-C. Leu. Study on the Structural Change and Lithium Ion Conductivity for the Perovskite-Type $LaAlO_3$-$La_{0.50}Li_{0.50}TiO_3$ Solid Solution. *Journal of Alloys and Compounds*, 438:207–216, 2007.

[29] O Bohnke. The Fast Lithium-Ion Conducting Oxides $Li_{3x}La_{2/3-x}TiO_3$ From Fundamentals to Application. *Solid State Ionics*, 179:9–15, 2008.

[30] V. Thangadurai, J. Schwenzel, and W. Weppner. Tailoring Ceramics for Specific Applications: A Case Study of the Development of All-Solid-State Lithium Batteries. *Ionics*, 11:11–23, 2005.

[31] H. Aono, E. Sugimoto, Y. Sadaoka, N. Imanaka, and G. Adachi. Electrical Property and Sinterability of $LiTi_2(PO_4)_3$ Mixed With Lithium Salt (Li_3PO_4 or Li_3BO_3). *Solid State Ionics*, 47:257–264, 1991.

[32] K. Arbi, J.M. Rojo, and J. Sanz. Lithium Mobility in Titanium Based Nasicon $Li_{1+x}Ti_{2-x}Al_x(PO_4)_3$ and $LiTi_{2-x}Zr_x(PO_4)_3$ Materials Followed by NMR and Impedance Spectroscopy. *Journal of the European Ceramic Society*, 27:4215–4218, 2007.

[33] P. G. Bruce and A. R. West. The A-C Conductivity of Polycrystalline LISICON, $Li_{2+2x}Zn_{1-x}GeO_4$, and a Model for Intergranular Constriction Resistances. *Journal of the Electrochemical Society*, 130:662–669, 1983.

[34] Noriaki Kamaya, Kenji Homma, Yuichiro Yamakawa, Masaaki Hirayama, Ryoji Kanno, Masao Yonemura, Takashi Kamiyama, Yuki Kato, Shigenori Hama, Koji Kawamoto, and Akio Mitsui. A Lithium Superionic Conductor. *Nature Materials*, 10:682–686, 2011.

[35] S. Stramare, V. Thangadurai, and W. Weppner. Lithium Lanthanum Titanates: A Review. *Chemi*, 15:3974–3990, 2003.

[36] A. D. Robertson, A. R. West, and A. G. Ritchie. Review of Crystalline Lithium-Ion Conductors Suitable for High Temperature Battery Applications. *Solid State Ionics*, 104:1–11, 1997.

[37] Research Progress: Next-Generation Secondary Batteries, 2013.

[38] R. A. Huggins. *Advanced Batteries: Material Science Aspects*. Springer, 2009.

[39] W. H. Bragg and W. L. Bragg. The Reflection of X-rays by Crystals. *Proceedings of the Royal Society of London A*, 88:428–438, 1913.

[40] P. Scherrer. Bestimmung der Größe und der inneren Struktur von Kolloidteilchen mittels Röntgenstrahlen. *Nachricthen von der Gesellschaft der Wissenschaften zu Göttingen*, 2:98–100, 1918.

[41] A. R. Stokes and A. J. C. Wilson. The Diffraction of X Rays by Distorted Crystal Aggregates-I. *Proceedings of the Physical Society*, 56:174–181, 1944.

[42] H. M. Rietveld. A profile refinement method for nuclear and magnetic structures. *Journal of Applied Crystallography*, 2:65–71, 1969.

[43] R. B. von Dreele. Rietveld Refinement. In R. E. Dinnebier, editor, *Powder Diffraction: Theory and Practice*, chapter 9, pages 266–281. Royal Society of Chemistry, 1st edition, 2008.

[44] A. C. Larson and R. B. von Dreele. Report LAUR 86-784, General Structure Analysis System (GSAS). Technical report, Los Alamos National Laboratory, 1994.

[45] J. Ross Macdonald and W. B. Johnson. Fundamentals of Impedance Spectroscopy. In E. Barsoukov and J. R. Macdonald, editors, *Impedance Spectroscopy: Theory, Experiment and Applications*, chapter 1, pages 1–26. Wiley-Interscience, 2nd edition, 2005.

[46] D. Sveinbjörnsson. *Metal Borohydrides for Hydrogen Storage and Solid Electrolytes*. Msc thesis, University of Copenhagen, 2010.

[47] S. M. Haile, D. L. West, and J. Campbell. The Role of Microstructure and Processing on the Proton Conducting Properties of Gadolinium-Doped Barium Cerate. *Journal of Materials Research*, 13:1576–1595, 1998.

[48] E. Barsoukov. Electrochemical Power Sources. In E. Barsoukov and J. R. Macdonald, editors, *Fundamentals of Impedance Spectroscopy*, chapter 4.5.1-4.5., pages 430–468. Wiley-Interscience, 2nd edition, 2005.

[49] J. E. B. Randles. Kinetics of Rapid Electrode Reactions. *Discussions of the Faraday Society*, 1:11–19, 1947.

[50] N. M. Beekmans and L. Heyne. Correlation Between Impedance, Microstructure and Composition of Calcia-Stabilized Zirconia. *Electrochimica Acta*, 21:303–310, 1976.

[51] H. Näfe. Ionic Conductivity of ThO_2- and ZrO_2-based Electrolytes Between 300 and 2000 K. *Solid State Ionics*, 13:255–263, 1984.

[52] M. Bée. *Quasielastic Neutron Scattering*. Adam Hilger, 1988.

[53] N. Jalarvo. *Quasielastic Neutron Scattering Study on the Dynamical Properties of an Aromatic Hydrogen Bond*. Phd thesis, Technical University of Berlin, 2005.

[54] P. Martelli, A. Remhof, A. Borgschulte, R. Ackermann, T. Strässle, J. P. Embs, M. Ernst, M. Matsuo, S.-I. Orimo, and A. Züttel. Rotational motion in LiBH4/LiI solid solutions. *The Journal of Physical Chemistry A*, 115:5329–5334, 2011.

[55] N. Verdal, T. J. Udovic, J. J. Rush, H. Wu, and A. V. Skripov. Evolution of the Reorientational Motions of the Tetrahydroborate Anions in Hexagonal LiBH4-LiI Solid Solution by High-Q Quasielastic Neutron Scattering. *Journal of Physical Chemistry C*, 117:12010–12018, 2013.

[56] C. T. Chudley and R. J. Elliott. Neutron Scattering from a Liquid on a Jump Diffusion Model. *Proceedings of the Physical Society*, 77:353–361, 1961.

[57] J. S. G. Mýrdal. *Computational Design and Characterization of New Battery Materials*. Phd thesis, Technical University of Denmark, 2013.

[58] A. Le Bail, H. Duroy, and J. L. Fourquet. Ab-Initio Structure Determination of LiSbWO by X-ray Powder Diffraction. *Materials Research Bullettin*, 23:447–452, 1988.

[59] M. Wojdyr. Fityk: A General-Purpose Peak Fitting Program. *Journal of Applied Crystallography*, 43:1126–1128, 2010.

[60] V. A. Dyadkin. SNBL Tool Box, Swiss-Norwegian Beam Lines at ESRF, Grenoble, France. Technical report, ESRF, 2012.

[61] A. P. Hammersley, S. O. Sveinson, M. Hanfland, A. N. Fitch, and D. Hausermann. Two-dimensional Detector Software: From Real Detector to Idealised Image or Two-Theta Scan. *High Pressure Research*, 14:235–248, 1996.

[62] R. Viskinde. *Electrode/Electrolyte Interfaces in an All-Solid-State Lithium Battery*. Msc thesis, 2013.

[63] V. F. Sears. Thermal-Neutron Scattering Lengths and Cross-Sections for Condensed Matter Research. Technical report, Chalk River Nuclear Laboratories, Chalk River, Ontario, Canada, 1984.

[64] J-Ph. Soulié, G. Renaudin, R. Černý, and Yvon. K. Lithium Boro-Hydride $LiBH_4$ Crystal Structure. *Journal of Alloys and Compounds*, 346:200–205, 2002.

[65] A. Züttel, S. Rentsch, P. Fischer, P. Wenger, P. Sudan, Ph. Mauron, and Ch. Emmenegger. Hydrogen Storage Properties of LiBH4. *J. Alloys Comp.*, 356-357:515–520, August 2003.

[66] J. K. Kang, S. Y. Kim, Y. S. Han, R. P. Muller, and W. A. Goddard. A candidate $LiBH_4$ for Hydrogen Storage: Crystal Structures and Reaction Mechanisms of Intermediate Phases. *Applied Physics Letters*, 87:111904, 2005.

[67] L. Mosegaard, B. Møller, J.-E. Jørgensen, U. Bösenberg, M. Dornheim, J. C. Hanson, Y. Cerenius, G. Walker, H. J. Jakobsen, F. Besenbacher, and T. R. Jensen. Intermediate Phases Observed During Decomposition of $LiBH_4$. *Journal of Alloys and Compounds*, 446-447:301–305, 2007.

[68] D. Blanchard, Q. Shi, C. B. Boothroyd, and T. Vegge. Reversibility of Al/Ti Modified $LiBH_4$. *Journal of Physical Chemistryd C*, 113:14059–14066, 2009.

[69] J. Lang, A. Gerhauser, Y. Filinchuk, T. Klassen, and J. Huot. Differential Scanning Calorimetry (DSC) and Synchrotron X-ray Diffraction Study of Unmilled and Milled $LiBH_4$: A Partial Release of Hydrogen at Moderate Temperatures. *Crystals*, 2:1–21, 2012.

[70] A. Züttel, A. Borgschulte, and S.-I. Orimo. Tetrahydroborates as new hydrogen storage materials. *Scripta Materialia*, 56:823–828, 2007.

[71] K. Miwa, N. Ohba, S.-I. Towata, Y. Nakamori, and S.-I. Orimo. First-Principles Study on Lithium Borohydride $LiBH_4$. *Physical Review B*, 69:1–8, 2004.

[72] E. Orgaz, A. Membrillo, R. Castañeda, and A. Aburto. Electronic Structure of Ternary Hydrides Based on Light Elements. *Journal of Alloys and Compounds*, 404-406:176–180, 2005.

[73] Z. Lodziana and T. Vegge. Structural Stability of Complex Hydrides: $LiBH_4$ Revisited. *Physical Review Letters*, 93:145501, 2004.

[74] Z. Lodziana and T. Vegge. Structural Stability of Complex Hydrides: $LiBH_4$ Revisited Comment: Lodziana and Vegge Reply. *Physical Review Letters*, 97:119602, 2006.

[75] J. S. Hummelshøj. *Computational Investigation and Design of Coordination Compounds for Hydrogen Storage*. Phd thesis, Technical University of Denmark, 2009.

[76] T. Ikeshoji, E. Tsuchida, T. Morishita, K. Ikeda, M. Matsuo, Y. Kawazoe, and S.-I. Orimo. Fast-Ionic Conductivity of Li^+ in $LiBH_4$. *Physical Review B*, 83:144301, 2011.

[77] P. C. Aeberhard. *Computational Modelling of Structure and Dynamics in Lightweight Hydrides*. Phd thesis, University of Oxford, 2012.

[78] P. C Aeberhard, K. Refson, and W. I. F. David. Molecular Dynamics Investigation of the Disordered Crystal Structure of Hexagonal $LiBH_4$. *Physical Chemistry Chemical Physics*, 15:8081–7, 2013.

[79] M. R. Hartman, J. J. Rush, T. J. Udovic, R. C. Bowman Jr., and S. J. Hwang. Structure and Vibrational Dynamics of Isotopically Labeled Lithium Borohydride Using Neutron Diffraction and Spectroscopy. *Journal of Solid State Chemistry*, 180:1298–1305, 2007.

[80] Y. Filinchuk and D. Chernyshov. Looking at Hydrogen Atoms with X-Rays: Comprehensive Synchrotron Diffraction Study of $LiBH_4$. *Acta Crystallographica A*, 63:240, 2007.

[81] Y. Filinchuk and D. Chernyshov. The Lightest Borohydride Probed by Synchrotron Diffraction: Experiment Calls for a new Theoretical Revision. *Journal of Physical Chemistry C*, 112:10579–10584, 2008.

[82] Y. Filinchuk, D. Chernyshov, and V. Dmitriev. Light Metal Borohydrides: Crystal Structures and Beyond. *Zeitschrift für Kristallographie*, 223:649–659, 2008.

[83] S. K. Callear, E. A. Nickels, M. O. Jones, M. Matsuo, P. P. Edwards, and W. I. F. David. Order and disorder in lithium tetrahydroborate. *Journal of Materials Science*, 46:566–569, 2011.

[84] M. Matsuo, Y. Nakamori, S.-I. Orimo, H. Maekawa, and H. Takamura. Lithium Superionic Conduction in Lithium Borohydride Accompanied by Structural Transition. *Applied Physics Letters*, 91:224103, 2007.

[85] V. Epp and M. Wilkening. Fast Li Diffusion in Crystalline $LiBH_4$ Due to Reduced Dimensionality: Frequency-Dependent NMR Spectroscopy. *Physical Review B*, 82:020301, 2010.

[86] V. Epp and M. Wilkening. Motion of Li^+ in Nanoengineered $LiBH_4$ and $LiBH-4$:Al_2O_3 Comparison with the Microcrystalline Form. *ChemPhysChem*, 14:3706–3713, 2013.

[87] M. Matsuo and S.-I. Orimo. Lithium Fast-Ionic Conduction in Complex Hydrides: Review and Prospects. *Advaced Energy Materials*, 1:161–172, 2011.

[88] H. Maekawa, M. Matsuo, H. Takamura, M. Ando, Y. Noda, T. Karahashi, and S.-I. Orimo. Halide-Stabilized $LiBH_4$, a Room-Temperature Lithium Fast-Ion Conductor. *Journal of the American Chemical Society*, 131:894–895, 2009.

[89] C. R. Schlaikjer and C. C. Liang. Ionic Conduction in Calcium Doped Polycrystalline Lithium Iodide. *Journal of the Electrochemical Society*, 118:1447–1450, 1971.

[90] H. Maekawa. Size-dependent ionic conductivity observed for ordered mesoporous alumina-LiI composite. *Solid State Ionics*, 175:281–285, 2004.

[91] H. Oguchi, M. Matsuo, J. S. Hummelshøj, T. Vegge, J. K. Nørskov, T. Sato, Y. Miura, H. Takamura, H. Maekawa, and S. Orimo. Experimental and Computational Studies on Structural Transitions in the LiBH4-LiI Pseudobinary System. *Applied Physics Letters*, 94:141912, 2009.

[92] R. Miyazaki, T. Karahashi, N. Kumatani, Y. Noda, M. Ando, H. Takamura, M. Matsuo, S. Orimo, and H. Maekawa. Room Temperature Lithium Fast-Ion Conduction and Phase Relationship of LiI Stabilized $LiBH_4$. *Solid State Ionics*, 192:143–147, 2011.

[93] L. H. Rude, Y. Filinchuk, M. H. Sørby, B. C. Hauback, F. Besenbacher, and T. R. Jensen. Anion Substitution in $Ca(BH_4)_2$-CaI_2 : Synthesis ,

Structure and Stability of Three New Compounds. *Journal of Physical Chemistry C*, 115:7768–7777, 2011.

[94] P. C. Aeberhard, S. R. Williams, D. J. Evans, K. Refson, and W. I. F. David. Ab initio Nonequilibrium Molecular Dynamics in the Solid Superionic Conductor $LiBH_4$. *Physical Review Letters*, 108:095901, 2012.

[95] K. Miwa, M. Aoki, T. Noritake, N. Ohba, Y. Nakamori, S.-I. Towata, A. Züttel, and S.-I. Orimo. Thermodynamical stability of calcium borohydride $Ca(BH_4)_2$. *Physical Review B*, 74:1–5, 2006.

[96] E. Rönnebro and E. H. Majzoub. Calcium borohydride for hydrogen storage: catalysis and reversibility. *Journal of Physical Chemistry B*, 111:12045, 2007.

[97] M. D. Riktor, M. H. Sørby, K. Clopek, M. Fichtner, F. Buchter, A. Züttel, and B. C. Hauback. In situ synchrotron diffraction studies of phase transitions and thermal decomposition of $Mg(BH_4)_2$ and $Ca(BH_4)_2$. *Journal of Material Chemistry*, 17:49394942, 2007.

[98] J.-H. Kim, S.-A. Jin, J.-H. Shim, and Y. W. Cho. Thermal decomposition behavior of calcium borohydride $Ca(BH_4)_2$. *Journal of Alloys and Compounds*, 461:L20–L22, 2008.

[99] M. Aoki, K. Miwa, T. Noritake, N. Ohba, M. Matsumoto, H. W. Li, Y. Nakamori, S.-I. Towata, and S.-I. Orimo. Structural and dehydriding properties of $Ca(BH_4)-2$. *Applied Physics A*, 92:601–605, 2008.

[100] M. D. Riktor, M. H. Sørby, K. Clopek, M. Fichtner, and B. C. Hauback. The identification of a hitherto unknown intermediate phase CaB_2H_x from decomposition of $Ca(BH_4)_2$. *Journal of Materal Chemistry*, 19:2754–2759, 2009.

[101] D. Blanchard, M. D. Riktor, J. B. Maronsson, H. S. Jacobsen, J. Kehres, D. Sveinbjörnsson, E. G. Bardají, A. Léon, F. Juranyi, J. Wuttke, B. C. Hauback, M. Fichtner, and T. Vegge. Hydrogen Rotational and Translational Diffusion in Calcium Borohydride from Quasielastic Neutron Scattering and DFT Calculations. *Journal of Physical Chemistry C*, 114:20249–20257, 2010.

[102] I. Llamas-Jansa, O. Friedrichs, M. Fichtner, E. G. Bardaji, A. Züttel, and B. C. Hauback. The Role of $Ca(BH_4)_2$ Polymorphs. *Journal of Physical Chemistry C*, 116:13472–13479, 2012.

[103] T. Noritake, M. Aoki, M. Matsumoto, K. Miwa, S. Towata, H.-W. Li, and S. Orimo. Crystal structure and charge density analysis of $Ca(BH_4)_2$. *Journal of Alloys and Compounds*, 491:57–62, 2010.

[104] Y. Filinchuk, E. Ronnebro, and D. Chandra. Crystal structures and phase transformations in $Ca(BH_4)_2$. *Acta Materialia*, 57:732–738, 2009.

[105] F. Buchter, Z. Lodziana, A. Remhof, O. Friedrichs, A. Borgschulte, P. Mauron, A. Züttel, D. Sheptyakov, G. Barkhordarian, R. Bormann, K. Clopek, M. Fichtner, M. Sørby, M. Riktor, B. Hauback, and S. Orimo. Structure of $Ca(BD_4)_2$ beta-phase from combined neutron and synchrotron X-ray powder diffraction data and density functional calculations. *Journal of Physical Chemistry B*, 112:8042–8048, 2008.

[106] F. Buchter, Z. Lodziana, A. Remhof, O. Friedrichs, A. Borgschulte, P. Mauron, and A. Züttel. Structure of the Orthorhombic γ-Phase and Phase Transitions of $Ca(BD_4)_2$. *Journal of Physical Chemistry C*, 113:17223–17230, 2009.

[107] P. C. Aeberhard, K. Refson, P. P. Edwards, and W. I. F. David. High-pressure crystal structure prediction of calcium borohydride using density functional theory. *Physical Review B*, 83:174102, 2011.

[108] A. Borgschulte, R. Gremaud, A. Züttel, P. Martelli, A. Remhof, A. Ramirez-Cuesta, K. Refson, E. Bardaji, W. Lohstroh, M. Fichtner, H. Hagemann, and M. Ernst. Experimental evidence of librational vibrations determining the stability of calcium borohydride. *Physical Review B*, 83:024102, 2011.

[109] R. Kanno, Y. Takeda, and O. Yamamoto. Ionic Conductivity of Solid Lithium Ion Conductors With the Spinel Structure: Li_2MCl_4 (M = Mg, Mn, Fe, Cd). *Material Research Bulletin*, 16:999–1005, 1981.

[110] J. Y. Lee, D. Ravnsbæk, Y. Lee, Y. Kim, Y. Cerenius, J. Shim, T. R Jensen, N. H. Hur, and Y. W. Cho. Decomposition Reactions and Reversibility of the $LiBH_4$-$Ca(BH_4)_2$ Composite. *Journal of Physical Chemistry C*, 113:15080–15086, 2009.

[111] Z.-Z. Fang, X.-D. Kang, J.-H. Luo, P. Wang, H.-W. Li, and S.-I. Orimo. Formation and Hydrogen Storage Properties of Dual-Cation (Li,Ca) Borohydride. *Journal of Physical Chemistry C*, 114:22736–22741, 2010.

[112] D. N. Batchelder and R. O. Simmons. Lattice Constants and Thermal Expansivities of Silicon and of Calcium Fluoride between 6 °and 322 °K. *The Journal of Chemical Physics*, 41:2324–2329, 1964.

[113] J.-F. Brice, A. Courtoist, and J. Aubry. Preparation de la solution solide hydrurofluoree $CaF_{2-x})H_x$ ($0 < x < 1{,}24$) etude structurale par diffraction des rayons x et par diffraction des neutrons. *Journal of Solid State Chemistry*, 24:381–387, 1978.

[114] J. Y. Lee, Y.-S. Lee, J.-Y. Suh, J.-H. Shim, and Y. W. Cho. Metal halide doped metal borohydrides for hydrogen storage: The case of $Ca(BH_4)_2$-CaX_2 (X=F, Cl) mixture. *Journal of Alloys and Compounds*, 506:721–727, 2010.

[115] H. Smithson, C. Marianetti, D. Morgan, A. Van der Ven, A. Predith, and G. Ceder. First-principles study of the stability and electronic structure of metal hydrides. *Physical Review B*, 66:144107, 2002.

[116] E. R. Pinatel, L. H. Rude, M. Corno, M. Kragelund, P. Ugliengo, T. R. Jensen, and M. Baricco. Thermodynamic Tuning of Calcium Hydride by Fluorine Substitution. *MRS Proceedings*, 1441:5–16, 2012.

[117] Bing Li, Yinwei Li, Kaifeng Yang, Qiliang Cui, Yanming Ma, and Guangtian Zou. Raman evidence of a new high-pressure phase in calcium hydride. *Journal of Physics: Condensed Matter*, 19:226205, 2007.

[118] C. E. Messer, J. C. Eastman, R. G. Mers, and A. J. Maeland. Ternary Perovskite Phases in Systems of Lithium Hydride with Barium, Strontium and Calcium Hydrides. *Inorganic Chemistry*, 2:776–778, 1964.

[119] G. Will and B. Kiefer. Electron Deformation Density in Rhombohedral α-Boron. *Zeitschrift für anorganische und allgemeine Chemie*, 627:2100–2104, 2001.

[120] O. Friedrichs, A. Remhof, A. Borgschulte, F. Buchter, S.-I. Orimo, and A. Züttel. Breaking the passivation–the road to a solvent free borohydride synthesis. *Physical Chemistry Chemical Physics*, 12:10919–10922, 2010.

[121] W. Grochala and P. P Edwards. Thermal decomposition of the non-interstitial hydrides for the storage and production of hydrogen. *Chemical Review*, 104:1283–1315, 2004.

[122] M. Söderlund, P. Mäki-Arvela, K. Eränen, T. Salmi, R. Rahkola, and D. Y. Murzin. Catalyst Deactivation in Diborane Decomposition. *Catalysis Letters*, 105:191–202, 2005.

[123] J. H. Weaver, M. Gupta, and D. T. Peterson. Electronic structure and bonding in CaH_2: Experiment and theory. *Solid State Communications*, 51:805–808, 1984.

[124] K. Takahashi, K. H., T. Yamazaki, K. Takada, M. Matsuo, S. Orimo, H. Maekawa, and H. Takamura. All-Solid-State Lithium Battery With $LiBH_4$ Solid Electrolyte. *Journal of Power Sources*, 226:61–64, 2013.

[125] K. Takahashi, H. Maekawa, and H. Takamura. Effects of intermediate layer on interfacial resistance for all-solid-state lithium batteries using lithium borohydride. *Solid State Ionics*, pages 3–6, 2013.

[126] T. Ohzuku, A. Ueda, and N. Yamamota. Zero-Strain Insertion Material of $Li[Li_{1/3}Ti_{5/3}]O_4$ for Rechargeable Lithium Cells. *Journal of the Electrochemical Society*, 142:1431–1435, 1995.

[127] R. D. Armstrong and K. Landles. Electrochemical behaviour of lithium iodide monohydrate. *Journal of Applied Electrochemistry*, 11:247–251, 1981.

[128] R. D. Armstrong. The electrochemical behaviour of lithium iodide monohydrade and lithium bromide monohydriate. *Solid State Ionics*, 5:397–398, 1981.

[129] D. V. Safronov, S. A. Novikova, A. M. Skundin, and A. B. Yaroslavtsev. Lithium intercalation and deintercalation processes in $Li_4Ti_5O_{12}$ and $LiFePO_4$. *Inorganic Materials*, 48:57–61, 2012.

[130] G. Girishkumar, B. McCloskey, A. C. Luntz, S. Swanson, and W. Wilcke. Lithium-Air Battery: Promise and Challenges. *Journal of Physical Chemistry Letters*, 1:2193–2203, 2010.

Appendix A

Articles

Paper A

THE JOURNAL OF PHYSICAL CHEMISTRY C

Article

pubs.acs.org/JPCC

Effect of Heat Treatment on the Lithium Ion Conduction of the $LiBH_4$–LiI Solid Solution

Dadi Sveinbjörnsson,[†] Jon Steinar Gardarsson Myrdal,[†,‡] Didier Blanchard,[†] Janet Jonna Bentzen,[†] Takumi Hirata,[§] Mogens Bjerg Mogensen,[†] Poul Norby,[†] Shin-Ichi Orimo,[§] and Tejs Vegge*[,†]

[†]Department of Energy Conversion and Storage, Technical University of Denmark, Frederiksborgvej 399, P.O. Box 49, DK-4000 Roskilde, Denmark

[‡]Center for Atomic-Scale Materials Design, Department of Physics, Technical University of Denmark, Anker Engelunds Vej 1, DK-2800 Lyngby, Denmark

[§]Institute for Materials Research, Tohoku University, 2-1-1 Katahira, Aoba-ku, Sendai 980-8577, Japan

Supporting Information

ABSTRACT: The $LiBH_4$–LiI solid solution is a good Li^+ conductor and a promising crystalline electrolyte for all-solid-state lithium based batteries. The focus of the present work is on the effect of heat treatment on the Li^+ conduction. Solid solutions with a LiI content of 6.25–50% were synthesized by high-energy ball milling and annealed at 140 °C. Powder X-ray diffraction and scanning electron microscopy were used for characterizing the samples and for comparing their crystallite sizes and the density of defects before and after the annealing. The Li^+ conductivity was measured using impedance spectroscopy, resulting in conductivities exceeding 0.1 mS/cm at 30 °C and 10 mS/cm at 140 °C. It was found that the formation of defect-rich microstructures during ball milling increased the specific conductivities of these compounds significantly. The phase transition temperatures between the orthorhombic and hexagonal structures of $LiBH_4$ were measured using differential scanning calorimetry (DSC). The measured transition temperatures range from 100 to −70 °C and show a linear decrease of 70 °C for every 10% of LiI addition up to a LiI content of 25%. The relative stability of the two structures was calculated using density functional theory, and together with the DSC measurements, the calculations were used to evaluate the change in entropic difference between the structures with LiI content.

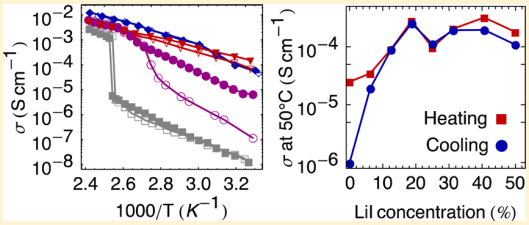

1. INTRODUCTION

Lithium battery research is growing ever more important as the need for more efficient and more sustainable methods for energy storage continues to grow rapidly. This is in particular true for the energy and transportation sectors. Today, the primary application of lithium batteries is in the portable electronics sector. But, when it comes to applications in systems on a larger scale, existing battery technologies fall short on price, energy density, safety, and charge–discharge cycle lifetime. Commercial Li ion batteries use flammable organic liquid or gel electrolytes. Their main attractive property is their high Li^+ conductivity. Examples of such electrolytes include 1 M $LiPF_6$ in EC-DMC (organic liquid, 12 mS/cm at 27 °C),[1] 1 M $LiBF_4$–$EMIBF_4$ (ionic liquid, 9 mS/cm at 27 °C)[2] and 1 M LiPF6 in EC-DMC and PVDF-HFP (gel, 3 mS/cm at 27 °C).[1] However, the main disadvantage of such electrolytes is their inflammability, which causes safety issues that only grow worse as the demands on the energy density of the systems increase.[3,4] Furthermore, the usage of liquid or gel electrolytes can result in diminished cell capacity and limited charge–discharge cycle life due to dendrite formation at the electrode–electrolyte interface.[5]

Replacing the currently used liquid and gel electrolytes with solid-state electrolytes would enhance the safety and extend the cycle life of the batteries. However, designing a suitable solid electrolyte material with sufficient chemical and electrochemical stability, as well as offering a sufficiently high lithium ion conduction and negligible electronic conduction, remains a challenge.[6]

Various types of crystalline solid-state Li^+ conducting materials are known.[3] Among these are Li_3N,[7] perovskite type oxides such as lithium lanthanum titanate (LLTO),[8−11] garnet-type structures such as $Li_6BaLa_2Ta_2O_{12}$,[12] NASICON-type structures,[13,14] LISICON-type structures,[15] and $Li_{10}GeP_2S_{12}$.[16] However, there are some problems with the usage of many of these materials as solid electrolytes in lithium batteries. The decomposition voltage of Li_3N is too low for practical use. LLTO and NASICON are not stable in contact with elemental lithium, and reducible Ti_4^+ ions make the electronic conductivity of LLTO too high.[17] The Li^+

Received: October 10, 2012
Revised: January 18, 2013
Published: January 30, 2013

   dx.doi.org/10.1021/jp310050g | J. Phys. Chem. C 2013, 117, 3249–3257

conductivity of LISICON is rather low and in some cases decreases with time.[18]

A Li^+ conductivity of at least 1 mS/cm is often mentioned as the minimum conductivity required for an electrolyte to work well in consumer batteries.[19,20] The conductivity of the above-mentioned crystalline solid electrolytes is considerably lower than this, with the exception of $Li_{10}GeP_2S_{12}$ that has a Li^+ conductivity of 12 mS/cm at 27 °C.[16] The search for other crystalline electrolyte materials with Li^+ conductivities above 1 mS/cm is of both fundamental and practical interest for secondary lithium battery research.

Lithium borohydride, $LiBH_4$, is lightweight (0.666 g/cm^3) and has been investigated extensively as a possible hydrogen storage material.[21−27] In recent years, lithium borohydride has also gained increased attention as a potential crystalline solid electrolyte material for lithium batteries.[28−30] At room temperature, $LiBH_4$ has a poorly Li^+ conducting orthorhombic crystal structure (*Pnma*, approximately 10^{-8} S/cm at 30 °C), but around 110 °C, it undergoes a reversible structural transition to a highly Li^+ conducting hexagonal structure ($P6_3mc$, approximately 1 mS/cm at 120 °C).[28,31] In the following, the two polymorphs will be referred to as the LT phase (orthorhombic) and HT phase (hexagonal), respectively. $LiBH_4$ is an electrical insulator in both structures, with calculations showing a large band gap of approximately 6.7 eV.[32,33] A working all-solid-state battery cell using $LiBH_4$ in the HT phase as an electrolyte has recently been reported.[34]

The HT phase of $LiBH_4$ can be stabilized at room temperature by adding lithium halides (LiI, LiBr, and LiCl), with the LiI addition giving the best Li^+ conduction results.[35] It should be noted that the low-temperature modification of LiI below 0 °C, known as β-LiI, has a $P6_3mc$ structure[36] and is thus isostructural with the HT phase of $LiBH_4$. The $LiBH_4$−LiI system forms a solid solution,[37] and studies on its structure and properties have recently been published. Rude et al.[38] have investigated the $LiBH_4$−LiI solid solution as a hydrogen storage material, and Miyazaki et al.[39] have studied its properties as a Li^+ conductor.

In the present work, we present a systematic study on the $(1 - x)LiBH_4+xLiI$ solid solutions: on their crystalline structure, Li^+ conduction properties, relative phase stabilities, and phase transition temperatures for a wide range of LiI content x. In a continuation and complementary to the work of Miyazaki et al.,[39] the present work provides a thorough understanding of the correlations between LiI content, microstructure, and Li^+ conductivity, as well as addressing phase stabilities and entropic behavior. The aim is both to provide a fundamental understanding of the microstructural properties of the solid solution and to address the more practical question of how its Li^+ conductivity can be optimized. The results are based both on experimental work and on density functional theory calculations.

2. EXPERIMENTAL SECTION

2.1. Synthesis. $LiBH_4$ powder (purity 95%) and LiI beads (purity 99%) were purchased from Alfa Aesar Co. The $(1 - x)LiBH_4+xLiI$ samples were synthesized by planetary ball milling under Ar atmosphere. Pure $LiBH_4$ was also ball milled for comparison. In each milling, a stainless steel vial with an inner volume of 250 mL was rotated at 650 rpm for 2 h using a Fritsch Pulverisette P6. A total of 2 g of precursor powder was inserted into the vial for each milling. Twenty-five tungsten carbide balls were used, and the sample to ball mass ratio was 1/100. No contamination from the milling vial or the balls was found in the diffraction patterns of the milled samples.

For the sample used in the impedance spectroscopy temperature cycling measurement (see Figure 7), the procedure was the same as described above, except that a total of 0.5 g of precursor powder was rotated in a 45 mL vial on a Fritsch Pulverisette P7. Here, the sample to ball mass ratio was 1/180.

2.2. Powder X-ray Diffraction. After ball milling, the samples were characterized using a Cu Kα Bruker D8 diffractometer with a Bragg−Brentano geometry and a LynxEye detector, operating at 40 kV and 40 mA. All X-ray diffraction (XRD) measurements were performed at room temperature and under Ar atmosphere using an airtight polyethylene sample holder from Bruker Co. The exposure time was 3 s/step with a step size of 0.02°. The measurements were performed using a variable slit size. After the measurement, the data intensity was corrected for the variable slit size and the Kα2 signal was subtracted.

A fraction of each sample was annealed in a furnace at 140 °C for 70 h. XRD measurements were subsequently performed on the annealed powder in order to detect, by comparison with the nonannealed powder, the anticipated sintering effect of the heat treatment.

The diffraction peak positions were found using the GSAS refinement software. The full width at half-maximum (fwhm) of the diffraction peaks was calculated using the peak fitting software FITYK.[40] The contributions to the fwhm from the crystallite size and from the crystallographic defects were separated by fitting the size and strain parameters in

$$B(\theta) = \sqrt{\left(\frac{k\lambda}{D\cos\theta}\right)^2 + (4\eta\tan\theta)^2 + {B_0}^2} \quad (1)$$

to the measured fwhm values in each diffractogram. This expression for the peak broadening is a combination of the Scherrer equation for size broadening[41] and the Stokes and Wilson expression for strain broadening,[42] where D is the average crystallite size and η is the strain. The shape factor k was assumed to be 0.9, and the instrumental broadening B_0 was 0.01.

2.3. Scanning Electron Microscopy. The microstructure was characterized using a JEOL 840 scanning electron microscope (SEM) with an acceleration voltage of 10 kV. The samples were transferred under vacuum from the glovebox to the microscope using a portable vacuum transference system.

2.4. Impedance Spectroscopy. The conductivity of the samples was determined by AC impedance spectroscopy using a PARSTAT 2273 potentiostat. The ball-milled powder was pressed into pellets with a diameter of 13 mm and a thickness of approximately 2.5 mm. Lithium foil was placed onto both faces of the pellets as electrodes. The powder and the lithium foil were pressed simultaneously at 1 ton/cm^2. The porosity of the pellets was estimated to be around 0.5. All preparation and measurements were carried out under Ar atmosphere. The frequency range of the impedance measurements was set from 100 mHz to 1 MHz. The samples were heated up from 30 to 140 °C in steps of 5 or 10 °C and then cooled back down to 30 °C using the same step size. The samples were equilibrated at a constant temperature for at least 40 min prior to each measurement.

For the measurement of the conductivity of the $^1/_2LiBH_4+^1/_2LiI$ sample during five heating and cooling cycles (see Figure 7), a Hioki 3532-80 potentiostat was used, and the

dx.doi.org/10.1021/jp310050g | J. Phys. Chem. C 2013, 117, 3249−3257

pellet dimensions were 8 mm in diameter and 0.9 mm in thickness.

2.5. Differential Scanning Calorimetry. The phase transition temperatures of the $(1 - x)LiBH_4+xLiI$ samples were determined by differential scanning calorimetry (DSC), using a Netzsch DSC 200 F3 calorimeter. For each measurement, 10 mg of sample was sealed in an aluminum crucible under Ar atmosphere. The samples were heated from room temperature to 140 °C at 2 °C/min, kept at 140 °C for 30 min, and thereafter, cooled to −170 °C at 2 °C/min. A liquid nitrogen cryostat was used to control the temperature.

3. COMPUTATIONAL SECTION

Calculations were performed using density functional theory as it is implemented in the Vienna Ab-initio Simulation Package (VASP)[43] with a plane wave basis set. For exchange and correlation, we used the PBE functional.[44] All lithium electrons were included in the calculation, but for nonvalence boron electrons, we used the projector augmented wave method (PAW).[45,46] The energy cutoff was set to 350 eV, and a 4 × 4 × 4 Monkhorst−Pack k-point mesh was used. The preparation of atomic structures and the setup of computational parameters was performed using the atomic simulation environment (ASE).[47]

The ground-state energy for the $(1 - x)LiBH_4+xLiI$ system was calculated for seven different values of x, that is, $x = 0$, $^1/_{16}$, $^1/_8$, $^3/_{16}$, $^1/_4$, $^1/_2$, or 1, both in the LT (*Pnma*) and HT ($P6_3mc$) crystal structures of $LiBH_4$. For structural optimization, all atomic forces were relaxed down below 0.01 eV/Å.

4. RESULTS AND DISCUSSION

4.1. Density Functional Theory. Figure 1 shows the calculated energy difference between the $P6_3mc$ (HT) and *Pnma* (LT) structures as a function of the content of LiI that has been substituted into the system. The stabilization of the HT structure relative to the LT structure is approximately linear up to a LiI content of 25%. The dotted line shows a linear fit of the data points for LiI contents from 0% to 25% to emphasize this.

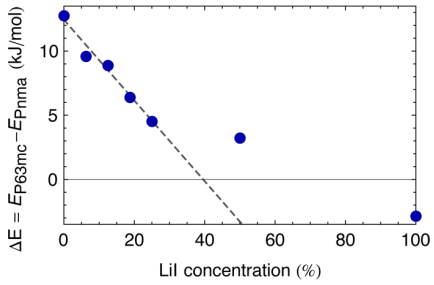

Figure 1. Ground-state energy difference between the $P6_3mc$ (HT) and *Pnma* (LT) structures of $LiBH_4$ as a function of the content of LiI that has been substituted into the system. The stabilization of the HT structure relative to the LT structure is approximately linear up to a LiI content of 25%. The dotted line shows a linear fit of the data points for LiI contents from 0% to 25% to emphasize this.

Pnma (LT) structures as a function of LiI content in the $(1 - x)LiBH_4+xLiI$ system. Up to a LiI content of 25%, there is a close to linear stabilization with increasing LiI content, about 33 kJ/mol of I. There seems to be little addition in stability by going from 25% LiI content to 50%, but for pure LiI, the HT structure has become more stable than the LT structure. However, this increased stability of the HT structure versus the LT structure is a poor indicator of the real HT stability for pure LiI because the LT structure of $LiBH_4$ is not the ground-state structure of LiI. Nonetheless, we do believe that, for smaller iodine contents, the ground-state energy calculations give a good estimate of the real stabilization in the $(1 - x)LiBH_4+xLiI$ system, since we expect them to have a similar entropy behavior as a function of temperature. This claim is supported further in Section 4.5 by comparing the calculation results with the results of DSC measurements.

4.2. X-ray Diffraction. The diffraction patterns of both the annealed and the nonannealed $(1 - x)LiBH_4+xLiI$ samples are shown in Figure 2. A diffraction pattern of nonannealed $LiBH_4$ that has been ball milled for 2 h is also shown for comparison. The pure ball-milled $LiBH_4$ has the LT structure, while the sample with 6.25% LiI is a blend of the LT and HT structures. For all samples with LiI content equal to or greater than 12.5%, only the HT phase is detected.

The positions of the reflections from the crystallographic planes ($hk0$), parallel to the hexagonal plane, are only slightly shifted to higher values when the LiI content is increased, reflecting a small expansion of the a axis with increased LiI content. The c axis, perpendicular to the hexagonal plan, is found to shrink with increasing LiI content up to 30% and then to expand with increasing LiI content between 30% and 50% (see Figure 2, in which a line is drawn to emphasize the shift of the (002) reflection).

The evolution of the lattice parameter c is plotted as a function of the LiI content in Figure 3a. The nonmonotonic evolution of the c axis is unexpected, and the contraction of c with increasing LiI content below a LiI content of 30% differs from what has previously been reported by Miyazaki et al.[39] For a LiI content above 30%, the c axis expands as expected when compared with the unit cell parameters of the hexagonal phases of pure $LiBH_4$ and pure LiI, respectively, and is in agreement with the values reported by Miyazaki et al.[39] and Rude et al.[38]

One possible explanation for this behavior is the presence of solid solutions containing different amounts of iodine and different lattice constants that merge into one upon heating as reported by Rude et al.[38] Another possibility is the existence of some intermediate phases as described by Oguchi et al.[37] These effects could be the origin of the very asymmetric peak shapes and large peak broadening visible in Figure 2 for low LiI content. Such broadening at low LiI content is also visible in the diffraction patterns of refs 25 and 26.

Sintering and/or annealing effects are observed for the annealed $LiBH_4$−LiI solid solutions in the form of narrower peaks for the annealed samples than for the nonannealed ones. However, the peculiar behavior of the c axis is still present in the annealed samples. As an example of the peak sharpening, the evolution of the fwhm of the (002) reflection with LiI content is shown in Figure 3b. The fwhm of the nonannealed powder varies with the LiI content and has a minimum at around 30% LiI content. This is also the LiI content for which the cell parameter c (see Figure 3a) is closest to the value reported for the cell parameters of pure $LiBH_4$.[31] After the annealing, the fwhm values are almost independent of the LiI content.

The broadening contribution from the strain and the crystallite sizes was analyzed using eq 1. This analysis was performed on the fwhm of four to six peaks depending on the diffraction patterns. Due to the limited quality of the data, no absolute values for D and η are reported herein. However, their relative contribution and evolution will be commented on in connection with the LiI content and the effect of the annealing.

It was found that, before the annealing, the broadening due to the strain is dominant over the size effect up to a LiI content of 25%. Knowing that the fwhm values are larger for the sample

dx.doi.org/10.1021/jp310050g | J. Phys. Chem. C 2013, 117, 3249−3257

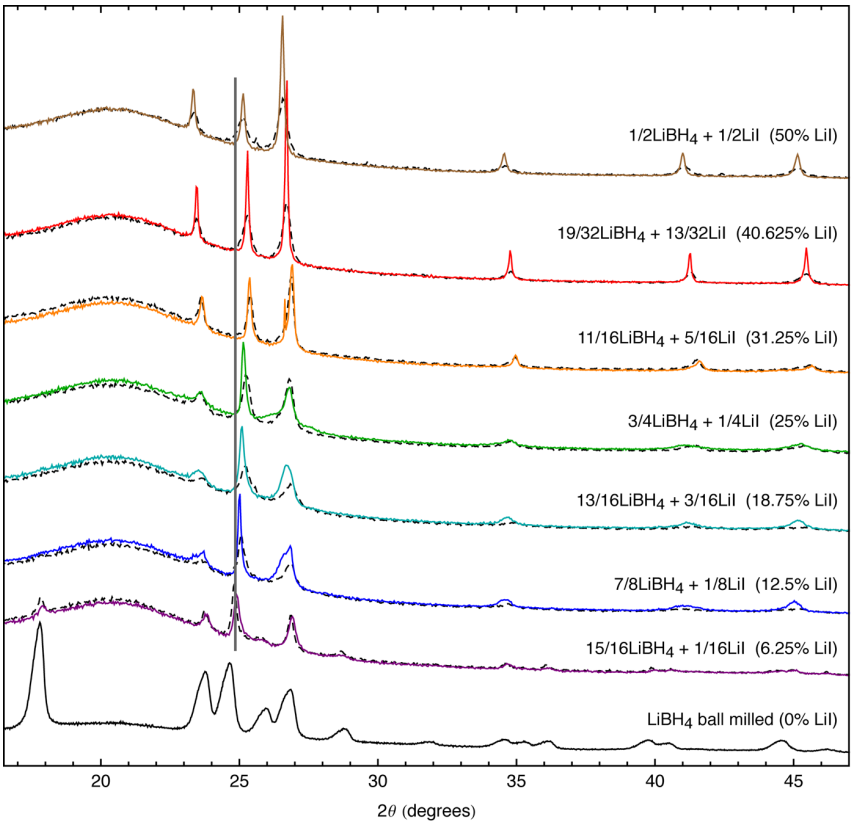

Figure 2. XRD patterns of $(1 - x)LiBH_4+xLiI$ solid solutions. The black, dashed lines show diffraction patterns of nonannealed samples, and the colored, solid lines show diffraction patterns of samples that have been annealed at 140 °C for 70 h. The black, solid line shows the diffraction pattern of pure ball-milled, nonannealed $LiBH_4$ for comparison. The vertical line at around 25° is drawn to emphasize the shift of the (002) reflection with LiI content. All measurements were performed at room temperature. The broad bump at the lowest angles is due to the polyethylene sample holder. The intensity of the diffraction pattern of pure $LiBH_4$ has been scaled down by $^1/_3$ in order to better fit the intensities of the remaining patterns in the figure. The molar percentage of LiI is shown in parentheses after the sample name for easier comparison with other figures in this work.

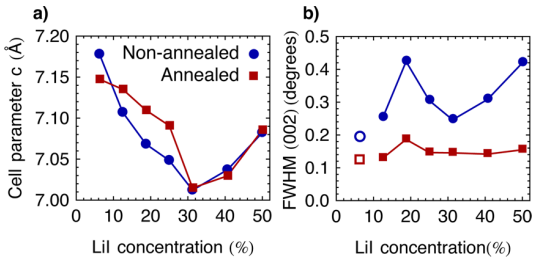

Figure 3. (a) Evolution of the unit cell parameter c in $(1 - x)LiBH_4+xLiI$ with LiI content. (b) The fwhm of the (002) reflection of the $(1 - x)LiBH_4+xLiI$ diffraction patterns as a function of LiI content. The fwhm of the samples with 6.25% LiI content are shown with empty dots; their values are not reliable because of overlapping diffraction peaks from the LT and HT structures of $LiBH_4$.

with 18.75% LiI content than for samples with a higher content of LiI, the density of defects is greater for the former than for the latter. After annealing, the strain values are smaller and almost independent of the LiI content. Furthermore, the crystallite sizes of the annealed powders are found to be around three times greater than those of the nonannealed powders for samples with LiI contents larger than 25%. Overall, the fwhm are found to be lowered by the heat treatment.

It should be noted that the difference in strain before and after the annealing is found to be smallest for the sample with 30% LiI content, which is the LiI content at which the minima in the cell parameter c and the fwhm before annealing are observed (see Figure 3). It should also be noted that the sample with 6.25% LiI content contains two coexisting structures with overlapping diffraction peaks at the position of the (002) reflection of the HT phase. Therefore, the measured fwhm values are probably not accurate for this sample and have been left out for this analysis.

4.3. Scanning Electron Microscopy. Figure 4 shows SEM images of $^1/_2LiBH_4+^1/_2LiI$ powder. The sample in Figure 4a was ball milled (as described in Section 2.1) but did not receive any heat treatment. The sample in Figure 4b was ball milled and annealed in a furnace at 140 °C for 70 h. A comparison of the two images shows that sintering does occur during the heat treatment, as the average size of the particles and the agglomerates in the powder are larger after the annealing than before it. This supports the results on the fwhm of the XRD data shown in Figures 2 and 3b.

4.4. Conductivity. The impedance spectroscopy measurements resulted in a Nyquist plot showing a single arc. The explanation for this can either be that only one contribution to the conduction is present or that two or more arcs, each corresponding to concurrent bulk and/or grain boundary

dx.doi.org/10.1021/jp310050g | J. Phys. Chem. C 2013, 117, 3249−3257

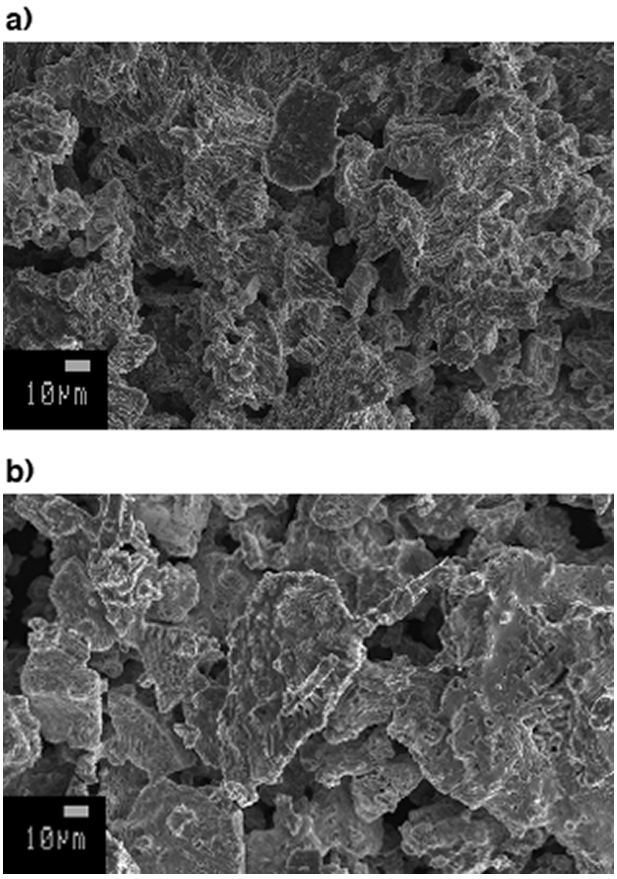

Figure 4. SEM images of $^1/_2LiBH_4+^1/_2LiI$. The scale in the lower left corner of the images shows the length of 10 μm. (a) After ball milling but before annealing. (b) After ball milling and annealing. It is clear that the average particle and agglomerate sizes are larger in the annealed sample than in the nonannealed sample.

contributions, overlap completely in the Nyquist plots. In such a case, however, it is not possible to separate the contributions from the bulk and the grain boundary conductivities using only impedance spectroscopy.[48,49] Therefore, the conductivity values presented in the following are to be taken as the total conductivity of the sample. No contribution to the Nyquist plots from the Li electrodes was observed. The Nyquist plots were all fitted using an (RQ) equivalent circuit model, that is, a resistor and a constant phase element in parallel. The conductivity of the samples is given by

$$\sigma = \frac{d}{AR} \tag{2}$$

where R is the resistance obtained from the fit, d is the thickness of the sample, and A is its area.

Figure 5 shows an Arrhenius plot of the Li^+ conductivities measured for the different samples during heating and cooling (Nyquist plots and additional Arrhenius plots can be found in the Supporting Information). The pellets consisted of the as-milled powders, and the measurements were performed while first heating the pellets from room temperature to 140 °C and then cooling them back down to room temperature. The $(1-x)LiBH_4+xLiI$ solid solutions show very high ionic conductivity, with the sample with 40% LiI content exceeding 0.1 mS/cm at

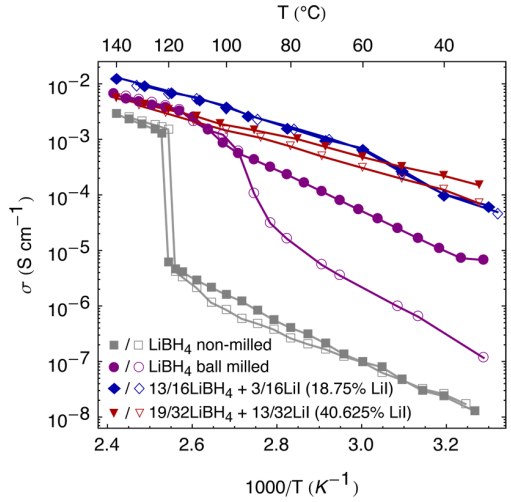

Figure 5. Li^+ conductivities of pure $LiBH_4$, both ball-milled and nonmilled, and of two mixing ratios of $(1-x)LiBH_4+xLiI$, obtained from impedance spectroscopy. For each sample, the filled symbols denote heating runs, and the empty symbols denote cooling runs.

30 °C and the 18.75% LiI containing sample exceeding 10 mS/cm at 140 °C.

Generally, the slopes of the Arrhenius plots vary with both LiI content and temperature. There is a general trend that the slope of the plots decreases with increasing LiI content. This indicates that the activation energy of the Li^+ conduction decreases with increasing LiI content. Furthermore, as a result of the decreasing slopes with increasing LiI content, the samples with a low LiI content generally have a higher Li^+ conductivity at the highest measured temperatures than the samples with high LiI content.

Ball milling and heat treatment of the samples are also important for their conductivity. The as-received (nonmilled) $LiBH_4$ is in its poorly conducting LT phase. At around 120 °C, the sample changes to the HT phase, and the conductivity increases by more than 2 orders of magnitude, as expected.[28] This trend in the conductivity is fully reversible upon cooling, with a very small hysteresis. The ball-milled $LiBH_4$ is also in the poorly conducting LT phase (see Figure 2). However, defects arising during the ball milling may open up new Li^+ conduction pathways. This causes an increase in conductivity by almost 3 orders of magnitude close to room temperature, compared to the nonmilled $LiBH_4$. When the ball-milled $LiBH_4$ is heated up above the phase transition temperature, it takes on the HT structure, presumably mending some of the defects caused by the ball milling. The return to the LT phase when cooling the sample down should mend the defects even further. Some of the conduction pathways present during the heating run are then closed as illustrated by the large fall of the conductivity between the heating and the cooling runs. After the thermal treatment, however, the sample is not defect-free, and the conductivity of the ball-milled sample is still higher than that of the as-received $LiBH_4$.

The conductivity values at 50 °C are shown as a function of the LiI content in Figure 6. This temperature is chosen because it represents an approximate temperature at which a lithium battery could be operated. At 50 °C, the conductivity is 0.3 mS/cm for LiI contents of 18% and 40%. Although this temperature is at the upper limit of consumer battery usage, the $LiBH_4$–LiI

dx.doi.org/10.1021/jp310050g | J. Phys. Chem. C 2013, 117, 3249–3257

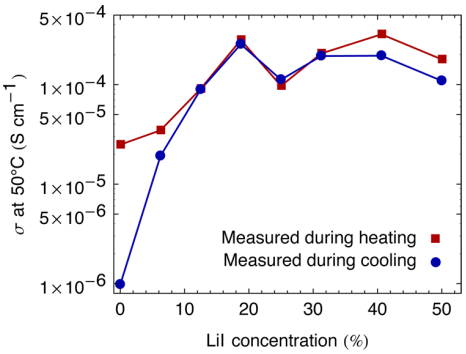

Figure 6. Li^+ conductivity of the $(1 - x)LiBH_4+xLiI$ samples at 50 °C as a function of LiI content for nonannealed (red rectangles) and annealed (blue circles) samples. The data points for pure $LiBH_4$ (0% LiI content) in this figure are from a measurement on ball-milled $LiBH_4$.

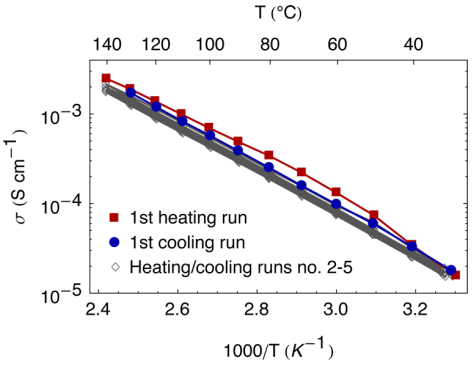

Figure 7. Li^+ conductivity of $^1/_2LiBH_4+^1/_2LiI$ obtained by impedance spectroscopy during five heating/cooling cycles. The red rectangles and blue circles show the results of the first heating and cooling runs, respectively. The diamonds show the results of the four subsequent heating and cooling cycles.

solid solution is still at least a factor of 3 away from the 1 mS/cm target.

The conductivity values at 50 °C are equal or higher during the heating runs than during the cooling runs. The difference in the conductivity between the heating and the cooling measurements is smallest for samples with LiI content between 18% and 30%. This result is in good harmony with the result shown in Figure 3b, namely, that the particle size and/or density of defects in the nonannealed samples are closest to those in the annealed samples for solid solutions with moderate LiI content.

Together, the XRD and conductivity results indicate that the microstructure of the samples is important for their conductivity and that freshly ball-milled samples with defect-rich microstructure yield higher conductivity values than those in which the defects have been mended by annealing. This is also emphasized by the fact that the measured conductivity does not follow the evolution of the lattice parameter c (see Figure 3a), which has a minimum at a LiI content of 30%. If the left part of Figure 3a is omitted (as it most probably does not reflect the trend of a single phase), one would expect an increase in conductivity in connection with the lattice expansion in the c direction. However, this is not found to be the case here and strongly suggests that a part of the Li^+ conduction might occur along the defects, for example, grain boundaries or dislocations. However, the exact Li^+ conduction mechanism in the $(1 - x)LiBH_4+xLiI$ solid solution is currently under investigation.

Figure 7 shows the conductivity of the sample with 50% LiI content measured during five consecutive heating and cooling cycles. As shown for the sample with 50% LiI content in Figure 6, the conductivity during cooling is lower than that during heating. However, during the next four temperature cycles, the conductivity performance is very stable and reproducible, confirming the good thermal stability of the HT phase of the solid solution. As explained in Section 2, this sample was prepared and measured using different ball-milling conditions and a different impedance spectroscopy experimental setup than the other samples used in this work. Because the density of defects and particle size are important parameters for the conductivity of the samples, it was to be expected that the conductivity values from this measurement could differ from those presented in Figures 5 and 6. This explains why the conductivity of the sample in Figure 7 is higher at 50 °C than shown for the sample with 50% LiI content in Figure 6. This also gives an indication of how reproducible the conductivity results are between different laboratory equipment.

4.5. Differential Scanning Calorimetry. Figure 8 shows the results of the DSC measurements. Some of the DSC spectra

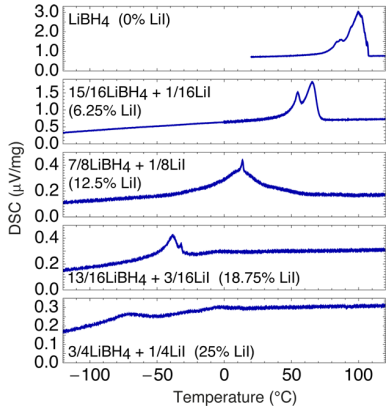

Figure 8. DSC results for different mixing ratios of $(1 - x)LiBH_4+xLiI$, obtained during cooling.

show two maxima of different intensity, most probably due to microstructural inhomogeneity in the samples. In these cases, the phase transition temperature is taken to be that at which the greater maximum is located.

In Figure 9, the phase transition temperature between the HT and the LT phases of the $LiBH_4$–LiI system is shown as a function of LiI content. For the measured LiI content, there is a clear linear dependency, with the transition temperature decreasing by approximately 70 °C for every 10% of LiI addition. For all measured mixtures with a LiI content equal to or above 12.5%, the transition temperature lies below room temperature.

In Figure 10, the calculated energy differences $\Delta E(x)$ between the HT and LT phases (shown in Figure 1) are plotted against the transition temperatures measured using DSC. Here, x denotes the LiI content of the samples. At each phase transition temperature, the Gibbs free energy difference between the two phases is zero. Since contributions from the zero point energy difference and the volume change between the two phases are small, we set $\Delta H(x) \approx \Delta E(x)$, where

dx.doi.org/10.1021/jp310050g | J. Phys. Chem. C 2013, 117, 3249–3257

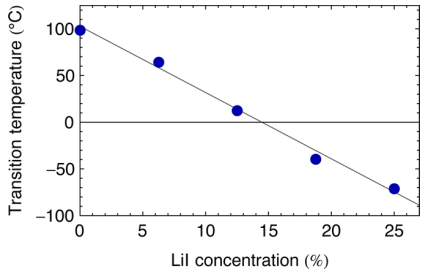

Figure 9. Phase transition temperatures between the hexagonal HT phase and the orthorhombic LT phase in the $(1 - x)LiBH_4+xLiI$ solid solution as a function of LiI content. For all measured mixtures with $x \geq 12.5\%$, the transition temperature lies below room temperature.

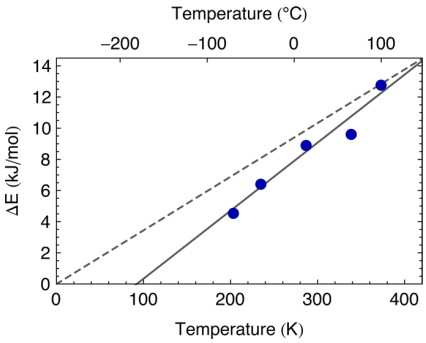

Figure 10. Calculated ground-state energy difference between the HT and the LT structures, $\Delta E(x)$, for different iodine contents x as a function of the measured phase transition temperature. The slopes of the lines in the figure represent the entropy change $\Delta S(x)$ between the two phases. The dashed line shows the limit of $\Delta S(x) = 0$.

$\Delta H(x)$ is the enthalpy change for a given ratio of iodine x. Therefore, we can write

$$\Delta E(x) = T\Delta S(x) \quad (3)$$

As a result, the slopes of the lines in Figure 10 represent the entropy difference ΔS between the two phases.

For the iodine free system, we get an entropy difference between the two phases of $\Delta S(0) = 34.7$ J/(mol K). If the addition of iodine was purely an enthalpy effect, $\Delta S(x)$ should remain constant for the different contents of iodine, and all data points should fall on the dashed line in Figure 10. It is apparent that the entropic difference $\Delta S(x)$ is reduced with addition of iodine by roughly 0.5 J/(mol K) per percentage point of increased iodine content in the system, but it is not possible to quantify how much should be attributed to the changes in the LT or HT, respectively, resulting from, for example, changes in directional bonding or configurational entropy.

The calculated value of $\Delta E(0) = 12.8$ kJ/(mol K) is also significantly higher than the published enthalpy values from Kharbachi et al.[50] ($\Delta H_{Kharbachi} = 5.1$ kJ/(mol K)) and Gorbunov et al.[51] ($\Delta H_{Gorbunov} = 6.2$ kJ/(mol K)). This overestimate of the ground-state energy difference also leads to an overestimate of the entropy difference between the two phases. Our calculated value is $\Delta S(0) = 34.4$ J/(mol K) compared to the published values from Pistorius et al.[52] ($\Delta S_{Pistorius} = 16.5$ J/(mol K)) and from Kharbachi et al.[50] ($\Delta S_{Karbachi} = 13.1$ J/(mol K)). Assuming that $\Delta E(x)$ is similarly overestimated, $\Delta S(x)$ should probably be scaled down by a factor of 2.0−2.5. Although $\Delta S(x)$ varies with iodine content, the governing factor comes from the change in the ground-state energy difference $\Delta E(x)$, which can be used as a predictor for the change in stability between the two phases.

5. SUMMARY AND OUTLOOK

The LiI content and the phase transition temperature between the HT and the LT phases are linearly dependent up to at least 25% LiI content as measured using DSC. A decrease in the transition temperature by 70 °C for every 10% of LiI addition was found. Density functional theory calculations also show that there is a close to linear stabilization of the HT structure with LiI addition up to a LiI content of 25%. For all samples with a LiI content equal to or greater than 12.5%, the phase transition temperature lies below room temperature, and after ball milling, the samples only contain the HT phase as observed using XRD.

The $(1 - x)LiBH_4+xLiI$ solid solutions show a high Li^+ conductivity. At 30 °C, the conductivity exceeds 0.1 mS/cm (for the sample with 40% LiI content), and at 140 °C, it exceeds 10 mS/cm (for the sample with 18.75% LiI content) as measured using impedance spectroscopy. Which mixing ratio of $(1 - x)LiBH_4+xLiI$ yields optimal conductivity depends greatly on which temperature range is in question. The conductivity is equal or higher during heating than during cooling, with the least difference between heating and cooling results for a LiI content between 18% and 30%.

Nonannealed samples with a low LiI content have apparent densities of defects greater than those with a high LiI content, as revealed by analyzing the fwhm of the reflections in the XRD data. This could be an artifact due to the presence of inhomogeneities and/or intermediate phases with similar but different cell parameters. After annealing, the density of defects appears to be almost the same for all samples, but the crystallite sizes grow with increasing LiI content. This could explain why samples with low LiI content tend to have a higher conductivity at high temperature than the samples with low LiI content, emphasizing the importance of the grain boundaries for the conduction mechanism.

The least change between the nonannealed and annealed samples is observed for a LiI content of around 30%. By combining information obtained from XRD and from impedance spectroscopy, it is found that samples with defect-rich microstructure, most probably dislocations and/or grain boundary defects, yield higher conductivity values than those in which the defects have been mended by heat treatment and where only intrinsic point defects might exist. This shows that microstructure and heat treatment are important for the conductivity of the samples. Finally, it is found that the expansion of the lattice parameter c is not a predominant parameter for increased conductivity.

The Li^+ conductivity must be high if the $(1 - x)LiBH_4+xLiI$ solid solution should be used as an electrolyte in a working battery cell. However, the performance of the electrolyte must also remain stable during the lifetime of the battery. In this work, a LiI content around 30% yields the optimal combined room-temperature performance in terms of microstructural stability under heat treatment and in terms of high Li^+ conductivity. Impedance spectroscopy measurements during five temperature cycles show that the conductivity of the material is stable and reproducible. However, working battery cells using this system as an electrolyte are still to be tested and characterized, and the exact Li^+ conduction mechanism must still be determined.

dx.doi.org/10.1021/jp310050g | J. Phys. Chem. C 2013, 117, 3249−3257

■ ASSOCIATED CONTENT

Supporting Information

Examples of Nyquist plots and additional Arrhenius plots from impedance spectroscopy measurements. This material is available free of charge via the Internet at http://pubs.acs.org.

■ AUTHOR INFORMATION

Corresponding Author

*Phone: +45 46775818; fax: +45 4677 5688; e-mail: teve@dtu.dk.

Author Contributions

The manuscript was written through contributions of all authors. All authors have given approval to the final version of the manuscript.

Notes

The authors declare no competing financial interest.

■ ACKNOWLEDGMENTS

The authors would like to acknowledge support from the Copenhagen Graduate School for Nano Science and Technology, COST Action MP1103 "Nanostructured materials for solid-state hydrogen storage", the Danish Center for Scientific Computing (DCSC), the Center of Atomic-Scale Materials Design (CAMD), and the Energy Research Fund of Landsvirkjun, Iceland.

■ REFERENCES

(1) Song, J. Y.; Wang, Y. Y.; Wan, C. C. Conductivity Study of Porous Plasticized Polymer Electrolytes Based on Poly(vinylidene fluoride) A Comparison with Polypropylene Separators. *J. Electrochem. Soc.* **2000**, *147*, 3219−3225.

(2) Nakagawa, H.; Izuchi, S.; Kuwana, K.; Nukuda, T.; Aihara, Y. Liquid and Polymer Gel Electrolytes for Lithium Batteries Composed of Room-Temperature Molten Salt Doped by Lithium Salt. *J. Electrochem. Soc.* **2003**, *150*, A695.

(3) Knauth, P. Inorganic Solid Li ion Conductors: an Overview. *Solid State Ionics* **2009**, *180*, 911−916.

(4) Goodenough, J. B.; Kim, Y. Challenges for Rechargeable Li Batteries. *Chem. Mater.* **2010**, *22*, 587−603.

(5) Tarascon, J.-M.; Armand, M. Issues and Challenges Facing Rechargeable Lithium Batteries. *Nature* **2001**, *414*, 359−67.

(6) Tarascon, J.-M. Key Challenges in Future Li-Battery Research. *Philos. Trans. R. Soc., A* **2010**, *368*, 3227−41.

(7) Rabenau, A. Lithium Nitride and Related Materials, Case Study of The Use of Modern Solid State Research Techniques. *Solid State Ionics* **1982**, *6*, 277−293.

(8) Belous, A. G.; Novitskaya, G. N.; Polyanetskaya, S. V.; Gornikov, Y. I. *Izv. Akad. Nauk SSSR* **1987**, *23*, 470−472.

(9) Inaguma, Y.; Liquan, C.; Itoh, M.; Nakamura, T.; Uchida, T.; Ikuta, H.; Wakihara, M. High Ionic Conductivity in Lithium Lanthanum Titanate. *Solid State Commun.* **1993**, *86*, 689−693.

(10) Yang, K.-Y.; Fung, K.-Z.; Leu, I.-C. Study on the Structural Change and Lithium Ion Conductivity for the Perovskite-Type $LaAlO_3$−$La_{0.50}Li_{0.50}TiO_3$ Solid Solution. *J. Alloys Compd.* **2007**, *438*, 207−216.

(11) Bohnke, O. The Fast Lithium-Ion Conducting Oxides $Li_{3x}La_{2/3-x}TiO_3$ From Fundamentals to Application. *Solid State Ionics* **2008**, *179*, 9−15.

(12) Thangadurai, V.; Schwenzel, J.; Weppner, W. Tailoring Ceramics for Specific Applications: a Case Study of the Development of All-Solid-State Lithium Batteries. *Ionics* **2005**, 11.

(13) Aono, H.; Sugimoto, E.; Sadaoka, Y.; Imanaka, N.; Adachi, G. Electrical Property and Sinterability of $LiTi_2(PO_4)_3$ Mixed with Lithium Salt (Li_3PO_4 or Li_3BO_3). *Solid State Ionics* **1991**, *47*, 257−264.

(14) Arbi, K.; Rojo, J. M.; Sanz, J. Lithium Mobility in Titanium Based Nasicon $Li_{1+x}Ti_{2-x}Al_x(PO_4)_3$ and $LiTi_{2-x}Zr_x(PO_4)_3$ Materials Followed by NMR and Impedance Spectroscopy. *J. Eur. Ceram. Soc.* **2007**, *27*, 4215−4218.

(15) Bruce, P. G.; West, A. R. The A-C Conductivity of Polycrystalline LISICON, $Li_{2+2x}Zn_{1-x}GeO_4$, and a Model for Intergranular Constriction Resistances. *J. Electrochem. Soc.* **1983**, *130*, 662−669.

(16) Kamaya, N.; Homma, K.; Yamakawa, Y.; Hirayama, M.; Kanno, R.; Yonemura, M.; Kamiyama, T.; Kato, Y.; Hama, S.; Kawamoto, K.; et al. A Lithium Superionic Conductor. *Nat. Mater.* **2011**, *10*, 682−686.

(17) Stramare, S.; Thangadurai, V.; Weppner, W. Lithium Lanthanum Titanates: a Review. *Chem. Mater.* **2003**, *15*, 3974−3990.

(18) Robertson, A. D.; West, A. R.; Ritchie, A. G. Review of Crystalline Lithium-Ion Conductors Suitable for High Temperature Battery Applications. *Solid State Ionics* **1997**, *104*, 1−11.

(19) Brodd, R. J.; Huang, W.; Akridge, J. R. Polymer Battery R&D in the U.S. *Macromol. Symp.* **2000**, *159*, 229−245.

(20) Park, M.; Zhang, X.; Chung, M.; Less, G. B.; Sastry, A. M. A Review of Conduction Phenomena in Li-Ion Batteries. *J. Power Sources* **2010**, *195*, 7904−7929.

(21) Züttel, A.; Rentsch, S.; Fischer, P.; Wenger, P.; Sudan, P.; Mauron, P.; Emmenegger, C. Hydrogen Storage Properties of $LiBH_4$. *J. Alloys Compd.* **2003**, *356*−*357*, 515−520.

(22) Łodziana, Z.; Vegge, T. Structural Stability of Complex Hydrides: $LiBH_4$ Revisited. *Phys. Rev. Lett.* **2004**, *93*, 145501.

(23) Kang, J. K.; Kim, S. Y.; Han, Y. S.; Muller, R. P.; Goddard, W. a. A candidate $LiBH_4$ for Hydrogen Storage: Crystal Structures and Reaction Mechanisms of Intermediate Phases. *Appl. Phys. Lett.* **2005**, *87*, 111904.

(24) Łodziana, Z.; Vegge, T. Structural Stability of Complex Hydrides: $LiBH_4$ Revisited Comment: Łodziana and Vegge Reply. *Phys. Rev. Lett.* **2006**, *97*, 119602.

(25) Mosegaard, L.; Møller, B.; Jørgensen, J.-E.; Bösenberg, U.; Dornheim, M.; Hanson, J. C.; Cerenius, Y.; Walker, G.; Jakobsen, H. J.; Besenbacher, F.; et al. Intermediate Phases Observed during Decomposition of $LiBH_4$. *J. Alloys Compd.* **2007**, *446*−*447*, 301−305.

(26) Blanchard, D.; Shi, Q.; Boothroyd, C. B.; Vegge, T. Reversibility of Al/Ti Modified $LiBH_4$. *J. Phys. Chem. C* **2009**, *113*, 14059−14066.

(27) Lang, J.; Gerhauser, A.; Filinchuk, Y.; Klassen, T.; Huot, J. Differential Scanning Calorimetry (DSC) and Synchrotron X-ray Diffraction Study of Unmilled and Milled $LiBH_4$: a Partial Release of Hydrogen at Moderate Temperatures. *Crystals* **2012**, *2*, 1−21.

(28) Matsuo, M.; Nakamori, Y.; Orimo, S.; Maekawa, H.; Takamura, H. Lithium Superionic Conduction in Lithium Borohydride Accompanied by Structural Transition. *Appl. Phys. Lett.* **2007**, *91*, 224103.

(29) Epp, V.; Wilkening, M. Fast Li Diffusion in Crystalline $LiBH_4$ Due to Reduced Dimensionality: Frequency-Dependent NMR Spectroscopy. *Phys. Rev. B* **2010**, *82*, 020301.

(30) Ikeshoji, T.; Tsuchida, E.; Morishita, T.; Ikeda, K.; Matsuo, M.; Kawazoe, Y.; Orimo, S. Fast-Ionic Conductivity of Li^+ in $LiBH_4$. *Phys. Rev. B* **2011**, *83*, 144301.

(31) Soulié, J.-P.; Renaudin, G.; Černý, R.; K, Y. Lithium Boro-Hydride $LiBH_4$ I. Crystal Structure. *J. Alloys Compd.* **2002**, *346*, 200−205.

(32) Miwa, K.; Ohba, N.; Towata, S.; Nakamori, Y.; Orimo, S. First-Principles Study on Lithium Borohydride $LiBH_4$. *Phys. Rev. B* **2004**, *69*, 1−8.

(33) Orgaz, E.; Membrillo, A.; Castañeda, R.; Aburto, A. Electronic Structure of Ternary Hydrides Based on Light Elements. *J. Alloys Compd.* **2005**, *404*−*406*, 176−180.

(34) Takahashi, K.; Hattori, K.; Yamazaki, T.; Takada, K.; Matsuo, M.; Orimo, S.; Maekawa, H.; Takamura, H. All-Solid-State Lithium Battery with $LiBH_4$ Solid Electrolyte. *J. Power Sources* **2013**, *226*, 61−64.

(35) Maekawa, H.; Matsuo, M.; Takamura, H.; Ando, M.; Noda, Y.; Karahashi, T.; Orimo, S. Halide-Stabilized $LiBH_4$, a Room-Temper-

ature Lithium Fast-Ion Conductor. *J. Am. Chem. Soc.* **2009**, *131*, 894−895.
(36) Fischer, D.; Müller, A.; Jansen, M. Existiert Eine Wurtzit-Modifikation Von Lithiumbromid? Untersuchungen Im System LiBr/LiI. *Z. Anorg. Allg. Chem.* **2004**, *630*, 2697−2700.
(37) Oguchi, H.; Matsuo, M.; Hummelshøj, J. S.; Vegge, T.; Nørskov, J. K.; Sato, T.; Miura, Y.; Takamura, H.; Maekawa, H.; Orimo, S. Experimental and Computational Studies on Structural Transitions in the $LiBH_4$−LiI Pseudobinary System. *Appl. Phys. Lett.* **2009**, *94*, 141912.
(38) Rude, L. H.; Groppo, E.; Arnbjerg, L. M.; Ravnsbæk, D. B.; Malmkjær, R. a.; Filinchuk, Y.; Baricco, M.; Besenbacher, F.; Jensen, T. R. Iodide Substitution in Lithium Borohydride, $LiBH_4$−LiI. *J. Alloys Compd.* **2011**, *509*, 8299−8305.
(39) Miyazaki, R.; Karahashi, T.; Kumatani, N.; Noda, Y.; Ando, M.; Takamura, H.; Matsuo, M.; Orimo, S.; Maekawa, H. Room Temperature Lithium Fast-Ion Conduction and Phase Relationship of LiI Stabilized $LiBH_4$. *Solid State Ionics* **2011**, *192*, 143−147.
(40) Wojdyr, M. FITYK: a General-Purpose Peak Fitting Program. *J. Appl. Crystallogr.* **2010**, *43*, 1126−1128.
(41) Patterson, A. L. The Scherrer Formula for X-Ray Particle Size Determination. *Phys. Rev.* **1939**, *56*, 978−982.
(42) Stokes, A. R.; Wilson, A. J. C. The Diffraction of X Rays by Distorted Crystal Aggregates-I. *Proc. Phys. Soc.* **1944**, *56*, 174−181.
(43) Kresse, G.; Furthmüller, J. Efficient Iterative Schemes for ab Initio Total-Energy Calculations Using a Plane-Wave Basis Set. *Phys. Rev. B* **1996**, *54*, 11169.
(44) Perdew, J. J.; Burke, K.; Ernzerhof, M. Generalized Gradient Approximation Made Simple. *Phys. Rev. Lett.* **1996**, *77*, 3865.
(45) Blöchl, P. E. Projector Augmented-Wave Method. *Phys. Rev. B* **1994**, *50*, 17953.
(46) Blöchl, P. E.; Först, C. J.; Schimpl, J. Projector Augmented Wave Method: ab Initio Molecular Dynamics with Full Wave Functions. *Bull. Mater. Sci.* **2003**, *26*, 33.
(47) Bahn, S. R.; Jacobsen, K. W. An Object-Oriented Scripting Interface to a Legacy Electronic Structure Code. *Comp. Sci. Eng.* **2002**, *4*, 56−66.
(48) Beekmans, N. M.; Heyne, L. Correlation between Impedance, Microstructure and Composition of Calcia-Stabilized Zirconia. *Electrochim. Acta* **1976**, *21*, 303−310.
(49) Haile, S. M.; West, D. L.; Campbell, J. The Role of Microstructure and Processing on the Proton Conducting Properties of Gadolinium-Doped Barium Cerate. *J. Mater. Res.* **2011**, *13*, 1576−1595.
(50) El Kharbachi, A.; Nuta, I.; Hodaj, F.; Baricco, M. Above Room Temperature Heat Capacity and Phase Transition of Lithium Tetrahydroborate. *Thermochim. Acta* **2011**, *520*, 75−79.
(51) Gorbunov, V. E.; Gavrichev, K. S.; Zalukaev, V. L.; Sharpataya, G. A.; Baku, M. S. I. Heat Capacity and Phase Transformation of Lithium Borohydride. *Zh. Neorg. Khim.* **1984**, *29*, 2333−2337.
(52) Pistorius, C. W. F. T. Melting and Polymorphism of Lithium Tetrahydroborate to 45 kbar. *Z. Phys. Chem.* **1974**, *88*, 253−263.

Supporting Information for:

The Effect of Heat Treatment on the Lithium Ion Conduction of the $LiBH_4$-LiI Solid Solution

Dadi Sveinbjörnsson[1], Jón Steinar Gardarsson Mýrdal[1,2], Didier Blanchard[1], Janet Jonna Bentzen[1], Takumi Hirata[3], Mogens Bjerg Mogensen[1], Poul Norby[1], Shin-ichi Orimo[3], Tejs Vegge[1].*

[1]Department of Energy Conversion and Storage, Technical University of Denmark, Frederiksborgvej 399, P.O. Box 49, DK-4000 Roskilde, Denmark.

[2]Center for Atomic-Scale Materials Design, Department of Physics, Technical University of Denmark, Anker Engelunds Vej 1, DK-2800 Lyngby, Denmark.

[3]Institute for Materials Research, Tohoku University, 2-1-1 Katahira, Aoba-ku, Sendai 980-8577, Japan.

* Corresponding author: Tel.: +45 46775818, Fax: +45 4677 5688, E-mail: teve@dtu.dk

S1. CONDUCTIVITY RESULTS

S1.1. Nyquist plots

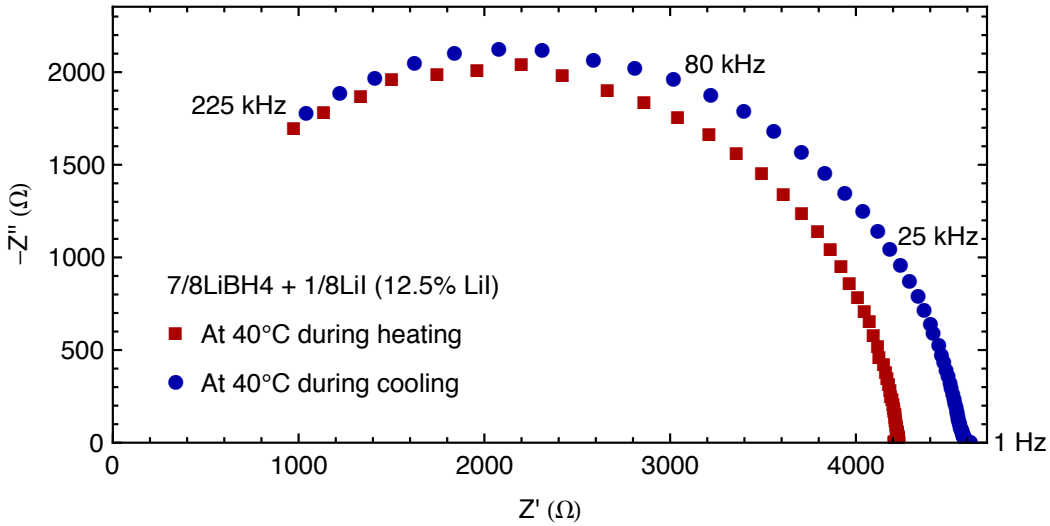

Figure S.1. Typical examples of Nyquist plots obtained from the impedance spectroscopy measurements on the (1-*x*)$LiBH_4$+*x*LiI samples. The impedance measurements were performed during heating/cooling cycles from 30°C to 140°C and back to 30°C. The red squares were measured at 40°C at the beginning of such a heating/cooling cycle and the blue circles were measured at 40°C at the end of the cycle. The Nyquist plots all show a single arc and were fitted using an (*RQ*) equivalent circuit model.

S1.2. Arrhenius plots

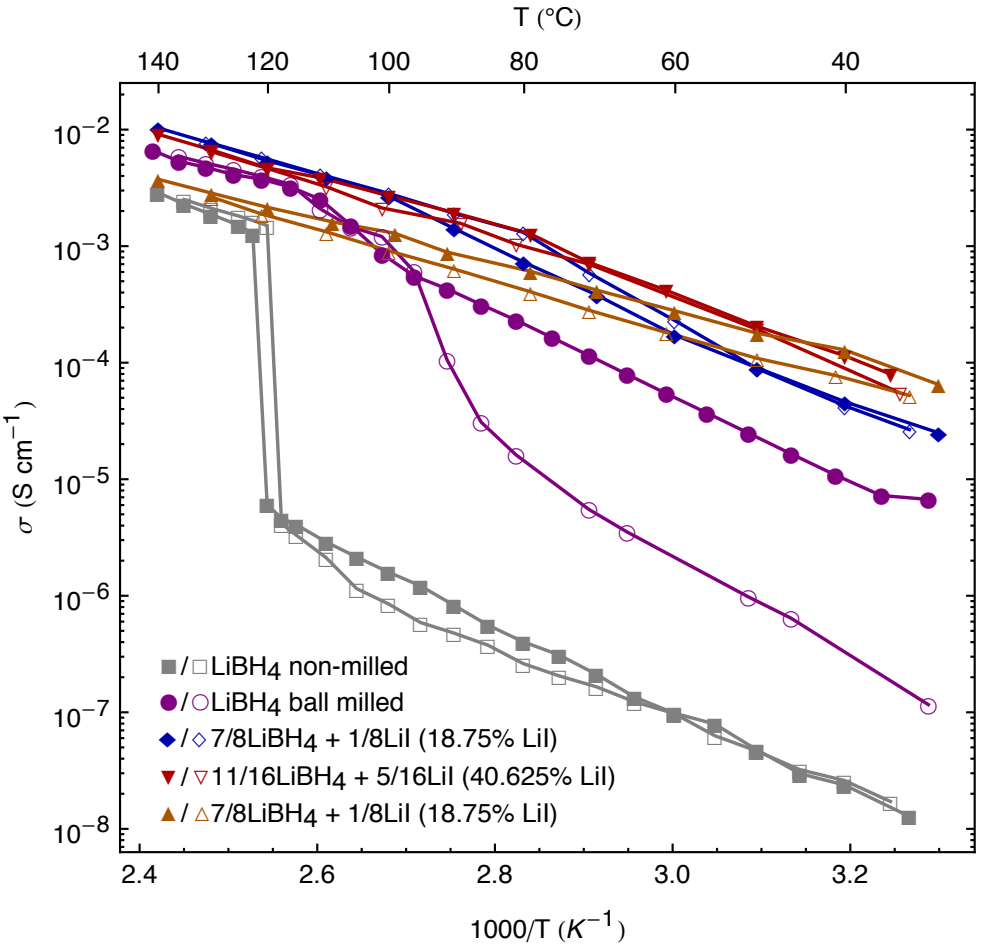

Figure S.2. Additional Arrhenius plots obtained from impedance spectroscopy measurements. For each sample, the filled symbols denote heating runs and the empty symbols denote cooling runs.

Paper B

THE JOURNAL OF PHYSICAL CHEMISTRY C

Article

pubs.acs.org/JPCC

Li-ion Conduction in the $LiBH_4$:LiI System from Density Functional Theory Calculations and Quasi-Elastic Neutron Scattering

Jon Steinar Gardarsson Myrdal,[†,‡] Didier Blanchard,[†] Dadi Sveinbjörnsson,[†] and Tejs Vegge*[,†]

[†]Department of Energy Conversion and Storage, Technical University of Denmark, Frederiksborgvej 399 Building 238, DK-4000 Roskilde, Denmark

[‡]Center for Atomic-Scale Materials Design and Department of Physics, Technical University of Denmark, DK-2800 Lyngby, Denmark

ABSTRACT: The hexagonal high-temperature polymorph of $LiBH_4$ is stabilized by solid solution with LiI to exhibit superionic Li^+ ionic conductivity at room temperature. Herein, the mechanisms for the Li^+ diffusion are investigated for the first time by density functional theory (DFT) calculations coupled to quasi-elastic neutron scattering (QENS) measurements with and without an applied bias potential of 3 V. DFT calculations show that lithium defects such as Frenkel pairs are easily formed at room temperature (formation energy of 0.44 eV) and low energy barriers (0.2 to 0.3 eV) are found between stable defect sites, giving rise to high defect mobility. QENS results at 380 K show long-range diffusion of Li^+, with jump lengths of one unit cell and jump rates in agreement with those obtained from DFT, and the application of the bias potential increases the diffusion constant by a factor of 2. At 300 K, the QENS data reveal jump events of shorter length (~2 Å), which could correspond to a jump process of Li^+ interstitials to an intermediate lattice site, in agreement with DFT calculations.

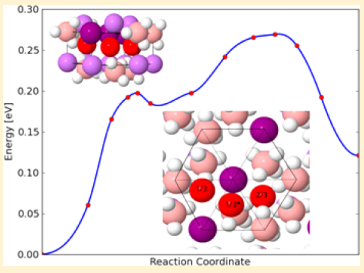

1. INTRODUCTION

Consumer demands for better reliability, longer lifetime, and sustainability is fueling the need for advanced energy storage technologies in a broad range of applications. Today, the battery market is driven by consumer electronics and dominated by Li-ion batteries,[1] but since their commercialization in 1991[2,3] only small improvements have been made[1,4] and new developments are needed to reduce battery prices and improve the reliability, safety, and energy/power density. The typical limitations of the Li-ion batteries are well known: the liquid electrolytes are flammable, the cathodes tend to dissolve and reduce the overall efficiency of the batteries, and short circuits between the electrodes can occur due to lithium dendrite formation over cycling. Solid-state electrolytes with sufficient chemical and electrochemical stability could offer better safety and enhanced cycle life, but finding suitable materials with sufficiently high lithium ion conduction and negligible electronic conduction remains a challenge.[5]

Lithium borohydride ($LiBH_4$) could offer a possible solution and represents a promising class of solid, crystalline materials with super-ionic Li^+ conduction. At room temperature, $LiBH_4$ has a slow Li^+-conducting orthorhombic *Pnma* structure (~10^{-8} S/cm at 30 °C), but at ~110 °C it undergoes a reversible structural transition to a highly Li^+ conducting hexagonal phase[6] (~10^{-3} S/cm at 120 °C), generally ascribed to space group $P6_3mc$. In the following, these polymorphs will be referred to as the LT phase (orthorhombic) and HT phase (hexagonal), respectively. The HT polymorph can be stabilized at room temperature by solid solution of lithium halides (e.g., LiI, LiBr, LiCl) in the borohydride, with LiI giving the best Li ion conductivities.[7,8] We have recently shown that an optimal conductivity is reached near the $Li(BH_4)_{0.8}I_{0.2}$ mixture.[9]

The mechanisms of the super-ionic conduction in the HT phase of $LiBH_4$ have previously been investigated with molecular dynamics by Ikeshoji et al.[10] and Aeberhard et al.[11] In their publications, they report a double splitting in the Li^+ lattice sites along the z axis and the existence of metastable Li^+ interstitial sites playing a large role in the high ionic conductivity. Furthermore, a molecular dynamic study and NMR measurements suggest that the conduction is two dimensional (2D), taking place in the hexagonal plane.[6,11,12]

Here we report the first combined results from density functional theory (DFT) calculations and quasi-elastic neutron scattering (QENS) measurements[13−15] performed to study the fast Li^+ conduction in the HT polymorph of the $Li(BH_4)_{0.75}I_{0.25}$ system as a function of temperature and applied bias potential.

2. COMPUTATIONAL DETAILS

All calculations presented here were prepared and executed using the atomic simulation environment (ASE).[16] DFT calculations[17,18] are performed with the real-space grid code GPAW.[19,20] GPAW uses the projector-augmented wave method[21] with a frozen core approximation. The PBE exchange and correlation functional,[22] a 4 × 4 × 4 Monkhorst-Pack k-point mesh, and a grid spacing of 0.15 Å are used in the calculations. For ground-state energy calculations, the atomic

Received: December 5, 2012
Revised: February 26, 2013
Published: March 11, 2013

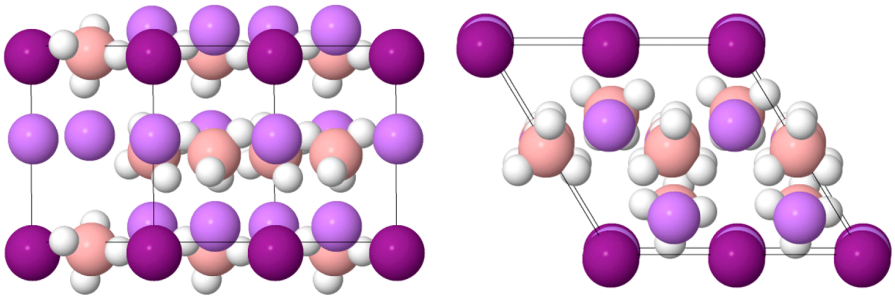

Figure 1. Supercell used in the DFT calculations along with a few neighboring atoms for better visualization of the model structure. Difference in local environments, iodide -rich areas close to neighboring I^- ions, iodide-sparse areas in iodide-free crystal planes, and areas with moderate iodide concentration between neighboring BH_4^- and I^- ions. Li: pale purple, I: dark purple, B: pink, and H: white.

positions were relaxed until all atomic forces were <0.01 eV/Å. The formation of Li^+ interstitials (Li^+_{int}) and vacancies (V^-_{Li}) have been studied by the addition/removal of Li plus a hole to the supercell, made of 2 × 2 × 1 lattice units (i.e., 8 f.u.); see Figure 1. The supercell was kept neutral by adding a compensating, uniform background charge.

Transition barriers were identified using the nudged elastic band (NEB) method,[23,24] which is a method to find minimum energy paths between two (local) minima. The climbing image method[25] was used to find the highest energy point along the ridge, that is, the transition state (TS). Reaction rates were evaluated using harmonic transitional state theory (HTST).[26] In the harmonic approximation, the prefactor is given as the ratio between the products of the vibrational frequencies of the initial state and the vibrational frequencies of TS,[23] yielding a reaction rate of

$$k^{\mathrm{HTST}} = \frac{\prod_i \nu^{\mathrm{IS}}}{\prod_i \nu^{\mathrm{TS}}} e^{-E_{\mathrm{TS}}/k_{\mathrm{B}}T} \quad (1)$$

The vibrational frequencies of both the initial and TSs are calculated using a finite-difference approximation with displacements of 0.01 Å.

The structure of the high-temperature polymorph of $LiBH_4$ remains an open question due to the complex role of dynamical disorder in the system.[10,11,27−29] The presented calculations were performed on a system of $Li(BH_4)_{0.75}I_{0.25}$, with an atomic configuration based on the hexagonal $LiBH_4$ HT structure, as characterized by Filinchuk et al.[29] Our reference system is composed of 2 × 2 × 1 lattice units (8 f.u.) (see Figure 1), where every fourth BH_4^- group has been substituted for I^- and the cell parameters and atomic configuration relaxed. The relaxed lattice unit lengths are a = 4.31 Å, b = 4.19 Å, and c = 6.95 Å. In the case of Frenkel pair formation, the super cell was extended to 4 × 2 × 1 lattice units.

3. EXPERIMENTAL SECTION

$^7Li^{11}BH_4$ (purity >94%), $^7Li^{11}BD_4$ (purity >94%), and ^7LiI (purity >98%) were purchased from Katchem. ^7Li, ^{11}B, and D isotope-enriched compounds were used to avoid the high neutron absorption by natural B and Li and the high incoherent cross section of H that would screen the quasi-elastic signal from ^7Li. The hydrogenated compound is used as a benchmark for the BH_4^- and H dynamics to separate the signal from the dynamics of the proton and other dynamics, for example, the lithium ion diffusion. The $^7Li(^{11}BH_4)_{0.75}I_{0.25}$ and $^7Li(^{11}BD_4)_{0.75}I_{0.25}$ solid solutions were obtained by mechanical milling of 2 g of the precursors in a stainless-steel vial, inner volume 250 mL, and rotating speed 650 rpm for 2 h. Twenty-five tungsten carbide balls were used, giving a powder-to-ball ratio of 1/100. The crystal structure of the obtained solid solution was confirmed by X-ray diffraction to be the HT hexagonal phase (space group $P6_3mc$). The transition temperature from the LT to the HT was determined by differential scanning calorimetry to be 200 K.[9]

The QENS measurements were performed at IN10, the backscattering spectrometer located at the Institut Laue-Langevin, Grenoble, France. We loaded 0.5 to 1 g of sample in a specially designed aluminum flat cell of dimensions 30 × 40 × 0.5 mm^3. The two sides of the cell, separated by a Teflon flange, used as sealing and electrical insulator, were connected to a potentiostat combining in situ impedance measurements as well as the application of a potential to the solid electrolyte during the QENS spectra acquisition. The Al container was oriented at 135° with respect to the direct beam. Si(111) monochromator and analyzer crystals were used in a back-scattering geometry, giving a final neutron wavelength of 6.271 Å and an energy resolution of 1 μeV with an energy-transfer range of ±13.5 μeV. The spectra were recorded by seven detectors corresponding to a scattering vector ranging from 0.50 to 1.96 $Å^{-1}$. The spectra were analyzed by using the curve fitting utility (PAN) included in the DAVE package.[30]

4. RESULTS AND DISCUSSION

4.1. Density Functional Theory. To study the origin and the mechanisms for the Li^+ conduction, we performed DFT calculations on lithium interstitials and vacancies in the $Li(BH_4)_{0.75}I_{0.25}$ solid solution. The model structure used in the calculations includes different local environments to mimic the different configurations that can exist in the solid solution. These local environments include iodide-rich areas close to neighboring I^- ions, iodide-sparse areas in every other crystal plane that does not include any I^- ions, and areas with moderate iodide concentration between neighboring BH_4^- and I^- ions; see Figure 1. The relationships between the local iodide concentration and the stability of defect sites and the diffusion barriers between these sites were also investigated.

In the HT hexagonal crystal structure, triangular areas exist between all groups of three neighboring Li^+ ions. Each Li^+ ion has an anion neighbor placed directly below it, ~2.5 Å for the pure BH_4^- layers and ~2.9 Å for the layers that include I^-. Together, these neighboring anions and cations form a triangular prism. The crystal layers then have an ABAB stacking, which means that centered above (~0.8 Å) every other triangular prism there is an anion from the next layer. (See Figures 1−3.)

dx.doi.org/10.1021/jp311980h | J. Phys. Chem. C 2013, 117, 9084−9091

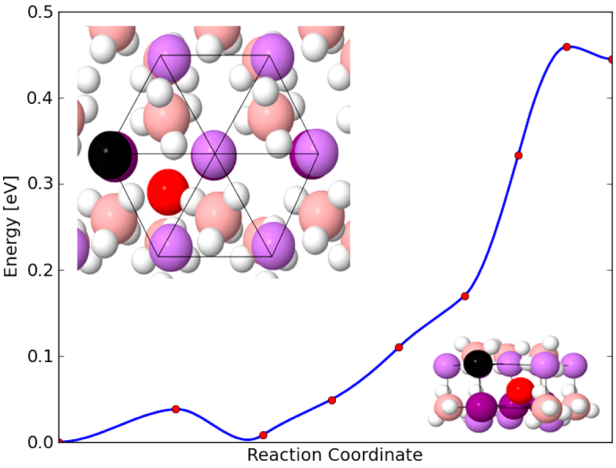

Figure 2. Minimum energy path for the formation of a Frenkel defect pair and the corresponding atomic structure. The created Li^+ interstitial, seated in a 1/3 site, and vacancy are shown as red and black spheres, respectively. The transition barrier for creating the defect pair is 0.46 eV. The lattice atoms are displayed as follows: Li: pale purple, I: dark purple, B: pink, and H: white.

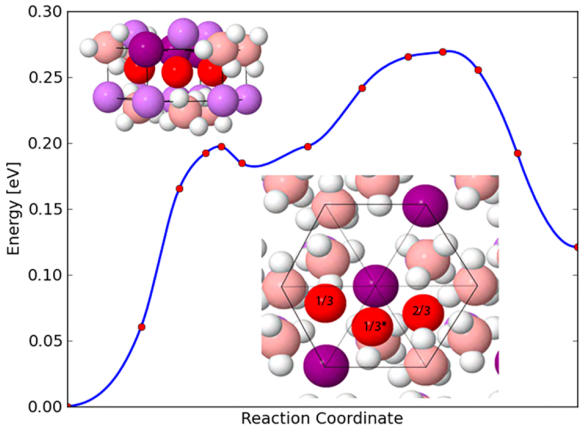

Figure 3. Minimum energy path from a 1/3 to a 2/3 interstitial site, passing through a 1/3* interstitial site. The atomic positions of the interstitial in the three different sites are shown from left to right in the same order that the sites occur along the path. The 1/3* site opens up the possibility for interstitials with lower kinetic energy. The lattice atoms are displayed as follows; Li: pale purple, I: dark purple, B: pink, and H: white.

We performed calculations on Li^+_{int} placed inside previously explained triangular prism structures with four different local environments (three of which can be seen in Figure 3); the calculated sites will be referred to as 1/3, 2/3, 3/3, and 1/3*, respectively. The labeling refers to the ratio of surrounding BH_4^- ions in the prism grid. The first three sites do not have ions from the neighboring crystal planes positioned directly above or below the site, whereas the 1/3* site is centered between ions from neighboring layers. In the three "non-sandwiched" sites, the Li^+_{int} can be found 0.8 to 1.1 Å above (depending on the ratio of I^- neighbors) the central position between the three neighboring anions in the hexagonal plane. In the 1/3* site, the Li^+_{int} is located significantly closer to the two neighboring I^- ions than the in-plane BH_4^- ion.

The 1/3 site is the energetically most favorable, whereas the 3/3 and the 2/3 sites are almost equal in energy, being 0.14 and 0.15 eV, respectively, less favorable than the 1/3 site. The 1/3* site is the least favorable one, 0.18 eV less favorable than the 1/3 site.

Calculations were performed on lithium vacancies (V^-_{Li}) in two different local environments, that is, with a neighboring I^- ion (an I^- site) and a second site without I^- neighbors (a BH_4^- site). The BH_4^- site is more favorable than the I^- site, but the energy difference is small, only 0.05 eV.

A Frenkel pair is created when a lattice Li^+ ion is moved into an interstitial site, thereby creating a V^-_{Li} and Li^+_{int} defect pair. A calculation on a Frenkel pair, where the interstitial is sitting in a 1/3 site, was performed, giving a formation energy for the defect pair as low as $E_{Frenkel}$ = 0.44 eV. Figure 2 shows the minimum energy path from a NEB calculation for the formation of the Frenkel pair, starting from the defect-free system. The transition barrier to form the defect is $E_{Frenkel\_TS}$ = 0.47 eV, meaning that there is a very small threshold for the interstitial to recombine with the vacancy, unless the oppositely charged defects become further separated, for example, by an applied bias.

We have also performed NEB calculations on different possible diffusion mechanisms for individual Li^+_{int} and V^-_{Li} originating from the electrodes; all TS energies and jump lengths are presented in Table 1.

Possible Li^+_{int} conduction pathways were investigated from a 1/3 site to the four different, neighboring sites. An interstitial jump from a 1/3 site to an identical 1/3 site, one lattice unit away, has a transition barrier of $E_{1/3-1/3\_TS}$ = 0.26 eV. During the jump, a clear shift of a neighboring lattice Li^+ ion is visible along the z axis of ~0.6 Å to make room for the diffusing

Table 1. Calculated Transition Barriers, Jump Lengths, and Rates for Different Diffusion Mechanisms in the $Li(BH_4)_{0.75}I_{0.25}$ System[a]

defect	mechanism	transition barrier (eV)	jump length (Å)	rate 300 K (s^{-1})	rate 380 K (s^{-1})
Li^+ interstitial	1/3 to 1/3 site	0.26	4.32	1.0×10^9	8.3×10^9
	1/3 to 2/3 site	0.28/0.14	4.31	4.6×10^8	4.5×10^9
	1/3 to 3/3 site	0.32/0.18	4.36	9.8×10^7	1.3×10^9
	exchange 1/3 to 1/3 site	0.44	3.00/4.07	9.4×10^5	3.4×10^7
	1/3 to 1/3* site	0.20/0.02	2.34	7.3×10^9	3.7×10^{10}
	1/3* to 2/3 site	0.09/0.15	3.30	7.7×10^{12}	9.1×10^{12}
Li^+ vacancy	I^- to I^- site	0.23	4.27	3.2×10^9	2.1×10^{10}
	I^- to BH_4^- site	0.33/0.28	4.27	6.6×10^7	9.8×10^8
Frenkel pair	formation	0.46/0.02	3.32	4.4×10^5	2.9×10^6

[a]All mechanisms are single-particle jumps except for the exchange mechanism. Different transition barriers depending on the direction of the jumps are caused by relative energy differences between different sites.

dx.doi.org/10.1021/jp311980h | J. Phys. Chem. C 2013, 117, 9084−9091

interstitial. This shift along the z axis is analogous to the double splitting previously reported.[10,11] Similarly, a rotational motion of neighboring BH_4^- ions around the z axis and in the direction following the moving interstitial is visible. Whether the diffusion between 1/3 sites could take place through an exchange mechanism was also analyzed, where a lattice ion moves from its lattice site to a 1/3 interstitial site while the interstitial ion moves into the lattice site. This exchange mechanism is possible but significantly more expensive than the single particle jump, with a transition barrier of $E_{exchange\_TS}$ = 0.44 eV. The exchange gives two different jump lengths, 3.00 Å for the lattice ion moving to the interstitial site and 4.07 Å for the interstitial ion moving into the lattice site.

An interstitial jump from a 1/3 site to a 2/3 site has a similar barrier as the jump between 1/3 sites with $E_{1/3-2/3\_TS}$ = 0.28 eV. Because the 2/3 site is less stable than the 1/3 site, the transition barrier for going from 2/3 to 1/3 site is lowered by $E_{2/3-1/3\_TS}$ = 0.14 eV. (See Figure 3.)

The 1/3* site lies in between the 1/3 and the 2/3 sites, and because the transition barrier for going from the 1/3 site to the 1/3* site is only $E_{1/3-1/3^*\_TS}$ = 0.20 eV, there is a possibility that at lower temperatures the interstitials will equilibrate in the shallow 1/3* site. If the interstitial is then to continue from the 1/3* site to the 2/3 site it has to overcome a second transition barrier of $E_{1/3^*-2/3\_TS}$ = 0.09 eV. It is, however, more likely that the interstitial will jump back to the 1/3 site because the 1/3* sites stability toward the 1/3 site is very low ($E_{1/3^*-1/3\_TS}$ = 0.02 eV) or to other intermediate sites not identified here, for example, due to a different distribution of I^- in the lattice.

A jump from a 1/3 site to a 3/3 site is different from the previously addressed jumps because it is a jump between crystal planes, whereas the others are jumps in the same hexagonal plane. Going from the 1/3 site to the 3/3 site gives $E_{1/3-3/3\_TS}$ = 0.32 eV, whereas the opposed direction yields $E_{3/3-1/3\_TS}$ = 0.18 eV.

V^-_{Li} vacancy diffusion calculations were performed for a jump between two I^- sites as well as a jump between an I^- site and a BH_4^- site. The transition barrier between the I^- sites is found to be E_{I-I_TS} = 0.23 eV, while the barriers for the second mechanism are $E_{I\text{-}BH4\_TS}$ = 0.33 eV and $E_{BH4\text{-}I\_TS}$ = 0.28 eV. For both mechanisms the jump lengths are 4.27 Å.

The calculations show that the most favorable mechanisms for the Li^+ conduction are taking place in the hexagonal plane, the jumps with a component in the c direction having higher energy barriers; this supports the previously proposed 2D conductivity.[6,11,12]

4.2. Quasi-Elastic Neutron Scattering. Figure 4 displays the temperature dependence of the normalized elastic intensity for $^7Li(^{11}BH_4)_{0.75}I_{0.25}$ and $^7Li(^{11}BD_4)_{0.75}I_{0.25}$ and the deduced mean-square displacement $\langle u^2\rangle$ for $3\,^7Li^{11}BH_4$+^7LiI, collected during temperature scans performed from T = 3 to 430 K at a heating ramp of 2 K·min^{-1}. For each temperature, the intensity is the summation of the intensities collected on the seven detectors. The plots for the hydrogenated and deuterated samples display similar trends. The loss of intensity for the hydrogenated sample is more important because of the large incoherent cross section of hydrogen ($\sigma_H \approx 80$ barns), but the changes occur at the same temperatures, showing that there are no significant shifts detectable with this instrument in the characteristic times of the observed dynamics because of the isotope exchange. In Figure 4, three different regions can be distinguished with different evolution of $\langle u^2\rangle$ with T, corresponding to the existence of the two polymorphs (LT

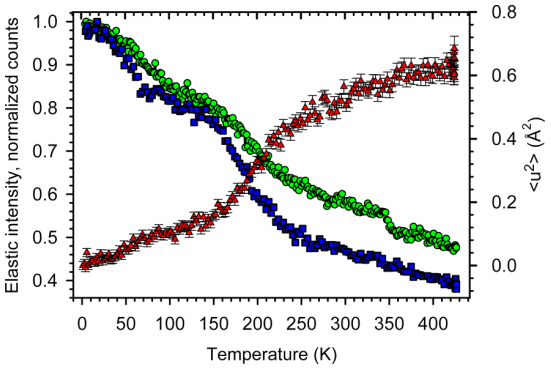

Figure 4. Evolution of the normalized elastic intensities as a function of the temperature for $^7Li(^{11}BD_4)_{0.75}I_{0.25}$ (green circles) and $^7Li(^{11}BH_4)_{0.75}I_{0.25}$ (blue squares), from 3 to 430 K, heating ramp 2 K·min^{-1}, measured with a IN10 spectrometer. Evolution of the deduced mean-square displacement for $^7Li(^{11}BH_4)_{0.75}I_{0.25}$ in the same temperature range (red triangle). $\langle u(T)^2\rangle$ is obtained from the fit of the elastic intensity with the following expression $I(T) = I(0)\cdot\exp[-Q^2\cdot\langle u(T)^2\rangle]$, where Q is taken as the average momentum transfer for the seven detectors.

structure from 3 to 180 K, HT structure from 220 to 430 K) and the transition region from ∼180 to 220 K. For the deuterated sample at ∼350 K, the evolution of the elastic intensity shows deviations when compared with the nearly monotonic decrease in the intensity obtained for the hydrogenated sample in that temperature range, indicating dynamical events not seen in the presence of hydrogen. These first measurements confirmed the two temperature ranges, where the different polymorphs exist, LT below 180 K and HT above 220 K, and show the differences between the evolution with temperature of the elastic lines of the hydrogenated and deuterated solid solutions. For the hydrogenated sample, the large drop of the elastic intensity when the temperature is increased is mainly related to the dynamics of the hydrogen atoms because of the large incoherent scattering cross section of hydrogen ($\sigma_H \approx 80$ barns). Deuterium has a much smaller scattering cross section than hydrogen ($\sigma_D \approx 2$ barns); therefore, it is possible to observe the dynamics of other atoms in the deuterated sample and especially of lithium, with a scattering cross section of $\sigma_{Li} \approx 0.8$. Boron (^{11}B) has a scattering cross section of $\sigma_B \approx 0.22$, and iodine has a scattering cross section of $\sigma_I \approx 0$ barns.

QENS spectra were collected at different temperatures and were fitted with one or two Lorentzian functions, $L(\Gamma,\omega)$, of half-width at half-maximum (hwhm), Γ, modeling the inelastic signal and a Dirac delta function, $\delta(\omega)$, modeling the elastic signal. Both functions were convoluted with the instrumental resolution function, $R(Q,\omega)$, obtained from measurements at 4 K, a temperature at which no dynamical motions were observed on the time scale of the instrument. If needed, a linear baseline $B(Q)$ was used to model the inelastic background in the quasi-elastic region, which originates from processes much faster than those observable within the time scale of the instrument used. Thus the following expression was applied:[31]

$$S^{tot}_{inc}(Q,\omega) = R(Q,\omega) \otimes (A_0(Q)\delta(\omega) + \sum A_i(Q)L(\Gamma_i,\omega)) + B(Q) \quad (2)$$

For the hexagonal $^7Li(^{11}BH_4)_{0.75}I_{0.25}$ mixture, a series of QENS spectra were recorded at constant temperatures, ranging

dx.doi.org/10.1021/jp311980h | J. Phys. Chem. C 2013, 117, 9084−9091

from 4 to 440 K. At temperatures above ~220 K, that is, temperatures at which the solid solution is in the HT hexagonal crystal structure, quasi-elastic broadenings emerging from the resolution of the instrument were observed. One Lorentzian was used to fit the spectra. At 240 and 300 K, for example, with and without the application of a bias potential (f = 1 kHz, U = 3 V, I = 0.3 mA and f = 1 kHz, U = 3 V, I = 0.4 mA, respectively) the widths where found to be Q- and potential-independent over the measured Q range at values of ~7.44 and ~15.0 μeV, respectively. These quasi-elastic lines originate from localized atomic motion[31] and according to previous QENS studies on hexagonal $LiBH_4$ correspond to the BH_4^- reorientation mechanisms.[32] A fit of the experimental elastic incoherent structure factor (A_0 in eq 1)[31] with the theoretical expression of the "high temperature model", detailed in ref 32, confirmed that the observed proton dynamic might originate from the rotation of the BH_4^- anions.

For the hexagonal $^7Li(^{11}BD_4)_{0.75}I_{0.25}$, QENS spectra were again measured at different constant temperatures from 80 to 400 K. Below 300 K and above 380 K, no clear quasi-elastic signal was observed. At low temperature (<300 K), the signal could be of too low intensity or embedded in the elastic line; at high temperature (>380 K), the signal might be too broad and only present as a flat background. Thus, given the instrumental resolution, the spectra recorded at 300 and 380 K, temperatures at which the solid solution is in the HT hexagonal crystal structure, with and without the application of a potential (f = 1000 Hz, U = 3 V and I = 0.4 mA and U = 3 V and I = 1 mA, respectively) yielded a clear diffusional broadening. Figure 5

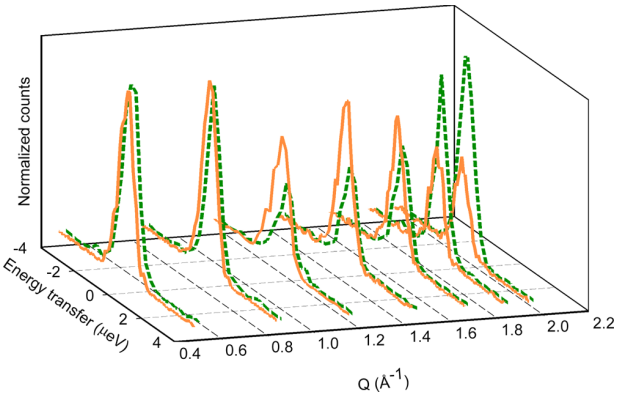

Figure 5. QENS spectra recorded for $^7Li(^{11}BD_4)_{0.75}I_{0.25}$, at 300 K, without (orange solid line) and with (green dashed line) the application of a potential (f = 1 kHz, U = 3 V, and I = 0.4 mA). Note the pronounced change in the intensity, at high Q, between the two measurements.

presents the spectra, recorded at 300 K with and without the application of the potential. One should note the large effect of the potential, with the large gain in the elastic lines intensities at high Q and the different broadenings obtained at the same Q value. See Figure 6 for an example of the spectra obtained at Q = 1.85 Å and Figure 7 showing the values of the broadening as a function of Q. No strong effect was observed at 380 K. At 300 K, two Lorentzians were used, one having a constant width of 15 μeV for all of the detectors to take into account the quasi-elastic signals from the BD_4^- reorientation. This line broadening was obtained for the hydrogenated sample at the same temperature and is used assuming, from the elastic temperature

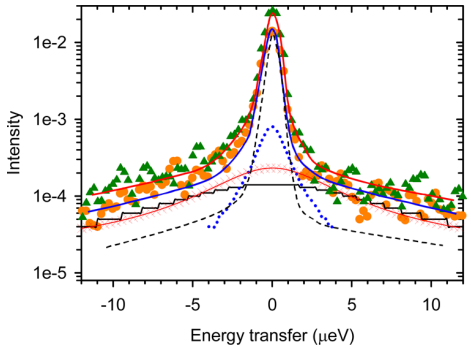

Figure 6. Example of the fitted QENS spectra taken at 300 K with (orange circles) or without the applied bias potential (green triangles) at Q = 1.85 Å. The blue and red solid lines are the total fits. The fine black line is the Lorentzian of width 15 μeV used to model to the rotation of the BD_4 tetrahedra. The broken black line is the instrumental resolution. The crossed red line is the Lorentzian modeling the lithium dynamic when the potential is applied, the dotted blue line with no potential.

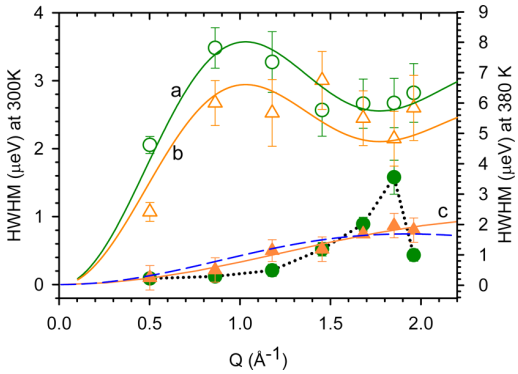

Figure 7. Q and potential-dependent half-width at half maximum (hwhm) of the Lorentzian for the nonlocalized dynamics. Upper plots: measurement performed at 380 K (hwhm values displayed on the right-side axis). Lower plots: measurements performed at 300 K (hwhm values displayed on the left-side axis). Filled circles: measurements performed with potential (f = 1 kHz, U = 3 V, and I = 0.4 mA); open circles: (f = 1 kHz, U = 3 V, and I = 1 mA); and triangles: without potential. The solid lines (a–c) are the results of the fits with the Chudley–Elliott model (eq 2) with L and τ_D fitted, the long dashed blue line is the result when only τ_D was set free to vary (L fixed to 2.3 Å), and the black broken line is to guide the eye.

scans, that there is no significant differences in the reorientation rates of the hydrogenated and deuterated tetrahedra. At 380 K, a constant flat background was used to take into account this "fast" motion (compared with the resolution of the instrument) at high temperatures. Henceforth, Q and potential-dependent quasi-elastic broadenings were found for the two temperatures. They can be attributed to nonlocalized dynamics,[31] and the hwhm values have been fitted with the Chudley–Elliott model[31] (Figure 7); that is, the dynamics observed were treated in a first approximation as a random walk diffusive mechanism of a defect in the crystal lattice. In the Chudley–Elliott model, the Q dependence of the hwhm (Γ_D) is given by:

$$\Gamma_D(Q) = \frac{\hbar}{\tau_D}\left(1 - \frac{\mathrm{Sin}(QL)}{QL}\right) \quad (3)$$

dx.doi.org/10.1021/jp311980h | J. Phys. Chem. C 2013, 117, 9084–9091

Table 2. Values for the Jump Length (L) and Rate (τ_D^{-1}) Obtained from the Chudley–Elliott Fit (eq 2) of the Experimental hwhm (Γ) of the QENS Spectra Plotted versus Q for the $^7Li(^{11}BD_4)_{0.75}I_{0.25}$ Solid Solution at 300 and 380 K with or without the Application of a Potential (3 V)[a]

temp. (K)	300		380	
potential (V)	0	0	0	3
L (Å)	1.7 ± 0.3	2.34 (fixed)	3.6 ± 0.3	4.3 ± 0.2
$\tau_D^{-1} \times 10^9$ (s^{-1})	1.25 ± 0.16	1 ± 0.2	8.3 ± 0.3	10 ± 0.16
$D \times 10^{-7}$ (cm^2/s) for $n = 4$	0.9 ± 0.3	1.4 ± 0.4	27 ± 3	46 ± 3

[a]Values of the corresponding diffusion rate for the different dimensionality.

where L is the effective jump length and τ_D is the resident time between two jumps. In this equation, the prefactor ($\hbar/\tau_D$), determines the amplitude of the maxima, whereas their abscissa are determined by the argument of the sinus (QL). When τ_D increases, the amplitude of the maxima decreases, and when the jump length L increases, the value of the abscissa decreases.

4.3. Combined Analysis. At 300 K and with an applied potential, it is not possible to fit the experimental data satisfactorily with eq 2. For the broadening obtained in the absence of an applied potential, an unconstrained fitting of the two parameters, L and τ_D, yields a short jump length of 1.7 ± 0.3 Å. This distance does not correspond to any interatomic Li distances or local minima as obtained from the DFT calculations. A fit with L fixed to 2.34 Å, the shortest jump value identified with DFT calculations, that is, for the 1/3 to 1/3* defect diffusion, was therefore performed. Any longer jump length, and particularly one corresponding to the cell parameter in the hexagonal plan (4.31 Å), would lead to the presence of a first maximum around $Q \approx 1$ $Å^{-1}$, and no such maximum is visible in the experimental data. The Chudley–Elliott least-squares fits from the constrained and unconstrained fitting yields similar values for the jump frequency, $\tau_D^{-1} \approx 1 \times 10^9$ s^{-1}, which is not surprising because it relates to the maximum of the plot. This value is in quite good agreement with the value obtained from DFT for the 1/3 to 1/3* defect diffusion. (See Table 1.) From the shallow 1/3* site, the next available site is the 2/3, but at a longer jump distance, 3.3 Å, and as previously discussed, the atom will most probably jump to the 1/3 site again. Jumps between these inequivalent sites (1/3 and 1/3*) should, however, appear in the QENS data as a localized motion and give Q-independent quasi-elastic broadenings, as would, for example, the double splitting in the Li^+ lattice sites along the z axis.[10,11] It is therefore difficult to pair the experimentally observed short jumps definitely with those determined from DFT, but because of the short distance, they are expected to originate from jumps to interstitial sites. It should be noted that the DFT calculations are effectively performed at 0 K, and the role of, for example, dynamical disorder may be significant at higher temperatures, as observed for $LiBH_4$.[10] This could affect the stability of intermediate sites, as could a different distribution of the iodine ions in the lattice, but given the complexity of the LiBH4:LiI system, it is beyond the scope of this manuscript to quantify this effect; see ref 9. It is also possible that a more complex mechanism, which is not captured by the simple Chudley–Elliott model, is needed to describe the short jumps.

The fits for the measurements at 380 K were applied successfully, especially with an applied bias, which displays a well-defined maximum in the plot. As seen in Table 2, the numerical values of τ_D^{-1} and L obtained for the different fits at 300 ($\tau_D^{-1} \approx 10^9$ s^{-1} and $L \approx 2$ Å) and 380 K ($\tau_D^{-1} \approx 10^{10}$ s^{-1} and $L \approx 4$ Å) indicate different mechanisms at the two temperatures. Furthermore, it should be noted that the application of the potential is influencing the observed dynamics.

If the dynamics is diffusion-related, then the diffusion rates can be calculated from[31]

$$D = L^2/(n\tau_D) \quad (4)$$

where n = 2, 4, or 6 depending on the dimensionality of the diffusion, that is, 1, 2, or 3, respectively. Because the DFT calculations show favorable results for a 2D conductivity, only the values of D obtained for $n = 4$ are presented in Table 2. At 300 K, the values are, not surprisingly, lower than those published for the high-temperature phase of pure $LiBH_4$ at 535 K,[11] (5.82 and 2.28) $\times 10^{-6}$ cm^2/s,[6] but when translated to 535 K and assuming an Arrhenius temperature dependency, values $>10^{-4}$ cm^2/s are obtained, in agreement with the higher conductivity measured for the solid solution compared with that of the pure compound.[9] At 380 K, the diffusion rates are found to be on the same order of magnitude as the published one even though the temperature is lower. Again, this is in agreement with the higher conductivity measured for the solid solution than that for the pure compound[9] and a likely consequence of the changes in directional bonding associated with the I/BH_4 substitution.

5. CONCLUSIONS

To summarize, the QENS results show that two different jump lengths were observed at 300 and 380 K. At 300 K, the observed diffusion events have shorter jump length than the unit cell dimensions, and at 380 K, the lengths correspond to the unit cell dimensions.

The strong effect due to the applied bias potential at 300 K on the observed broadening and intensities of the QENS spectra should be noted. Because of the limited data available, it is, unfortunately, not possible to quantify this effect, but the application of the potential is expected to increase the V^-_{Li}/Li^+_{int} defect concentrations and mobilities. Under an applied bias, a significant number of additional defects will be created at the electrode interfaces, and the lifetime of the Frenkel pairs will also increase due to the charge difference (outlined below), but further experiments are needed to quantify these effects.

The super-ionic conductivity in the $Li(BH_4)_{(1-x)}I_x$ must originate from the high mobility of lithium defects in the hexagonal crystal lattice. The DFT calculations show that Frenkel pairs have a low formation energy (0.44 eV) and are thus present in a concentration of $\sim 5 \times 10^{18}$ cm^{-3} in a $Li(BH_4)_{0.75}I_{0.25}$ solid solution at room temperature, even without an applied bias. The formation energy of individual interstitials and vacancies is therefore expected to be very low, and the solid solution can be classified as a Type I ionic conductor, after Rice and Roth classification of ionic solids[33,34] and for which the conduction mechanism is governed by

dx.doi.org/10.1021/jp311980h | J. Phys. Chem. C 2013, 117, 9084–9091

vacancy migration. The DFT results for the defect diffusion are nicely supported by the QENS results obtained at 380 K. Indeed, we observe diffusional motion with jump lengths of about one unit cell and diffusion rates of $\sim 8 \times 10^9$ s^{-1}, in agreement with the calculated direct jumps between the more favorable interstitial and vacancy sites, with comparable jump lengths and rates of 8.3×10^9 s^{-1} for the direct Li^+_{int} 1/3 to 1/3 site jumps and 9.8×10^8 s^{-1} for the V^-_{Li}, I^- to BH_4^- migration. As mentioned, the typically short lifetime of the thermal Frenkel pairs will increase under an applied bias, which will drive the oppositely charged Li^+_{int} and V^-_{Li} defects apart. In a real battery application, the main source of defects in that case will be generated at the electrolyte/electrode interfaces, where Li^+ ions leave and enter the electrolyte.

The calculations show that the most favorable mechanism for the Li^+ conduction is taking place in the hexagonal plane, with the jumps with a component in the z direction having higher energy barriers, supporting a 2D conductivity, as previously suggested.[6,11,12] It should also be noted that the D values are almost doubled when a 3 V potential was applied.

An approach to directly determine the dimensionality of the conductivity would be to perform QENS measurements using a single crystal of the borohydride, but sufficiently large single crystals are difficult to obtain. Finally, more QENS experiments at different temperatures or energy resolution combined with further calculations on the role of disorder could yield even more insight into this promising electrolyte.

AUTHOR INFORMATION

Corresponding Author

*E-mail: teve@dtu.dk.

Notes

The authors declare no competing financial interest.

ACKNOWLEDGMENTS

We acknowledge support from the Copenhagen Graduate School for Nano Science and Nano Technology, Center for Atomic-scale Materials Design (CAMD), Catalysis for Sustainable Energy (CASE), Danish Center for Scientific Computing and the ReLiable project funded by the Danish Council for Strategic Research − Program Commission on Sustainable Energy and Environment (project #11-116792).

REFERENCES

(1) Shukla, A. K.; Prem Kumar, T. Materials for Next-Generation Lithium Batteries. *Curr. Sci.* **2008**, *94*, 314−332.

(2) Mizushima, K.; Jones, P. C.; Wiseman, P. J.; Goodenough, J. B. A New Cathode Material for Batteries of High Energy Density. *Mater. Res. Bull.* **1980**, *15*, 783−789.

(3) Thackeray, M. M.; David, W. I. F.; Bruce, P. G.; Goodenough, J. B. Lithium Insertion into Manganses Spinels. *Mater. Res. Bull.* **1983**, *18*, 461−472.

(4) Armand, M.; Tarascon, J.-M. Building Better Batteries. *Nature* **2008**, *451*, 652−657.

(5) Tarascon, J.-M. Key Challenges in Future Li-Battery Research. *Philos. Trans. R. Soc., A* **2010**, *368*, 3227−3241.

(6) Matsuo, M.; Nakamori, Y.; Orimo, S.; Maekawa, H.; Takamura, H. Lithium Superionic Conduction in Lithium Borohydride Accompanied by Structural Transition. *Appl. Phys. Lett.* **2007**, *91*, 224103.

(7) Maekawa, H.; Matsuo, M.; Takamura, H.; Ando, M.; Noda, Y.; Karahashi, T.; Orimo, S. Halide-Stabilized $LiBH_4$, a Room-Temperature Lithium Fast-Ion Conductor. *J. Am. Chem. Soc.* **2009**, *131*, 894−895.

(8) Oguchi, H.; Matsuo, M.; Hummelshøj, J. S.; Vegge, T.; Nørskov, J. K.; Sato, T.; Miura, Y.; Takamura, H.; Maekawa, H.; Orimo, S. Experimental and Computational Studies on Structural Transitions in the $LiBH_4$−LiI Pseudobinary System. *Appl. Phys. Lett.* **2009**, *94*, 141912.

(9) Sveinbjörnsson, D.; Myrdal, J. S. G.; Blanchard, D.; Bentzen, J. J.; Hirata, T.; Mogensen, M. B.; Norby, P.; Orimo, S.-I.; Vegge, T. Effect of Heat Treatment on the Lithium Ion Conduction of the $LiBH_4$−LiI Solid Solution. *J. Phy. Chem. C* **2013**, *117*, 3249−3257.

(10) Ikeshoji, T.; Tsuchida, E.; Morishita, T.; Ikeda, K.; Matsuo, M.; Kawazoe, Y.; Orimo, S. Fast-Ionic Conductivity of Li^+ in $LiBH_4$. *Phy. Rev. B.* **2011**, *83*, 144301-1−144301-5.

(11) Aeberhard, P.; Williams, S.; Evans, D.; Refson, K.; David, W. Ab Initio Nonequilibrium Molecular Dynamics in the Solid Superionic Conductor $LiBH_4$. *Phys. Rev. Lett.* **2012**, *108*, 095901-1−09590-5.

(12) Epp, V.; Wilkening, M. Fast Li Diffusion in Crystalline $LiBH_4$ due to Reduced Dimensionality: Frequency-Dependent NMR Spectroscopy. *Phys. Rev. B.* **2010**, *82*, 020301-4−020301-7.

(13) Blanchard, D.; Maronsson, J. B.; Riktor, M. D.; Kehres, J.; Sveinbjörnsson, D.; Bardají, E. G.; Léon, A.; Juranyi, F.; Wuttke, J.; Lefmann, K.; et al. Hindered Rotational Energy Barriers of BH_4^- Tetrahedra in β-$Mg(BH_4)_2$ from Quasielastic Neutron Scattering and DFT Calculations. *J. Phys. Chem. C.* **2012**, *116*, 2013−2023.

(14) Blanchard, D.; Riktor, M. D.; Maronsson, J. B.; Jacobsen, H. S.; Kehres, J.; Sveinbjörnsson, D.; Bardají, E. G.; Léon, A.; Juranyi, F.; Wuttke, J.; et al. Hydrogen Rotational and Translational Diffusion in Calcium Borohydride from Quasielastic Neutron Scattering and DFT. *J. Phys. Chem. C.* **2010**, *114*, 20249−20257.

(15) Voss, J.; Shi, Q.; Jacobsen, H. S.; Zamponi, M.; Lefmann, K.; Vegge, T. Hydrogen Dynamics in Na_3AlH_6 - A Combined Density Functional Theory and Quasielastic Neutron Scattering Study. *J. Phys. Chem. B.* **2007**, *111*, 3886−3892.

(16) Bahn, S.; Jacobsen, K. An Object-Oriented Scripting Interface to a Legacy Electronic Structure Code. *Comput. Sci. Eng.* **2002**, *4*, 56−66.

(17) Kohn, W.; Sham, L. J. Self-Consistent Equations Including Exchange and Correlation Effects. *Phys. Rev.* **1965**, *140*, A1133-1−A1133-6.

(18) Hohenberg, P.; Kohn, W. Inhomogeneous Electron Gas. *Phys. Rev.* **1964**, *136*, 864−871.

(19) Enkovaara, J.; Rostgaard, C.; Mortensen, J. J.; Chen, J.; Dułak, M.; Ferrighi, L.; Gavnholt, J. Electronic Structure Calculations with GPAW: A Real-Space Implementation of the Projector Augmented-Wave Method. *J. Phys.: Condens. Matter* **2010**, *22*, 253202-1−253202-24.

(20) Mortensen, J. J.; Hansen, L. B.; Jacobsen, K. W. Real-Space Grid Implementation of the Projector Augmented Wave Method. *Phys. Rev. B.* **2005**, *71*, 035109-1−035109-11.

(21) Blöchl, P. E. Projector Augmented-Wave Method. *Phys. Rev.* **1994**, *50*, 17953-1−17953-27.

(22) Perdew, J.; Burke, K.; Ernzerhof, M. Generalized Gradient Approximation Made Simple. *Phys. Rev. Lett.* **1996**, *77*, 3865−3868.

(23) Henkelman, G.; Jónsson, H. Improved Tangent Estimate in the Nudged Elastic Band Method for Finding Minimum Energy Paths and Saddle Points. *J. Chem. Phys.* **2000**, *113*, 9978−9985.

(24) Jonsson, H.; Mills, G.; Jacobsen, K. W. *Classical and Quantum Dynamics in Condensed Phase Systems*; Berne, B. J., Cicotti, G., Coker, D. F., Eds.; World Scientific: River Edge, NJ, 1998.

(25) Henkelman, G.; Uberuaga, B.; Jónsson, H. A Climbing Image Nudged Elastic Band Method for Finding Saddle Points and Minimum Energy Paths. *J. Chem. Phys.* **2000**, *113*, 9901−9904.

(26) Vineyard, G. Frequency Factors and Isotope Effects in Solid State Rate Processes. *J. Phys. Chem. Solids.* **1957**, *3*, 121−127.

(27) Łodziana, Z.; Vegge, T. Structural Stability of Complex Hydrides: $LiBH_4$ Revisited. *Phys. Rev. Lett.* **2004**, *93*, 145501.

(28) Łodziana, Z.; Vegge, T. Łodziana and Vegge Reply. *Phys. Rev. Lett.* **2006**, *97*, 119602.

(29) Filinchuk, Y.; Chernyshov, D.; Cerny, R. Lightest Borohydride Probed by Synchrotron X-ray Diffraction: Experiment Calls for a New Theoretical Revision. *J. Phys. Chem. C.* **2008**, *112*, 10579−10584.

(30) Azuah, R. T.; Kneller, L. R.; Qiu, Y.; Brown, C. M.; Copley, J. R. D.; Dimeo, R. M. DAVE: A Comprehensive Software Suite. *J. Res. Natl. Inst. Stand. Technol.* **2009**, *114*, 341−358.
(31) Bée, M. *Quasielastic Neutron Scattering*; Adam Hilger: Philadelphia, PA, 1988.
(32) Verdal, N.; Udovic, T. J.; Rush, J. J. The Nature of BH_4 Reorientations in Hexagonal $LiBH_4$. *J. Phys. Chem. C.* **2012**, *116*, 1614−1618.
(33) Rice, M. J.; Roth, W. L. Ionic Transport in Super Ionic Conductors: a Theoretical Model. *J. Solid State Chem.* **1972**, *4*, 294−310.
(34) Chandra, S. *SuperIonic Solids*; North-Holland Publishing Company: New York, 1981.

Paper C

Journal of Solid State Chemistry 211 (2014) 81–89

Contents lists available at ScienceDirect

Journal of Solid State Chemistry

journal homepage: www.elsevier.com/locate/jssc

Ionic conductivity and the formation of cubic CaH_2 in the $LiBH_4$–$Ca(BH_4)_2$ composite

Dadi Sveinbjörnsson [a], Didier Blanchard [a], Jon Steinar Gardarsson Myrdal [a,b], Reza Younesi [a], Rasmus Viskinde [a], Marit Dalseth Riktor [c], Poul Norby [a], Tejs Vegge [a,*]

[a] Department of Energy Conversion and Storage, Technical University of Denmark, Frederiksborgvej 399, P.O. Box 49, DK-4000 Roskilde, Denmark
[b] Center for Atomic-Scale Materials Design, Department of Physics, Technical University of Denmark, Anker Engelunds Vej 1, DK-2800 Lyngby, Denmark
[c] Physics Department, Institute for Energy Technology, Instituttveien 18, P.O. Box 40, NO-2027 Kjeller, Norway

ARTICLE INFO

Article history:
Received 8 October 2013
Received in revised form
4 December 2013
Accepted 8 December 2013
Available online 16 December 2013

Keywords:
Lithium borohydride
Calcium borohydride
Calcium hydride
Solid electrolyte
Ionic conductivity
X-ray diffraction

ABSTRACT

$LiBH_4$–$Ca(BH_4)_2$ composites were prepared by ball milling. Their crystal structures and phase composition were investigated using synchrotron X-ray diffraction and Rietveld refinement, and their ionic conductivity was measured using impedance spectroscopy. The materials were found to form a physical mixture. The composites were composed of α-$Ca(BH_4)_2$, γ-$Ca(BH_4)_2$ and orthorhombic $LiBH_4$, and the relative phase quantities of the $Ca(BH_4)_2$ polymorphs varied significantly with $LiBH_4$ content. The formation of small amounts of orthorhombic CaH_2 and cubic CaH_2 in a CaF_2-like structure was observed upon heat treatment. Concurrent formation of elemental boron may also occur. The ionic conductivity of the composites was measured using impedance spectroscopy, and was found to be lower than that of ball milled $LiBH_4$. Electronic band structure calculations indicate that cubic CaH_2 with hydrogen defects is electronically conducting. Its formation along with the possible precipitation of boron therefore has an effect on the measured conductivity of the $LiBH_4$–$Ca(BH_4)_2$ composites and may increase the risk of an internal short-circuit in the cells.

1. Introduction

Research on lithium batteries is an important part of developing more sustainable and more efficient energy storage methods. Lithium batteries are dominant in the portable electronics sector today. However, for applications on a larger scale, such as in the transportation sector, substantial improvements are needed in terms of energy density, safety, charge–discharge cycle lifetime and price. Conventional Li-ion batteries use electrolytes made of organic liquids or gels. The main advantage of such electrolytes is their high Li^+ conductivity. They are, however, flammable and can cause safety issues. They can also allow for dendrite formation at the electrode–electrolyte interface, resulting in a decrease in cell capacity and a limited charge–discharge cycle life [1–3].

The usage of solid-state electrolytes, instead of the currently used liquids or gels, would increase the safety and should lead to an extended cycle life of the batteries. It is, however, challenging to develop solid electrolyte materials with sufficient chemical and electrochemical stability while offering high Li^+ conduction but negligible electronic conduction [4]. There are many currently known crystalline solid-state Li^+ conductors [2]. Among these are Li_3N [5], perovskite type oxides such as lithium lanthanum titanate (LLTO) [6–8], garnet type structures such as $Li_6BaLa_2Ta_2O_{12}$ [9], NASICON type structures [10,11], LISICON type structures [12] and $Li_{10}GeP_2S_{12}$ [13]. Most of these materials, however, have problems such as too low decomposition voltage (Li_3N), instability towards contact with elemental lithium (LLTO and NASICON) or too high electronic conductivity (LLTO) [14].

A Li^+ conductivity of 1 mS/cm is often cited as the minimum conductivity required for electrolytes to function well in consumer batteries [15,16]. For comparison 1M $LiPF_6$ in EC-DMC (ethylene carbonate plus dimethyl carbonate), a widely used organic liquid electrolyte, has a Li^+ conductivity of 12 mS/cm at 27 °C [17]. All above-mentioned crystalline solid electrolytes have considerably lower Li^+ conductivities, with the exception of $Li_{10}GeP_2S_{12}$ which has a Li^+ conductivity of 12 mS/cm at 27 °C [13].

Lithium borohydride has been investigated extensively in recent years, both as a hydrogen storage material [18–23] and as a crystalline solid electrolyte material for lithium batteries [24–26]. It is lightweight (0.666 g/cm^3) and has been shown to be electrochemically stable up to 5 V [27]. At room temperature, $LiBH_4$ has an orthorhombic crystal structure (*Pnma*) with a low Li^+ conduction (approx. 10^{-8} S/cm at 30 °C), but undergoes a reversible phase transition at around 110 °C to a hexagonal crystal structure ($P6_3m_c$) with a high Li^+ conduction (approx. 10^{-3} S/cm at 120 °C) [24,28]. The hexagonal structure can be stabilized at

* Corresponding author. Fax: +45 46775688.
E-mail address: teve@dtu.dk (T. Vegge).

0022-4596/$ - see front matter © 2013 Elsevier Inc. All rights reserved.
http://dx.doi.org/10.1016/j.jssc.2013.12.006

room temperature by adding lithium halides (LiI, LiBr and LiCl) [29,30]. Such addition has been found to result in an even higher Li^+ conductivity than seen in hexagonal $LiBH_4$. Studies on the structural and Li^+ conduction properties of the $LiBH_4$–LiI solid solution have recently been published [31–34].

Calcium borohydride has also been investigated extensively as a hydrogen storage material [35–42]. The crystal structures of $Ca(BH_4)_2$ were only resolved relatively recently, and four polymorphs of calcium borohydride have been characterized. α-$Ca(BH_4)_2$ has an orthorhombic structure (*Fddd* [35] or *F*2*dd* [43]). β-$Ca(BH_4)_2$ has a tetragonal crystal structure (*P*-4[43] or $P4_2/m$ [44]). β-$Ca(BH_4)_2$ is sometimes referred to as a high-temperature polymorph, as it has been observed to become the dominant phase above 130 °C [44]. γ-$Ca(BH_4)_2$ has an orthorhombic crystal structure (*Pbca*) [45]. The fourth polymorph, α′-$Ca(BH_4)_2$, is a high-temperature modification of the α structure that appears by a second order phase transition at around 220 °C. This polymorph has a tetragonal crystal structure (*I*-42*d*, a supergroup of *F*2*dd*) [43] and was not observed in this work.

As the enthalpy differences between the α, β, and γ polymorphs are rather small (35–135 meV) [45,46], these usually coexist. The relative quantity of the phases can even differ significantly between batches [42]. As shown in this work, the addition of $LiBH_4$ possibly has a large effect on the relative quantities of the $Ca(BH_4)_2$ polymorphs, which depend heavily on the mixing ratio of the two compounds. Furthermore, the possibility of Ca^{2+} substitution in $LiBH_4$ is discussed in this work, as such introduction of relatively large cations in $LiBH_4$ could lead to compensating vacancies, which would likely enhance the Li^+ conduction. As an example, divalent doping of chlorides has been found to increase their ionic conductivity [47].

Reports on the structure and hydrogen storage properties of the $LiBH_4$–$Ca(BH_4)_2$ composite have been published [48,49]. Accounts of the nature of the $LiBH_4$–$Ca(BH_4)_2$ mixtures differ, however, as Fang et al. reported on the formation of a dual-cation borohydride $LiCa(BH_4)_3$, while Lee et al. concluded that $LiBH_4$ and $Ca(BH_4)_2$ coexist as a physical mixture but not as a compound or a solid solution. We shall seek to resolve this controversy by reporting on the structural properties of the $LiBH_4$–$Ca(BH_4)_2$ mixtures using synchrotron X-ray diffraction. In the present work we report on the crystal structures and the phase composition of $(1-x)LiBH_4+xCa(BH_4)_2$ mixtures in various ratios. The main focus of the work is on the ionic conductivity of the composites and on the formation of CaH_2 in both orthorhombic and cubic structures that was observed upon heat treatment of the $LiBH_4$–$Ca(BH_4)_2$ composites. Furthermore, we will discuss how the low chemical stability of $LiBH_4$–$Ca(BH_4)_2$, illustrated by the formation of CaH_2, affects the suitability of the mixtures for usage as solid electrolytes, and how this can increase the risk of a short-circuit in the cell.

2. Experimental and computational methods

2.1. Preparation of the composites

$LiBH_4$ powder (purity 95%) and $Ca(BH_4)_2$ were purchased from Alfa Aesar Co. and Sigma Aldrich Co. respectively. The $(1-x)LiBH_4+xCa(BH_4)_2$ samples were prepared in nine different ratios, with x ={0, 0.125, 0.1875 0.25, 0.33, 0.5, 0.67, 0.75, 1.0}. The mixing was performed by planetary ball milling under Ar atmosphere. In each milling, a stainless steel vial with an inner volume of 250 ml was rotated at 650 rpm for 2 h on a Fritsch Pulverisette P6. 1.0, 1.5 or 2.0 g of precursor powder were inserted into the vial for each milling along with 25 tungsten carbide balls, resulting in a sample to balls mass ratios of 1/400, 1/300 or 1/200 respectively.

2.2. Powder X-ray diffraction (XRD)

The samples were characterized using powder X-ray diffraction (XRD). The measurements were performed on the as-milled samples. The diffraction patterns used in this work were obtained at three different instruments.

The diffraction patterns of the $(1-x)LiBH_4+xCa(BH_4)_2$ samples with x={0.125, 1.0} were measured at the BM01A beam line of the Swiss-Norwegian Beamlines (SNBL) located at the European Synchrotron Radiation Facility (ESRF) in Grenoble, France. The samples were mounted in glass capillaries sealed under Ar atmosphere using an epoxy adhesive. The two-dimensional diffraction data were collected at the Pilatus@SNBL diffractometer, using a Pilates 2 M detector, with a distance of 310 mm between the sample and the detector. The wavelength was 0.69386 Å. Data processing was carried out using the SNBL Tool Box [50]. The two-dimensional data were calibrated with a NIST LaB_6 standard sample.

The diffraction patterns of the samples with x={0.25, 0.5} were measured at the beamline I11 located at the Diamond Light Source in Oxfordshire, England. The sample mounting was the same as described above. A Mythen II PSD detector was used at 2θ angles ranging from 1° to 91°. The wavelength was 0.82712 Å. The data were calibrated using Si as an external standard.

The diffraction patterns of the samples with x={0,.1875, 0.33, 0.67, 0.75} were measured using a Cu $K\alpha$ Bruker D8 diffractometer with a Bragg–Brentano geometry, operating at 40 kV and 40 mA. The samples were sealed under Ar atmosphere in an airtight polyethylene sample holder from Bruker Co. The exposure time was 3 s/step with a step size of 0.02°. The measurements were performed using a variable divergence slit. After the measurement, the intensity of the data was corrected for the variable slit size and the $K\alpha_2$ signal was subtracted. All XRD measurements were performed at room temperature. The synchrotron data were integrated into one-dimensional powder diffraction patterns using the Fit2D software [51].

For all diffraction patterns, Rietveld refinement was carried out using the GSAS software [52]. The phase factors, the unit cell parameters as well as the strain and the size broadening parameters were refined for all phases. Pseudo-Voigt profiles were used for modeling the shapes of the diffraction peaks. The background signal was modeled using a polynomial expression, and the zero point was refined. The isotropic thermal motion parameters were refined for all atoms except hydrogen and preferred diffraction orientations in the powder were modeled if needed. The occupancy of Ca^{2+} was refined in α-$Ca(BH_4)_2$ and the γ-$Ca(BH_4)_2$ phases. The resulting values for γ-$Ca(BH_4)_2$ are shown in Table 1. For α-$Ca(BH_4)_2$ the refinement of the Ca^{2+} positions showed full occupancies. The peak to parameter ratio was greater than 2 for all refinements and greater than 5 for most refinements. The weighted profile agreement factor R_{wp} at the end of the refinements ranged from 2.2% to 4.25% and the data were refined for convergence, i.e. until the squared sum of all parameter shifts divided by the estimated standard deviation (i.e. $\Sigma(\text{shift}/\sigma)^2$) reached <0.1.

2.3. Impedance spectroscopy (EIS)

The conductivities of the samples were measured by AC impedance spectroscopy using a Parstat 2273 potentiostat. The ball-milled powder was pressed into pellets with a diameter of 13 mm and a thickness of approx. 2 mm. Lithium foil was pressed onto both faces of the pellets as electrodes. The powder and the lithium foil were pressed simultaneously at 1 t/cm^2. The porosity of the pellets was found to be around 0.4. All preparation and measurements were carried out under Ar atmosphere. The frequency range of the impedance measurements was set from

Table 1
The relative phase quantities (in weight percentage) in the $(1-x)LiBH_4+xCa(BH_4)_2$ samples, obtained from the Rietveld refinement of the XRD data. There are large variations in the phase quantities of the α and γ phases of $Ca(BH_4)_2$ with $LiBH_4$ content, but the β phase is only present in pure $Ca(BH_4)_2$. The phase quantity of orthorhombic $LiBH_4$ is expected to equal the actual $LiBH_4$ weight percentage in each sample. This means that, for an optimal refinement, the values of the fifth column of the table are expected to approach those in the sixth column. The Rietveld refinements are, however, somewhat imperfect with regard to this, most probably due to the low scattering power of $LiBH_4$ relative to $Ca(BH_4)_2$. The rightmost column of the table shows the refined Ca^{2+} occupancies in the α-Ca $(BH_4)_2$ phase, but only for those mixtures for which synchrotron data were available. The Ca^{2+} occupancies in the β-$Ca(BH_4)_2$ and γ-$Ca(BH_4)_2$ phases were found to be 1.0 in all diffractograms.

Sample (x in mol)	*α-Ca $(BH_4)_2$ (wt%)*	*β-Ca $(BH_4)_2$ (wt%)*	*γ-Ca $(BH_4)_2$ (wt%)*	*$LiBH_4$ LT (wt%)*	*Actual $LiBH_4$ wt% in sample*	*Ca^{2+} occupancy in α-$Ca(BH_4)_2$*
0.0	0.0	0.0	0.0	100.0	100.00	N/A
0.125	24.1	0.0	3.2	72.7	68.61	0.972
0.1875	22.1	0.0	13.2	64.7	57.50	N/A
0.25	39.0	0.0	10.6	50.4	48.37	0.931
0.33	6.2	0.0	46.5	47.3	38.50	N/A
0.50	8.7	0.0	62.4	28.9	23.80	0.975
0.67	18.0	0.0	65.0	17.0	12.97	N/A
0.75	15.8	0.0	62.7	21.5	9.43	N/A
1.00	0.0	36.9	63.1	0.0	0.00	N/A

100 mHz to 1 MHz. The samples were heated up from 30 °C to 100 °C in steps of 5 °C and cooled down to 30 °C using the same step size. The samples were equilibrated at a constant temperature for at least 40 min prior to each measurement.

2.4. Energy-dispersive X-ray spectroscopy (EDS)

A Hitachi TM3000 scanning electron microscope (SEM) operating at 15 kV was used for performing EDS on a $0.875LiBH_4+0.125Ca(BH_4)_2$ sample after heat treating it up to a temperature of 100 °C during the impedance spectroscopy measurements. The EDS samples were prepared by applying a thin layer of powder on carbon tape. The samples were transferred to the SEM instrument under Ar atmosphere. Elemental mapping was performed after each area scan or line scan of the sample.

2.5. X-ray photoelectron spectroscopy (XPS)

XPS measurements were performed on a $0.875LiBH_4+0.125Ca(BH_4)_2$ sample after heat treating it up to a temperature of 100 °C during the impedance spectroscopy measurements. A PHI 5500 spectrometer was used, with monochromatic Al *Kα* radiation (1487 eV) and an electron emission angle of 45°. All the XPS spectra were energy calibrated by the hydrocarbon peak positioned at the binding energy of 285.0 eV. The XPS samples were prepared by applying a thin layer of powders on copper tape. The samples were transferred from a glove box to the XPS analysis chamber using a specially built airtight argon-filled chamber to avoid contamination from the air.

2.6. Electronic structure calculations

All electronic structure calculations presented in this work were performed using density functional theory (DFT) [53,54] as it is implemented in the GPAW code [55,56], using the atomic simulation environment (ASE) [57]. GPAW is based on real space grids and uses the projector-augmented wave method (PAW) to describe non-valence electrons [58,59]. All atomic structural relaxations were calculated using the PBE exchange and correlation functional [60] with a 0.15 Å grid spacing and a (4,4,4) k-point mesh. Each calculation was continued until all forces were below 0.01 eV/Å. Calculations of charged vacancy defects were performed with an extra electron in the computational supercell. The extra electron was treated exactly like all other electrons in the DFT calculations, but to prevent an infinite charge build-up over the periodic images of the cell, an equal opposite charge was smeared uniformly over the cell. Because of the uniform distribution of the compensation charge, its effect on the chemistry of the cell is negligible. Band gap calculations were performed using the GLLB-sc exchange and correlation functional [61], which has been shown to improve band gap description significantly from standard GGA functionals [62].

3. Results and discussion

3.1. Crystal structure and phase composition

The diffraction patterns of pure $LiBH_4$, pure $Ca(BH_4)_2$ and four composites of the two compounds are shown in Fig. 1, along with a Rietveld refinement of each diffraction pattern. The diffraction pattern presented for $LiBH_4$ is from a ball-milled sample. For Ca $(BH_4)_2$, diffraction patterns were acquired for as-received and ball milled powders. We present only the diffraction pattern of the as-received compound since the milling alters the crystallinity of the powder, reducing the quality of the diffraction pattern and the Bragg peak intensities of the already poorly scattering $Ca(BH_4)_2$ powder. It was thus not possible to perform a trustworthy Rietveld refinement of the milled $Ca(BH_4)_2$.

The relative phase quantities of the mixtures in weight percentage, as obtained by Rietveld refinement, are shown in Table 1. The milled $LiBH_4$ sample only contains orthorhombic $LiBH_4$, as expected. The pure, as-received $Ca(BH_4)_2$ sample contains β-$Ca(BH_4)_2$ and γ-$Ca(BH_4)_2$, but no α-$Ca(BH_4)_2$ is present.

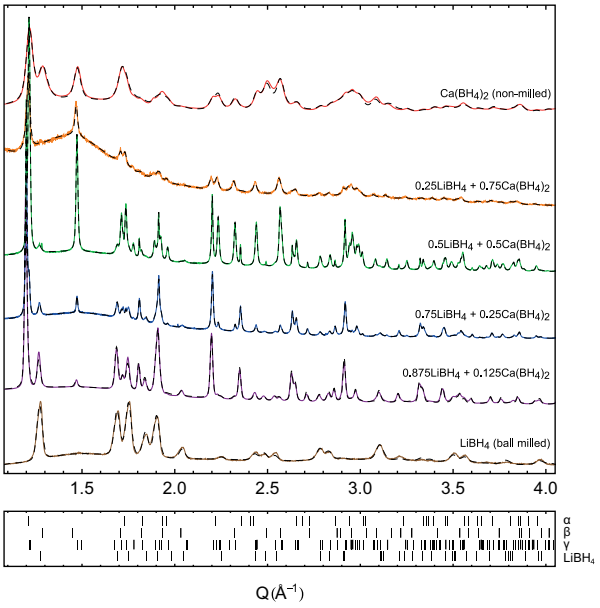

Fig. 1. Powder X-ray diffraction patterns for different ratios of $(1-x)LiBH_4+xCa(BH_4)_2$. The solid, colored lines show the measured data, the dashed, black lines show the Rietveld refinement of each measurement. The tick marks below the diffraction patterns show the locations of the Bragg reflections of α-$Ca(BH_4)_2$, β-Ca $(BH_4)_2$ γ-$Ca(BH_4)_2$ and orthorhombic $LiBH_4$. No other phases were detected in the samples. The diffraction pattern of pure $LiBH_4$ only contains orthorhombic $LiBH_4$. In the diffraction pattern of pure $Ca(BH_4)_2$, β-$Ca(BH_4)_2$ and γ-$Ca(BH_4)_2$ coexist, but no α-$Ca(BH_4)_2$ is detected. In the $(1-x)LiBH_4+xCa(BH_4)_2$ mixtures, α-$Ca(BH_4)_2$, γ-Ca $(BH_4)_2$ and orthorhombic $LiBH_4$ coexist, but no β-$Ca(BH_4)_2$ is detected. All data in the Figure comes from synchrotron measurements except for the sample with $x = 0.75$. (For interpretation of the references to color in this figure caption, the reader is referred to the web version of this paper.)

All composites are composed of orthorhombic $LiBH_4$, α-$Ca(BH_4)_2$ and γ-$Ca(BH_4)_2$ only; no other phases or new compounds are formed during the ball milling. Note that the amount of $LiBH_4$ in the composite samples is generally overestimated compared to the actual mixing ratios of the samples. This indicates the accuracy of the Rietveld refinements performed on $LiBH_4$, which is composed of elements with low electron densities and is thus a poor X-ray scatterer relative to $Ca(BH_4)_2$. Small sample inhomogeneities may also contribute to the discrepancy in the $LiBH_4$ phase quantities.

As mentioned in the introduction, the enthalpy differences between the different $Ca(BH_4)_2$ phases are small, and therefore the relative phase quantities of the $Ca(BH_4)_2$ polymorphs are very sensitive to modifications of the mixture. Interestingly, no β-$Ca(BH_4)_2$ is detected in the composites although it is present in pure $Ca(BH_4)_2$. This is consistent with the findings of Lee et al. [48]. The relative quantities of the two remaining $Ca(BH_4)_2$ phases are very sensitive to any modifications of the mixture. α-$Ca(BH_4)_2$ is found to have the largest relative phase quantity for $x=0.25$. For samples with large amounts of $LiBH_4$, only small amounts of γ-$Ca(BH_4)_2$ are found, but for composites with $x \geq 0.5$ it becomes the dominant phase with a similar relative phase quantity as in the pure $Ca(BH_4)_2$ sample.

The formation of α-$Ca(BH_4)_2$, which is not present in the as-received $Ca(BH_4)_2$, is either facilitated by the introduction of $LiBH_4$ (even in small amounts), or simply by the ball milling process. As already mentioned, the crystallinity of the pure, ball-milled $Ca(BH_4)_2$ samples was very poor, and it was unfortunately not possible to deduce the relative quantities of the $Ca(BH_4)_2$ polymorphs from the diffraction pattern. It can thus not be inferred with certainty whether the polymorph changes in $Ca(BH_4)_2$ take place due to $LiBH_4$ addition or due to the milling itself. It is, however, clear that the introduction of $LiBH_4$ increases the crystallinity of the $Ca(BH_4)_2$ polymorphs, as compared to the as-received and ball-milled $Ca(BH_4)_2$ samples.

The lattice parameters in all samples were found to deviate by less than 1% from those previously published for orthorhombic $LiBH_4$ [28], α-$Ca(BH_4)_2$ [35], β-$Ca(BH_4)_2$ [44] and γ-$Ca(BH_4)_2$ [45]. The lattice parameters of the composite samples are in all cases very similar to those of the phases in the precursor compounds and do not change much with the mixing ratio x. We therefore conclude that the $(1-x)LiBH_4+xCa(BH_4)_2$ composites are physical mixtures rather than solid solutions. This finding is in good agreement with those previously reported by Lee et al. [48].

After ball milling, a fraction of each sample was annealed in a glass container at 100 °C for 60 h under Ar atmosphere. XRD measurements of the annealed powders show that such heat treatment does not change the phase compositions, which remain very close to those presented in Table 1. It was therefore not expected that the heat treatment during the impedance spectroscopy measurements would alter the phase composition of the samples.

3.2. CaH_2 formation

When the samples were heated up to 100 °C during the impedance spectroscopy measurements (under Ar atmosphere), a new phase formed over the course of a few hours. This phase consisted of a black layer, growing at the interfaces between the Li electrodes and the electrolyte. This surprising finding was observed even if no potential was applied to the sample. In order to identify this phase, synchrotron XRD was performed on a black colored part of a sample. The resulting diffraction pattern is shown in Fig. 2, along with a Rietveld refinement of the data. The majority of the powder consists of α-$Ca(BH_4)_2$ and orthorhombic $LiBH_4$. However, the data refinement reveals two additional phases that were not detected in the diffraction patterns of the as-milled samples shown in Fig. 1. One of the phases was identified as CaH_2 in its regular orthorhombic (*Pnma*) crystal structure (3.6 wt%). The second phase was indexed as a cubic structure with the space group *Fm*-3*m*, isostructural with CaF_2. Its lattice parameter is 5.490 Å, compared to 5.4 Å for CaF_2. After further investigations, this cubic phase was identified as CaH_2 (4.2 wt%). The crystal structures and the lattice parameters of the detected phases in the diffraction pattern in Fig. 2 are shown in Table 2. No other phases or unexplained Bragg peaks were detected in the diffraction pattern. That does, however, not fully exclude the presence of small amounts of poorly scattering phases such as elemental boron or lithium.

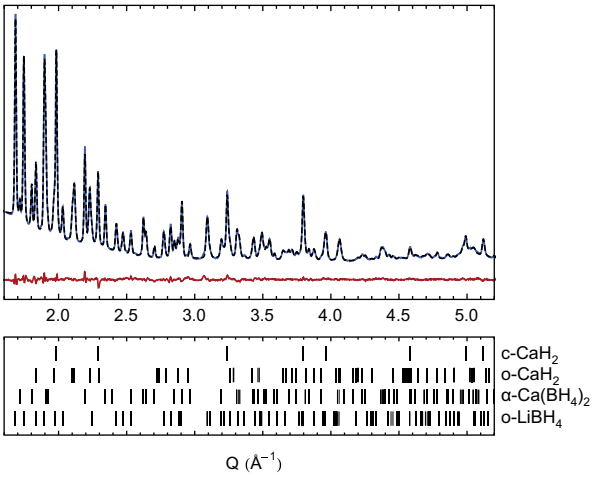

Fig. 2. Synchrotron XRD data (from SNBL) and a Rietveld refinement of a black-colored part of a $0.875LiBH_4+0.125Ca(BH_4)_2$ sample after it had been heat treated up to a temperature of 100 °C during the impedance spectroscopy measurements. The blue, solid line shows the measured data, the black, dashed line shows the Rietveld refinement of the data and the red, solid line on the bottom shows the difference between the measured data and the refinement. The Rietveld refinement reveals that the diffraction pattern consists of α-$Ca(BH_4)_2$, and orthorhombic $LiBH_4$, along with 3.6 wt% of orthorhombic CaH_2 and 4.2 wt% of cubic CaH_2 (in a CaF_2 crystal structure). No other phases were detected. The tick marks below the diffraction patterns show the locations of the diffraction peaks for the four phases according to the Rietveld refinement. (For interpretation of the references to color in this figure caption, the reader is referred to the web version of this paper.)

Table 2
The crystal structures and the lattice parameters of the refined structures in Fig. 2. The lattice parameters of the $LiBH_4$ and $Ca(BH_4)_2$ phases are very similar to those in the refinements shown in Fig. 1.

Phase	*Crystal structure*	*a* (Å)	*b* (Å)	*c* (Å)
o-$LiBH_4$	*Pnma*	7.201	4.452	6.857
α-$Ca(BH_4)_2$	*F2ddd*	8.815	13.184	7.543
o-CaH_2	*Pnma*	5.974	3.617	6.849
c-CaH_2	*Fm*-3*m*	5.488	5.488	5.488

Solid solutions of $CaH_{2-x}F_x$ in the cubic CaF_2 crystal structure with various concentrations of hydrogen have previously been reported, first by Brice et al. [63] and more recently in connection with research on $Ca(BH_4)_2$ thermal decomposition [64,65]. Smithson et al. [66] have performed ab initio calculations that show that at zero pressure, the formation energies for orthorhombic CaH_2 and cubic CaH_2 are very similar. Pinatel et al. [67] have recently calculated the phase diagram of the $CaH_{2-x}F_x$ solid solution and found that the cubic and orthorhombic phases can coexist near room temperature with very a low concentration of fluoride. Furthermore, Li et al. have detected a high-pressure phase of CaH_2 using in situ Raman scattering, which reportedly starts forming at about 15.5 GPa and is thought to possess a higher symmetry than orthorhombic CaH_2 [68].

To investigate the possibility of the formation of cubic CaH_2 without any fluoride content, the relative stability of the orthorhombic and the cubic CaH_2 phases was calculated. The calculations were performed for structures with and without a 1/8 density of hydrogen vacancies. The charge state of the vacancies is likely to be heavily dependent on the potential over the CaH_2. Therefore, the calculations were performed both for neutral vacancies and for vacancies with a single negative elementary charge. For the structures with no vacancies, orthorhombic CaH_2 is found to be more stable than cubic CaH_2 by 0.23 eV. However, when the hydrogen vacancies are introduced, cubic CaH_2 is found to be more stable than orthorhombic CaH_2 by 0.02 eV for neutral vacancies and 0.34 eV for charged vacancies. This indicates that for structures with crystal defects, cubic CaH_2 could form and probably coexist with orthorhombic CaH_2.The relative stability of the two phases in the case of no defects and in the case of charged vacancies are shown in Fig. 3.

Note that the particular density of vacancies used for the calculations was simply chosen as a representative number and is not based on experimental findings. The main goal of the calculations was to see if the presence of vacancies would increase the stability of the orthorhombic phase relative to the cubic phase. The actual density of defects in the structure, if any, cannot be determined using the experimental techniques presented here, but could be measured using neutron diffraction as a part of further studies on this subject.

In the light of these results, we consider it very likely that the local environment in the powder, the heat treatment up to 100 °C and the direct contact of the $(1-x)LiBH_4+xCa(BH_4)_2$ sample with the lithium electrodes facilitates the formation of both orthorhombic and cubic CaH_2 with hydrogen defects. Further research would be needed to clarify the exact mechanism for such a formation. Note that it cannot be fully excluded that trace amounts of fluoride are present in this phase, and that it is in fact a $CaH_{2-x}F_x$ solid solution with a very small fluoride concentration. However, since the only source of fluoride would in this case be a TEFLON rig in the impedance spectroscopy experimental setup, with which the sample was never in direct contact, this is considered very unlikely. It can also not be excluded that some of the detected CaH_2 is indeed $Ca_{1-x}Li_xH_{2-x}$, since the formation of the new phase takes place in close proximity with the Li electrodes. No indications of this could, however, be found in the Rietveld refinement of the diffraction pattern in Fig. 2, and the formation of such a phase is not expected as LiH_2 and CaH_2 do not easily form a new compound, but rather form a eutectic mixture [69].

The two CaH_2 phases detected in the diffraction pattern in Fig. 2 are expected to be a product of a reaction between some combination of $Ca(BH_4)_2$, $LiBH_4$ and/or Li. It must therefore be assumed that one or more phases containing the corresponding amount of boron are formed as well. No such phase is observed in the XRD data, and the formation of CaB_6 or some other phase containing the relatively highly scattering calcium atom is therefore not expected. As already mentioned, elemental boron would not necessarily be detectable in the diffraction pattern, and could be present although no diffraction peaks are assigned to it. Crystalline boron is black and could possibly be responsible for the black color of the layers that form at the interface between the composites and the lithium electrodes. Its formation along with the formation of CaH_2 cannot be fully excluded. It must, however, be noted that elementary boron is considered very difficult to obtain, and is generally not observed as a reaction product of thermal decomposition of borohydrides below temperatures around 250 °C [70,71]. Therefore, we do not consider it very likely that the majority of the boron atoms that become available during the reaction that forms CaH_2 go into the formation of elemental boron.

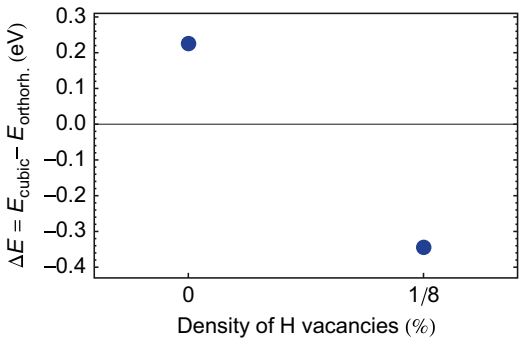

Fig. 3. The calculated stability of cubic CaH_2 relative to orthorhombic CaH_2 for structures with no defects and for structures with a 1/8 (12.5%) density of hydrogen vacancies. The cubic structure is found to be slightly more stable than the orthorhombic structure with the introduction of the H vacancies.

It is, on the other hand, considered very likely that diborane (B_2H_6) gas is released along with the formation of CaH_2. Diborane is typically released during thermal decomposition of borohydrides below 250 °C [23,72,73], but dissociates at that temperature [74]. It has proven difficult to avoid its formation in research on borohydrides for reversible hydrogen storage applications [71], and was very likely formed during this work as well. Its formation could not be observed with the experimental methods used in this work, but this could be addressed using mass spectroscopy in further studies on this topic. Although the reaction responsible for the formation of CaH_2 in this work does not necessarily involve thermal decomposition of the borohydrides, we still consider it very likely that diborane is released during the formation of CaH_2.

To gain more information on the surface composition, chemical bonds and morphology of the black-colored powder, XPS and SEM/EDS measurements were performed. The XPS results (which are included as supporting information) indicate that the only type of chemical bonds in the sample that involves calcium are Ca–H bonds. No Ca–F bonds were detected. This strongly suggests that the two CaH_2 phases are the only new calcium phases that have been formed in the sample during the heat treatment, and that no CaF_2 or amorphous phases are present. The only chemical bonds of boron detected in the XPS measurements were B–H bonds and B–O bonds. A very small signal of the latter bond type was detected, most likely originating from slight impurities in the sample. It should, however, be noted that B–B bonds have a binding energy very similar to B–H bonds, and a possible signal from boron bonds may therefore be drowned out by the signal from hydrogen bonds.

Fig. 4 shows a SEM image of a black colored part of $0.875LiBH_4+0.125Ca(BH_4)_2$ powder after the heat treatment during the impedance spectroscopy measurement. An additional SEM image is included as supporting information. Elemental mapping of the microscope image was performed using the EDS technique. The bulk of the powder appears dark gray on the image and is found to have a rather constant concentration of both calcium and boron. These areas are expected to mainly consist of a physical mixture of $LiBH_4$ and $Ca(BH_4)_2$. The powder also contains small areas that appear light gray and were found to be calcium-rich. These areas are, however, not boron-rich, excluding the possibility that they consist of $Ca(BH_4)_2$. The EDS instrument is unfortunately not capable of detecting hydrogen, which is limiting for the conclusions that can be drawn from the SEM/EDS measurements in this study. But since the XPS results only indicate the presence of Ca–H bonds and no other bonds involving calcium, it is reasonable to assume that the calcium-rich areas in the SEM image are in fact CaH_2. It is of course also possible that these areas consist of pure calcium, but after the heat treatment this is not considered very likely. Although the EDS results are not strictly conclusive on their own, they are in good agreement with the XRD and XPS data, and strengthen the hypothesis that CaH_2 is formed. With the combined results from the calculations and from the XRD, XPS

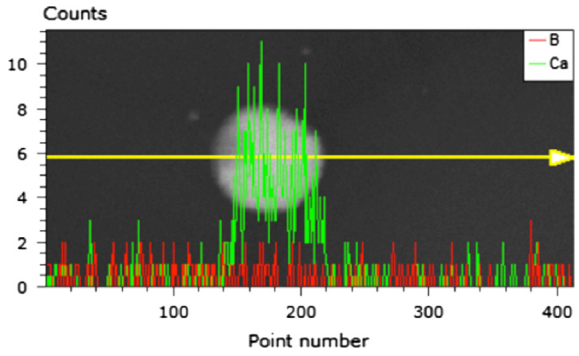

Fig. 4. A SEM image of a black-colored part of a $0.875LiBH_4+0.125Ca(BH_4)_2$ sample after heat treating it up to a temperature of 100 °C during the impedance spectroscopy measurements. Elemental mapping using EDS revealed that the bulk of the powder is a physical mixture of $LiBH_4$ and $Ca(BH_4)_2$, possibly along with some elemental boron, while areas that appear light gray in the microscope were found to be calcium-rich. The light gray particle in the middle of the image is approximately 10 μm in diameter. The result of an elemental mapping line scan is shown. A clear increase in calcium concentration is detected at the position of the light gray area, but no increase in the concentration of boron (or any other element) is detected. Note that the EDS equipment cannot detect hydrogen or lithium. Also note that the colors of the SEM image do not represent the actual colors of the sample, and that the light gray area in the Fig. may thus well be black in reality. (For interpretation of the references to color in this figure caption, the reader is referred to the web version of this paper.)

and EDS measurements, we thus conclude that the two CaH_2 phases (orthorhombic and cubic) have been formed during the heat treatment.

3.3. Conductivity

The conductivity of $(1-x)LiBH_4+xCa(BH_4)_2$ was measured for three mixing ratios, i.e. $x=\{1/4, 1/2, 3/4\}$. Fig. 5 shows examples of Nyquist plots obtained by impedance spectroscopy. All Nyquist plots showed one arc (a slightly depressed semi-circle). The explanation for this can be either that only one contribution to the conduction is present, or that two or more arcs of concurrent bulk and/or grain boundary contributions overlap completely in the Nyquist plots. Unfortunately, it is not possible to separate different contributions to the conductivity in such a case using only impedance spectroscopy [75,76]. At the highest temperatures, some of the Nyquist plots also showed a small tail at the low-frequency end, which is attributed to the lithium electrodes.

As the Nyquist plots only show one arc, they were fitted using an (RQ) equivalent circuit model, i.e. a resistor and a constant phase element (CPE) in parallel. The Nyquist plots containing a low-frequency tail were fitted using two such circuits in series. The sample resistance R was taken to be the point of intersection between the Z' axis and the low-frequency end of the large arc. The conductivity of the samples is given by

$$\sigma = \frac{d}{AR} \quad (1)$$

where R is the resistance obtained from the (RQ) fit, d is the thickness of the sample and A its area.

The ionic conductivities of the $(1-x)LiBH_4+xCa(BH_4)_2$ samples are shown in Fig. 6. The conductivity of pure $LiBH_4$, both as-received (non-milled) and ball-milled, is shown for comparison. Attempts were made at measuring the conductivity of pure $Ca(BH_4)_2$. This did, however, not succeed, most probably due to the ionic conduction of $Ca(BH_4)_2$ being too poor for measurements with this experimental setup (i.e. $< 10^{-9}$ S/cm).

The ionic conductivity of the samples is very sensitive to defects in the crystal structure of the powders. The ball-milled $LiBH_4$ has a much higher conductivity (4.6×10^{-5} S/cm at 40 °C) than the non-milled (as-received) sample (2.4×10^{-8} S/cm at 40 °C), although both samples are in the orthorhombic, poorly conducting phase. This can be explained by the formation of defects during the milling which may open new Li^+ conduction

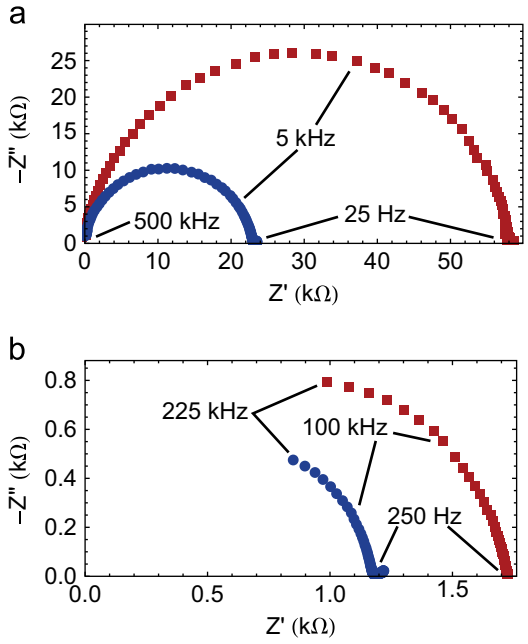

Fig. 5. Examples of Nyquist plots obtained by impedance spectroscopy on $0.5LiBH_4+0.5Ca(BH_4)_2$. The red squares are measured during heating, the blue circles are measured during cooling. (a) Measurements performed at 40 °C. (b) Measurements performed at 80 °C. The Nyquist plots mostly show only one arc, but at the higher temperatures a small contribution from the electrodes is sometimes observed at the low-frequency end of the plots. (For interpretation of the references to color in this figure caption, the reader is referred to the web version of this paper.)

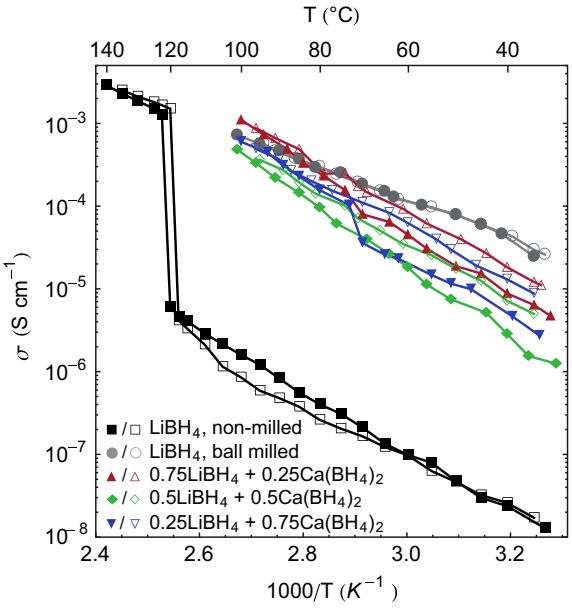

Fig. 6. An Arrhenius plot of the ionic conductivity of the $LiBH_4+Ca(BH_4)_2$ mixtures. The ionic conductivity of non-milled and ball-milled pure $LiBH_4$ is shown for comparison. The filled symbols denote measurements during heating runs, the empty symbols denote measurements during cooling runs. The conductivity of the composites is in all cases lower than that of the ball-milled $LiBH_4$. Note that the conductivity of the composite samples is in all cases higher during cooling than during heating. This is most probably an artifact due to the formation of a defect-rich, electronically conducting CaH_2 phase at the electrode–electrolyte interfaces of the pellets, but not due to an increase in the ionic conductivity of the samples.

pathways[33]. As the sample is only heated up to 100 °C, and not above the $LiBH_4$ phase transition temperature of approximately 110 °C, the defects are not mended by the heat treatment and the conductivity of the ball-milled $LiBH_4$ remains similar during cooling.

The $(1-x)LiBH_4+xCa(BH_4)_2$ pellets consisted of as-milled powders. The $3/4LiBH_4+1/4Ca(BH_4)_2$ sample has the highest conductivity of the measured composites, or 8.8×10^{-6} S/cm at 40 °C. A comparison of the phase compositions shown in Fig. 1 with the conductivities of the composite samples shown in Fig. 6 indicates that the presence of α-$Ca(BH_4)_2$ grain boundaries might be slightly more favorable for the conductivity than the presence of γ-$Ca(BH_4)_2$ grain boundaries. The ionic conductivity of all the composite samples is, however, in the range of 0.001–0.01 mS/cm, and thus considerably lower than the aforementioned conductivity target of 1 mS/cm. This is probably too low for application as a bulk electrolyte in working battery cells. However, at 100 °C the $3/4\ LiBH_4+1/4Ca(BH_4)_2$ sample reaches a conductivity of 1 mS/cm, which might be of interest in battery applications at elevated temperatures.

The fact that the Nyquist plots (see Fig. 5) only show one arc that can be related to bulk and/or grain boundary conduction strongly suggests that Li^+ is the only charge carrier in the composite, i.e. that the contribution of Ca^{2+} to the conduction is negligible, This hypothesis is further strengthened by the observation that the conductivities of the $(1-x)LiBH_4+xCa(BH_4)_2$ samples are only slightly lower than that of ball-milled pure $LiBH_4$ (see Fig. 6) while the ionic conduction of pure $Ca(BH_4)_2$ is very poor.

The presence of Ca^{2+} vacancies in α-$Ca(BH_4)_2$ (which is indicated by the Rietveld refinement of the synchrotron data, see Table 1) could indicate that some Ca^{2+} substitute into $LiBH_4$, or that they form a grain boundary interface of Ca^{2+}. The formation of such an interface could enhance the ionic conduction in the $LiBH_4$–$Ca(BH_4)_2$ composite. The difference in the activation energies, which are derived from the slope of the Arrhenius plots, could also be an indication that the conduction mechanisms differ slightly between the pure $LiBH_4$ and the composites. The activation energy of the ball-milled $LiBH_4$ is found to be around 0.55 eV while the activation energies of the composites are found to be approximately 0.8 eV in all cases. Further work using other experimental techniques would be needed to determine which conductive species contribute to the ionic conductivity of the $(1-x)LiBH_4+xCa(BH_4)_2$ composite.

In the impedance spectroscopy measurements, the conductivity of the composites is in all cases found to be higher during cooling runs (see Fig. 6), i.e. after the samples have been heated to 100 °C in the impedance spectroscopy setup and the black powder discussed in Section 3.2 has formed. If one or both of the CaH_2 phases were electronically conducting, so that the resistivity of the layers in which they form were negligible compared to the resistivity of the $(1-x)LiBH_4+xCa(BH_4)_2$ composites, the contribution of the CaH_2 containing layers would not be visible in the impedance spectroscopy measurements. This also holds true if elemental boron is formed, as boron has an electronic conductivity of 0.1 mS/cm at room temperature, which is almost 2 orders of magnitude higher than the composite samples. Furthermore, since the thickness of the pelletized samples is used to estimate the conductivity of the composites (see Eq. (1)), the formation of such electronically conducting layers would result in a reduction of the effective thickness of the sample that can be related to the ionic conduction. Consequently, the measured pellet thickness d would no longer have the right value for Eq. (1) and the ionic conductivity σ would be overestimated. With a continuing formation of such electronically conducting layers in the electrolyte, the pellet would eventually short circuit.

To investigate if this could be the case, and if the increased conductivity of the black layer could originate from the formation of CaH_2, the density of electronic states for the two CaH_2 phases was calculated. The density of electronic states of cubic CaH_2, as obtained from calculations with the PBE exchange correlation functional, is shown in Fig. 7. In the case of cubic CaH_2, the calculations were performed with no crystal defects and with a 1/8 density of hydrogen vacancies. The band gap of orthorhombic CaH_2 was calculated to be 5.84 eV, which is in good agreement with published experimental work [77]. The band gap of defect-free, cubic CaH_2 was calculated to be 2.26 eV, which makes it a semi-conductor. This value is also not far off the result of Weaver et al. [77] who calculated the band structure of a 'hypothetical' CaH_2 phase with a cubic CaF_2 structure but a slightly smaller lattice parameter. Furthermore, cubic CaH_2 with 1/8 density of hydrogen vacancies has electronic states that reach below the Fermi level and is therefore electronically conducting, according to the calculations. This is the case both for charged (shown in Fig. 7) and charge neutral vacancies. This could explain the increase in conduction of the samples that takes place upon the formation of CaH_2. Calculations of the band gap of cubic $CaH_{2-x}F_x$ in various mixing ratios are included as Supporting Information.

The total thickness of the two black layers in each pellet was, in most cases, estimated to be around 50% of the pellet's total thickness. Assuming that these layers are electronically conducting (with an electronic conduction that is much higher than the ionic conduction of the samples), one would expect the measured conductivity to double compared to the original pellet. A comparison of the conductivity values of the composite samples near room temperature before and after the heat treatment shows that this estimate is not far off. As an example, the conductivity of $0.75LiBH_4+0.25Ca(BH_4)_2$ at 35 °C is measured at 6.4×10^{-6} S/cm before the heat treatment and 1.21×10^{-5} S/cm after the heat treatment, which is an increase by a factor of 1.9. If a thicker conducting layer were to be formed in the cell, or if the cells had a thinner layer of electrolyte to begin with, this effect would pose a serious risk of an internal short circuit in the cell.

The conclusion is therefore, that the measured conductivity after the heat treatment is always higher than prior to the heat treatment because of the unwanted formation of electronically conducting cubic CaH_2 with hydrogen defects near the lithium electrodes of the pelletized samples, along with the possible formation of elemental boron. Further research is needed and to clarify if elemental boron is formed or not and if its possible presence also contributes to the increased conductivity of the samples. This artifact, which arises due to a low chemical stability of the composites, poses a serious risk that the pelletized samples would eventually short-circuit with continued formation of the conducting layer. This observation is not encouraging for the idea

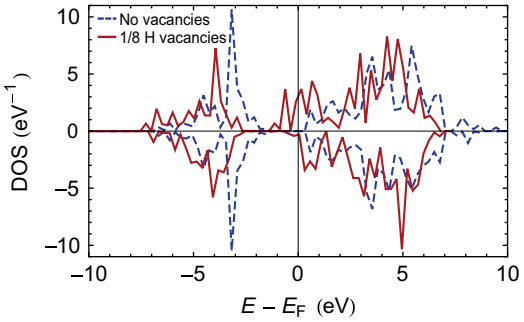

Fig. 7. The calculated density of states of CaH_2 in the cubic CaF_2 crystal structure. E_F denotes the Fermi energy of the system. The results are shown for a structure without vacancies (blue, dashed lines), and for a structure with 1/8 density of hydrogen vacancies (red, solid lines). In the structure containing vacancies, there are states that extend below the Fermi level, which suggests that the phase is electronically conducting. (For interpretation of the references to color in this figure caption, the reader is referred to the web version of this paper.)

of developing working battery cells containing the composite, but could nonetheless be of fundamental scientific interest. This finding furthermore highlights a serious general issue, namely that a slow formation of an electronically conducting layer in any solid electrolyte might eventually lead to a short-circuit. The chemical stability of any potential solid electrolyte material must therefore be investigated thoroughly before its introduction in commercial battery cells.

4. Summary and outlook

The $(1-x)LiBH_4+xCa(BH_4)_2$ composite forms a physical mixture of three phases, as measured with synchrotron X-ray diffraction; α-$Ca(BH_4)_2$, γ-$Ca(BH_4)_2$ and orthorhombic $LiBH_4$. The formation of a solid solution is not observed. Rietveld refinement of the diffraction patterns reveals that the relative fractions of the two $Ca(BH_4)_2$ phases changes considerably with $LiBH_4$ content, and γ-$Ca(BH_4)_2$ is found to be the dominant phase for $x \geq 0.5$. No β-$Ca(BH_4)_2$ is observed in the composite samples, although a third of the precursor $Ca(BH_4)_2$ powder had that crystal structure. Instead, a considerable fraction of the powder takes on the α-$Ca(BH_4)_2$ structure when small amounts $LiBH_4$ are added.

The formation of small amounts of two different phases of CaH_2 is observed upon heat treatment up to 100 °C during the impedance spectroscopy measurements. These are CaH_2 in its regular orthorhombic (*Pnma*) crystal structure and CaH_2 in a cubic (*Fm*-3*m*) CaF_2-type crystals structure. This result from the Rietveld refinement of synchrotron X-ray data is further supported by XPS and SEM/EDS data. The possibility of the formation of elemental boron is not excluded, and further research is needed to clarify that. The relative stability of CaH_2 was calculated for both phases. The results indicate that cubic and orthorhombic CaH_2 with a 1/8 density of hydrogen defects are approximately equally stable, supporting the observed coexistence of the two phases.

As no hexagonal $LiBH_4$ was observed in the composites, the ionic conductivity of $(1-x)LiBH_4+xCa(BH_4)_2$ is not as high as for example that of the $LiBH_4$+LiI solid solution [24]. Defects induced by ball milling do, however, increase the ionic conduction of orthorhombic $LiBH_4$ considerably (4.6×10^{-5} S/cm at 40 °C). The ionic conduction of $(1-x)LiBH_4+xCa(BH_4)_2$ is, for all measured values of *x*, lower than that of the ball-milled $LiBH_4$. The $0.75LiBH_4+0.25Ca(BH_4)_2$ mixture has the best conductivity of the composites; 8.8×10^{-6} S/cm at 40 °C and 1 mS/cm at 100 °C. Near room temperature, this is considerably lower than the conductivity target of 1 mS/cm, which is often mentioned as the minimum conductivity required for an electrolyte in a consumer battery. The composite, might, however, be of potential interest for battery applications at elevated temperatures.

It is not clear if lithium ions are the only charge carrier in the composites, or if calcium ions also participate in the conduction. The single-arc Nyquist plots and the slightly lower conductivity than ball-milled $LiBH_4$ suggest that Li^+ is the only charge carrier. However, the difference in the activation energy of the conduction between $LiBH_4$ and the composites indicates that the systems do not share the exact same conduction mechanism. Further work would be needed to clarify this.

The results of electronic band structure calculations for orthorhombic and cubic CaH_2, with and without hydrogen defects, indicate that the cubic structure with defects is electronically conducting. Elemental boron, if present, is also electronically conducting. This most probably explains the high conductivity observed for the heat-treated composites. The formation of an electronically conducting layer within the electrolyte in the cells is an unwanted artifact in the conductivity measurements, which increases the risk of short-circuiting in the cells. This finding reveals a more general issue that could be detrimental to other solid electrolytes and is thus of interest for further studies.

Acknowledgments

The authors would like to acknowledge support from the Danish Ministry of Science Globalization Fund, the European Graduate School on Sustainable Energy – The Molecular Approach, the Danish Center for Scientific Computing, the Danish Council for Strategic Research (the ReLiable project), the Diamond Light Source in Oxfordshire, UK, the Swiss-Norwegian Beam Lines at ESRF in Grenoble, France and the Catalysis for Sustainable Energy (CASE) initiative. CASE is funded by the Danish Ministry of Science, Technology, and Innovation.

Appendix A. Supporting information

XPS data, additional SEM data and additional band gap calculations are available as supporting information.

Supplementary data associated with this article can be found in the online version at http://dx.doi.org/10.1016/j.jssc.2013.12.006.

References

[1] J.-M. Tarascon, M. Armand, Nature 414 (2001) 359–367.
[2] P. Knauth, Solid State Ionics 180 (2009) 911–916.
[3] J.B. Goodenough, Y. Kim, Chem. Mater. 22 (2010) 587–603.
[4] J.-M. Tarascon, Phil. Trans. R. Soc. A 368 (2010) 3227–3241.
[5] A. Rabenau, Solid State Ionics 6 (1982) 277–293.
[6] A.G. Belous, G.N. Novitskaya, S.V. Polyanetskaya, Y.I. Gornikov, Izv. Akad. Nauk SSSR. 23 (1987) 470–472.
[7] Y. Inaguma, C. Liquan, M. Itoh, T. Nakamura, T. Uchida, H. Ikuta, et al., Solid State Commun. 86 (1993) 689–693.
[8] O. Bohnke, Solid State Ionics 179 (2008) 9–15.
[9] V. Thangadurai, J. Schwenzel, W. Weppner, Ionics (Kiel) 11 (2005).
[10] H. Aono, E. Sugimoto, Y. Sadaoka, N. Imanaka, G. Adachi, Solid State Ionics 47 (1991) 257–264.
[11] K. Arbi, J.M. Rojo, J. Sanz, J. Eur. Ceram. Soc 27 (2007) 4215–4218.
[12] P.G. Bruce, A.R. West, J. Electrochem. Soc. 130 (1983) 662–669.
[13] N. Kamaya, K. Homma, Y. Yamakawa, M. Hirayama, R. Kanno, M. Yonemura, et al., Nat. Mater. 10 (2011) 682–686.
[14] S. Stramare, V. Thangadurai, W. Weppner, Chem. Mater. 15 (2003) 3974–3990.
[15] R.J. Brodd, W. Huang, J.R. Akridge, Macromol. Symp. 159 (2000) 229–245.
[16] M. Park, X. Zhang, M. Chung, G.B. Less, A.M. Sastry, J. Power Sour. 195 (2010) 7904–7929.
[17] J.Y. Song, Y.Y. Wang, C.C. Wan, J. Electrochem. Soc 147 (2000) 3219–3225.
[18] A. Züttel, S. Rentsch, P. Fischer, P. Wenger, P. Sudan, P. Mauron, et al., J. Alloy. Compd. 356-357 (2003) 515–520.
[19] Z. Łodziana, T. Vegge, Phys. Rev. Lett. 93 (2004) 145501.
[20] J.K. Kang, S.Y. Kim, Y.S. Han, R.P. Muller, W. a. Goddard, Appl. Phys. Lett. 87 (2005) 111904.
[21] Z. Łodziana, T. Vegge, Phys. Rev. Lett. 97 (2006) 119602.
[22] L. Mosegaard, B. Møller, J.-E. Jørgensen, U. Bösenberg, M. Dornheim, J.C. Hanson, et al., J. Alloy. Compd. 446-447 (2007) 301–305.
[23] D. Blanchard, Q. Shi, C.B. Boothroyd, T. Vegge, J. Phys. Chem. C. 113 (2009) 14059–14066.
[24] M. Matsuo, Y. Nakamori, S. Orimo, H. Maekawa, H. Takamura, Appl. Phys. Lett. 91 (2007) 224103.
[25] V. Epp, M. Wilkening, Phys. Rev. B 82 (2010) 020301.
[26] T. Ikeshoji, E. Tsuchida, T. Morishita, K. Ikeda, M. Matsuo, Y. Kawazoe, et al., Phys. Rev. B. 83 (2011) 144301.
[27] M. Matsuo, S. Orimo, Adv. En. Mat 1 (2011) 161–172.
[28] J.-P. Soulié, G. Renaudin, R. Černý, Y. K, J. Alloy. Comp 346 (2002) 200–205.
[29] H. Maekawa, M. Matsuo, H. Takamura, M. Ando, Y. Noda, T. Karahashi, et al., J. Am. Chem. Soc. 131 (2009) 894–895.
[30] H. Oguchi, M. Matsuo, J.S. Hummelshøj, T. Vegge, J.K. Nørskov, T. Sato, et al., Appl. Phys. Lett. 94 (2009) 141912.
[31] R. Miyazaki, T. Karahashi, N. Kumatani, Y. Noda, M. Ando, H. Takamura, et al., Solid State Ionics. 192 (2011) 143–147.
[32] L.H. Rude, E. Groppo, L.M. Arnbjerg, D.B. Ravnsbæk, R. a. Malmkjær, Y. Filinchuk, et al., J. Alloy.Comp 509 (2011) 8299–8305.
[33] D. Sveinbjörnsson, J.S.G. Myrdal, D. Blanchard, J.J. Bentzen, T. Hirata, M. B. Mogensen, et al., J. Phys. Chem. C. 117 (2013) 3249–3257.
[34] J.S.G. Myrdal, D. Blanchard, D. Sveinbjörnsson, T. Vegge, J. Phys. Chem. C. 117 (2013) 9084–9091.

[35] K. Miwa, M. Aoki, T. Noritake, N. Ohba, Y. Nakamori, S. Towata, et al., Phys Rev. B. 74 (2006) 1–5.
[36] E. Rönnebro, E.H. Majzoub, J. Phys. Chem B. 111 (2007) 12045–12047.
[37] M.D. Riktor, M.H. Sørby, K. Chłopek, M. Fichtner, F. Buchter, A. Züttel, et al., J. Mater. Chem. 17 (2007) 49394942.
[38] J.-H. Kim, S.-A. Jin, J.-H. Shim, Y.W. Cho, J. Alloy Compd. 461 (2008) L20–L22.
[39] M. Aoki, K. Miwa, T. Noritake, N. Ohba, M. Matsumoto, H.W. Li, et al., Appl. Phys. A 92 (2008) 601–605.
[40] M.D. Riktor, M.H. Sørby, K. Chłopek, M. Fichtner, B.C. Hauback, J. Mater. Chem. 19 (2009) 2754–2759.
[41] D. Blanchard, M.D. Riktor, J.B. Maronsson, H.S. Jacobsen, J. Kehres, D. Sveinbjörnsson, et al., J. Phys. Chem. C 114 (2010) 20249–20257.
[42] I. Llamas-Jansa, O. Friedrichs, M. Fichtner, E.G. Bardaji, A. Züttel, B.C. Hauback, J. Phys. Chem C 116 (2012) 13472–13479.
[43] Y. Filinchuk, E. Ronnebro, D. Chandra, Acta Mater. 57 (2009) 732–738.
[44] F. Buchter, Z. Łodziana, A. Remhof, O. Friedrichs, A. Borgschulte, P. Mauron, et al., J. Phys. Chem. B 112 (2008) 8042–8048.
[45] F. Buchter, Z. Łodziana, A. Remhof, O. Friedrichs, A. Borgschulte, P. Mauron, et al., J. Phys. Chem. C. 113 (2009) 17223–17230.
[46] A. Borgschulte, R. Gremaud, A. Züttel, P. Martelli, A. Remhof, A. Ramirez-Cuesta, et al., Phys. Rev. B. 83 (2011) 024102.
[47] R. Kanno, Y. Takeda, O. Yamamoto, Mat. Res. Bull. 16 (1981) 999–1005.
[48] J.Y. Lee, D. Ravnsbæk, Y. Lee, Y. Kim, Y. Cerenius, J. Shim, et al., J. Phys. Chem. C 113 (2009) 15080–15086.
[49] Z. Fang, X. Kang, J. Luo, P. Wang, H. Li, S. Orimo, J. Phys. Chem. C. 114 (2010) 22736–22741.
[50] V.A. Dyadkin, SNBL Tool Box, Swiss-Norwegian Beam Lines at ESRF, Grenoble, France, 2012.
[51] A.P. Hammersley, S.O. Sveinson, M. Hanfland, A.N. Fitch, D. Hausermann, High Press. Res. 14 (1996) 235–248.
[52] A.C. Larson, R.B. von Dreele, Report LAUR 86-784, General Structure Analysis System (GSAS), 1994.
[53] P. Hohenberg, W. Kohn, Phys. Rev. 136 (1964) 864–871.
[54] W. Kohn, L.J. Sham, Phys. Rev. 140 (1965) 1133–1138.
[55] J. Mortensen, L. Hansen, K. Jacobsen, Phys. Rev. B 71 (2005) 035109.
[56] J. Enkovaara, C. Rostgaard, J.J. Mortensen, J. Chen, M. Dułak, L. Ferrighi, et al., J. Phys. Condens. Matter 22 (2010) 253202.
[57] S.R. Bahn, K.W. Jacobsen, Comp. Sci. Eng. 4 (2002) 56–66.
[58] P.E. Blöchl, Phys. Rev. B 50 (1994) 17953.
[59] P.E. Blöchl, C.J. Först, J. Schimpl, Bull. Mater. Sci. 26 (2003) 33.
[60] J.J. Perdew, K. Burke, M. Ernzerhof, Phys. Rev. Lett. 77 (1996) 3865.
[61] M. Kuisma, J. Ojanen, J. Enkovaara, T.T. Rantala, Phys. Rev. B 82 (2010) 115106.
[62] I.E. Castelli, T. Olsen, S. Datta, D.D. Landis, S. Dahl, K.S. Thygesen, et al., Energy Environ. Sci. 5 (2012) 5814–5819.
[63] J. Brice, A. Courtoist, J. Aubry, J. Solid State Chem. 24 (1978) 381–387.
[64] J.-H. Kim, J.-H. Shim, Y.W. Cho, J. Power Sour. 181 (2008) 140–143.
[65] J.Y. Lee, Y.-S. Lee, J.-Y. Suh, J.-H. Shim, Y.W. Cho, J. Alloy Compd. 506 (2010) 721–727.
[66] H. Smithson, C. Marianetti, D. Morgan, A. Van der Ven, A. Predith, G. Ceder, Phys. Rev. B 66 (2002) 144107.
[67] E.R. Pinatel, L.H. Rude, M. Corno, M. Kragelund, P. Ugliengo, T.R. Jensen, et al., MRS Proc. 1441 (2012) 5–16.
[68] B. Li, Y. Li, K. Yang, Q. Cui, Y. Ma, G. Zou, J. Phys. Condens. Matter 19 (2007) 226205.
[69] C.E. Messer, J.C. Eastman, R.G. Mers, A.J. Maeland, Inorg. Chem. 2 (1964) 776–778.
[70] G. Will, B. Kiefer, Z. Anorg. Allg. Chem. 627 (2001) 2100–2104.
[71] O. Friedrichs, A. Remhof, A. Borgschulte, F. Buchter, S.I. Orimo, A. Züttel, Phys. Chem. Chem. Phys. 12 (2010) 10919–10922.
[72] W. Grochala, P.P. Edwards, Chem. Rev. 104 (2004) 1283–1315.
[73] A. Züttel, A. Borgschulte, S.-I. Orimo, Scr. Mater 56 (2007) 823–828.
[74] M. Söderlund, P. Mäki-Arvela, K. Eränen, T. Salmi, R. Rahkola, D.Y. Murzin, Catal. Lett. 105 (2005) 191–202.
[75] N.M. Beekmans, L. Heyne, Electrochim. Acta 21 (1976) 303–310.
[76] S.M. Haile, D.L. West, J. Campbell, J. Mat. Res. 13 (1998) 1576–1595.
[77] J.H. Weaver, M. Gupta, D.T. Peterson, Solid State Commun. 51 (1984) 805–808.

Supporting information: Ionic conductivity and the formation of cubic CaH2 in the LiBH4-Ca(BH4)2 composite

Dadi Sveinbjörnsson[1], Didier Blanchard[1], Jon Steinar Gardarsson Myrdal[1,2], Reza Younesi[1], Rasmus Viskinde[1], Marit Dalseth Riktor[3], Poul Norby[1], Tejs Vegge[1].

[1]*Department of Energy Conversion and Storage, Technical University of Denmark, Frederiksborgvej 399, P.O. Box 49, DK-4000 Roskilde, Denmark.*
[2]*Center for Atomic-Scale Materials Design, Department of Physics, Technical University of Denmark, Anker Engelunds Vej 1, DK-2800 Lyngby, Denmark.*
[3]*Physics Department, Institute for Energy Technology, Instituttveien 18, P.O. Box 40, NO-2027 Kjeller, Norway.*

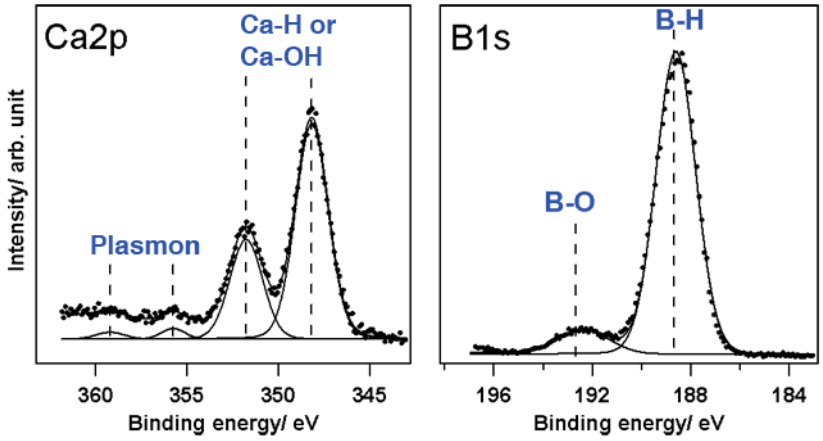

Figure S1 The XPS results for calcium and boron. The chemical bonds corresponding to the measured peaks are marked in the figure. Boron is almost exclusively found to have hydrogen bonds, although a small amount of oxygen bonds (related to impurities in the sample) is observed. Due to the low concentration of calcium atoms on the surface of the sample, it is more difficult to analyze the results for Ca. The calcium is detected by looking at the *p* orbital, and due to spin-orbital coupling two peaks are observed for each type of bonds for calcium atoms. The two low intensity peaks between 355 eV and 360 eV do not denote chemical bonds, but originate from plasmon interactions. The two larger peaks between 345 eV and 355 eV represent one type of bond; Ca-H or Ca-OH bonds. Since the powder is expected to contain Ca-H bonds but no Ca-OH bonds, and since the XRD and EDS results do not suggest that Ca-OH bonds are present, we conclude that these two peaks correspond to Ca-H bonds. No other chemical bonds involving calcium are detected.

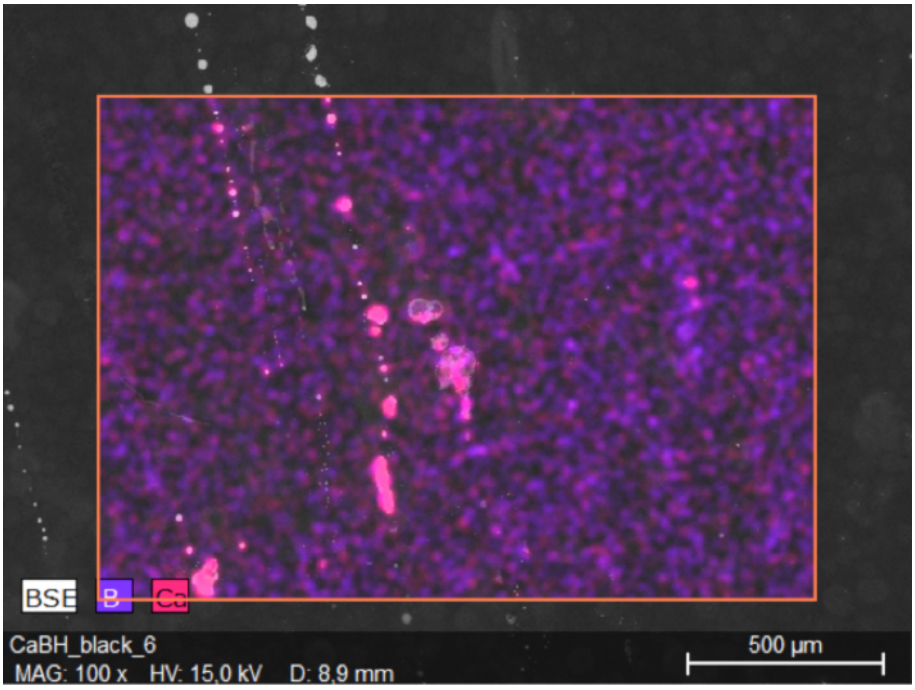

Figure S2 A SEM image of the a black-colored part of a $0.875LiBH_4+0.125Ca(BH_4)_2$ sample after heat treating it up to a temperature of 100°C during the impedance spectroscopy measurements. Elemental mapping using EDS has been carried out within the area of the orange rectangle. Note that the EDS technique does not detect hydrogen or lithium. The bulk of the powder consists of $LiBH_4$ and $Ca(BH4)_2$, as indicated by the rather homogeneous distribution of B and Ca in the image. The pink, calcium rich spots in the middle of the figure do, however, not contain any boron. Using the XRD and XPS results, it can be concluded that these areas consist of CaH_2.

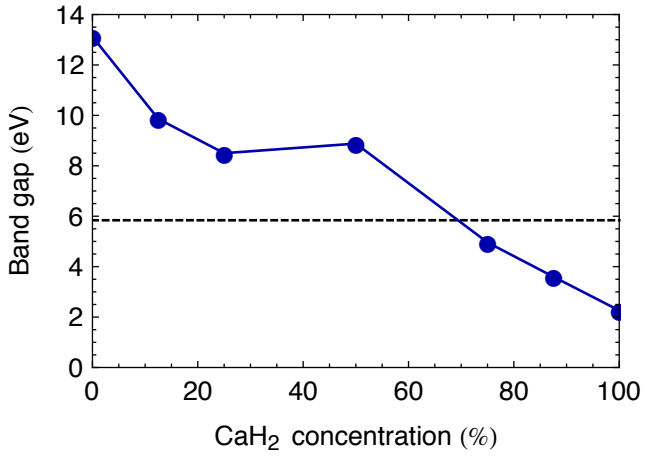

Figure S3 The calculated band gap for different mixing ratios of the $CaH_{2-x}F_x$ solid solution in the cubic (*Fm-3m*) CaF_2 crystal structure. The cell used for the calculations did not include hydrogen vacancies or any other crystal defects. The dashed line shows the calculated band gap of orthorhombic (*Pnma*) CaH_2, for comparison. The band gap of the cubic $CaH_{2-x}F_x$ is found to decrease with increasing CaH_2 concentration and reaches a minimum value of 2.26 eV for pure cubic CaH_2. This is considerably lower than the band gap of orthorhombic CaH_2, which was calculated to be 5.84 eV.

Paper D

Journal of The Electrochemical Society, **161** (9) A1432-A1439 (2014)
0013-4651/2014/161(9)/A1432/8/$31.00 © The Electrochemical Society

The $LiBH_4$-LiI Solid Solution as an Electrolyte in an All-Solid-State Battery

Dadi Sveinbjörnsson, Ane Sælland Christiansen,* Rasmus Viskinde, Poul Norby, and Tejs Vegge,z**

Department of Energy Conversion and Storage, Technical University of Denmark, 4000 Roskilde, Denmark

The charge and discharge performance of an all-solid-state lithium battery with the $LiBH_4$-LiI solid solution as an electrolyte is reported. Lithium titanate ($Li_4Ti_5O_{12}$) was used as the positive electrode and lithium metal as the negative electrode. The performance of the all-solid-state cell is compared with a cell with an identical electrode setup but a liquid electrolyte (1 M $LiPF_6$ in EC:DMC). All measurements were carried out at a temperature of 60°C. For the all-solid-state cells, 81% of the theoretical discharge capacity is reached for a discharge rate of 10 μA, but a capacity fade of 1.6% per charge-discharge cycle is observed. The electrochemical stability of the $LiBH_4$-LiI solid solution was investigated using cyclic voltammetry and is found to be limited to 3 V. The impedance of the battery cells was measured using impedance spectroscopy. A strong correlation is found between the change in the discharge capacity of the cells and changes in the cell impedance over 200 charge-discharge cycles. This is expectedly due to the possible formation of passivating areas in the cell and/or loss of contact area between the electrolyte and the electrodes.

Manuscript submitted March 27, 2014; revised manuscript received June 12, 2014. Published June 24, 2014.

Lithium based batteries play an important role in modern society. Not only are they dominant in the portable electronics sector, but have also made their way into applications in larger systems, e.g. in the transportation sector and load balancing of the electric grid. However, for such applications, further research on lithium batteries is needed, especially with regard to energy density, safety, charge-discharge cycle life-time and price. Current lithium batteries have organic liquid or gel electrolytes, which are flammable. Furthermore, liquid electrolytes allow for the formation of dendrites at the electrode-electrolyte interface, which can grow into the electrolyte area and thereby increase the risk of short-circuit in the cell. It is widely acknowledged that replacing the organic liquid or gel electrolytes with solid-state electrolytes could enhance the safety and the energy density of the batteries and improve the cycle life-time by reducing the formation of dendrites.[1–3]

The main attractive property of liquid and gel electrolytes is their high Li^+ conductivity (e.g. 12 mS^{-1} for 1 M $LiPF_6$ in EC-DMC at 27°C).[4] It has proven challenging to design suitable solid-state electrolyte materials with sufficient chemical and electrochemical stability as well as high Li^+ conductivity and negligible electronic conductivity.[5] Many crystalline solid-state Li^+ conductors are known, such as Li_3N,[6] perovskite type oxides (e.g. lithium lanthanum titanate),[7–9] garnet type structures (e.g. $Li_6BaLa_2Ta_2O_{12}$),[10] NASICON type structures,[11,12] LISICON type structures.[13] However, these materials all have shortcomings such as too low decomposition voltage (Li_3N), instability toward contact with lithium metal (lithium lanthanum titanates (LLTO) and NASICON) or too high electronic conductivity (LLTO).[14] The only solid electrolyte material that has been reported to match the Li^+ conductivity of the currently used liquid electrolytes is the relatively recently discovered $Li_{10}GeP_2S_{12}$ with a Li^+ conductivity of 12 mS cm^{-1} at 27°C.[15] A Li^+ conductivity of at least 1 mS cm^{-1} is often cited as the minimum conductivity an electrolyte with a thickness on the order of 1 mm should have for practical applications in consumer batteries.[16,17] Further search for crystalline solid electrolyte materials with such high Li^+ conductivity is both practically and fundamentally relevant for lithium battery research.

Lithium borohydride has been extensively investigated as a hydrogen storage material.[18–25] It is lightweight (0.666 g cm^{-3}) and has an orthorhombic (*Pnma*) crystal structure at room temperature.[26] In this crystal structure, $LiBH_4$ is a poor Li^+ conductor (approximately 10^{-8} S cm^{-1} at 30°C). However, at around 110°C, a reversible structural transition to a hexagonal structure ($P6_3mc$) occurs, rendering $LiBH_4$ highly Li^+ conducting (approximately 1 mS cm^{-1} at 120°C), as first reported by Matsuo et al.[27] This discovery has caused $LiBH_4$ to gain significant attention in recent years as a potential crystalline solid electrolyte for lithium batteries.[28,29] $LiBH_4$ is an electrical insulator in both crystal structures, with a bandgap of approximately 6.7 eV according to calculations.[30,31] Furthermore, it has been shown to be electrochemically stable up to 5 V.[32]

The hexagonal, highly Li^+ conducting phase of $LiBH_4$ can be stabilized at room temperature by the addition of lithium halides (LiI, LiBr and LiCl), with LiI addition yielding the highest Li^+ conduction, as reported by Maekawa et al.[33,34] LiI and $LiBH_4$ form a homogeneous solid solution that takes on the highly Li^+ conducting hexagonal crystal structure of $LiBH_4$. For a LiI addition of >12.5 molar percentage, only hexagonal $LiBH_4$ and no orthorhombic $LiBH_4$ is detected at room temperature, as measured by X-ray diffraction.[35] The addition of LiI mainly serves the purpose of stabilizing the hexagonal structure of $LiBH_4$ at room temperature, but its presence in the hexagonal structure of $LiBH_4$ also raises the Li^+ conductivity of the solid solution above that of pure hexagonal $LiBH_4$.[35] Studies on the structure, hydrogen storage properties and Li^+ conduction properties of the $LiBH_4$-LiI solid solution have recently been published.[35–38] Quasi-elastic neutron scattering studies on the rotations of the borohydride groups and on the Li^+ conduction mechanism have also been published.[39,40] Furthermore, a recent publication by Unemoto et al. provides an excellent overview of complex hydrides as solid electrolyte materials.[41]

An all-solid-state battery with $LiBH_4$ as an electrolyte has recently been reported by Takahashi et al.[42,43] There, lithium is used as a negative electrode and Li_3PO_4-coated $LiCoO_2$ as a positive electrode. However, as the hexagonal structure of pure $LiBH_4$ is only stable above 110°C, all measurements in their work were carried out at 120°C. By adding LiI, the hexagonal, highly Li^+ conducting phase of $LiBH_4$ is stabilized at temperatures below room temperature. Conductivity values close to 1 mS cm^{-1} are reached at 60°C, as measured using impedance spectroscopy on a cylindrical pellet with lithium metal electrodes.[35] This is not far from desired operating temperatures for batteries in various applications. In the present work we report on an all-solid-state battery with $LiBH_4$-LiI as an electrolyte. Lithium metal is used as the negative electrode and spinel $Li_4Ti_5O_{12}$ (LTO) is used as the positive electrode. LTO has a theoretical capacity of 175 mAh/g and a flat Li^+ intercalation plateau at around 1.56 V vs. Li^+/Li. LTO has the advantage that it exhibits no volume change during Li^+ intercalation,[44] which makes it well suited as electrode material in an all-solid-state battery. All measurements were carried out at 60°C. The aim of this work is to investigate the performance of the $LiBH_4$-LiI solid solution in working battery cells, as well as to provide an understanding of some of the benefits, challenges and limitations of this solid electrolyte material. This knowledge will hopefully be beneficial for further understanding and optimization of the electrolyte properties of this class of solid Li^+ electrolytes.

*Electrochemical Society Student Member.
**Electrochemical Society Active Member.
zE-mail: teve@dtu.dk

Experimental

Sample preparation.— The positive electrodes were made by coating a mixture of 80 wt% $Li_4Ti_5O_{12}$ (Sigma-Aldrich Co.), 10 wt% Super C65 (Timcal), and 10 wt% polyvinylidene fluoride in N-Methyl-2-pyrrolidone (NMP) on aluminum foil. The electrodes were dried at 80°C in air, followed by compression in a roll press, and then punched into discs of 10 mm in diameter. Afterwards the cathodes were transferred to an argon filled glove box and dried in a vacuum oven at 80°C overnight. The electrodes had a layer thickness of 3 μm and an active particle load of 0.5 mg cm^{-2}.

The solid electrolytes, (1–*x*)$LiBH_4$-*x*LiI solid solutions, were synthesized using $LiBH_4$ powder (purity 95%) and LiI beads (Alfa Aesar Co., purity 99%). All samples in this work contained solid solutions with $x = 3/16$ (18.75% LiI molar content), except the sample used for the cyclic voltammetry measurement in which $x = 1/4$ (25% LiI molar content). The synthesis was performed with a Fritsch Pulverisette P6 planetary ball mill. During each milling, a stainless steel vial with an inner volume of 250 ml was rotated at 650 rpm for 2 hours. 2.0 g of precursor powder were inserted into the vial along with 25 tungsten carbide balls, resulting in a sample to ball mass ratio of 1/200. The loading of the vial and the milling of the powder took place under Ar atmosphere.

The negative electrodes consisted of 0.38 mm thick lithium foil (Sigma Aldrich Co., purity 99.9%). Any oxidized layers were scratched off the lithium foil before punching it in discs with 10 mm in diameter and a mass of approximately 10 mg.

Cells containing a liquid electrolyte were assembled for comparison with the all-solid-state cells. In these cells, the positive and negative electrodes were the same as in the cells described above. However, instead of the $LiBH_4$-LiI solid solution, a porous glass fiber membrane filled with 1 M $LiPF_6$ in EC:DMC (1:1, vol., Merck & Co). was used as an electrolyte.

Cell assembly.— The all-solid-state battery cells were assembled inside a cylindrical polyetherketone (PEEK) die containing a cylindrical hole with a diameter of 10 mm. A stainless steel piston was inserted at the bottom of the mould. The components of the battery cell were stacked on top of the piston; first a 10 mm lithium disc, then 50 mg of the LiBH4-LiI solid solution and finally a disc of LTO deposited on aluminum foil. A second steel piston was inserted into the top of the mould before pressing the cell at approximately 1 ton cm^{-2}. Pieces of hard rubber were used as padding on both sides between the steel pistons and the press to prevent short-circuiting of the battery cells while pressing. The cell assembly was carried out under Ar atmosphere, but after pressing, the cells were sealed tightly in the mould to allow for atmospheric measurements. The porosity of the $LiBH_4$-LiI solid solution after pressing the powder was estimated to be around 0.5. The porosity was calculated as $\Phi = 1 - \rho_{pellet} / \rho_{th}$, where ρ_{pellet} is the measured density of the pelletized powder and ρ_{th} is the theoretical density of the electrolyte material. The thickness of the electrolyte was approximately 1.2 mm. These cells will be referred to as LTO | $LiBH_4$-LiI | Li cells in the following discussion.

Cells containing a steel electrode instead of the positive electrodes were assembled for electrochemical testing of the electrolyte. In these cells, one lithium electrode, 50 mg of (1–*x*)LiBH4-*x*LiI powder and a stainless steel disc of 10 mm in diameter were pressed in the same manner as described above. These cells were used for investigating lithium transfer through the electrolyte, and for estimating the electrochemical stability of the electrolyte. We will refer to these cells as Steel | $LiBH_4$-LiI | Li.

The battery cells containing a liquid electrolyte were assembled under Ar atmosphere, and strips of copper and aluminum foil were placed on opposite sides of the cell as current collectors. The cells were sealed in polymer-coated aluminum laminate cells (pouch bag cells), using a vacuum sealer. We will refer to these cells as LTO | $LiPF_6$ | Li.

X-ray diffraction.— After ball milling, the LiBH4-LiI samples were characterized using a Cu Kα Bruker D8 diffractometer with a Bragg-Brentano geometry and a Lynx-Eye detector. The instrument was operating at 40 kV and 40 mA. All X-ray diffraction (XRD) measurements were carried out at room temperature and under Ar atmosphere, using an airtight polyethylene sample holder from Bruker Co. The exposure time was 3 s/step with a step size of 0.02°.

Electrochemical measurements.— Charge and discharge measurements on the LTO | $LiBH_4$-LiI | Li cells and the LTO | $LiPF_6$ | Li cells were performed with a Biologic VMP3 multichannel potentiostat. The charge-discharge measurements of the LTO | $LiBH_4$-LiI | Li cells were performed at a temperature of 60°C, but the measurements of the LTO | $LiPF_6$ | Li were carried out at room temperature. The all-solid-state cells were under a mechanical load of 1.2 MPa during the measurements. The cells were charged and discharged with a constant current *I* (galvanostatic). An array of current values was tried, with $I \in \{2\ \mu A, 5\ \mu A, 10\ \mu A, 20\ \mu A\}$. The open circuit voltage (OCV) of LTO against lithium is approximately 1.56 V. The cells were charged and discharged until reaching a voltage limit, which was set at 2.6 V or 3.0 V for charge and 1.0 V for discharge. The cells are assembled in the charged state, and upon discharge the following reaction occurs from left to right at the LTO electrode:

$$Li_4Ti_5O_{12} + 3Li^+ + 3e^- \leftrightarrow Li_7Ti_5O_{12} \quad [1]$$

Upon charge, the reaction takes place from right to left.

AC electrochemical impedance spectroscopy (EIS) measurements were performed after each charge and discharge of the battery cells using the Biologic VMP3 potentiostat. The measurements were performed under near-equilibrium conditions, i.e. after resting the cell in open circuit mode for at least 10 minutes prior to the EIS measurements. The frequency range of the impedance measurements was set from 1 Hz to 300 kHz. In order to decrease noise in the resulting data, each data point is an average value of five consecutive measurements. The temperature during the impedance spectroscopy measurements was the same as during the charge-discharge measurements for each cell.

The resistance *R* to Li^+ conduction in the solid electrolyte can be estimated from the results of the impedance spectroscopy measurements. Furthermore, the conductivity σ of the electrolyte is related to the resistance as

$$\sigma = \frac{d}{RA}, \quad [2]$$

where *d* is the thickness of the electrolyte and *A* is the area.

The coulombic efficiency η_C of a battery charge and discharge cycle, used in section "Charge and discharge of cells with a LiBH4-LiI electrolyte," is defined as the ratio of the charge transfer during the discharge run *i* to the charge transfer during the preceding charge run, i.e.

$$\eta_C = \frac{Q_{discharge}(i)}{Q_{charge}(i-1)}. \quad [3]$$

The Pearson product-moment correlation coefficient $\rho_{x,y}$ is used in section "Impedance of cells with a LiBH4-LiI electrolyte" to evaluate the correlation of the electrolyte resistance *R* in the discharged state and the discharge capacity *c*. It is a measure of the linear correlation of two variables *x* and *y*. The coefficient is defined as

$$\rho_{x,y} = \frac{\mathrm{cov}(x, y)}{\sigma_x \sigma_y}, \quad [4]$$

i.e. the covariance of the two variables divided by the product of their standard deviations.[45] It takes on values ranging from −1 to 1, where 1 denotes full positive linear correlation, −1 denotes full negative linear correlation and 0 means no correlation.

Cyclic voltammetry measurements were performed on a Steel | $LiBH_4$-LiI | Li cell using a Princeton PARSTAT 2773 potentiostat. A scan rate of 1 mV/s was used. The voltage was cycled three times from 0 V to 2V, then three times from 0 V to 3 V, another three times from 0 V to 4 V and a final three times from 0 V to 5 V.

A galvanostatic electric signal was applied to a Steel | $LiBH_4$-LiI | Li cell to estimate the amount of Li^+ that could be deposited on the surface of the steel electrode (lithium plating), in order to get an idea of which process limits the discharge capacity of the all-solid-state batteries. A Princeton PARSTAT 2773 potentiostat was used for running a constant current of −10 μA through the cell.

Results and Discussion

Crystal structure.— A powder X-ray diffraction pattern of the 13/16$LiBH_4$ + 3/16LiI solid solution used for the all-solid-state battery cells is shown in Figure 1. The observed diffraction peaks all correspond to the crystal structure of hexagonal $LiBH_4$, and no diffraction peaks from LiI or orthorhombic $LiBH_4$ are detected. As seen in Figure 1, the peaks in the diffraction pattern are rather broad. This broadening effect has been found to be dominated by strain broadening after the ball milling, although the small crystallite size also contributes to the broadening.[35]

Cyclic voltammetry.— As mentioned in section 1, $LiBH_4$ has been shown to be electrochemically stable up to voltages of 5 V.[32] In order to investigate the electrochemical stability of the $LiBH_4$-LiI solid solution, cyclic voltammetry measurements were performed on a Steel | $LiBH_4$-LiI | Li cell containing 3/4$LiBH_4$ + 1/4 LiI. The results of the measurements are shown in Figure 2. Almost no current is drawn in the voltage range of 0–2 V, indicating that the electrolyte is stable in this range. No increase in current flow was observed in the range of 0–3 V until toward the end of the third (and last) cycle in that range, during which a small increase in the current flow was observed. This indicates that the electrolyte may be unstable under prolonged exposure to voltages close to 3 V. In the voltage ranges of 0–4 V and 0–5 V, a considerable current flows. During the measurement from 0–5 V, a total charge of $9.1*10^{-3}$ C is found to accumulate in the system. In the measurement from 0–5 V, the observed current decreases with each cycle, indicating that a passivating process takes place.

To see if a charge accumulation of this magnitude can be explained solely by a capacitive behavior of the system, this number can be compared to the expected charge accumulation in a simple parallel plate capacitor with $LiBH_4$-LiI as a dielectric. In such a capacitor, the capacitance is

$$C = \frac{Q}{U} = \frac{A\varepsilon_0\varepsilon_r}{d}, \qquad [5]$$

where U is the voltage between the plates, A is the area of each plate and d is the thickness of the dielectric. The constant ε_0 is the vacuum permittivity and ε_r is the relative permittivity of $LiBH_4$-LiI, which is estimated to be on the order of 10.[30] For a voltage of 5 V, the capacitive charge accumulation Q in the system is found to be on the order of 10^{-11} C using Eq. 4. It is thus clear that the charge accumulation cannot be explained by capacitive effects only. It is therefore expected that the charge accumulation during the measurements up to 4 V and 5 V occurs because of a decomposition of the electrolyte. Since pure $LiBH_4$ is electrochemically stable across a wider voltage range, it is most likely that it is iodine that begins to be drawn out of the solid solution already at a voltage of 3 V. It therefore seems that the operating voltage of batteries with LiBH4-LiI as an electrolyte must be constrained to voltages smaller than 3 V.

We have also assembled all-solid-state batteries with $LiFePO_4$ as a positive electrode instead of LTO. Such cells have an open circuit voltage (OCV) of approximately 3.3 V. These cells did not accept charging, and after trying to charge, the OCV dropped to around 2 V. However, a short plateau at around 3.5 V was observed during the attempts to charge the cells. Interestingly, the standard hydrogen electrode potential for $I_{2\,(s)} + 2e^- \Leftrightarrow 2I^-$ is 0.54 V, and for $Li^+ + e^- \Leftrightarrow Li_{(s)}$ the standard potential is −3.04 V. This suggests that extraction of iodine from the electrolyte takes place close to a voltage of 3.5 V, which has also been reported to occur in similar systems.[46,47] These observations on the $LiFePO_4$ cells strengthen our conclusion

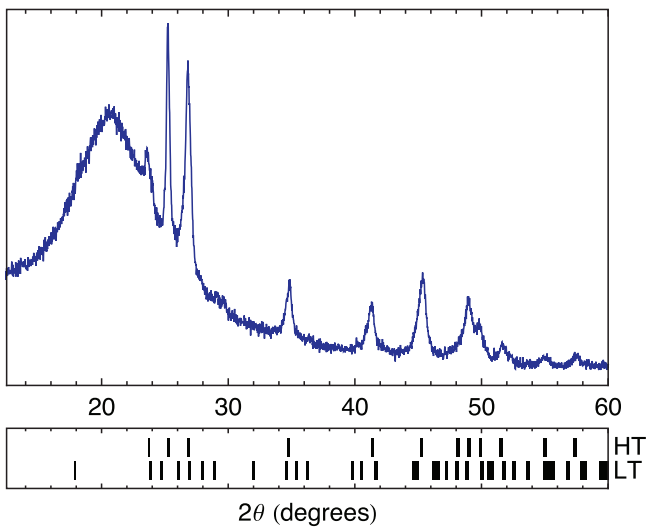

Figure 1 A powder X-ray diffraction pattern of a 13/16LiBH4 + 3/16LiI solid solution (18.75% LiI molar content). The tick marks below the diffraction pattern show the locations of the Bragg reflections of orthorhombic $LiBH_4$ (LT) and hexagonal $LiBH_4$ (HT).[26] Only the hexagonal phase is detected, and no diffraction peaks corresponding to orthogonal $LiBH_4$ or to LiI are detected. The large, broad bump centered at around 20° is due to the polyethylene sample holder.

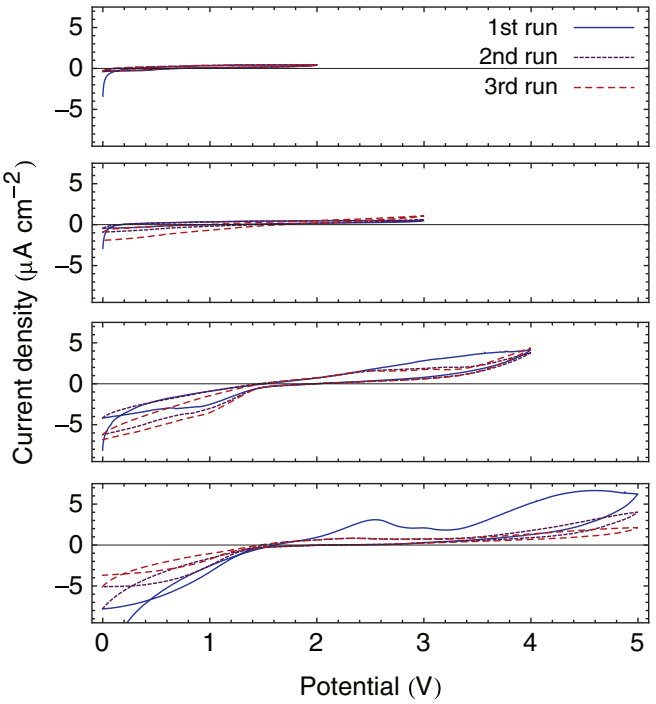

Figure 2 The results of a cyclic voltammetry measurement on a 3/4LiBH4 + 1/4LiI solid solution. A scan rate of 1 mV s^{-1} was used. The open circuit voltage of the cell at the start of the measurement was 1.12 V. Each graph shows three consecutive measurement cycles. The first cycle is shown with a solid, blue line, the second cycle is shown with a purple, dashed line and the third cycle is shown with a dashed, red line. Very low current values are observed when potentials up to 3 V are applied. However, when potentials up to 4 V and 5 V are applied, a larger current flows, indicating electrolysis of the solid solution. It is considered most likely that this corresponds to an extraction of iodine from the electrolyte.

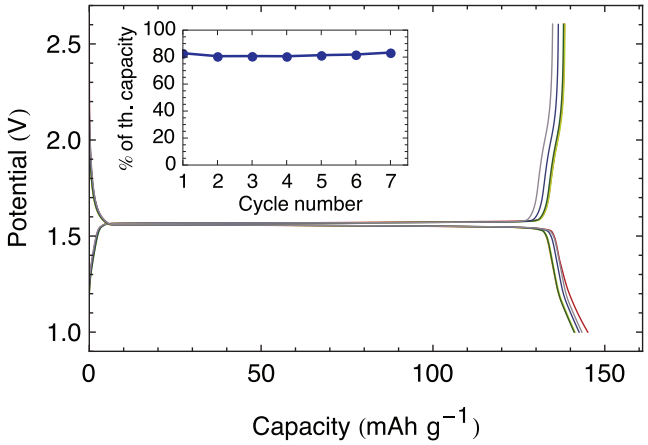

Figure 3 The first seven discharge/charge cycles of a LTO | $LiPF_6$ | Li battery cell. The measurement was performed at room temperature with a constant current of 10 μA (i.e. a current density of 12.7 μA cm^{-2}). The inset shows the development of the discharge capacity with increasing discharge cycle number. The discharge capacity and the overvoltage do not change significantly during the first seven cycles.

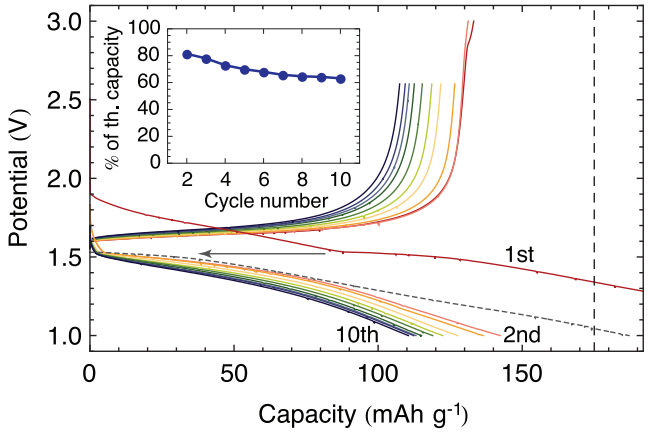

Figure 4 The first ten discharge and charge curves for a LTO | $LiBH_4$-LiI | Li battery cell. The measurements were performed at 60°C with a constant current of 10 μA (i.e. a current density of 12.7 μA cm^{-2}). During the first two charge runs, the upper voltage limit was set to 3.0 V, but was changed to 2.6 V for the remaining runs. The lower voltage limit was set to 1.0 V for all runs. A significant overvoltage and slope are observed, especially during discharge. The first discharge curve is much longer than the subsequent ones and continues until a capacity of 277 mAh g^{-1} is reached. The gray, dashed curve serves as a guide to the eye and shows how the first discharge curve would lie if it were translated to the left by 90 mAh g^{-1} so that it starts from approximately 1.54 V. The vertical, dashed line at 175 mAh g^{-1} indicates the theoretical Li^+ intercalation capacity of the LTO positive electrode. The inset shows how the capacity, expressed as a percentage of the theoretical capacity, decreases with every discharge cycle, starting from the second discharge.

that operating voltages above 3 V should be avoided in cells containing $LiBH_4$-LiI.

A cell with a liquid electrolyte.— Cells containing a liquid electrolyte were measured for comparison with the all-solid-state cells. Figure 3 shows the results of the first seven discharge and charge cycles of a battery cell containing a liquid electrolyte. The LTO | $LiPF_6$ | Li cells have a discharge capacity corresponding to approximately 82% of the theoretical capacity and retain this capacity over the first seven cycles, at least. The cells have an open circuit voltage (OCV) of 1.56 V. Both the charge and the discharge curves are very flat. The overvoltage is very low, or on the order of 10 mV. This overvoltage can, at least partly, be explained by noting that $Li_7Ti_5O_{12}$ has a slightly lower conductivity that $Li_4Ti_5O_{12}$.[48] The resistance of the cells is very low compared to the all-solid-state cells, or in the range of 10–100 Ω. The charge and discharge curves are highly reproducible, with only very small changes in capacity and overvoltage over the seven cycles. The excellent charge and discharge properties of this cell show that the experimental methods and the preparation of the LTO electrode work as expected, and provide a good reference point for the results on the all-solid-state cells presented in next section.

Charge and discharge of cells with a LiBH4-LiI electrolyte.— The charge and discharge curves for the first ten cycles of a LTO | $LiBH_4$-LiI | Li cell are shown in Figure 4. During the second discharge, the cell has a discharge capacity of around 142 mAh g^{-1}, corresponding to 81% of its theoretical discharge capacity. This is similar to the discharge capacity of the LTO | $LiPF_6$ | Li cells. The performance of the all-solid-state cell does, however, differ considerably from the cell containing a liquid electrolyte (see Figure 3) in that it has a larger overvoltage, the curves have a steeper slope and a higher loss of capacity is observed with cycling. An average discharge capacity loss of 1.6% per cycle was observed for an all-solid-state cell that was charged and discharged 200 times. Charge and discharge curves for that measurement are provided as supporting information.

One likely reason for the differences between the two cell types is that in the LTO | $LiPF_6$ | Li cell, the electrodes are soaked in the liquid electrolyte, but in an all-solid-state cell the electrodes have relatively well defined interfaces with the solid electrolyte. This most likely causes contact issues that would increase the resistance to Li^+ transport in the all-solid-state cell, which in turn may reduce the charge and discharge performance of the cell.

As shown in Figure 4, the first discharge exhibits a much larger capacity than the successive discharge runs, and even greatly surpasses the theoretical discharge capacity of the cell, which is 175 mAh/g. The presence of three distinct regions in the first discharge curve can be noted by observing the changes in its slope and shape. The first part of the curve lies above the expected open circuit voltage of the cell, and is therefore not expected to correspond to the intercalation of Li^+ in LTO, but rather to other electrochemical reactions or formation of interface layers in the cell. The curve has an almost constant slope until reaching 1.54 V, which is very close to the expected open circuit voltage of the cell. Here, the second region begins, as the slope of the curve changes and its shape becomes very similar to the shape of the subsequent discharge curves. This is indicated by the gray, dashed line in Figure 4, which is the first discharge curve shifted along the x-axis. This region is expected to correspond to the actual discharge of the cell, i.e. Li^+ intercalation in LTO. The third region of the first discharge curve begins at around 1.3 V, where the curve deviates from the shape of the subsequent discharge curves and again takes on a slope that is very similar to the slope of the first region. We expect the reason for this to be that the Li^+ intercalation reaction and the formation of the passivating layer possibly become concurring reactions at 1.3 V. In that case, the passivating layer formation may take over again during the last region of the curve. The total intercalation of Li^+ during the first discharge curve is thus expected to amount to approximately 140–150 mAh g^{-1}. The capacity exceeding this is expected to correspond to the electrochemical formation of new species close to the surface of the positive electrode, which may have a passivating effect.

This surprising finding was observed for the first discharge curves of all LTO | $LiBH_4$-LiI | Li cells measured during this work. This is, however, not observed for the LTO | $LiPF_6$ | Li cells, and is therefore expected to be related to the solid electrolyte. $LiBH_4$ is known to have a very good chemical stability toward lithium metal electrodes.[42] $LiBH_4$ is a strong reducing agent and is known to have a risk of reacting with oxidative positive electrodes, but we do not expect that $LiBH_4$ will reduce the LTO in the positive electrode at the potentials used in this work. The fact that more than 80% of the theoretical discharge capacity is available during the second discharge cycle supports the claim that $LiBH_4$ has not reacted with LTO during the first discharge run. $LiBH_4$ does, however, react readily with water and oxygen. Trace

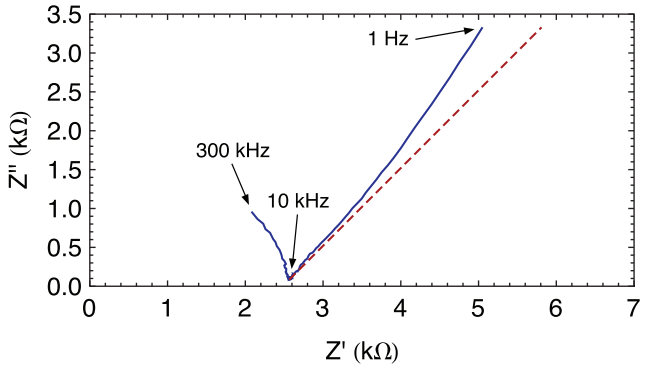

Figure 5 A Nyquist plot from an impedance spectroscopy measurement of a newly assembled all-solid-state cell. The cell was measured in the charged state, i.e. before the first cell discharge. The impedance spectrum can be fitted using the equivalent circuit model in Figure 6. The long tail arises due to diffusion and is described by the Warburg element, which has a constant phase of 45°. The diffusion is of a finite length and therefore the slope of tail increases toward its end. The red, dashed line has a slope of 45° and is only drawn on the graph as a guide to the eye.

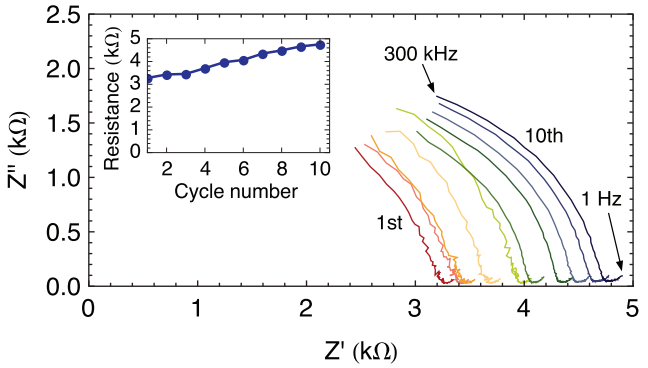

Figure 6 Nyquist plots from impedance spectroscopy measurements of the LTO | $LiBH_4$-LiI | Li cell in Figure 4 after the first 10 discharge runs. The frequency ranges from 300 kHz to 1 Hz and decreases from left to right in the plots. Only the right side of the high-frequency impedance arcs is visible in this frequency range, as higher frequencies than 300 kHz would be needed for the measurement to display the whole arcs. The resistance of the cell is taken as the intercept of the arcs with the Z' axis. The inset shows how the resistance increases with every discharge cycle.

amounts of atmospheric oxygen and/or moisture were most likely present in the samples when the cells were assembled, although the assembly took place inside an argon-filled glove box. It is also possible that such impurities can enter the cell in trace amounts during its operation. When a potential is applied to the cells, those impurities can oxidize $LiBH_4$ in an electrochemical redox reaction. In this reaction, charge would be transferred through the electrodes without any lithium intercalation in LTO taking place, which would explain how the first discharge can appear to have a capacity greatly exceeding the lithium intercalation capacity of the LTO electrode. The species formed in the reaction would form especially at the interface with the positive electrode. It should be noted that the mass of the electrolyte exceeds the mass of LTO in the cell by more than a factor of 100. The reaction of trace amounts of impurities with $LiBH_4$ can therefore easily have a large effect on the measured electron transport through the cell. Further research is needed to explain the behavior during the first discharge with certainty.

It should furthermore be noted that the battery cells that were prepared for this work were all enclosed in a thick PEEK die and situated between two steel pistons; a setup which is unfortunately not well suited for in-situ studies of the phase composition and the morphology of the passivation layers in the cells. The pelletized cells are furthermore destroyed upon removal from the sample holder, making subsequent characterization extremely difficult. For identifying the passivating layers, a new design of the sample holder and characterization methods such as X-ray diffraction (XRD), X-ray-photon spectroscopy (XPS) and energy-dispersive X-ray spectroscopy (EDS) would clearly be beneficial in future studies.

Each discharge curve in Figure 4 is slightly longer than the preceding charge curve. As a result, the coulombic efficiency of the cell, defined in Equation 3, appears to be slightly higher than 100% for each cycle. A graph of the coulombic efficiency as a function of cycle number is provided as supporting information. As discussed above, the measured charge transfer during the discharge run is a combination of the charge transfer due to the formation of a passivating areas and the charge transfer due to the intercalation of Li^+ in LTO. During charge, the current is reversed and less (if any) fraction of the charge contributes to the formation of the passivating areas. Because the formation of the passivating areas is a non-reversible process, the charge fraction that is used for the formation of those areas rather than for the Li^+ intercalation reaction appears as a coulombic efficiency above 100% when calculated using Equation 3. The coulombic efficiency thus gives an indication of the extent of the passivating layer formation during each cycle.

Impedance of cells with a LiBH4-LiI electrolyte.— The impedance to Li^+ conduction in the cells was measured directly after assembling the cells as well as after each discharge. A Nyquist plot of a newly assembled cell is shown in Figure 5. Nyquist plots measured after the ten first discharge cycles are shown in Figure 6. Additional Nyquist plots, measured after discharge of an all-solid-state cell that was charged and discharged 200 times, are provided as supporting information.

The Nyquist plots were fitted using the equivalent circuit model shown in Figure 7, which is composed of an *(RQ)* circuit and a Randles circuit[49] connected in series. The large, high-frequency arc in each Nyquist plot was fitted with the *(RQ)* sub-circuit. The large arc of the newly assembled cell arises due to the impedance to Li^+ conduction through the bulk and the grain boundaries of the solid electrolyte.[35] The electrolyte is expected to have the largest impedance contribution of the cell components in the newly assembled cell, based on its thickness and Li^+ conductivity. Note that it cannot be excluded that the electrolyte contribution to the impedance spectrum is in fact comprised of two or more arcs of different sizes that completely overlap in the Nyquist plot, i.e. one arc that corresponds to the bulk impedance and other arcs that correspond to grain boundary impedance[50,51] It is, however, not possible to distinguish multiple electrolyte arcs in the Nyquist plots in this work. In the equivalent circuit model of the cell impedance in Figure 7, the *(RQ)* circuit is thus interpreted as the total electrolyte contribution to the impedance in the samples. The long tail at the low frequency end in Figure 5 and the small tails at the low-frequency end of each Nyquist plot in Figure 6 are described by the Randles circuit. The Randles circuit describes an arc and a tail,

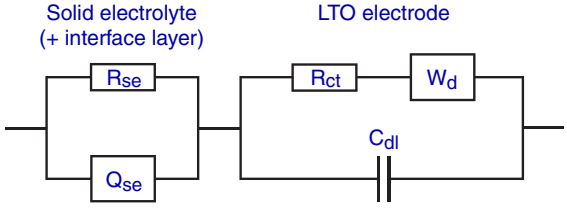

Figure 7 The equivalent circuit used to model the measured impedance spectra. R denotes a resistor, C a capacitor, Q is a constant-phase element (CPE) and W is a Warburg element (a distributed circuit element with a constant phase of 45°). The circuit elements R_{se} and Q_{se} account for the combined contribution from the solid electrolyte and a possible interface layer between the electrolyte and the LTO electrode. The sub-circuit on the right is the Randles circuit, which describes the contribution of the LTO electrode. R_{ct} denotes a charge transfer resistance in the electrode, C_{dl} is a double-layer capacitance at the electrode and W_d describes Li^+ diffusion.

and small arcs are most likely hidden within the tails in the Nyquist plots. The circuit describes the impedance spectrum of a lithium intercalation electrode,[49,52] i.e. the LTO electrode. The components in the circuit correspond to a Li^+ charge transfer resistance in the LTO electrode (R_{ct}), a double-layer capacitance at the LTO electrode interface (C_{dl}) and a finite-length diffusion of Li^+ to and from the reaction interface between the LTO electrode and the electrolyte (W_d). No contribution to the impedance spectrum is observed from the lithium electrodes,[35] as it is most likely hidden within the arc corresponding to the electrolyte.

The impedance of the low-frequency tails in Figure 6 is smaller than that of the high-frequency arcs by approximately a factor of 100, and it proved difficult to obtain reliable values for the resistance R_{ct} in the equivalent circuit fits. Furthermore, the impedance of the large, high-frequency arcs in the Nyquist plots increases substantially with each charge and discharge cycle number, while the impedance of the low-frequency tails shows very small changes. Because of this, the small, constant contribution from the resistance R_{ct} is neglected in the following discussion and the cell resistance $R \approx R_{se}$ is taken to be the point of intersection between the Z' axis and the low-frequency end of the large arc. Using this approximation, the cell resistance after the first discharge is found to be around 3.2 kΩ. This is a very large resistance compared to the LTO | $LiPF_6$ | Li cell, but can largely be explained by the fact that the conductivity of the $LiBH_4$-LiI solid solution at 60°C is at least 12 times lower than that of 1 M $LiPF_6$ in EC:DMC.[4,35]

Further evidence for the formation of passivating areas in the cell can be found by considering the Nyquist plots in Figures 5 and 6. A Nyquist plot of the newly assembled LTO | $LiBH_4$-LiI | Li cell, before discharging it for the first time, is shown in Figure 5. The plot shows that the cell has a considerably lower resistance (approximately 2.5 kΩ) in the newly assembled state than after it has been discharged once (approximately 3.2 kΩ). The plot also features a long tail with an initial slope of around 45° and a slightly increasing slope with decreased frequency. As discussed earlier, the tail arises due to finite-length diffusion of Li^+ to the reaction surface of the LTO electrode and the electrolyte and can be described by a Warburg element. This tail is not observed in any of the other impedance spectra, which suggests that the time dependency of this diffusion changes during the first discharge of the cell, so that it is not observed within the measured frequency range. This change in the diffusion time dependency, as well as the increase in resistance, could be explained by the formation of passivating areas in the cell during the first discharge. The impedance of those areas would not necessarily be identified in the impedance spectra of the discharged cell, because its contribution to the impedance could easily be overshadowed by the larger contribution from the electrolyte impedance.

The charge and discharge curves in Figure 4 do not exhibit flat plateaus, but all have a considerable slope. Towards the end of the curves, the discharge curves are observed to have a steeper slope than the charge curves. The slope can probably partially be explained by contact issues between the LTO electrode and the electrolyte. It is possible that during discharge, some channels across the electrode-electrolyte interface get blocked. This could for example happen if poorly conducting layers grow too thick and hinder Li^+ transport across the interface. This would make Li^+ intercalation in the LTO electrode increasingly difficult as the discharge proceeds. The increased slope toward the end of the discharge curves probably arises because it would be natural for Li^+ to first be intercalated into the areas of the LTO electrode that are in good contact with the electrolyte. As the discharge proceeds, the intercalation must take place in areas with ever less contact, resulting in an ever-greater overvoltage and consequently a steeper slope of the discharge curve. At the set potential limit of 1.0 V, this development most likely still takes place and some discharge capacity remains in the cell. This can explain why there is not a sudden change in the slope of the discharge curves at the end of each discharge run, as there is for the charge runs. Charge and discharge curves for various discharge rates, as well as Tafel plots of the overvoltage during discharge are provided as supporting information.

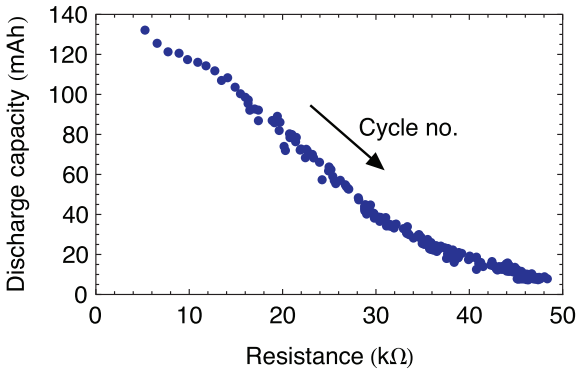

Figure 8 The discharge capacity as a function of the cell resistance from a measurement of 200 charge and discharge cycles. The arrow indicates how the number of discharge cycles increases. The two variables follow a near-linear relationship, with a Pearson correlation coefficient of −0.975.

Capacity and resistance in the All-Solid-State cells.— The inset in Figure 4 shows how the discharge capacity of the LTO | $LiBH_4$-LiI | Li cell decreases with the number of charge and discharge cycles. Furthermore, the inset in Figure 6 shows how the cell resistance, as estimated from the Nyquist plots, increases with the number of charge and discharge cycles. To see how well these parameters are correlated, a plot of the discharge capacity as a function of the resistance is shown in Figure 8. In this plot, data from measurements of 200 charge and discharge cycles of a single LTO | $LiBH_4$-LiI | Li cell were used (charge/discharge curves and Nyquist plots for this cell can be found in the supporting information). As seen in Figure 8, the discharge capacity and the resistance values are highly correlated, with the plot of the two closely resembling a straight line. The Pearson product-moment correlation coefficient (see Equation 4) of the two variables is $\rho_{c,R} = -0.975$, which indicates an almost linear negative correlation. The excellent correlation of the discharge capacity and the cell resistance strongly suggests that the development of both parameters with the number of charge and discharge cycles mostly has its roots in the same physical process in the cell.

The processes that can explain the correlation of the discharge capacity and resistance are a decrease in contact between the LTO electrode and the solid electrolyte with cycle number, and a possible formation of passivating areas in the cell that hinder Li^+ transport and intercalation. This can be explained as follows: The slope of each discharge curve, especially toward its end, governs how quickly the voltage limit of 1.0 V is reached upon discharge. The slope thus has a major influence on how large the discharge capacity of the cell will be. As discussed in sections "Charge and discharge of cells with a $LiBH_4$-LiI electrolyte" and "Impedance of cells with a $LiBH_4$-LiI electrolyte," we expect the slope to be a consequence of insufficient contact between the electrolyte and the LTO electrode or of the formation of passivating areas. The increase in slope with every discharge curve can be explained further by loss of contact areas on this interface and/or by an increased growth of the poorly conductive areas. However, such loss of contact would also manifest as an increase in the measured resistance. If the effective contact area A between the electrolyte and one of the electrodes decreases, this leads to an increase in R (see Eq. 2), assuming that the thickness and the conductivity of the electrolyte material are constant. Thus, the loss of contact between the LTO electrode and the solid electrolyte most probably explains both the development of the cell resistance and of the discharge capacity with the number of cycles.

Using Equation 2, it can be estimated how much contact area would need to be lost (or rendered passive) on the electrode-electrolyte interface for such change to fully explain the increased cell resistance. In Figure 7, the measured cell resistance is 3.65 kΩ after the first discharge, but has increased to 47.6 kΩ after the 200th discharge. This corresponds to a loss of 92% of the contact area between the LTO

electrode and the electrolyte, assuming that all other contributions to the resistance remain constant. That assumption may, however, not hold strictly as other effects might contribute to an increase in the cell resistance. An example of this could be decreased grain boundary conduction within the electrolyte. The Li^+ conduction within the electrolyte is thought to take place at least partly along its internal grain boundaries, and a loss of such boundaries due to sintering (as the batteries operate at 60°C for long periods of time) might somewhat decrease the Li^+ conductivity in the electrolyte.[35] Such contribution to an increased resistance would lower the estimated loss in contact area needed to account for the change in resistance. The contact issues and possible passivation issues can, however, explain the excellent correlation observed between the increase in resistance and the decrease in discharge capacity. They are therefore thought to be the major factors in the development of the cell resistance with an increased number of charge and discharge cycles.

Charge transfer in the All-Solid-State cells.— To investigate which processes could be limiting for the capacity of the Li | LiBH4-LiI | LTO cells, a galvanostatic signal was applied to a Steel | $LiBH_4$-LiI | Li cell. This cell can be viewed as a half-cell where the LTO electrode has been removed. The supporting information includes a graph of the voltage over the Steel | $LiBH_4$-LiI | Li cell as a function of capacity while a constant current of -10 μA was applied to the cell. Approximately 490 μAh of Li^+ are transferred, corresponding to a charge transfer of 1.76 C, before the voltage drops and the Li^+ transport stops. The lithium-steel interface was subsequently examined. It was clearly observed that a thin layer of lithium had been plated onto the steel electrode during the charge transfer. It is not clear why Li^+ transfer stopped at this point, but this is most likely due to contact issues between the electrodes and the solid electrolyte. Such issues could arise in the all-solid-state cell when a large number of Li have been removed from one side and deposited on the other, as the electrodes in such a cell are not soaked in a liquid electrolyte.

The theoretical capacity of the LTO electrodes is 175 mAh g^{-1}. As discussed in section "Charge and discharge of cells with a LiBH4-LiI electrolyte," it proved possible to reach 80–90% of this capacity by using LTO electrodes with a thickness of 3 μm and a mass of 0.37 mg. This capacity corresponds to a charge transfer of around 0.20 C. However, if the thickness of the electrode is increased, the percentage of the theoretical capacity that can be reached decreases. During this work, LTO | $LiBH_4$-LiI | Li cells with electrodes with a thickness of 140 μm and a mass of 17 mg were also assembled and measured. Interestingly, these cells only reached less than 5% of their theoretical capacity, corresponding to a charge transfer of around 0.4 C. Since the theoretical charge transfer capacity of these cells is around 9.5 C, one would expect them to transfer charge at least equal to that of the Steel | LiBH4-LiI | Li cells, or 1.76 C.

The observation that the charge transfer capacity in the all-solid-state cells is much greater without the LTO electrode than with it, leads to the conclusion that a capacity limiting process in the Li | $LiBH_4$-LiI | LTO batteries is on the LTO electrode side and most probably has to do with Li^+ intercalation in LTO. Such problems are not observed in the LTO | $LiPF_6$ | Li cell discussed in section "A cell with a liquid electrolyte," but in the all-solid-state cells, the LTO electrode is not soaked in the electrolyte. This can give rise to contact issues, which prevent the intercalation from taking place in LTO layers far away from the electrolyte-electrolyte interface. A formation of an inactive layer at the electrode-electrolyte interface could also lead to difficulties with Li^+ intercalation.

Conclusions

The $LiBH_4$-LiI solid solution has a conductivity close to 1 mS cm^{-1} at 60°C[33,35] and is a promising solid electrolyte material for all-solid-state lithium batteries. It is, however, not stable at potentials above 3 V, as observed using cyclic voltammetry measurements. Lithium titanate ($Li_4Ti_5O_{12}$) was used as a positive electrode in this work, both because it has an open circuit voltage against lithium of 1.56 V (i.e. well below 3 V), and because it shows virtually no volume expansion upon lithium intercalation. The Li | LiBH4-LiI | LTO battery cells measured in this work have an initial discharge capacity of around 142 mAh g^{-1}, which is around 81% of the theoretical capacity of LTO. This is very similar to a Li | $LiPF_6$ | LTO cell, which was measured for comparison and has a discharge capacity of around 82% of its theoretical capacity. The all-solid-state cells do, however, have a higher overvoltage and a steeper slope in the charge and discharge curves than the cell with the liquid electrolyte. Furthermore, their discharge capacity retention is worse than that of the liquid cell, and 1.6% of the capacity is lost on average during each charge/discharge cycle.

The resistance of the all-solid-state cells in the discharged state is on the order of a few kΩ, which is typically considered rather large in a battery cell. The electrolyte provides by far the largest resistance contribution of the cell components. There is an almost linear correlation between the development of the discharge capacity of the cells and the change in the measured resistance after discharge when the cells are charged and discharged numerous times. This supports that the increased resistance is responsible for most of the loss in discharge capacity. The increase in resistance can be explained by an insufficient contact between the electrolyte and the LTO electrode, due to e.g. a rough interface with some empty space between the two components, and a possible formation of a passivating interface layer. This would hinder Li^+ intercalation into some areas of the interface and cause an increased overpotential at the LTO electrode. As each discharge proceeds, the most energetically favourable intercalation spots are filled up first and the intercalation process becomes increasingly difficult, causing an increased overvoltage. This leads to a steeper slope in the discharge curves, which in turn decreases the discharge capacity. Furthermore, such contact issues decrease the effective electrode area in the cell, causing an increase in the measured resistance.

Further research on batteries with LiBH4-LiI as an electrolyte is needed in order to fully understand this battery cell, especially regarding the interface of the electrolyte and the positive electrode. Many of the challenges with using this electrolyte material in battery cells could probably be solved by optimizing the fabrication methods. More sophisticated techniques than mechanical pressing, such as deposition or cold rolling, could allow for a much thinner layer of electrolyte, thereby reducing the resistance of the cells substantially. The incorporation of small amounts of the electrolyte material in cathodes produced by those methods could lower the interfacial resistance of the cells ever further. It could furthermore be beneficial to fabricate cells where the electrolyte has a lower porosity than 0.5, as this could decrease the total resistance of the electrolyte and reduce the risk of lithium dendrite formation even more. Further research on the interface between the electrolyte and the LTO electrode will hopefully give better insight into the relevant processes and more knowledge about how to prevent contact issues from affecting the performance of the all-solid-state battery cells.

Acknowledgments

The authors acknowledge support from the Danish Ministry of Science Globalization Fund, The Copenhagen Cleantech Cluster and the Danish Ministry for Science, Innovation and Higher Education. We would also like to thank Dr. Johan Hjelm at the Department of Energy Conversion and Storage, Technical University of Denmark, for valuable discussions.

References

1. J.-M. Tarascon and M. Armand, *Nature*, **414**, 359 (2001).
2. P. Knauth, *Solid State Ionics*, **180**, 911 (2009).
3. J. B. Goodenough and Y. Kim, *Chem. Mater.*, **22**, 587 (2010).
4. J. Y. Song, Y. Y. Wang, and C. C. Wan, *J. Electrochem. Soc.*, **147**, 3219 (2000).
5. J.-M. Tarascon, *Phil. Trans. R. Soc. A*, **368**, 3227 (2010).
6. A. Rabenau, *Solid State Ionics*, **6**, 277 (1982).
7. A. G. Belous, G. N. Novitskaya, S. V. Polyanetskaya, and Y. I. Gornikov, *Izv. Akad. Nauk SSSR*, **23**, 470 (1987).
8. Y. Inaguma et al., *Solid State Commun.*, **86**, 689 (1993).
9. O. Bohnke, *Solid State Ionics*, **179**, 9 (2008).

10. V. Thangadurai, J. Schwenzel, and W. Weppner, *Ionics (Kiel).*, **11**, 11 (2005).
11. H. Aono, E. Sugimoto, Y. Sadaoka, N. Imanaka, and G. Adachi, *Solid State Ionics*, **47**, 257 (1991).
12. K. Arbi, J. M. Rojo, and J. Sanz, *J. Eur. Ceram. Soc.*, **27**, 4215 (2007).
13. P. G. Bruce and A. R. West, *J. Electrochem. Soc.*, **130**, 662 (1983).
14. S. Stramare, V. Thangadurai, and W. Weppner, *Chem. Mater.*, **15**, 3974 (2003).
15. N. Kamaya et al., *Nat. Mater.*, **10**, 682 (2011).
16. R. J. Brodd, W. Huang, and J. R. Akridge, *Macromol. Symp.*, **159**, 229 (2000).
17. M. Park, X. Zhang, M. Chung, G. B. Less, and A. M. Sastry, *J. Power Sources*, **195**, 7904 (2010).
18. A. Züttel et al., *J. Alloy. Comp.*, **356–357**, 515 (2003).
19. Z. Łodziana and T. Vegge, *Phys. Rev. Lett.*, **93**, 145501 (2004).
20. J. K. Kang, S. Y. Kim, Y. S. Han, R. P. Muller, and W. a. Goddard, *Appl. Phys. Lett.*, **87**, 11904 (2005).
21. Z. Łodziana and T. Vegge, *Phys. Rev. Lett.*, **97**, 119602 (2006).
22. L. Mosegaard et al., *J. Alloy. Comp.*, **446–447**, 301 (2007).
23. D. Blanchard, Q. Shi, C. B. Boothroyd, and T. Vegge, *J. Phys. Chem. C*, **113**, 14059 (2009).
24. J. Lang, A. Gerhauser, Y. Filinchuk, T. Klassen, and J. Huot, *Crystals*, **2**, 1 (2012).
25. N. Verdal et al., *J. Phys. Chem. C*, **117**, 17983 (2013).
26. J.-P. Soulié, G. Renaudin, R. Černý, and R. Y. K, *J. Alloy. Comp.*, **346**, 200 (2002).
27. M. Matsuo, Y. Nakamori, S. Orimo, H. Maekawa, and H. Takamura, *Appl. Phys. Lett.*, **91**, 224103 (2007).
28. V. Epp and M. Wilkening, *Phys. Rev. B*, **82**, 020301 (2010).
29. T. Ikeshoji et al., *Phys. Rev. B*, **83**, 144301 (2011).
30. K. Miwa, N. Ohba, S. Towata, Y. Nakamori, and S. Orimo, *Phys. Rev. B*, **69**, 1 (2004).
31. E. Orgaz, A. Membrillo, R. Castañeda, and A. Aburto, *J. Alloys Compd.*, **404–406**, 176 (2005).
32. M. Matsuo and S. Orimo, *Adv. En. Mat.*, **1**, 161 (2011).
33. H. Maekawa et al., *J. Am. Chem. Soc.*, **131**, 894 (2009).
34. H. Oguchi et al., *Appl. Phys. Lett.*, **94**, 141912 (2009).
35. D. Sveinbjörnsson et al., *J. Phys. Chem. C*, **117**, 3249 (2013).
36. R. Miyazaki et al., *Solid State Ionics*, **192**, 143 (2011).
37. L. H. Rude et al., *J. Alloy. Comp.*, **509**, 8299 (2011).
38. V. Epp and M. Wilkening, *ChemPhysChem*, **14**, 3706 (2013).
39. J. S. G. Myrdal, D. Blanchard, D. Sveinbjörnsson, and T. Vegge, *J. Phys. Chem. C*, **117**, 9084 (2013).
40. N. Verdal, T. J. Udovic, J. J. Rush, H. Wu, and A. V. Skripov, *J. Phys. Chem. C*, **117**, 12010 (2013).
41. A. Unemoto, M. Matsuo, and S. Orimo, *Adv. Funct. Mater.*, **24**, 2266 (2014).
42. K. Takahashi et al., *J. Power Sources*, **226**, 61 (2013).
43. K. Takahashi, H. Maekawa, and H. Takamura, *Solid State Ionics* (2013).
44. T. Ohzuku, A. Ueda, and N. Yamamota, *J. Electrochem. Soc.*, **142**, 1431 (1995).
45. K. Pearson, *Philos. Trans. R. Soc. London Ser. A*, **187**, 253 (1896).
46. R. D. Armstrong and K. Landles, *J. Appl. Electrochem.*, **11**, 247 (1981).
47. R. D. Armstrong, *Solid State Ionics*, **5**, 397 (1981).
48. D. V. Safronov, S. A. Novikova, A. M. Skundin, and A. B. Yaroslavtsev, *Inorg. Mater.*, **48**, 57 (2012).
49. J. E. B. Randles, *Discuss. Faraday Soc.*, **1**, 11 (1947).
50. N. M. Beekmans and L. Heyne, *Electrochim. Acta*, **21**, 303 (1976).
51. S. M. Haile, D. L. West, and J. Campbell, *J. Mat. Res.*, **13**, 1576 (1998).
52. E. Barsoukov, in *Fundamentals of Impedance Spectroscopy*, E. Barsoukov and J. R. Macdonald, Editors, p. 430–468, Wiley-Interscience (2005).

Supporting Information: The $LiBH_4$-LiI Solid Solution as an Electrolyte in an All-Solid-State Battery

Dadi Sveinbjörnsson, Ane Sælland Christiansen, Rasmus Viskinde, Poul Norby, Tejs Vegge.

Department of Energy Conversion and Storage, Technical University of Denmark, Frederiksborgvej 399, 4000 Roskilde, Denmark.

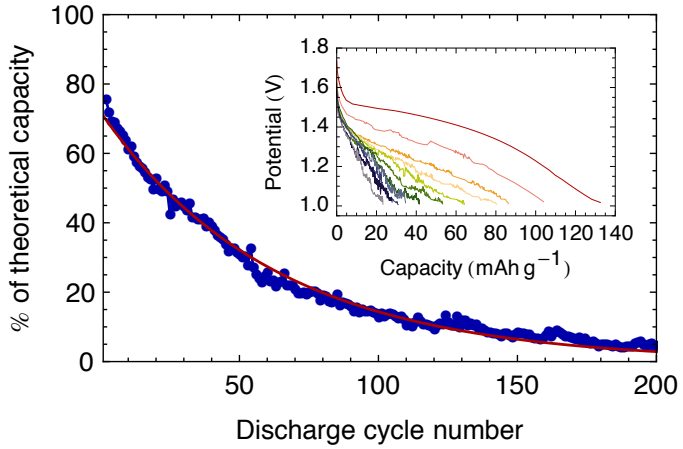

Figure S1 The development of the discharge capacity of a LTO | $LiBH_4$-LiI | Li cell over 200 discharge/charge cycles. The inset shows the discharge curves of every tenth measurement from cycles number 2 to 102 for a discharge current of 10 µA (i.e. a current density of 12.7 µA cm^{-2}). The average discharge capacity retention per cycle is 98.4%, which means 1.6% capacity degradation in every charge-discharge cycle.

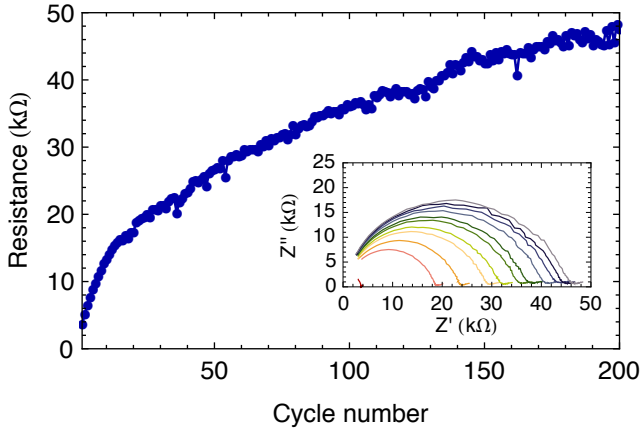

Figure S2 The development of the cell resistance after discharge of the LTO | $LiBH_4$-LiI | Li cell from Figure S1. The resistance increases by more than a factor of 10 over the course of 200 charge and discharge cycles. The inset shows the Nyquist plots of every 20th measurement from cycle number 1 to 191.

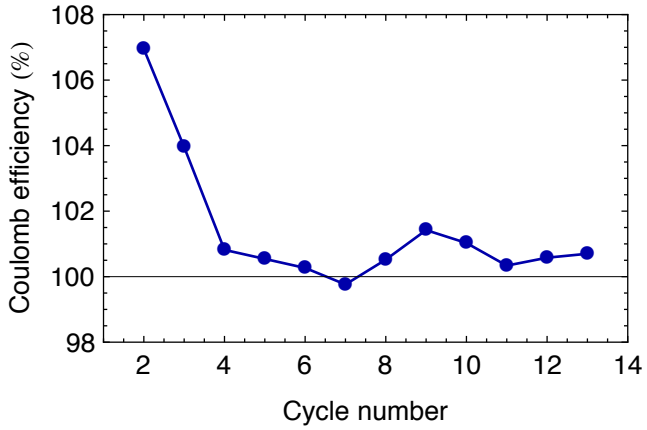

Figure S3 The coulombic efficiency of a LTO | $LiBH_4$-LiI | Li cell, calculated using Equation 3. The coulombic efficiency appears to be greater than 100% for each discharge, but this is most likely because a part of the charge that is transferred during discharge goes into the formation of an interface layer between the LTO electrode and the electrolyte. As a consequence, not all charge that is transferred takes part in the actual discharge of the cell by Li^+ intercalation into LTO.

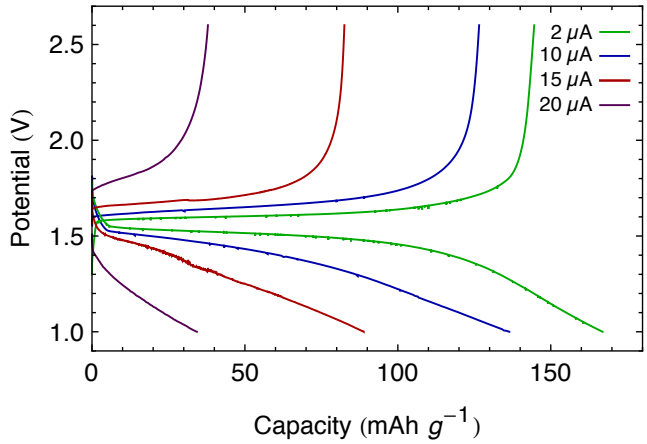

Figure S4 Charge and discharge curves of a LTO | $LiBH_4$-LiI | Li cell, measured for various charge rates. As expected, the overvoltage grows with increasing current, and correspondingly the capacity decreases. At a current of 2 μA (i.e. a current density of 2.54 μA cm^{-2}), the charge and discharge curves are rather flat, but the curves quickly become steeper with increased current. This is most probably an indication that the conductivity in the cell, or the contact at the interface of the electrolyte and the LTO electrode, are not good enough to sustain higher currents.

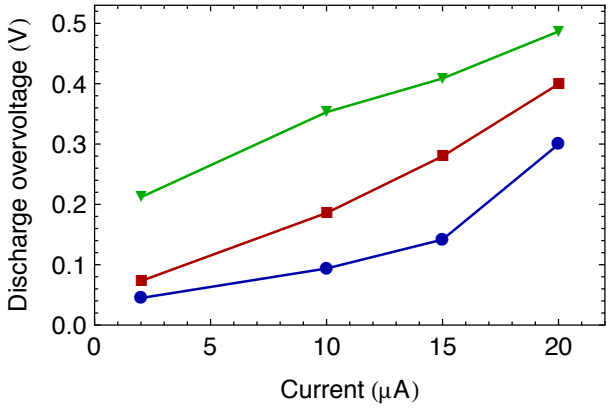

Figure 5 A Tafel plot of the development of the overvoltage with current for a LTO | $LiBH_4$-LiI | Li cell. The overvoltage at three different degrees of discharge are shown; 25% discharge (blue circles), 50% discharge (red rectangles) and 75% discharge (green triangles).

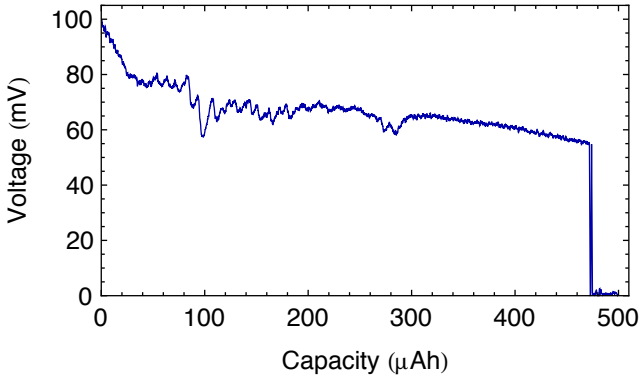

Figure S6 The voltage across a Steel | $LiBH_4$-LiI | Li cell during Li^+ transfer from the lithium electrode to the steel electrode (lithium plating on steel) at a constant current of -10 μA (i.e. a current density of 12.7 μA cm^{-2}). Approximately 490 μAh of Li^+ are transferred, corresponding to a charge transfer of 1.76 C. This is almost nine times the amount of charge transfer observed in the LTO | $LiBH_4$-LiI | Li cells, which shows that lithium transfer through the electrolyte is not a limiting factor in the capacity of the all-solid-state battery cells.